Nucleation and Equilibration via Surface Diffusion: An Experimental Study

A thesis submitted in partial fulfilment
of the requirements for the Degree of

Doctor of Philosophy in Physics
in the
University of Canterbury

by

David N. McCarthy

Department of Physics and Astronomy
University of Canterbury
2008

Acknowledgements

Firstly thankyou to my supervisor Simon Brown. I must admit to attending our meetings with some trepidation during the early stages of the thesis. I was always a little unsure of the importance of my results. Without fail though, I would leave our meetings with a stronger belief in the project, and with a clear direction for the next portion of work. This thesis has been a very positive experience for me, due largely to your good humour and support.

To Milo Kral and Suruj Seunarine, my co and associate supervisors, thankyou for your support. Milo, your input to the rod simulations encouraged me to reassess the work from a very fundamental perspective. As a result, I developed a deeper understanding of crystal growth, which benefited each section of the thesis.

Without colleagues and collaborators, a thesis would be a rather dull (and difficult) experience. Thanks to a long line of officemates and postdocs: Shelley, Martin, Rene, Ahmed, David, Toby, Jim, Franck, Euan, Pierre, Gaelle, Kiri, Daniel, Sattar. The office has always been a fun and productive environment. Thanks also to Shaun Hendy and his group at IRL, for being a helpful and friendly source of coding expertise.

Obviously a significant amount of this thesis was spent in the lab. With all the pumps, heaters, and adjustments to sample holders, help was constantly required from the mechanical and electrical technicians. Thanks to: Owen, Bob, Graeme Kershaw, Steve, Ross, Graeme Plank, and even Russel from Chemistry. Your technical know how and friendly advice was always appreciated.

Last but not least, my family. You've been wondering what i've been doing for the last (nearly) four years. This proves it wasn't all fun and games!

Abstract

Structures grown via self-assembly are a unique field in nanotechnology. The morphology of self-assembled structures is affected by the balance between kinetics and thermodynamics during growth. Hence structures with tailored morphologies and properties can be created with adjustments in growth conditions. In this thesis we study crystal nucleation and equilibration, for both real and model systems. The growth of thin bismuth films is investigated on three atomically flat surfaces; Mica, Molybdenum di Sulphide (MoS_2), and highly oriented pyrolitic graphite (HOPG). Films are grown under UHV conditions, and characterised using scanning electron microscopy and atomic force microscopy.

For coverages of only a few monolayers, bismuth particles are found to aggregate into flat, isolated islands. Islands have characteristic heights and morphologies for each substrate. By altering the deposition flux and coverage, the island density and morphology can be manipulated. On HOPG substrates, planar islands grown at low flux are replaced by 1D structures at high temperature. These anisotopic structures result from an anisotropy in bond strengths at the crystal-vapour interface.

Depositing Bi on HOPG substrates at low flux or high temperature conditions produces nanorods aligned (roughly) perpendicular to step edges on the graphite. The aspect ratios (ARs) of these 1D structures are found to increase as the deposition flux is lowered, or the substrate temperature is increased. The Arrhenius dependence of the AR is determined from experiment. A Kinetic Monte Carlo (KMC) model for high AR step-edge aggregates was developed, determining the likely growth mechanism for the nanorods. A scaling regime devised from the KMC results predicts the dependence of nanorod ARs on flux and temperature, and allows an estimation of the energy binding Bi dimers to the sides of nanorods.

Thin films can also be grown via the self-assembly of atomic clusters. After deposition coalescence of clusters has implications for the film morphology, and properties. We use KMC simulations to investigate the coalescence of pairs of 3D atomic clusters (15000 to 130000 atoms in size) via lattice based surface diffusion. For early coalescence stages, the radius of the neck region connecting the two clusters is found to develop with a different powerlaw to classical theory. For later coalescence stages, when the nucleation of new atomic layers on facets of the cluster is required for further coalescence the temperature, cluster size, and cluster orientation all influence the coalescence. Equilibration times for clusters coalescing at high temperature are found to be limited by the dissociation of atomic layers.

Contents

List of Tables

List of Figures

Preamble

Nanoscience and Nanotechnology

Nanoscience is the study of materials with dimensions from 100 nm down to a single atom (∼0.5 nm). At the lower end of the scale, materials can have markedly different properties to their bulk. The two main reasons for this are the larger surface area to volume ratios, and the emergence of quantum effects. A classic example of size-dependence is light emission from semi conducting quantum dots. The optical properties are due to quantum confinement of electrons within the dot, and the emission wavelength depends on the size of the dot [1].

Nanotechnology is the art of manipulating materials on an atomic or molecular scale. It is the application focused branch of nanoscience, with the potential to revolutionise numerous scientific fields: circuitry, biology, medicine and energy all stand to benefit from advances in nanotechnology. In these fields, nanotechnology is predicted to have advantages of cost, speed, and accuracy over conventional technologies.

The electronics industry clearly benefits from nanotechnology with the miniaturisation of integrated circuitry - desktop PCs now include transistors with sub 45 nm gate lengths, 32 nm transistors are set for production in 2009 [2]. Nanotechnology has potential to make more accurate gas or light sensors - nanotech materials potentially having greater selectivity and reliability than current sensors. Solar cells are being developed using nanotechnology to enable more efficient conversion of light into electricity.

Nowadays, nanotechnology is providing solutions to some of the biggest problem areas of human health, such as cancer therapy and pathogen detection [3]. Nanoparticles, due to their size and specificity, can provide safe and accurate vehicles for transporting drugs to tumors or diseased cells [4]. The focused drug delivery increases the effectiveness of the treatment, while reducing damage to healthy cells. Luminescent quantum dots have found use as biological markers [5], the small spectral linewidth and particle stability offer advantageous properties over conventional organic-dye markers. Hartgerink *et al.* [6] have replicated the construction of a bone-like material using nanotechnology, the results potentially aiding in bone reconstruction.

Possibly the most exciting aspect of nanoscience is the variety of materials yet to be tested at small scales, and the unknown properties these new materials might exhibit.

Self Assembly

A popular field in nanoscience is self-assembly. Self-assembly occurs in numerous natural systems, creating order from disorder, in an effort to minimise the free energy. Consituents of a self-assembling system must be able to move and interact with other components in the system. Some fascinating examples exist e.g. abalone proteins form a membrane on which $CaCO_3$ self-assembles, creating an extremely tough shell from otherwise weak constituent materials [7].

A disordered system of atoms will self-assemble to minimise the Gibb's free energy G, attaining a more thermodynamically stable state. The environment in which atoms self-assemble determines the morphology and therefore properties of the self-assembled structure. For instance, a snowflake's morphology is dependent on the ambient temperature and vapour pressure [8]. This classic system provides an example of the two competing forces affecting aggregation by self-assembly: the thermodynamic tendency to minimise G, and the kinetic speed (rate) at which energy minimisation can occur.

Since the exact path via which a system acts to minimise its energy is material dependent, there is a wide scope for investigating self-assembly in different material systems. Self-assembly is of benefit to nanotechnology, as self-assembled techniques invariably require less input, with potentially more desirable output. Self-assembly provides a means of constructing nanometre sized structures, sizes unachievable by current lithographic techniques, and less intensive than methods of atomic manipulation (i.e. STM).

Bismuth Films

Bismuth (Bi) is a group V semi-metal with interesting electronic and magnetic properties, due to its low carrier density, small effective electron mass ($\sim$0.002 m_e)[9], and a $\sim$50 nm Fermi wavelength at room temperature. Bismuth is the most diamagnetic of all the metals, exhibits the greatest Hall effect of any metal, and only Mercury has a lower thermal conductivity. A transition from semi metallic to semi conducting behaviour was observed for $\sim$70 nm diameter Bi wires [10, 11], the transition theoretically predicted to depend on crystal orientation [12].

Low coverage Bi films are likely candidates for observing quantum effects due to electron confinement. Understanding the growth conditions of Bi thin-films will aid in the production of novel, self-assembled structures. Bi thin-films grown by self-assembly condense into different crystal orientations and phases, with island morphologies typically less than 10 nm thick [13, 14]. Nagao *et al.* [14] observed a new allotrope for low coverage Bi films on reconstructed Si(111) surfaces. Nagao

et al. believe the allotrope is energetically favourable at low coverage, and is due to the pairing of Bi-layers, with the bulk Bi crystal structure favoured at higher coverage. Bi thin-films are commonly crystalline [13, 14, 15], though there is experimental evidence for an amorphous phase for 0.5 nm thick films [16].

A flux and coverage dependent (room temperature) study of ultra thin Bi films on highly oriented pyrolitic graphite (HOPG) has been performed by Scott [13]. For monolayer coverages, planar, star-shaped islands grow on HOPG terraces. A study of the island density flux dependence found islands to nucleate via homogeneous nucleation. For low flux growth conditions, aggregates nucleating from step-edges of the HOPG terrace preferred 1D morphologies, while 2D morphologies were preferred at high flux. 1D morphologies were not observed on HOPG terraces, and it is not obvious why they form. A focus of this thesis is to determine the growth mechanism for 1D structures nucleating from step-edges.

UC Cluster Research

Canterbury University has a large research group interested in the properties of nano-clusters, and the development of electronic devices using cluster wires/films. Using sputtering techniques, atomic clusters can be generated from most solids. Electrical measurements have been taken from percolating cluster films [17], or via lithographically defined cluster wires [18]. Hydrogen sensing cluster devices have been manufactured [19, 20], the devices utilising the hydrogen absorbing properties of palladium.

An important feature of any device is its long term stability. Devices composed of connected clusters are inherently unstable, since they have a natural tendency to minimise the surface energy via coalescence. How quickly clusters coalesce has implications for the device conductivity, and performance lifetime. Hence the coalescence of clusters is currently a topic of interest within the group.

Thesis Outline

This thesis studies three topics relevant to nanoscience: the self-assembly of Bi structures on planar substrates, the self-assembly of nanorods from step-edges of HOPG, and the coalescence of 3D crystalline nanoparticles. Both experimental and simulational methods are used. Due to the three distinct topics investigated, the thesis results are presented in three chapters. Each Chapter contains a brief literature review relevant to the Chapter topic.

In Chapter 1 a general introduction to crystal growth is provided, which is relevant to all three results Chapters.

In Chapter 2, experimental and simulational methods are discussed. Proce-

dures for depositing thin Bi films under vacuum are described, beginning with a description of the UHV apparatus, the sample preparation and cleaning methods, and the deposition procedure. Techniques for thinfilm characterisation are also discussed. Atomistic simulations developed in the thesis use Kinetic Monte Carlo (KMC) methods. Chapter 2 introduces the KMC technique, and also provides a brief description of two distinct KMC algorithms used in the thesis.

Chapter 3 discusses experimental investigations of Bi thin film growth on Mica, Molybdenum diSulphide, and HOPG surfaces. On HOPG a temperature dependent study is performed, extending previous work [13]. For each substrate, the analysis focuses on film morphology, and island density, as functions of the growth parameters.

In Chapter 4 the growth of anisotropically shaped Bi crystals (termed rods) from HOPG step edges is investigated, as a function of temperature. Measurements of rod aspect ratios (ARs) are taken for different growth conditions. In the second half of Chapter 4, an investigation of anisotropically shaped crystals growing from step-edges using KMC simulation is presented. A scaling relation between the rod AR and growth parameters is determined, then applied to the experimental results.

Chapter 5 applies KMC simulations to the coalescence of crystalline nanoparticles (nano-clusters), using a model system. Cluster pairs are allowed to coalesce for different initial conditions, the results focus on the growth of the neck region between the clusters, and total equilibration times.

Chapter 6 summarises the results of the thesis, and discusses further work which might extend the results.

Chapter 1

Diffusion, Nucleation, and Crystal Growth

This Chapter introduces some of the fundamental concepts of crystal growth. Chapters 3 and 4 both involve thin film growth via atomic beam epitaxy (ABE), therefore the terminology and basic processes are reviewed in Section 1.1. Surface diffusion is a common element to the results presented in Chapters 3, 4, and 5 of this thesis, therefore Section 1.2 includes a description of particle diffusion on surfaces. In Section 1.3 the subject of nucleation is reviewed, with a focus on the dependence of nucleation on experimental parameters. Section 1.4 then reviews aggregation models, and describes some of the characteristic crystal morphologies observed on surfaces. A number of review articles [21, 22, 23, 24] cover the material presented here in more detail.

1.1 Deposition

Figure 1.1 is a schematic of processes important to epitaxial film growth. In general there are three parameters which govern the film growth: the temperature of the surface, the rate at which new material is added to a surface (the flux F, ML/s or Å/s), and the amount of deposited material (coverage, θ), commonly refered to in units of atomic monolayers, ML.

During deposition atoms land on the surface at random positions. Atoms on the surface are referred to as adatoms. Once absorbed, adatoms can diffuse until they desorb from the surface, or come into contact with a stabilising obstacle. These obstacles can be step edges, defects on the surface, other adatoms, or larger aggregates. Aggregates and steps continually collect adatoms diffusing on the surface, but also lose material via dissociation. Nucleation occurs when aggregates achieve a

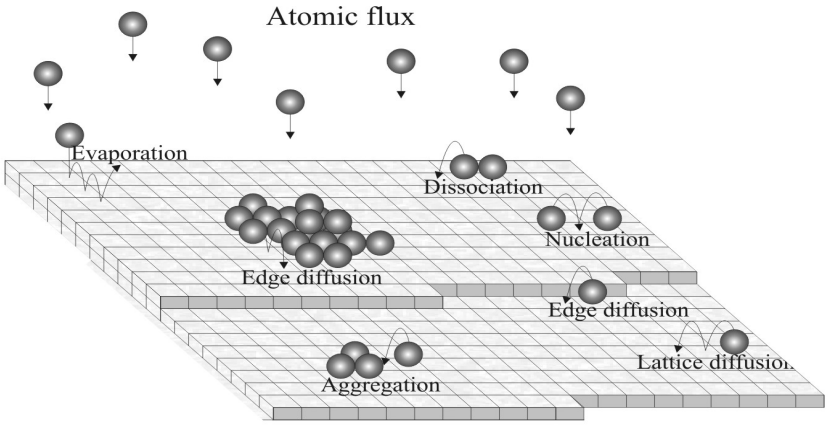

Figure 1.1: The fundamental processes of film growth. Particles are deposited on a surface, and diffuse until it aggregates with an obstacle, or evaporates from the surface. The schematic provides examples of diffusion, nucleation, and aggregation, the three main processes for ABE growth.

critical size above which they do not dissociate. For appropriate growth conditions, atoms can rearrange about the aggregate via edge-diffusion.

1.2 Diffusion

Diffusion is the process which variously describes the dispersion of solutes within a liquid, the space filling properties of gas, and the motions of atoms on a crystal lattice. The rate at which a species diffuses is governed by the diffusion coefficient, D.

There are two definitions for the diffusion coefficient. The first arises when describing the collective motion of interacting particles (refered to as chemical or Fickian diffusion). Consider a gas distributed unevenly within a volume. Fickian diffusion acts to homogenise the system. The general equation for the change in density of the gas is

$$\frac{\partial \rho(\mathrm{r},\mathrm{t})}{\partial \mathrm{t}} = \mathrm{D}\nabla^2 \rho(\mathrm{r},\mathrm{t}), \tag{1.1}$$

where ρ is the gas density, and D is the diffusion coefficient, r is the position, and t the time.

The second definition applies to systems in which individual particles diffuse via random walks, and is termed the tracer diffusion coefficient. In the tracer theory atoms move via uncorrelated jumps, the jumps usually defined to be of equal distance. The tracer diffusion coefficient is proportional to the mean square

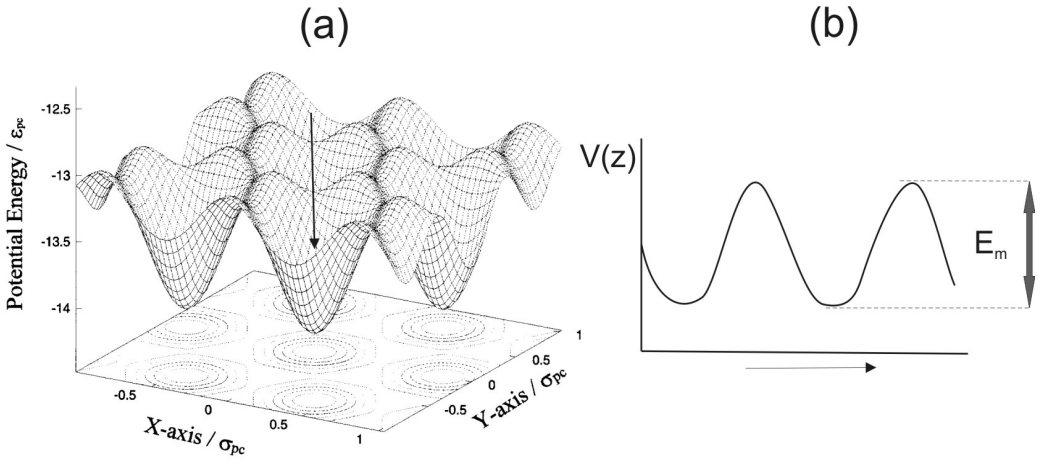

Figure 1.2: (a) Profile of the graphite surface potential modeled using the Steele potential [25]. (b) Schematic of the energy barriers experienced by an atom moving in the direction of the arrow in (a). E_m is the energy required for migration, and equals the difference in energy between the trough and peak of the curves

displacement of a particle performing a random walk via

$$\left\langle [\mathrm{r(t)} - \mathrm{r(0)}]^2 \right\rangle = 2\mathrm{dDt}, \tag{1.2}$$

where t the duration of the walk in d-dimensional space, and r is the position.

Surface Diffusion

Surface diffusion describes systems where diffusion is constrained to a phase boundary i.e. at the interface of a solid and a vapour. Associated with every surface is a potential landscape generated by the underlying atoms. The diffusion of atoms in the potential field is influenced by the size and positions of minima in the field. Figure 1.2 (a) reproduces a calculated potential field produced by carbon atoms on the surface of a graphite crystal [25]. The potential profile in Figure 1.2 (b) is a cross-section of the surface potential, used to demonstrate the potential barrier E_m restricting an atom moving along the arrow in Figure 1.2 (a). If the thermal energy k_BT is smaller than the diffusion barrier E_m, tracer diffusion will occur via thermally activated hops.

Tracer diffusion is expected to be applicable when adatom densities are sufficiently low that particles cannot interact with each other. Interatomic interactions span a few nanometres at most [26, 27], therefore tracer diffusion is a valid approximation for systems with low densities of diffusing particles (and low coverages). For diffusion via thermally activated hops, the hop rate ν is characterised by an attempt frequency, ν_0, and a thermodynamic factor which determines the probability each attempt

results in a successful hop. The hop rate is then [24]

$$\nu = \nu_0 \exp(-\mathrm{E_m}/\mathrm{k_B T}), \tag{1.3}$$

where $\mathrm{E_m}$ is the energy barrier restricting movement, $\mathrm{k_B}$ is the Boltzmann constant and T is the temperature. Further description of the theory of activated hops is provided in Chapter 2, though we briefly state here the relation between the diffusion coefficient D and the hop rate ν. Random walk theory calculates the mean square displacement of a particle performing a random walk to be $\mathrm{a}\sqrt{\mathrm{N}}$, where a is the hop distance and N the number of hops. For activated hops occurring at rate ν, the number of hops in time t is $\mathrm{N} = \nu\mathrm{t}$. Comparing with the definition of the tracer diffusion coefficient (Equation 1.2), we find

$$\mathrm{D} = \frac{\mathrm{a}^2}{2\mathrm{d}}\nu. \tag{1.4}$$

The temperature dependence of D can be studied to extract values for the energy barrier $\mathrm{E_m}$ and attempt frequency ν_0. A great number of investigations have been conducted for atoms diffusing on metal surfaces [28, 29, 30, 31], though much larger $\mathrm{Sb_{2300}}$ and $\mathrm{Au_{250}}$ clusters on HOPG surfaces were found to diffuse via Brownian motion [23], at rates comparable to the diffusion of single atoms.

Self-assembled aggregates can diffuse on a surface, and examples of small cluster (size 2-12 atoms) diffusion has been observed for the Rh/Rh(001) and Pt/Rh(001) systems [32]. The diffusion of small clusters has been predicted for the Al/Al(001) and Cu/Cu(001) systems [33], from theoretical calculations. For these epitaxial systems a cluster's displacement is ascribed to the successive movements of atoms about the cluster's perimeter.

1.3 Island Nucleation

Nucleation denotes a phase transition, and the formation of an interface between two phases. Common examples are the formation of droplets in a vapour, or bubbles within a liquid. Since nucleation requires the formation of an interface, it invariably requires work. Compensating the energy required to form the interface is the energy liberated in the formation of the new phase. To predict the probability of a nucleation event occurring, it is neccessary to calculate the change in free energy $\Delta\mathrm{G}$ associated with the growth of the new phase. A simple example to consider is the creation of a circular particle of radius R (and monatomic height a) from atoms

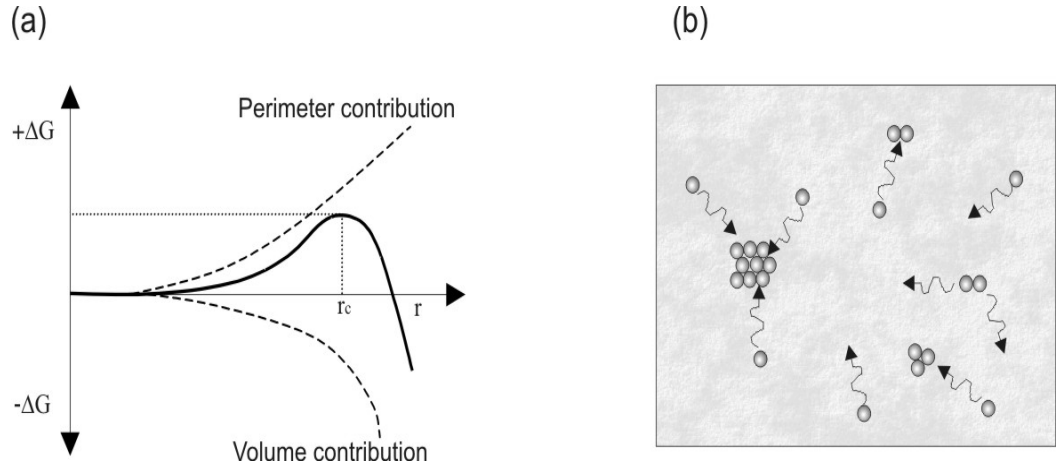

Figure 1.3: (a) Schematic of the change in free energy ΔG associated with the nucleation of an atomic layer, as a function of the layer size. (b) An illustration of island stability for different aggregate sizes.

diffusing on a surface. For homoepitaxy, ΔG contains contributions from the volume and perimeter terms,

$$\Delta G = [2\pi R\gamma - \pi R^2 \Delta\mu]a. \tag{1.5}$$

Equation 1.5 sums the energy used to create a new perimeter (1D analogy to surface area) of length $2\pi R$ and line tension (1D analogy to surface tension) γ or equivalently the free energy per unit area, and the energy released per unit volume of the new phase. $\Delta\mu$ is the difference in chemical potential between the two phases (termed the supersaturation).

Figure 1.3 (a) provides an illustration of ΔG, showing the positive and negative contributions of the perimeter and volume terms respectively. Equation 1.5 can be solved to find the particle size at which ΔG is maximised, where $R^* = \frac{\gamma}{\Delta\mu}$. R^* is termed the critical size, and is usually labeled i for epitaxial systems where the critical size is typically a few atoms. i is simply the number of atoms required to create the critically sized aggregate. Below i work is required to add atoms to a particle, above i energy is released by adding atoms. For spontaneous nucleation the maximum of ΔG must be within range of the thermal energy k_BT. The maximum of the free energy symbolises the point at which the cluster is least stable, as beyond this point the cluster tends to grow rather than decay.

1.3.1 The Supersaturation

For a system of adatoms diffusing on planar surface, (homogeneous) nucleation might occur when an adatom collides with another adatom to form a stable dimer. If

however the energy supplied via thermal activation is comparable to the bond energy between the two adatoms, the dimer may dissociate, while a larger cluster (e.g. a trimer) may be stable. In this example the critical particle size is therefore a dimer. Figure 1.3 (b) is a schematic illustrating the stabilising effect for planar clusters of atoms. In the schematic, doubly bonded atoms are stable against dissociation.

For an aggregate with surface energy γ, the probability for nucleation is largely governed by the supersaturation $\Delta\mu$, since this measures the amount of energy released by adding atoms to the cluster. From Equation 1.5 it is clear that at large supersaturation, i is small, and nucleation is energetically favourable. For small $\Delta\mu$, i is large, and nucleation is more difficult. Venables [22] and Pimpinelli [34] provide a formula for the supersaturation,

$$\Delta\mu = \mathrm{k_B T} \ln(\frac{\mathrm{p}}{\mathrm{p_e}}). \tag{1.6}$$

The symbols $\mathrm{p_e}$ and p are respectively the equilibrium and actual vapour pressures of atoms on a surface. For ABE, the ratio $\frac{\mathrm{p}}{\mathrm{p_e}} \approx \frac{\mathrm{F}\tau}{\rho_\mathrm{e}}$, where $\mathrm{F}\tau$ is the adatom density and ρ_e is equilibrium density [22, 34]. Equation 1.6 essentially says that, for systems with high adatom densities (through high flux) and high temperature, the supersaturation is large, and there is a large energy gain for adatoms to aggregate on the surface.

1.3.2 Nucleation Density

Consider two atoms bound together by an energy $\mathrm{E_b}$, and at non-zero temperature. The probability that the atoms gain enough energy via thermal activation to break the bond and dissociate obeys Boltzmann statistics, and the mean lifetime for dissociation is therefore $\tau_\mathrm{dimer} \propto \exp(\frac{\mathrm{E_b}}{\mathrm{k_B T}})$. Raising the temperature shortens the time required for the bond to be broken, therefore τ_{dimer} reduces, conversely reducing the temperature increases τ_{dimer}.

To create a stable trimer, another adatom must collide with the dimer before it dissociates i.e. within τ_{dimer}. At low adatom densities (low supersaturation), adatom collisions have a low probability. In this regime dissociation is probable, and few clusters grow larger than the critical size. For high adatom densities adatom-adatom collisions or adatom-dimer collisions occur more frequently, leading to a higher density of stable trimers. Hence increasing the beam flux in ABE growth can drive a system from a regime where nucleation is improbable into a regime where nucleation is probable. On the otherhand, high temperatures can prevent the formation of stable nuclei due to more frequent detachment events.

From the above discussion, it is clear that the growth of stable nuclei depends

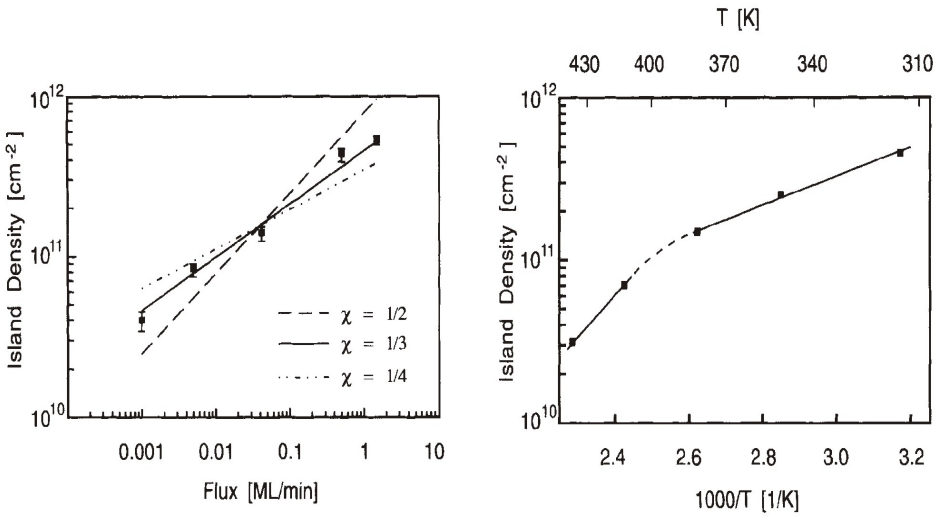

Figure 1.4: Images reproduced from Ref. [35] to illustrate the (a) flux dependence of the saturated island density, (b) the temperature dependence of the island density, for the Au/Au(001) system.

on the rate at which atoms aggregate with a critical nucleus. The interval between aggregation events must be smaller than the rate at which critically sized clusters lose material via detachment. Using rate equations, Venables [22] determines the nucleation rate J of stable clusters for a system in which only adatoms diffuse,

$$J = \sigma D n_1 n_i, \tag{1.7}$$

where D is the surface diffusion constant for single atoms, n_1 the density of adatoms, n_i the density of critically sized clusters, and σ a parameter describing the flow of atoms to critically sized clusters. In regimes where condensation is complete and only monomers diffuse, the density of stable islands quickly saturates at [21, 22]

$$N_{sat} \propto (\frac{F}{D})^{\chi}, \tag{1.8}$$

where F is the atomic flux, and $\chi = \frac{i}{i+1}$ is dependent on the critical island size i. Hence the island density is dependent on the adatom density (via F), and how quickly adatoms diffuse on the surface (via D). By measuring the island density as a function of flux and temperature, the critical island size and adatom diffusion barrier can be estimated.

For homogeneous nucleation on planar surfaces, the saturated island density N_{sat} is reached when the mean free path of an adatom equals the mean separation of existing islands. Further nucleation is suppressed, as additional material is predominantly captured and absorbed into growing aggregates.

Equation 1.8 relates the nucleation density to experimental parameters F and T (through the diffusion constant D). By monitoring the dependence of N_{sat} on experimental parameters, the critical island size, and diffusion mode for a system can be determined. Figure 1.4 (a) shows the expected increase in N_{sat} for islands grown on the Au(001) surface, as the flux is increased over three orders of magnitude [35]. Figure 1.4 (b) shows the reduction in N_{sat} as the temperature is increased (note the x-axis is 1/T). The change in slope in Figure 1.4 (b) was interpreted as an increase in the critical cluster size from i=1 to i=3 i.e. as the temperature is raised there is a transition from stable dimers to stable 4-atom aggregates.

1.4 Island Growth

Aggregation is a non-equilibrium process driven by the supersaturation $\Delta\mu$. In equilibrium systems, the chemical potential μ is globally constant, and there is no net flux of material between phases (detailed balance). In systems which are out of equilibrium (for instance during ABE growth), aggregation occurs because the rate of atomic attachment to an interface outweighs the detachment of material from the interface (see Figure 1.3 (b)). For systems where nucleation is saturated, additional material is incorporated into existing aggregates.

In this Section we review models of aggregation, then discuss island morphologies and their dependence on experimental parameters. Anticipating the thesis results presented in Chapters 3 and 4, the discussion focuses on 2D (planar) growth, i.e. we do not consider aggregation of 3D islands.

1.4.1 Early Aggregation Models

One of the earliest growth models was developed by Eden [36], to help explain the growth of cells in biology, specifically the development of cancerous tumors. A seed particle or cell has a perimeter of available sites where new material may be attached. A new particle is added randomly to one of these perimeter sites, enlarging the cell and the cell's perimeter. Since perimeter sites have equal probabilities of collecting the next particle, the cell is equally likely to grow in any direction, and after many iterations the resulting form of the cell is a compact circle. At large sizes the perimeter roughens, but the overall shape of the aggregate remains a circle. Figure 1.5 (a) illustrates the roughened circular shape characteristic of the Eden model.

The field of particle growth via diffusion was advanced with work by Mullins and

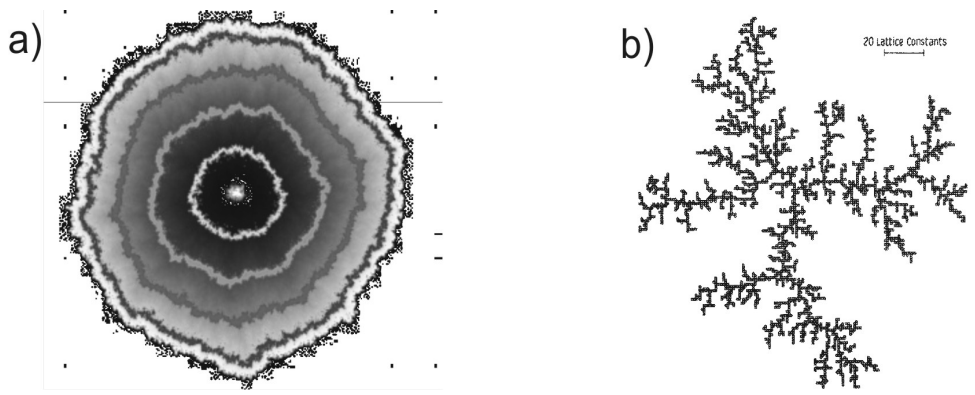

Figure 1.5: (a) Compact lateral growth predicted by the Eden model, image reproduced from Ref. [40] (b) Fractal shape typical of aggregates grown with the DLA model, image reproduced from Ref. [41]

Sekerka [37], which investigated spherical particles undergoing diffusion or thermally controlled growth. In the diffusion controlled regime, perturbations of the sphere were found to increase in size due to localised increases in concentration densities, and to decrease due to surface energy effects which act to minimise the perturbation. Mullins *et al.* [37] demonstrated that there is a critical radius R_c above which perturbations must increase in size. Therefore above R_c the irregularities on the surface of an Eden sphere would eventually lead to the development of a non-spherical object. The theory can be extended to thin film systems, where 2D islands may assume compact shapes at small island sizes, but have a dendritic (branched) morphology above the critical island size. The critical size at which the transition occurs depends on the competition between smoothing effects at the island boundary, and the enhanced capture probability of island edge perturbations which extend into the diffusion field [38].

To explain the fractal nature of coagulated aerosols with randomly branched structures, Witten and Sander [39] developed a theory for aggregation via the random and irreversible attachment of material to a growing nucleus. The structures clearly did not conform to the early equilibrium growth models formulated in [36] and [37], and the observations required a new explanation now recognised as diffusion limited aggregation (DLA) theory. The limiting factor of the model is the rate at which new material is added to the aggregate, i.e. there is no diffusion of particles within the aggregate.

DLA theory was investigated and analysed using simulations. To begin the diffusion on a 2D surface, a seed particle is placed at the centre of a lattice. Around this is circumscribed a circle from which additional particles are released. Further out is the bounding circle, and any particles which randomly diffuse past this circle

are removed from the simulation. These two circles are used to imitate isotropic flux. Diffusion proceeds randomly, i.e. a released particle can move in any direction, taking one step at each iteration in the code. Eventually it arrives at the aggregate and irreversibly attaches; another particle is released and the process continues. Witten and Sander discuss the form and properties of aggregates grown using such a model.

Figure 1.5 (b) shows a typical DLA pattern. Long branches develop from the centre seed, each of these major branches contains smaller extensions or instabilities. The fractal (self-similar) structure is not entirely obvious until small sections are enlarged - showing that small regions behave just as the larger arms. The random nature is clear, since none of the features demonstrate any sort of ordered growth. The branches extending outwards capture most of the new material, effectively shielding the inside. Hence the density of the central region is fixed, and this density falls off further from the seed.

The classic DLA patterns have never been experimentally observed (very similar aggregates are reviewed in Section 1.4.2) for epitaxial systems, since the temperatures at which terrace diffusion is initiated are high enough to allow atoms to edge diffuse around an aggregate's perimeter. Although fractal shapes are preferred at low temperatures, the branch width is not monoatomic, and so there must be atomic rearrangements at the pattern boundary.

1.4.2 Island Morphologies

The DLA and Eden models largely ignore microscopic processes at the crystal interface e.g. the diffusion and rearrangement of atoms about the island perimeter. Rearrangements act to minimise the surface energy of a crystal. Diffusion at the crystal interface is restricted by an energy barrier, therefore the rearrangement is sensitive to experimental conditions. By adjusting parameters such as T, F, and θ, aggregates can be driven from compact, equilibrium shapes, to kinetically limited morphologies.

Two epitaxial systems which illustrate the fundamental dependence of island morphologies on growth conditions are Ag/Pt(111) and Pt/Pt(111).

The flux and temperature dependence of the Ag/Pt(111) system has been investigated by Brune *et al.* [43, 21, 44, 42]. This particular system is interesting because of a counterintuitive flux dependent morphology transition. Figure 1.6 (a) displays a fractal like island grown at T=110 K and F=10^{-5} ML/s. Figure 1.6 (b) displays dendritic, or ramified growth with a trigonal symmetry, grown at 130 K and F=10^{-3}

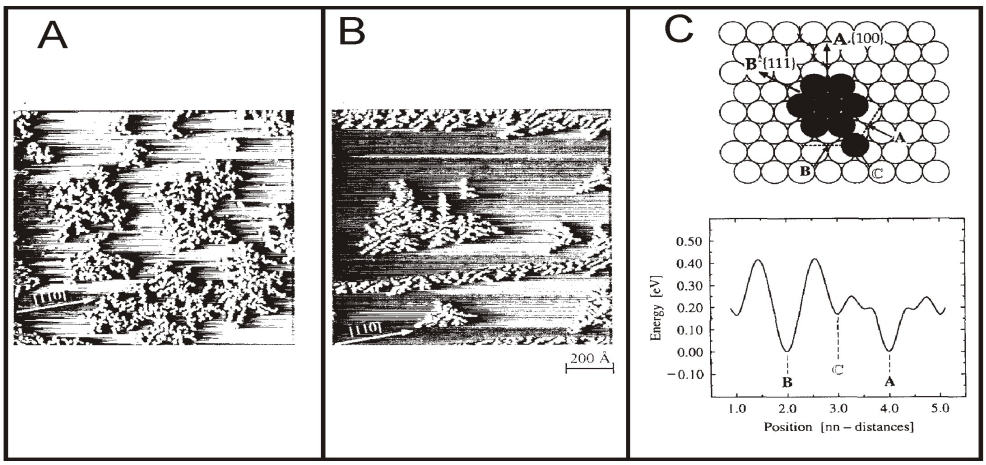

Figure 1.6: Island morphologies for Ag/Pt(111) system at 110K and 130K. An increase in adatom flux produces a transition from (a) random to (b) oriented growth [42, 21]. (c) is an energy profile for different edge sites of an Ag heptamer on the Pt(111) surface.

ML/s, two orders of magnitude greater than for (a). The transition from fractal to oriented growth is proved to be due solely to the higher flux (high temperature samples were grown at low flux producing shapes similar in form to (a)). Using effective mass theory (EMT) calculations, a potential profile (shown in (c)) was constructed for the diffusion of adatoms around the corners of a heptamer nucleated on the Pt(111) surface. The hexagonal symmetry of the substrate produces two sets of crystal facets with different potential barriers, these two sets are labelled as A and B steps. Atoms are unlikely to diffuse from C sites to B facets because of the relatively large diffusion barrier, and hence the atoms congregate at the A steps. The A steps are related by 120^o rotations, leading to the trigonal shape of the aggregates.

Both flux regimes in Figure 1.6 illustrate how low temperature growth leads to ramified shapes, due to kinetic limitations imposed by bonding at the island edges. At elevated temperatures, it is natural for an island to reduce its free energy by reducing the amount of surface area it presents. As a consequence, the fractal DLA islands seen at low temperatures are progressively replaced by more densely packed structures as the temperature is increased. For compact islands to form, it is necessary for adatoms to rearrange at the island edges, either via edge diffusion or a detachment/reattachment type mechanism.

Figure 1.7 [45] illustrates the characteristic Pt island morphologies found on the Pt(111) plane, as a function of temperature. At 200 K (diagram (a)), the islands have an fractal character similar to the dendrites shown in Figure 1.6 (a). At 400 K (diagram (b)), corner and edge diffusion are sufficiently activated to allow the formation of densely packed trigonal islands. Further increases in temperature

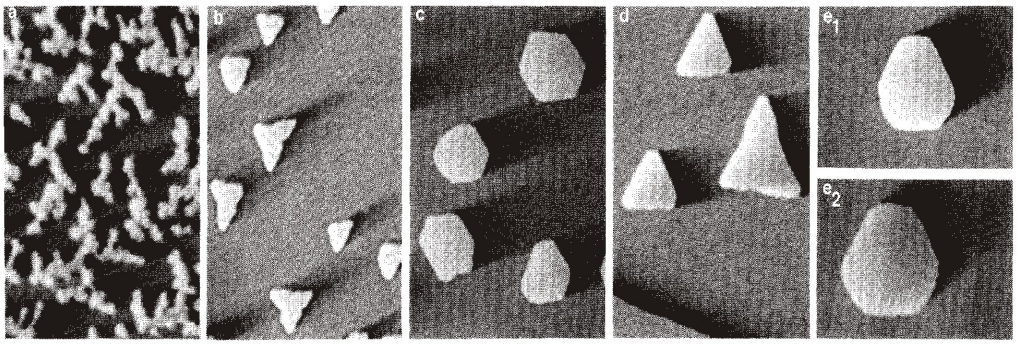

Figure 1.7: Island morphologies for Pt homoepitaxy as the substrate temperature is increased from 200 K through to 710 K [45].

produce an orientation transition (not discussed here), leading finally to the growth of compact hexagons at 700 K, corresponding to the 2D equilibrium shape on a hexagonal lattice.

Note that the larger triangular islands in Figures 1.7 (b) and (d) are distorted relative to the smaller islands. The tips of the triangle capture more material than the edges, since the tips lie further within the diffusion field. To maintain symmetric triangles atoms must be transported from the tips to the edges before additional material arrives. Larger triangles have more difficulty rearranging material, leading to the observed distortions. The distortions are an example of the Mullins-Sekerka instability.

Pimpinelli [38] presents simulated island morphologies on a square lattice. Figure 1.8 (a) shows simulation results for a high atomic flux, and Figure 1.8 (b) when the flux is lower by two orders of magnitude. In Figure 1.8 (a) there is a high density of small, square shaped islands, the square morphology thermodynamically favoured.

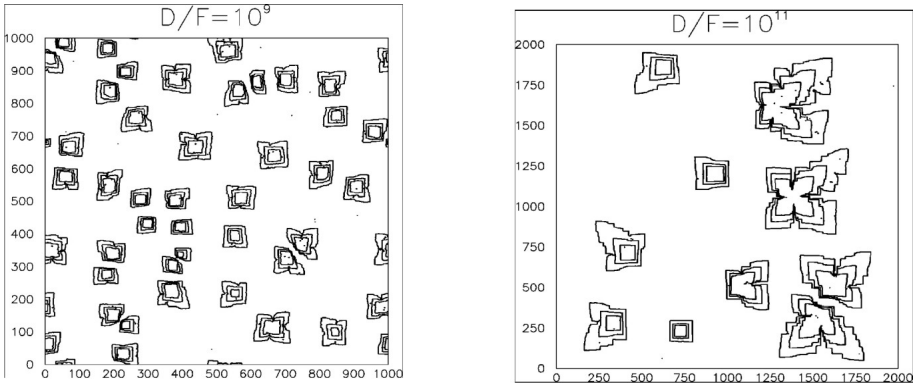

Figure 1.8: Images reproduced from Ref. [38]. As the surface coverage is increased from 0.05 ML to 0.2 ML for (a) high atomic flux, many small islands nucleate, (b) low flux creates fewer, larger islands, the dendritic (kinetically limited) morphologies more severe as coverage is increased.

The islands in Figure 1.8 (b) are larger, with dendritic morphologies. The morphology transition is interesting, since instabilities are presumably less likely at low flux conditions, when atoms have more time to rearrange about aggregates. However, since few islands nucleate at low flux (compared to high flux), the average island size is larger. With larger perimeters, and the smoothing properties of edge diffusion are less effective, leading to dendritic island shapes. The result illustrates the complex response of island growth to changes in experimental conditions i.e. lowering the flux does not guarantee equilibrium island shapes.

1.5 Crystal Growth Summary

This Chapter has reviewed the fundamental processes relevant to nucleation and growth of atomic islands. For non-equilibrium systems (such as ABE), the supersaturation promotes the incorporation of atoms into lattice defects, and the nucleation of new islands. The influences of atomic flux and substrate temperature on the supersaturation, and the critical island size, have been discussed.

Island growth models and morphologies have been reviewed, from the classic Eden and DLA models, to current day interpretations which allow for rearrangements at the crystal vapour interface. The importance of island morphology on flux, temperature, and island density has been discussed. Island morphologies occasionally have complex and counterintuitive responses to changes in experimental conditions.

Chapter 2

Methods: Experimental and Computational

This chapter details the equipment and experimental procedures employed in our study of Bismuth (Bi) thin-films, and outlines the Kinetic Monte Carlo (KMC) algorithms used in our simulations. Section 2.1 lists the materials used for the different film/substrate combinations investigated. Section 2.2 provides a description of the vacuum chamber and pumping elements, along with the basic experimental method that was repeated for all depositions. Section 2.3 details the sample preparation, annealing, and heating. Section 2.4 discusses the crucible configuration. In Section 2.5 the various techniques of film characterisation are described. Lastly in Section 2.6 the KMC technique is introduced, along with a description of the algorithms used in Chapters 5 and 6.

2.1 Materials

This section reviews the crystallographic structure of Bi, and the three substrates on which Bi films were grown: Mica, Molybdenum di-sulfide (MoS_2), and Highly Oriented Pyrolytic Graphite (HOPG).

2.1.1 Evaporant Material

Structurally similar to other group-V elements [46], bismuth has a rhombohedral crystal (space group $R\bar{3}m$) with two atoms per unit cell, and cell constants

$$\text{Bi:} \quad a_r = 4.75 \text{ Å}, \quad \alpha_r = 57°14'.$$

Each atom in a Bi crystal forms three nearest neighbour bonds (3.1 Å), and three next-nearest neighbour bonds (3.5 Å). The short bonds are occasionally referred to

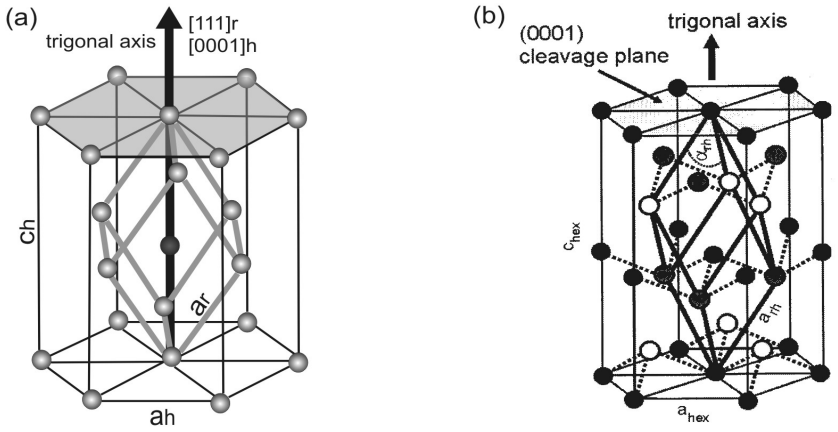

Figure 2.1: Crystal structure of Bismuth using a hexagonal cell. (a) the rhombohedral unit cell is inscribed within the hexagonal cell, (b) atoms from neighbouring unit cells are included, the strong intra-layer bonds shown using dotted lines. Images reproduced from Ref. [13].

as being covalent, but we refer to the 3.1 Å, and 3.5 Å bonds as intralayer and interlayer respectively.

The rhombohedral crystal structure can be translated into a hexagonal basis with lattice constants

$$\text{Bi:} \quad a_h = 4.54 \text{ Å}, \quad c_h = 11.86 \text{ Å}.$$

Since the hexagonal basis is more commonly used in the literature, this thesis makes reference to the Bi crystal structure assuming the hexagonal basis. Figure 2.1 displays the bismuth crystal (a) in reduced form with a hexagonal cell outlined, containing the highlighted rhombohedral unit cell, (b) all the atoms included, the intralayer bonds indicated using dashed lines. Interlayer bonds are not shown.

2.1.2 Substrate Materials

Figure 2.2 shows schematic crystal structures for the different substrate materials used in the thesis, along with a photograph of the bulk crystals from which substrates are cut.

Mica

To utilise the electrical properties of self-organised bismuth nanostructures, the structures need to be supported by insulating substrates. Mica ($2M_1$ muscovite, $KAl_2(AlSi_3O_{10})(OH)_2$) is a quartz-like clay mineral which is commonly used as a substrate in the growth of conducting thin films because of its flat crystal structure and insulating properties. Mica crystals are easily cleaved providing large contaminant free terraces, ideal for studies of atomic diffusion and crystal growth.

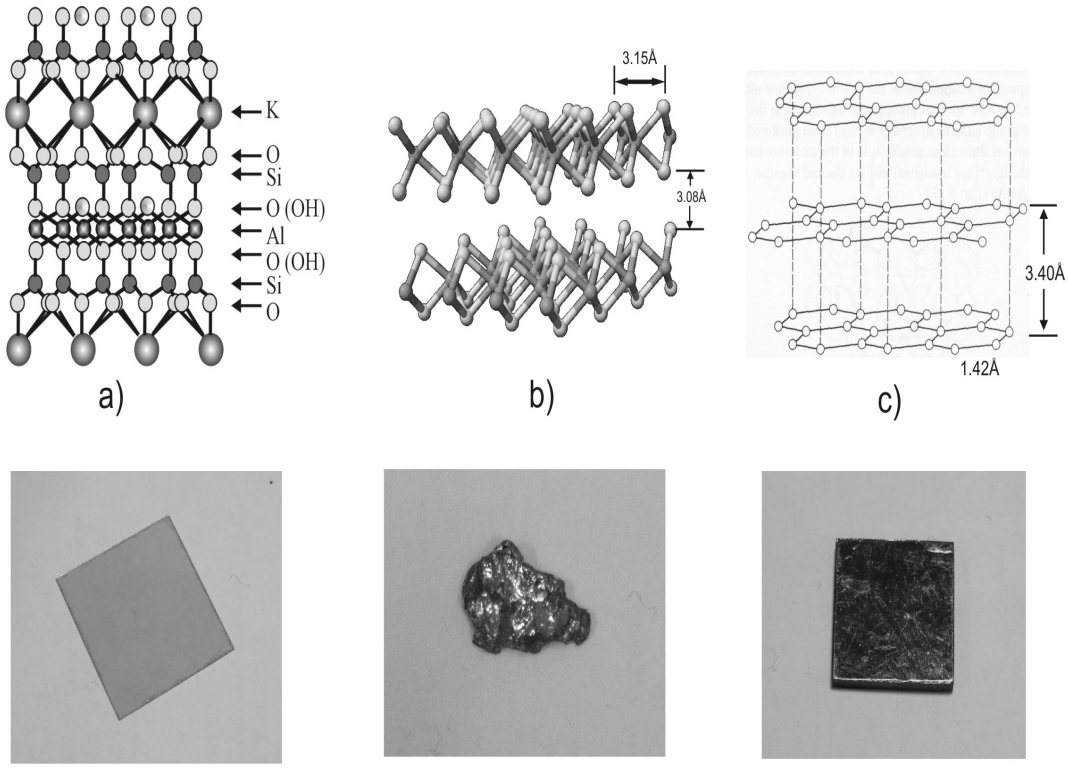

Figure 2.2: The crystal structure and bulk samples of (a) Mica, (b) MoS_2, and (c) HOPG.

Mica has a monoclinic crystal structure, with lattice constants $a = 5.189$ Å, $b = 9.004$ Å, and $c = 20.256$ Å, $\alpha = \gamma = 90°$ and $\beta = 95.74°$. Elements within the crystal (see Figure 2.2 (a)) form a sandwich type structure with layers of aluminium silicate separated by potassium ions. The crystal is believed to cleave along the layer of potassium ions, where the interlayer bonds are weakest. A cleaved surface exposes oxygen atoms from the silica, irregularly dotted with potassium ions, leaving the surface with a net negative electrostatic charge [47].

MoS_2

MoS_2 substrates are another candidate for diffusion studies, as the crystals have the layered structure ideal for adatom diffusion. MoS_2 crystals can be pictured as a layer of molybdenum atoms sandwiched between two layers of sulfur atoms (i.e. S-Mo-S, Figure 2.2 (b)), the sheets stacking together in the bulk crystal. Sulfur atoms at the interface of each layer interact via Van der Waals forces. Cleaving the samples exposes a surface of sulfur atoms, the atoms having hexagonal symmetry and lattice constant 3.15 Å. MoS_2 is mildly conductive, and therefore not ideal for studies of electrical characteristics.

HOPG

HOPG is an allotrope of carbon with a layered structure useful for atomic diffusion

studies. Atoms within the lattice are arranged in hexagonal pattern, with a C-C bond distance of 1.42 Å, and the central atom removed, resulting in the honeycombed structure of Figure 2.2 (c). Each layer is separated from the adjacent layer by 3.40 Å, the stacking sequence has each layer repeating every two layers. Layers interact with each other via weak van der Waals forces, hence when HOPG is cleaved the interlayer bonds are broken, leaving a chemically inert surface. HOPG is a conductive material.

2.2 The UHV System

This section details the vacuum chambers and pumping mechanisms, and gives the experimental procedure.

2.2.1 Apparatus and Experimental Procedure

Figure 2.3 contains a schematic and a photo of the vacuum system. Components refered to in the thesis are labeled in the images. To study the nucleation behaviour and crystal growth for each Bi/substrate combination, atomically clean surfaces are required. As the schematic in Figure 2.3 (a) illustrates, the system is capable of annealing substrates and depositing material while under vacuum. Sample analysis is performed *ex situ*. A simple experimental routine is followed to produce consistent results:

- Substrate samples are cleaved in air using either a scalpel or sellotape, exposing a contaminant free surface, the clean surface is positioned face down on the sample holder

- Three substrates are placed on the sample holder, which is then attached to the head of the linear translator located in the loading chamber. Once the flange to the loading chamber is replaced, the chamber is evacuated to a base pressure of 10^{-4} torr. At this point the gate valve is opened and the ion pump begins further evacuation of the chamber.

- When the Cold-Cathode gauge reads 10^{-6} torr the samples are wound along to the oven, and annealed for approximately fifteen hours.

- After annealing, the sample holder is cooled by water flowing to the Deposition Rate Monitor (DRM) head. The crucible generates an atomic beam which is directed onto the DRM and substrates via the linear translator.

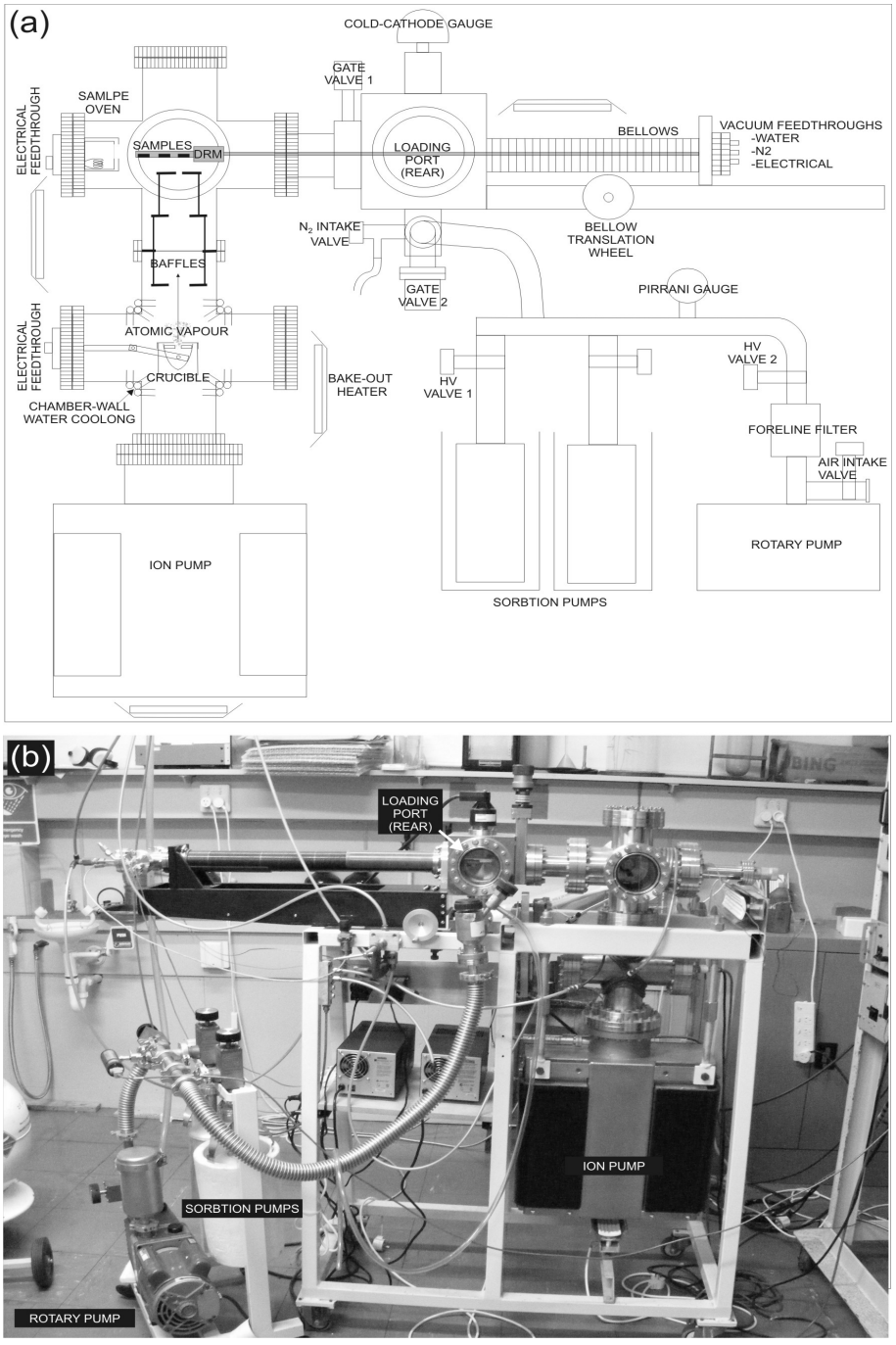

Figure 2.3: Schematic and photograph of the UHV system. The schematic is reproduced from Ref. [13].

- After deposition the samples are moved to the loading chamber, which is isolated from the ion pump after approximately half an hour. The loading chamber is vented with N_2 before the substrates are removed.

The above procedure is followed for each experiment, with minor adjustments depending on the particular substrate material being investigated. During the thesis small heaters were attached to the sample holder, therefore a number of depositions were performed for elevated substrate temperatures (further details provided in Section 2.3).

2.2.2 Pumping

Three pumping stages are used to reduce the pressure in the loading chamber, each stage using a different type of pump.

Rotary Pumping

The first pumping stage begins when the loading chamber is sealed off and isolated from the deposition chamber, performed using a rotary pump. The pump operates at a rate of 8 L/s, and is able to evacuate chambers to pressures approaching 10 milli-torr. While the rotary pump is in use, the pressure is read from the pirani gauge, giving a lower estimate of the pressure in the loading chamber. When $P_{\text{pirani}} = 10$ milli-torr the base pressure of the pump is reached, the pressure differential between either side of the rotary fan is effectively zero. At this point pump oils can back-stream into the system, contaminating the baffles and vacuum chambers. Helping to prevent contamination is a foreline filter installed between the pump and the baffles.

Sorption Pumping

The second pumping stage uses sorption pumping to reduce the pressure in the loading chamber to approximately 10^{-4} torr. Sorption pumping is one of the cleanest methods for evacuating a chamber, as it uses no oils. Sorption pumps act like molecular sieves in order to trap gases. A metal shell is filled with a dense aluminium mesh to create a porous medium with a large surface area. When the shell is immersed in a liquid nitrogen bath, the metal componentry ensures that the entire mesh is quickly brought to 77 K. Molecules which are solid at 77 K are frozen upon contact with the mesh, and a pressure gradient develops between the pump and loading chamber. When the sorption pumps are working the Cold Cathode (CC) gauge in the loading chamber is used to read the pressure. At $P_{\text{CC}} = 10^{-4}$ torr the sorption pump approaches its base pressure.

Sorption pumping can contaminate the vacuum system if trapped gases evaporate back into the chamber, which can be prevented by isolating the loading chamber at

$P_{CC} = 10^{-4}$ torr. Periodically baking and evacuating a sorption pump prolongs its effectiveness.

Ion Pumping

With the loading chamber isolated and at $\sim 10^{-4}$ torr, the gate valve to the deposition chamber is opened allowing the ion pump to evacuate the loading chamber. Ion pumps work by removing electrons from gas particles, then using magnetic and electric fields to sequester the ions in titanium blocks, a process known as gettering. Ion pumps are designed for continuous use, therefore the deposition chamber remains under vacuum. A base pressure of $\sim 10^{-9}$ torr is read from the ion pump controller when the deposition chamber is isolated. After opening the deposition chamber the pressure read by the ion pump increases to $P_I = 2 \times 10^{-8}$ torr, and the loading chamber reduces to $P_{CC} \sim 10^{-6}$ torr. After evacuating over a twelve hour period the pressures typically equilibriate at $P_{CC} \sim 9 \times 10^{-8}$ torr and $P_I = 6 \times 10^{-9}$ torr.

2.2.3 Vacuum Quality

The repeated opening of the loading and deposition chambers introduces contaminants to the system, contributing to an increase in the vacuum base pressure. Poor vacuums increase the potential for contamination of substrate surfaces. Potential contaminants are water molecules adsorbed on chamber walls or oil molecules from rotary pumps or sample handling. Periodically, a residual gas analyzer (RGA) was used to check the proportions of gases in the system. Essentially a mass analyzer, the RGA uses a high voltage anode-cathode setup to ionize compounds in a vacuum. The pressure and constituent molecules of the vacuum determines the ion current measured by the RGA. Each species of molecule has a different current signature, which the RGA uses to determine the partial pressures of each species. The RGA software thereby determines both the total vacuum pressure, and the relative proportions of each gas species in the vacuum.

Clean UHV systems have H_2 as the highest contributor to the base pressure. H_2 cannot be trapped indefinitely by ion pumps, unlike most other molecules. H_2O binds strongly to stainless steel, therefore the second most common observed contaminant is water.

Chamber cleanliness and vacuum is maintained via baking of the chamber at $\sim 120°$ C. The bake-out heaters are shown in the apparatus schematic of Figure 2.3. During baking the gate-valve between the loading chamber and deposition chamber is opened, and a fibre-glass cover placed over the entire system. The ion pump continues pumping while the exterior surface temperature held at $\sim 120°$ C for

roughly twelve hours. At this temperature water and oil contaminants should vaporise and then be trapped by the ion pump. Baking helps to lower the base pressure of the vacuum, consequently reducing the time taken to lower the pressure after a loading procedure.

2.3 Sample Preparation

In this section we present the two sample holder versions used for experiments, and describe the sample preparation routines for substrates on each holder. Lastly we give an overview of the procedure for cooling/heating samples during deposition.

2.3.1 Sample Holder

Schematics of the two sample holders are presented in Figure 2.4. Figure 2.4 (a) represents the version previously used for the study of Sb and Bi films on HOPG substrates at room temperature [13], but also used for Bi films grown for this thesis on Mica and MoS_2 substrates. The sample holder is made of oxygen free copper, separated from the DRM via a boron nitride (BN) spacer. Three equally spaced cavities are drilled in the top of the copper, providing positions for three substrates. Substrates are held in the cavities by gravity. Each cavity has a 3 mm diameter hole drilled through the copper, exposing the substrate undersides when aligned with the atomic beam. A copper screw holds the sample holder in place.

Figure 2.4 (b) shows the new sample holder designed for film growth above room temperature. Essentially the high thermal conductivity, three substrate holder design of Figure 2.4 (a) is kept, with the addition of two button heaters and two K-type thermocouples (T/Cs). Figure 2.4 shows the sample holder now consists of two parts, both machined from oxygen free copper, separated from the DRM by a macor spacer. Macor has a thermal conductivity nearly 40 times smaller than BN, providing better insulation. Additional wiring (not shown in the figure) is required for the heaters and T/Cs, the wires passing through alumina rods to UHV compatible feedthroughs at the rear of the baffles.

The button heaters were purchased from *Heatwave* [48], and are rated to 1400°C at 5 W, with lifetimes of 10000 hours under UHV conditions. The heaters consist of a tungsten filament potted in an alumina base, surrounded by a Molybdenum shell. One end of the filament is exposed, the other is grounded to the shell. Since the body of each heater is a contact, one electrical feedthrough is crimped to the exposed filament, the second is screwed to the sample holder adjacent the heater

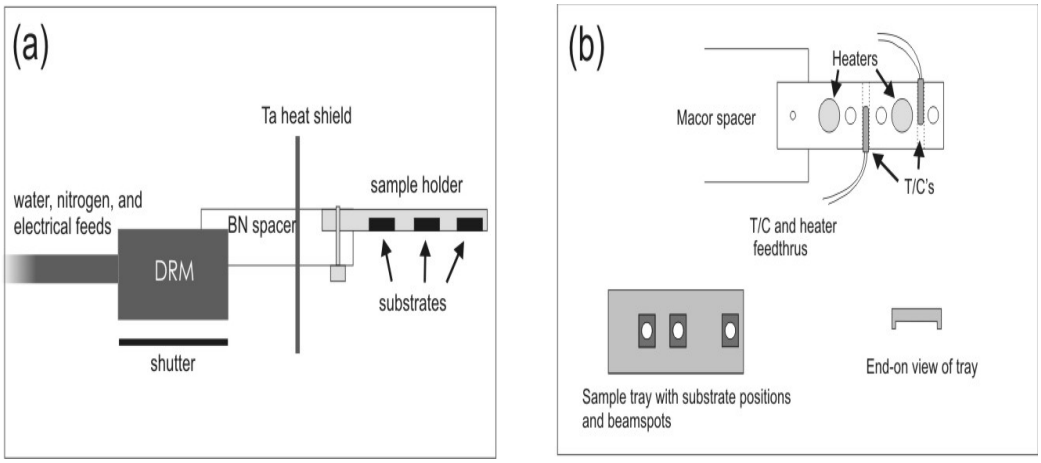

Figure 2.4: (a) Figure reproduced from Ref. [13], the sample holder design used for Mica and MoS_2 experiments. (b) New sample holder configuration providing a top down view of the holder base, and the sample tray (which fits on top of the base). The tray edges are apparent in the end-on view.

i.e. making use of copper's conductivity to provide a contact. Each heater is powered by a constant current supply, which is adjusted manually.

Temperature measurements were taken via two K-type thermocouples purchased from *Omega* [49], slotted into the sides of the sample holder. Copper has a high thermal conductivity, but with each end having different terminations, two T/Cs are used to check for temperature gradients along the holder during deposition. Temperature controllers determine the temperatures from each T/C using factory calibrations, the two controllers typically read within 1°C of each other at room temperature.

Heater filaments are crimped to the feedthrough wires, therefore the heaters and sample holder are permanently attached to the macor. To allow loading and unloading of samples, a copper tray was machined to fit on top of the heating base. The base is designed with the heaters protruding from the top of the copper base, the exposed portion of each heater then slotting into cavities drilled in the tray. The copper tray has lips over the long edges of the base to prevent lateral movements of the tray (see Figure 2.4). All screw holes and cavities in the copper have through-holes drilled to prevent air-pockets forming, since trapped air will outgas during pumping.

2.3.2 Material Preparation and Cleaning

Substrate preparation for each material follows the cleaving and annealing procedure outlined in Section 2.2.1. Figure 2.5 provides schematics of the annealing environments for the different sample holders. Figure 2.5 (a) shows the insertion of the

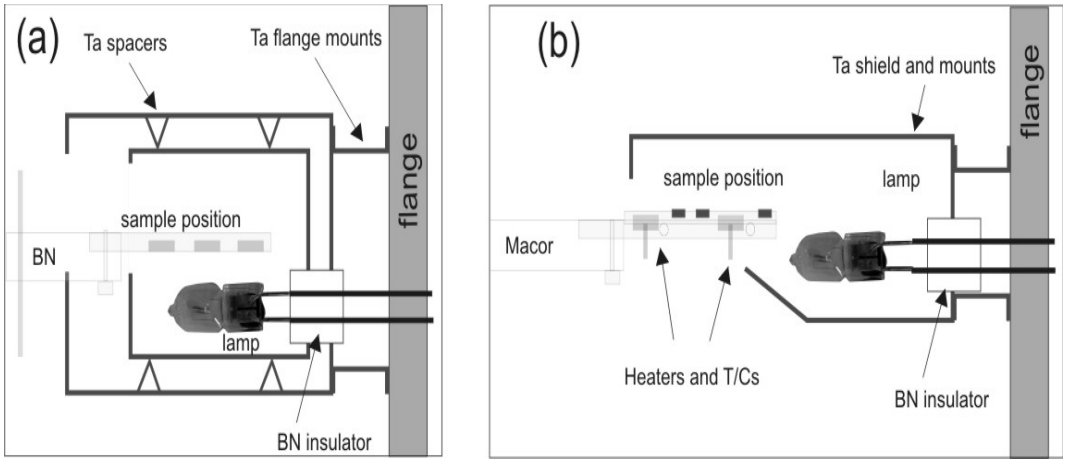

Figure 2.5: Annealing environments for the different sample holders. (a) Figure reproduced from Ref. [13], samples are annealed using radiation provided by a lamp. (b) Substrates on the new sample holder were annealed using a combination of conductive and radiative heating.

sample holder into concentric tantalum cylinders. Heating is provided by a 50 W lamp, though when run at $\sim$ 60 W the sample holder temperature is 420°C [13]. Tantalum shields prevent the DRM from heating, and confine the radiation within the oven. Figure 2.5 (b) is a schematic of the heating arrangement for the new sample holder design. The intention was to anneal substrates in the new holder solely with heat supplied by the button heaters, but even with the filaments redhot the holder temperature was T$\leq$ 400°C. To prevent damage to the filaments, the oven of Figure 2.5 (b) was designed to combine radiative and conductive heating. With the lamp at 50 W and heater inputs of $\sim$ 6 W each, the sample holder can reach $\sim$ 450°C. Usually a ten degree differential was measured between the two T/C positions when T$\sim$ 450°C.

Mica

Mica substrates (grade V2) were received from Electron Microscopy Sciences (EMS). Each substrate is approximately 20×20 mm^2, and has a transparent yellowy/brown tinge. Mica is a hard material, but the planar crystallography allows crystals to be cleaved into thinner sheets. Substrate pieces 4mm by 6mm were cut to fit the sample holder, the pieces then cleaved using sellotape or a fine blade (i.e. a scalpel) in atmospheric conditions. Samples are immediately transferred into the vacuum chamber and pumped to UHV, then annealed for roughly 15 hours using the configuration shown in Figure 2.5 (a).

Baking graphite substrates overnight at 420°C has been proven to sufficiently clean the surface for diffusion studies [13], achieved when 60 W is supplied to the lamp. Mica substrates were found to deteriorate with the lamp at 50 W, the substrates becoming opaque and developing a rippled/buckled morphology. Sample

imaging (discussed later) proved impossible on buckled samples, hence Mica substrates were annealed at temperatures below 420°C. We cannot estimate the actual cleaning temperature as no T/C was attached to the holder at that time.

MoS_2

MoS_2 substrates were received from SPI supplies. A clean MoS_2 surface exhibits a bright grey sheen, though often when cleaving or cutting the crystal a sulfur deposit is exposed. Sample preparation involves cutting a 4×6 mm^2 piece of MoS_2 from the bulk crystal, then repeatedly cleaving with sellotape to produce a clean surface.

Annealing procedures for the mica experiment are repeated with MoS_2 substrates, one advantage being that samples do not degrade with the lamp at 60 W, allowing higher sample holder temperatures. A disadvantage of using MoS_2 substrates is that freshly cut pieces outgas heavily. From the observation of sulfur deposits on cutting/cleaving, these substrates clearly have high quantities of impurities. After annealing new MoS_2 substrates the base CC-pressure is $\sim 2\times10^{-7}$ torr, substantially higher than the typical base pressure 9×10^{-8} torr with mica or HOPG substrates. Heating MoS2 substrates leaves a black residue on the sample holder (likely to be copper sulfide), which is removed by cleaning with solvents such as IPA or Acetone.

HOPG

The familiar sequence of steps - cleaving samples with sellotape followed by annealing for 15 hours - is repeated for HOPG substrates using the new sample holder (Figure 2.4 (b)). After loading and evacuating, samples remain in the loading chamber until $P_{CC} = 10^{-6}$ torr. Tungsten oxidises more easily at high temperature, therefore the filaments are not heated until $P_{CC} = 10^{-6}$ torr. The sample holder is wound under the oven, then the heater current and lamp power are ramped up in stages to prevent thermal shock to the filaments. To keep temperatures across the sample holder homogeneous the heater closest to the water cooled DRM required a current of 1.8 A, the second heater using 1.5 A.

As stated above, samples are annealed at T=450°C, slightly higher than for the annealing of Scott [13]. Due to the improved insulation provided by the macor spacer, cooling to room temperatures takes longer than for the previous setup. Longer cooling times raise the possibility of gases in the chamber contaminating substrates. A compromise between cooling and contamination was to select a lower bound for the substrate temperature of T=303 K, roughly 10 K higher than room temperature. Comparisons of SEM images from samples grown at T=303 K with images of samples grown at room temperature [13] do not show obvious morphological differences.

Depositions on HOPG were performed with substrate temperatures ranging from

T=303 K to 353 K. Button heaters are adjusted to maintain the sample at the desired temperature during and after deposition. Due to the relatively low temperature and good insulation, a current of ~ 0.5 A was typically applied to each heater.

2.4 Bi_2 Beam Generation

The atomic beam is generated by thermal evaporation, bimsuth having a relatively low melting point at 271.3°C, and a high vapour pressure. Bismuth vapour consists of monomers and dimers, the exact ratio of the two species varying with temperature [50]. This thesis assumes the smallest diffusing particle is a Bi dimer (Bi_2). A crucible constructed by Midwest Tungsten Service is used to heat the bismuth. The crucible consists of an alumina coated tungsten filament and is shown in Figure 2.6. Surrounding the crucible are ceramic spacers and tantalum shields. A boron nitride cap with a small aperture contains the melt within the crucible, and directs the vapour. Ceramic spacers (visible in the photo) provide electrical insulation between the filament and tantalum shields. The tantalum shields provide some thermal insulation, and a container for any melt overflow, preventing molten metal from dripping into the ion pump. The upper tantalum lid prevents excess vapour contaminating the walls of the vacuum chamber, and focuses the vapour into a 8 mm diameter beam. Further collimation of the beam is provided by the stainless steel baffles apparent in Figure 2.3, the baffles also preventing ions from the ion pump contaminating the substrates.

Atomic flux is measured by the quartz crystal microbalance, located on the underside of the DRM, labeled in Figure 2.3. With the crucible current between 9-13 A, particle fluxes ranging from F=0.001 Å/s to 0.5 Å/s are generated. The DRM microbalance is an STM-100 from Sycon Instruments. Once crucible heating begins (after the substrate cleaning stage), the linear translator shifts the microbalance over the atomic beam, without exposing the substrates to the vapour. The atomic flux is measured, and any required adjustments to the crucible temperature are made. Since flux is calculated by measuring the volume of material added to the crystal within a time period, alignment of the crystal with the entire beam is important. If the beam does not cover the entire crystal, a reduced flux is calculated. Comparisons of predicted film thicknesses with measured thicknesses (using a DEKTAK and Atomic Force Microscopy) found the calculated flux was within 10% of the value read from the DRM. With a chosen flux, aligning samples with the beam for a fixed period of time deposits a known coverage.

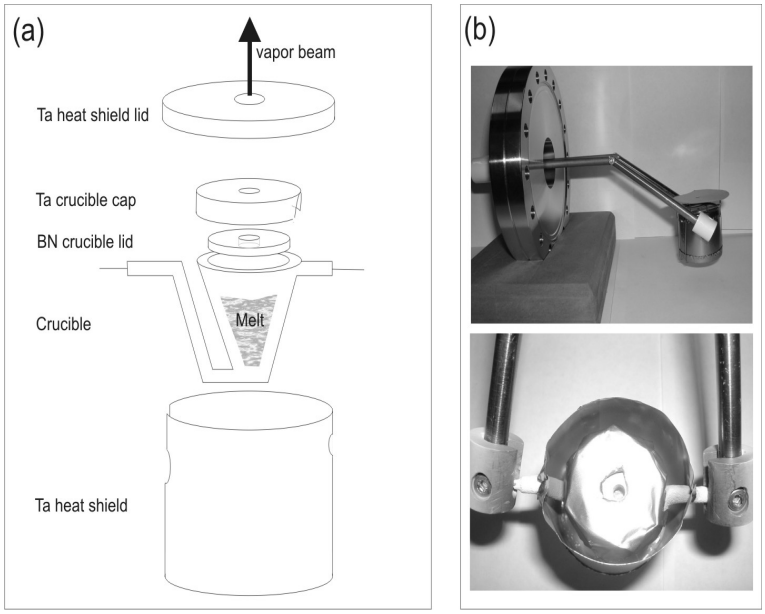

Figure 2.6: (a) A schematic of the crucible design showing the tungsten filament and various BN and tantalum spacers. (b) Photographs of the crucible and back plate. Image reproduced from Ref. [13]

2.5 Sample Characterisation

This section describes the equipment used to characterise Bi films. Two methods are used for sample imaging, Scanning Electron Microscopy (SEM), and Atomic Force Microscopy (AFM). Crystallographic information is determined using the Electron Back Scatter Diffraction (EBSD) technique. A brief description of the island density image analysis procedure is also given.

2.5.1 Electron Microscopy

SEM

Most of the sample imaging was performed using a Raith 150 field effect scanning electron microscope (FE-SEM). Typically the Bi features of interest are $\sim$1 μm^2 in size, therefore optical imaging techniques are not possible. AFM scans, although providing better resolution than SEM images, are time consuming and not ideal for imaging large areas of susbtrate.

Bismuth is a poor thermal conductor, and imaging under high kV electron beams can cause local heating, melting the film. An accelerating voltage of 4 kV was found to be a good compromise between image quality and sample damage. To standardise the imaging process, all images are taken at magnifications of 3000x or 10000x. At 3000x an image captures a surface region roughly 400 μm^2 in area, providing good

representation of film morphology.

EBSD

Crystallographic information of films was gathered using the electron backscatter diffraction (EBSD) technique. The samples were imaged using a JEOL JSM6100 SEM, fitted with an HKL Nordlys II detector. The detector captures backscattered electrons from the crystal surface on a phosphor screen, the patterns are then read by a CCD camera. Patterns exhibit symmetries of the crystal lattice, and using the HKL Channel5 software to compare the patterns to a library of crystal phases, the crystal structure of the film is determined. Results are presented using pole figures.

2.5.2 Atomic Force Microscopy

Atomic Force Microscopy (AFM) is a scanning method for collecting topographical information. For this thesis the AFM was operated in Tapping Mode, a low-contact method which reduces damage to the Bi film. In Tapping Mode the AFM operates by scanning a tip attached to an oscillating cantilever across a sample surface. The cantilever oscillates near its resonant frequency with a typical amplitude less than 100 nm. Tapping mode AFM can achieve very high lateral resolutions (1 nm to 5 nm at best), providing a more accurate picture of the film morphology than an SEM.

After a scan is taken, the scans are used for measuring film heights. The AFM is calibrated using bare graphite surfaces, which have step heights of 3.4 Å. A calibration factor (1.1) is automatically included in the height measurements presented in the thesis. Scans shown in this thesis are usually modified off-line using plane fits to remove tilt or bow from the image.

2.5.3 Image Analysis

The nucleation experiments for this thesis are typically for film thicknesses ≤ 2 monolayers (ML), the material aggregating into islands a number of monolayers high. SEM images are used to measure the island densities. Island densities are calculated simply by defining an area in an image, and comparing the area to the number of islands within the boundary to the area. Figure 2.7 provides an example of a boundary drawn on a HOPG surface. The area is calculated (in SI units) by first counting the pixels within the boundary, then comparing with the image scalebar. Both MoS_2 and HOPG samples have terraced regions surrounded by lattice steps, therefore when defining the boundary such features avoided.

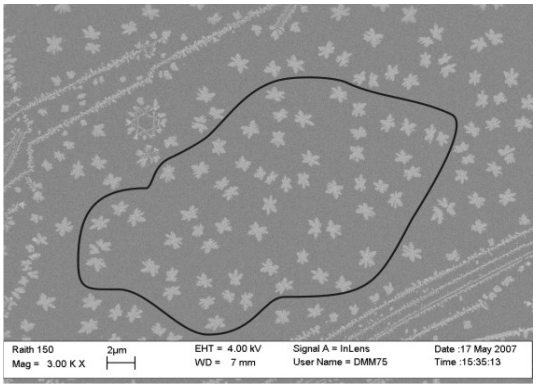

Figure 2.7: An SEM image of bismuth islands on a HOPG substrate. A boundary is defined for the island counting exercise, the outline avoiding island features and well away from steps in the graphite.

Across each sample are regions of high and low island density. Care is taken during the imaging step to find regions which exhibit the lowest, and most uniform, examples of nucleation. Hence the calculated island density is lower limit for a sample.

2.6 Kinetic Monte Carlo Simulations

In Chapters 4 and 5, we discuss simulation results found using kinetic Monte Carlo (KMC) algorithms. Chapter 4 uses a KMC algorithm to investigate surface diffusion processes important for the growth of high aspect ratio Bi structures grown by deposition on HOPG surfaces. Chapter 5 uses a different KMC algorithm to investigate the coalescence of atomic clusters via surface diffusion.

This section introduces the KMC technique, then describes the individual algorithms used in Chapters 4 and 5.

2.6.1 Introduction to KMC

Utilising the advances in computer processing speeds and memory, a number of computational techniques have been developed to study the statistical properties of physical systems. The Monte Carlo method is one such technique which uses a probabilistic description to evolve a dynamic system. The end state of the system is determined by the stochastic path of the algorithm. The probabilistic method is a different approach to deterministic methods such as Molecular Dynamics (MD). In solid state physics, Monte Carlo methods are often applied to atomic diffusion scenarios, where random walks generated by a basic MC algorithm replicate Brownian diffusion, while more sophisticated algorithms simulate nucleation and

aggregation processes. For epitaxial systems, KMC simulations reproduce island densities and size distributions predicted by mean field theories [51], while allowing the investigation of novel effects such as island shape.

2.6.2 MD versus KMC

Molecular Dynamics simulations consider interatomic forces, evolving a system of atoms with time using classical equations of motion. Assuming quantum effects are insignificant, given a correct interatomic potential MD simulations accurately predict the properties of the real system. The problem for MD simulations is that atoms remain in one state for long periods relative to their vibration frequency. Since the MD timestep must necessarily be smaller than the vibration frequency to accurately model the dynamics, thousands of MD timesteps (and therefore calculations) are required between each atomic event. MD simulations are clearly computationally intensive, and 'long' MD simulations might only simulate a real timescale of 1 μs. KMC performs state to state events with each iteration, assuming that the long time dynamics of the atomic vibrations are random diffusion events between states. Each 'state' represents the simulated collection of particles vibrating in a configuration which is a local minimum of the potential. KMC simulations can therefore investigate real timescales on the order of seconds.

2.6.3 A KMC Algorithm

Early adatom diffusion theories were based on concepts of an atom moving across a static potential field. This was formalised in a theory developed by Glasstone [52], and termed transition state theory (TST). Diffusion proceeds via thermally activated hops from an occupied site to a nearest neighbour site, the hop restricted by some potential barrier E_k. Successive jumps are uncorrelated (stochastic), and individual adatoms diffuse independently of other diffusing adatoms.

According to TST, adatoms hop between potential wells at rate [24, 53, 54],

$$r_k = m_k \nu_k \exp^{\frac{E_k}{k_B T}}, \tag{2.1}$$

where m_k is the multiplicity, ν_k is the adatom vibration or 'attempt' frequency, and the energy barrier is E_k. T is the temperature and k_B is Boltzmann's constant. We will refer to individual diffusion hops as an event. The multiplicity refers to the possible ways an event can occur, i.e. for an atom diffusing on a square lattice the factor is 4, for an atom diffusing in 1D the factor is 2. For solids the attempt

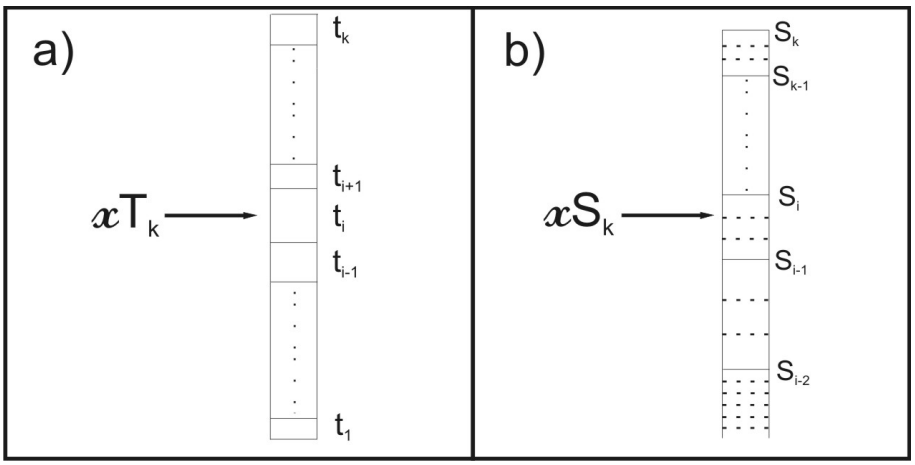

Figure 2.8: Event selection is performed by multiplying the cumulative function by a random number, x. Schematics of the cumulative functions are shown (a) for the standard KMC algorithm, the size of each box is just the rate constant for that event. (b) for the Schulze algorithm [58], the size of each box (full lines) is the number of events n_i occuring at rate s_i, multiplied by s_i. The Schulze algorithm is more efficient for large systems, since method (a) searches through all the transitions, while method (b) searches through the smaller rate list.

frequency is assumed to be the substrate phonon frequency, typically $\nu \sim 10^{13}$ s^{-1} [21]. The exponential term in Equation 2.1 determines the probability of success for each attempt, and follows a Boltzmann distribution. Diffusion barriers E_k vary depending on an atom's local environment i.e. the configuration of neighbouring atoms determines the shape and size of the potential well where an atom resides. Barriers can be calculated by theoretical methods (Embedded Atom Methods [55], Density Functional Theory [56], Nudged Elastic Band [57] methods), taken from experimental data, or approximated using concepts of bond breaking.

Different methods (or algorithms) exist for implementing KMC models, but the basic procedure is as follows:

1. Determine all the possible events k for a system in a given state, and assign a rate $t_i = \nu_i \exp^{\frac{E_i}{k_B T}}$ to each event. Note the multiplicity of Equation 2.1 is not included, as every possible event is counted separately

2. Calculate the cumulative function $T_k = \sum_{i=1}^{k} t_i$ for i=1...k, where k is the total number of events possible for the state. T_k is depicted in Figure 2.8 (a)

3. Generate a random number $x \in (0, 1]$ and find the event t_i such that $t_{i-1} < xT_k < t_{i+1}$, the event is typically found using a binary search method

4. Perform the event, and recalculate rates which may have changed due to the event

5. Increment the time $\tau = \tau + \Delta\tau$

6. Repeat

Time is usually incremented by one of two methods. The first method is to increment the time as the inverse of the total rate function, $\Delta\tau = \frac{1}{\mathrm{T_k}}$. A second method calculates $\Delta\tau = -\frac{\ln(\mathrm{x})}{\mathrm{T_k}}$, where ln of x (x $\in (0, 1]$ is a new random number) is an exponentially distributed random number. The latter method emphasises the exponentially distributed waiting times for state to state events occurring at rate R. Note that integrating ln(x) between 0 and 1 equals -1, so for many iterations (and many random numbers x $\in (0, 1]$) the times are equivalent.

If the correct diffusion barriers are assigned for each state of a system, the KMC algorithm will simulate the exact dynamical evolution of the system. In reality diffusion is too complex to efficiently model all the possible processes, and the rate lists are reduced to a few, 'important', events.

2.6.4 Details of our KMC Models

In Chapters 4 and 5 of this thesis, simulations are performed using two different KMC algorithms. In this section, a general introduction to each algorithm is provided, while details specific to the simulations are included later in the relevant chapters. Each algorithm uses a random number generator adapted for Fortran 77 from a Pascal Code presented by Park and Miller [59], and the computationally efficient binning technique of Schulze [58], which bins events with equivalent rates together. Note the binning procedure is different to that outlined in Section 2.6.3. The procedure is outlined as follows:

1. Determine all the possible events for a system in a given state, and assign a rate $\mathrm{s_i} = \nu_\mathrm{i} \exp^{\frac{\mathrm{E_i}}{\mathrm{k_B T}}}$ to each event.

2. Compute the partial sums $\mathrm{S_k} = \sum_{\mathrm{i}=1}^{\mathrm{k}} \mathrm{s_i n_i}$, where i=1,..,k, where k is the number of different rates, and $\mathrm{n_i}$ is the number of events occuring at rate $\mathrm{s_i}$. The partial sum $\mathrm{S_k}$ is shown in Figure 2.8 (b)

3. Generate a random number x $\in [0, 1]$

4. Select a partial sum $\mathrm{S_i}$ satisfying $\mathrm{S_{i-1}} < \mathrm{xS_k} \leq \mathrm{S_i}$

5. Select an event b from within the selected partial sum, $\mathrm{b} = [\frac{\mathrm{S_i - xS_k}}{\mathrm{s_i}}] + 1$

6. Execute the event and update the event lists

By binning together events with equal selection probability, and recording the positions of each event within the bin, the Schulze algorithm finds an event without searching through the entire list of events. We now describe the algorithms used in Chapters 4 and 5.

2.6.5 Anisotropic Growth Model

In Chapter 4 anisotropic growths from step edges are simulated, with simulation parameters chosen to approximate experimental conditions. The growths are referred to as rods [13, 60]. We now outline the code used for the simulations of Chapter 5.

The surface diffusion/step growth simulations are performed assuming a small set of atomistic diffusion events which are believed to be relevant to the growth of anisotropic structures [61, 54, 62]. Using a square lattice, we have defined ten individual diffusion events plus deposition, the events weighted by their respective rates. Event rates are defined using [1]

$$\mathrm{r_k} = \frac{\mathrm{k_B T}}{\mathrm{h}} \exp \frac{-\mathrm{E_k}}{\mathrm{k_B T}}, \tag{2.2}$$

where h is Planks constant.

Figure 2.9 shows a schematic of the possible diffusion events, and notation for the associated diffusion barriers. Adatoms are deposited onto the surface at a deposition rate F in units of monolayers per second (ML/s), the probability of deposition proportional to the lattice size. Adatoms diffuse on the terrace via nearest neighbour hops until reaching an obstacle, such as an aggregate or step-edge. The terrace diffusion barrier is $\mathrm{E_t}$, and the step-edge diffusion barrier $\mathrm{E_s}$. Atoms move along rod edges via the barrier $\mathrm{E_e}$. Along the edge there are vacancies, which atoms can hop into via e.g. $\mathrm{E_e^{AA}}$. Material can detach from a facet via the appropriate corner crossing barrier $\mathrm{E_c}$, or via detachment barrier $\mathrm{E_D}$.

Rod facets are distinguished as perpendicular (A), or parallel to the step-edge (B). Therefore the edge diffusion, corner crossing, and detachment events shown in Figure 2.9 are categorised according to which facet an atom is located on.

Since corner crossing is a next-nearest neighbour event, the algorithm considers the eight sites surrounding an atom when evaluating events. After each diffusion or deposition event, the eight sites surrounding the initial position and the eight sites surrounding the final position have their events re-evaluated according to the new atomic configuration.

[1] Reference [63] states the prefactor $\frac{\mathrm{k_B T}}{\mathrm{h}}$ leads to incorrect temperature scaling, persistently appearing in the literature due to its coincidental similarity to the substrate phonon frequency.

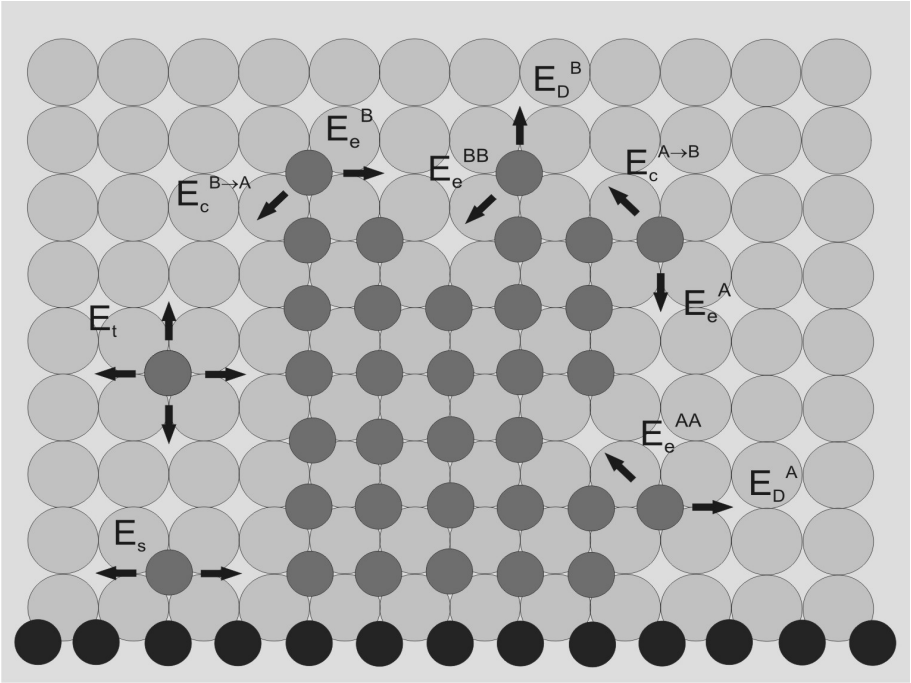

Figure 2.9: Schematic of a rod growing from a step on the (001) surface. Key diffusion events and energy barriers are labeled. The A and B notation respectively refers to rod facets perpendicular or parallel to the step-edge.

As shown in Figure 2.9, an atom can potentially diffuse via multiple events. For instance an atom located at the corner of an A facet can edge diffuse, cross the corner onto the B facet, or detach from the rod via two directions. These four events are stored in three different event lists, since the two detachment events occur at the same rate. Hence two entries are made on the detachment list, and a vector associates the position of the entry on the n_k list with a particular diffusion direction.

Rod Densities

To test whether our code correctly simulates the Brownian diffusion of atoms, we compare simulation results with predictions of mean field theory. Mulheran and co-workers [64, 65, 66] investigated nucleation on step features for both point and hemispherically shaped islands, finding that the density of nuclei at saturation scales as [66]

$$N_{sat} \propto (\frac{D}{Fw})^{-\sigma}, \tag{2.3}$$

where D is the diffusion coefficient (for atoms bonded to the terrace and/or step), F the flux, w the terrace width, and $\sigma = \frac{i}{3i+d}$ a parameter related to the critical island size i and dimension of diffusion d. Essentially this formula relates the density of

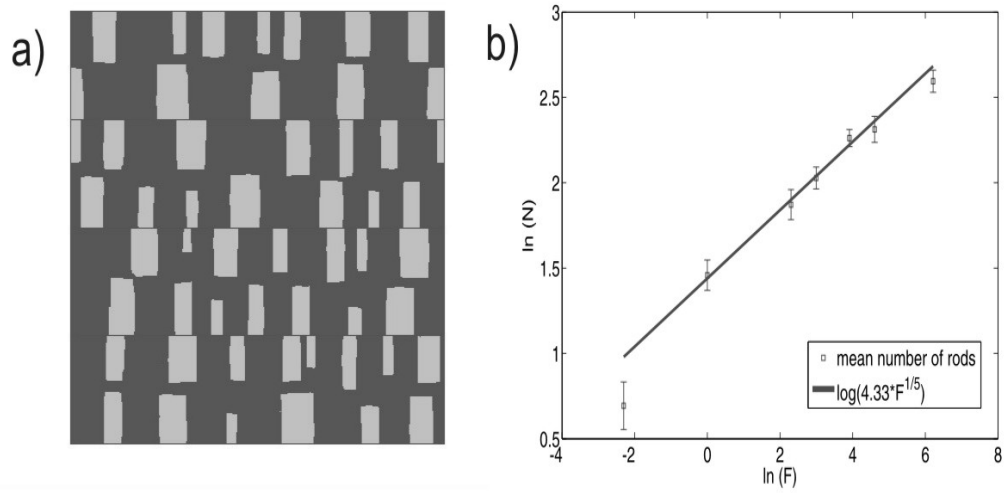

Figure 2.10: (a) Lattice shape and rod density with F=10 ML/s (b) Mean number of rods per step plotted against F using a natural log scale, where F ranges from 0.1 ML/s to 500ML/s.

step nucleated features to the rate at which particles arrive at the terrace edge ($\frac{\mathrm{D}}{\mathrm{Fw}}$), predicting a scaling exponent $\sigma = 1/5$ when d=2 and i=1.

Figure 2.10 (a) shows typical simulated step growth for a lattice with four terraces 100 atoms wide and 400 atoms long. Conditions leading to the rod morphologies in Figure 2.10 are described in Chapter 4, though i=1 and d=2 for the simulations. Figure 2.10 (b) plots the mean number of rods per step from F=0.1 ML/s to 500 ML/s, using a natural log scale. Deposited coverage is 0.3 ML. The slope of the data is fitted assuming a power law dependence of $N \propto \mathrm{F}^{\sigma}$, Excluding the F=0.1 ML/s data point we find an exponent $\chi = 1/5$ fits the data. At F=0.1 ML/s the rod densities are so low that most rods grow across the terrace onto the opposite step. This likely reduces the probability of nucleation on the opposite step, and is a different system to the growth considered by Pownall [66]. However, reproduction of predicted scaling laws for $\mathrm{N_{sat}}$ gives confidence that our code accurately models the Brownian diffusion of atoms.

2.6.6 Cluster Coalescence Model

In Chapter 5 we use a bond-breaking model to study the coalescence of atomic clusters. The structure of the code was supplied by Schulze [67], and is based on work by Combe and Jensen [68, 69, 70].

The bond-breaking model calculates diffusion rates assuming that diffusion barriers are exponentially proportional to an atom's coordination (or number of neighbours, n). Accordingly, atoms with few neighbours diffuse at higher rates than

atoms with high coordination. The model is an approximation to solid systems where surface diffusion is activated. In such systems, out of equilibrium shapes will relax into thermodynamically favourable shapes via the transport of material from regions of high curvature to regions of low curvature. In the model, atoms at regions of high curvature are loosely bound, and diffuse quickly into regions of lower curvature, creating a net flux of material into the low curvature regions. Objects modeled by a bond-breaking scheme naturally prefer compact shapes, and are therefore useful for studying the relaxation of non-equilibrium shaped objects.

In general the bond counting energy barrier assumption is incorrect, for example diffusion on metal (001) surfaces finds edge diffusion (n=5) is faster than terrace diffusion (n=4) [71, 54]. As argued by Combe and Jensen [68, 69, 70], if only global trends exhibited by the simulations are considered (for instance equilibration times), then the microscopic details of the diffusion are unimportant.

Chapter 5 simulates the coalescence and relaxation of fcc crystalline clusters via surface diffusion. Each atom in an fcc lattice has twelve nearest neighbour lattice sites. With the bond breaking model an atom is added to one of twelve event lists, depending how many of the twelve neighbour sites are occupied. Each event list is weighted by a rate

$$\mathrm{r_n} = \frac{\mathrm{k_B T}}{\mathrm{h}} \exp^{-\frac{\mathrm{n} * \mathrm{E_0}}{\mathrm{k_B T}}}, \tag{2.4}$$

where $\mathrm{E_0}$ is the energy for a single bond, and n=1,..,11. Atoms are not allowed to have zero neighbours hence n=0 is not considered, and atoms with twelve neighbours have no vacant neighbour sites to mode into, therefore $\mathrm{r_{12}} = 0$. Rates defined by Equation 2.4 decrease exponentially as n increases.

For the bond breaking model atoms are binned according to their coordination. Using the Schulze algorithm there are twelve partial sums, each weighted by their respective rate $\mathrm{r_n}$. The probability for an atom with n neighbours being selected is simply

$$\mathrm{P_n} = \frac{\mathrm{N_n} \exp^{\frac{\mathrm{wE_0}}{\mathrm{k_B T}}}}{\sum_{\mathrm{j=1}}^{12} \mathrm{N_j} \exp^{\frac{\mathrm{jE}}{\mathrm{k_B T}}}}, \tag{2.5}$$

where $\mathrm{N_j}$ is the number of atoms with j neighbours.

Once an atom has been selected, it is necessary to determine where the atom should move to. Since we are considering a model system, the rates of Equation 2.4 do not include a factor for the diffusion multiplicity (see Equation 2.1), even though atoms on a (111) plane (m$\sim$6) have different multiplicity to atoms on a (001) plane (m$\sim$4). Instead, only once an atom is selected for diffusion are the possible diffusion directions considered. Since only nearest neighbour hops are possible, one of the va-

cant neighbour sites is randomly selected for the event. The event is performed, and sites neighbouring the initial and final positions have their coordination adjusted.

2.7 Summary

We have discussed the experimental setup and procedure for growing Bi thin films on Mica, MoS_2, and HOPG substrates. An outline of the substrate preparation, heating, and film analysis has been provided. KMC algorithms have been discussed, including a general introduction to models of anisotropic growth and cluster coalescence. Specific simulation parameters will be provided in Chapters 4 and 5.

Chapter 3

Diffusion and Nucleation of Bismuth on Planar Surfaces

In this chapter experimental investigations of Bismuth (Bi) thin-films on Mica, Molybdenum disulfide (MoS_2), and HOPG substrates are detailed. The results investigate the dependence of film morphologies and island densities on experimental parameters. Section 3.1 provides a review of thin-film studies for each of these surfaces. In Section 3.2 a brief AFM study of bismuth films grown on Mica substrates is presented. Section 3.3 discusses results of a flux and coverage dependent study for the Bi/MoS_2 system. Section 3.4 discusses results from a temperature dependent study of island nucleation and growth for the Bi/HOPG system. Island densities measured from Bi/HOPG experiments are compared with predictions of mean field nucleation theory, and conclusions on the diffusion of bismuth particles on graphite are drawn.

3.1 Literature Review

This Section reviews self-assembled thin films (using atomic and multi atom seeds) on each of the three substrates used in the experiments.

3.1.1 Mica

Electrons in a Bi crystal can have a de Broglie wavelength of 500 Å [72] at room temperature. Bismuth films grown on insulating substrates are therefore good candidates for observing room temperature quantum size effects. Hence ultrathin bismuth films have been grown on mica, with an emphasis on the production of high quality films.

Electron diffraction studies by Komnik [73] of bismuth films grown on heated mica flakes found the trigonal Bi$\{0001\}$[1] orientation parallel to the mica substrate was predominant. The Bi$\{01\bar{1}1\}$ or Bi$\{01\bar{1}2\}$ orientations were also observed, more often for low coverage films. Deposition of bismuth onto alkali halide (e.g. NaCl) crystals produces films with similar orientations [74]. Work by Patel [15] proved the crystal orientation of bismuth films is influenced by growth conditions. Adjustments in the substrate temperature and atomic flux can eliminate both the $\{01\bar{1}2\}$ and $\{01\bar{1}1\}$ film orientations.

Rogacheva *et al.* [75] have made conductivity measurements of bismuth films on mica substrates for films ranging from 3 to 300 nm. Oscillatory dependences of the electrical conductivity, Hall coefficient, Seebeck coefficient and charge carrier mobility were characterised as a function of film thickness. Films were prepared at two temperatures T_1=380 K and T_2=300 K, and beyond the percolation threshold islands formed connected chains between two contacts. Electron microscopy found the crystallinity of films prepared at T_1 was better than films prepared at T_2, and the higher quality films showed an oscillatory behaviour of higher amplitude. Crystals grown at T_2 had smaller domains, enhancing electron scattering from grain boundaries, suppressing any quantum effects. Electrical measurements were all performed at room temperature, and the results attributed to electron confinement.

The above works have focused on the coverage range 3 nm to 300 nm, with deposition rates of 0.5 to 5 nm/s. Only in Ref. [76] has the evolution of the island density been investigated in the low coverage regime. Films were grown within the temperature range 308 K to 593 K, and flux between 0.03 and 0.4 Å/s, the depositions performed at high vacuum (pressure $\approx 5 \times 10^{-7}$ torr). Saturated island densities ranged from $N_{sat} = 2 \times 10^{11}$ cm^{-2} at the lower end of the temperature range, decreasing to $2{\times}10^{9}$ cm^{-2} at T=473 K. Above 473 K adatom desorption was too frequent to allow accurate counting of island densities.

No study has yet considered the morphology of Bi islands on Mica substrates, and the possible relation between morphology, growth conditions, and crystal orientation. Hence in Section 3.2 the results from an AFM study of Bi films on Mica substrates is presented.

3.1.2 Molybdenum diSulphide

Island densities of Bi films on Mica are orders of magnitude greater than on HOPG substrates [13] pg 103, likely due to the residual electrostatic charge on Mica sur-

[1]The convention for the use of brackets in crystallographic notation is: (hkl) specific plane, {hkl} family of equivalent planes, [hkl] specific direction,<hkl> family of equivalent directions

faces. As will be discussed, island nucleation on the MoS_2 surface is expected to be between the extremes of Mica and HOPG, and may therefore provide an interesting comparison. No known studies investigate Bi thin films on MoS_2 substrates.

Stegemann [77] reports a study of self-organised antimony films on MoS_2 substrates, using Sb tetramers as the diffusing species. Films less than 1 ML thick are grown at 90 K, and characterised using a UHV-STM. The tetramers aggregate into 2D islands. As deposition proceeds additional layers nucleate on top of the base layer, the growth therefore following a Volmer-Weber [78] type mode. Each layer is approximately 4 Å in height, corresponding to the height of a single tetramer. Material contributing to second and third layers is determined to have arrived directly from the vapour rather than the terrace, indicating an Ehrlich-Schwoebel type-barrier preventing interlayer transport. Island densities were reduced for depositions at room temperature, the islands having wider bases and $\sim$ 40 nm thick. Room temperature morphologies are comparable to Sb_4 islands grown on HOPG at room temperature, indicating antimony particles have similar diffusion behaviours on both MoS_2 and HOPG. Analysis of the bare MoS_2 substrate surface with the STM yields an intrinsic defect density of 2×10^9 cm^{-2}.

The adsorption and surface diffusion of Ag, Cu, and Au atoms on room temperature MoS_2 substrates has been investigated by Becker [79] using an STM. During early deposition stages islands of $\sim$monolayer thickness and lateral extensions of 2 nm (Ag), 8 nm (Cu), and 10 nm (Au) were found. Copper islands are subsequently observed to diffuse, *without* loss of size or shape, surface diffusion apparently hindered only by aggregation and coalescence with other islands. More limited diffusion of small Au islands is observed. The results suggest a weaker Cu-S interaction than for gold or silver.

Thin Bi films grown on Silicon and HOPG substrates have been observed to prefer different crystallographic orientations depending on film thickness [13, 80, 14] (discussed further in Section 3.1.3). The observation of a similar transition for Bi films on MoS_2 surfaces may help determine the origins of the transition. MoS_2 substrates exhibit the same hexagonal symmetry as the honeycomb HOPG lattice, therefore a study of Bi island morphology and density on MoS_2 would provide a useful comparison to results from HOPG surfaces [13].

3.1.3 HOPG

Graphite substrates are commonly used for diffusion and nucleation studies due to the large, contaminant free terraces of the freshly cleaved crystal. Honeycombed

layers of carbon atoms are held together by Van der Waals bonds, therefore interactions between the diffusing species and substrate are weak. Experiments for both atomic and cluster diffusion are detailed in the literature.

Atomic Diffusion

Darby and Wayman [81, 82] studied the growth of gold dendrites on graphite substrates. For substrate temperatures $\sim 100°$C, dendrites were found to grow with two distinctive shapes, a star-shape with primary branches symmetric under 60° rotations, or a 3-branched dendrite symmetric under 120° rotations. Samples were examined using Transmission Electron Microscopy (TEM). Diffraction experiments revealed the Au(111) plane oriented parallel to the HOPG(0001) surface, regardless of the type of dendrite. The in plane orientation of the gold film was found to be Au$[01\bar{1}]||[10\bar{1}0]$HOPG. The preferred alignment of the Au crystal with the substrate lattice is surprising considering the expected weak influence of the substrate. With increased substrate temperatures (350°C), the dendrites were replaced by compact crystals with hexagonal or trigonal morphology.

Anton [83, 84] has performed *in situ* TEM experiments of Au dendrite growth on graphite, as a function of temperature and coverage. TEM images taken during deposition allowed dendrite sizes to be monitored as a function of time. Dendrite heights were estimated to be 1.5 nm to 2 nm from calculations of deposition parameters and observed coverage. The adatom mean diffusion length was estimated as $\lambda = 400$ nm at room temperature. The diffusion length reduces to ≈ 6 nm at 350°C. At high temperatures the increased desorption of Au atoms from the graphite surface accounted for the small λ. Anton determined island densities in low defect areas to be 10^9 cm^{-2}, *independent* of temperature, suggesting the gold atoms were irreversibly trapped at defect sites. Island densities were not analysed as a function of particle flux.

Low coverage bismuth films grown on HOPG at room temperature by Scott [13] pg 90 found dendritic island growth similar to the results from Au experiments. For film coverages of 2 ML islands aggregated with heights $\sim$1 nm, three to four Bi monolayers tall, and island sizes typically 1 μm^2 [85]. Figure 3.1 reproduces an image from [13] pg 91, illustrating the flux dependence of island morphologies for 1.5 ML films. At F=0.0074 Å/s two island morphologies co-exist. One is hexagonal (with heights of $\sim$2 nm), the second is an elongated star. As the flux is increased only the star morphology is observed, and instabilities along the island edges become more common [13, 85]. A study of the island density determined an upper limit for the substrate defect density of 9×10^6 cm^{-2}, assuming Bi dimers are trapped by

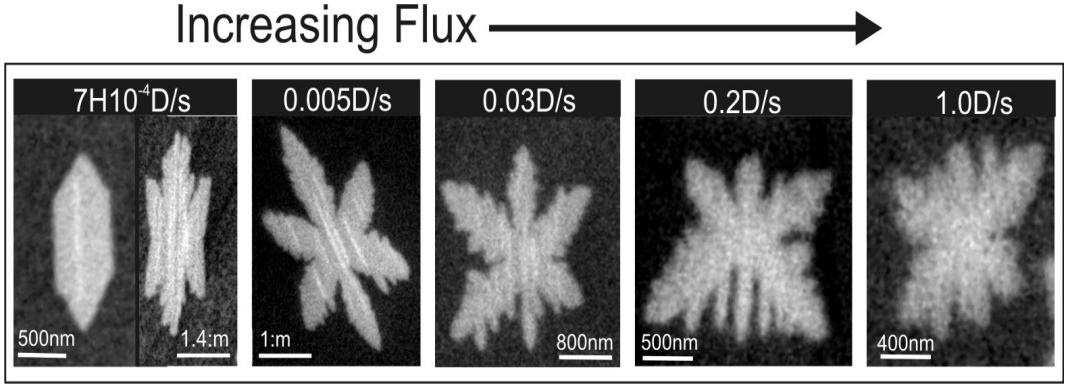

Figure 3.1: SEM images reproduced from Scott [13] pg 91. The images illustrate the flux dependence of room temperature island morphologies, for 1.5 ML Bi films on HOPG. As the flux is increased, island shapes develop dendritic characteristics.

defects. The defect density is two orders of magnitude lower than the value quoted by Anton [83].

For film coverages $\leq$12 ML, a preferred film orientation of Bi$\{01\bar{1}2\}$ parallel to the graphite surface was found using the EBSD technique. Above 16 ML, the films underwent a transition to a trigonal Bi$\{0001\}$ oriented film [13, 80]. Nagao *et al.* [14] investigated a similar transition for Bi films on reconstructed Si(111) surfaces, the transition occurring above 4 ML.

Previous work by Scott [13, 86] and Stegemann [87] investigated films grown by the deposition of Sb_4 particles onto room temperature HOPG substrates. Island morphologies were investigated as functions of coverage and flux, results finding islands prefer compact (low surface energy) morphologies at low flux, while for a high flux, fast-growth environment, branched structures were favoured. Kaiser *et al.* [88] have reported on self-organised growth in the Sb/HOPG system, where a size dependent phase transition from amorphous Sb islands into dendritic, crystalline islands was observed.

In a temperature dependent study of the Sb_4/HOPG system, Wang *et al.* [89] observed and characterised the different morphologies of Sb_4 islands on HOPG, as a function of substrate temperature. At room temperature amorphous islands grow with viscous fingering for high flux. At elevated temperatures (100°C) 2D-Sb crystals form on nucleation, the islands commonly featuring 1D stripes.

Cluster Diffusion

The diffusion of small, size selected metallic clusters on HOPG substrates has been observed by a number of authors [90, 91, 92, 93, 94]. Results find clusters typically 2-5 nm in diameter have appreciable diffusion coefficients at room temperature. Schulze *et al.* [95] find experimental evidence for the diffusion of 20nm bismuth

clusters on room temperature HOPG substrates.

By measuring the island density of an investigation of self-assembled cluster films on HOPG surfaces, and assuming cluster diffusion is described by $D = D_0 \exp \frac{-E_A}{k_B T}$ (see Chapter 1), Bardotti *et al.* [91, 92] found room temperature diffusion prefactors of $D_0 = 10^4$ cm^2s^{-1} for Sb_{2300} clusters, and $D_0 = 10^3$ cm^2s^{-1} for Au_{250} clusters. Activation energies were calculated to be $E_A = 0.7$ eV for Sb_{2300} and $E_A = 0.5$ eV for Ag_{250}. Approximate room temperature diffusion coefficients for both clusters are therefore 1×10^{-8} cm^2 s^{-1}, compared with $D \sim 1 \times 10^{-17}$ cm^2s^{-1} found for similarly sized Ag clusters on the Ag(001) surface [96]. Bardotti [92] also present KMC simulation results which allow diffusion of multi-cluster aggregates, assuming diffusion coefficients of $D_n = \frac{D_1}{n}$, where n is the aggregate size in terms of clusters, and D_1 is the diffusion coefficient of a single cluster. Simulation results found the saturated island density is proportional to $F^{0.42}$, in agreement with theoretical predictions (see Section 3.4.4) for mobile aggregates [97].

An interesting result from the cluster diffusion studies [92] was that although individual Sb_{2300} clusters diffuse freely, a flux dependent study of Sb_{250} island densities determined the critical particle size for this system was an Sb_{250} cluster, i.e. multi-cluster aggregates with fewer than 2300 atoms were immobile. Bardotti *et al.* concluded that colliding particles require a coalescence type process to shift material into a more uniform shape, the uniform shape required for diffusion. Coalescence occurs slowly relative to the timescale of aggregation, and therefore multi-cluster aggregates are immobile.

Molecular dynamics simulations [98, 99, 100] of ∼hundred atom Au clusters on graphite have been compared to the experimental results of Bardotti. Results predicted diffusivities of clusters containing hundreds of atoms to be comparable to that for single adatoms, the high diffusivitiy a consequence of the weak cluster-substrate interaction. In fact, cluster pairs were found to diffuse at rates comparable to single clusters. Lewis *et al.* [99] use Monte Carlo simulations to predict the scaling behaviour of N_{sat}, the saturated island density, when multi-cluster islands can diffuse. In their simulations, multi-cluster islands are allowed to diffuse via $D_N = D_0 N^{\frac{2}{3}}$, where N is the number of clusters in the island ($N^{\frac{2}{3}}$ its surface area) and D_0 is the diffusion coefficient of a single cluster. Results show the island density decreases as the maximum multi-cluster size (N_{max}) increases. Figure 7 of Ref. [99] shows N_{sat} scaling as $\approx N_{max}^{-1}$.

Summary

The flux dependent study [13, 85, 60] of Bi films on HOPG found interesting

island morphologies and transitions in crystal orientation depending on growth parameters. In Section 3.4 we present a temperature study of the transition from kinetically limited growth at room temperature to near-equilibrium growth for raised temperature. We also investigate the temperature dependence of the island density, adding to the flux dependence study of Scott [13]

3.2 Bismuth on Mica

In this section an AFM study of monolayer bismuth films on mica is presented, the results largely focus on island densities and island morphology.

3.2.1 Experimental Procedure

Results presented here are from *ex situ* AFM scans taken post-deposition. AFM characterisation of the film surface is necessary due to the insulating properties of mica substrates. Probing the samples with an electron beam leads to a buildup of electric charge on the film's surface, preventing the capture of high quality images using Electron Microscopy techniques. Using only the AFM places restrictions on the quality of the results, as it reduces the quantity of information gathered from each sample. A number of samples were coated with thin layers of carbon or gold to allow the imaging of substrates with an SEM. The trialled methods were all unsuccessful, the coatings either too thin to reduce surface charging, or too thick to distinguish features of the thin Bi films.

3.2.2 Results

Island morphologies observed in the AFM scans were studied as a function of flux and coverage. Figure 3.2 displays two AFM scans of islands grown at F=0.01 Å/s and coverages of 1 ML and 2 ML. Figure 3.2 (c) is a scan taken from a 2 ML sample grown at F=0.09 Å/s. Figure 3.2 (d) is an AFM trace from the scanline highlighted in (a).

Island morphologies are separated into two categories, islands have either oblong or circular shapes. Oblongs do not display a preferred orientation, as there is no common alignment to the islands, and their size seems to depend on how large their respective capture regions are, i.e. the proximity of other islands. As the trace of Figure 3.2 (d) reveals, the oblong shaped islands have heights of ∼4 nm, with the brighter, rounder islands ∼9 nm.

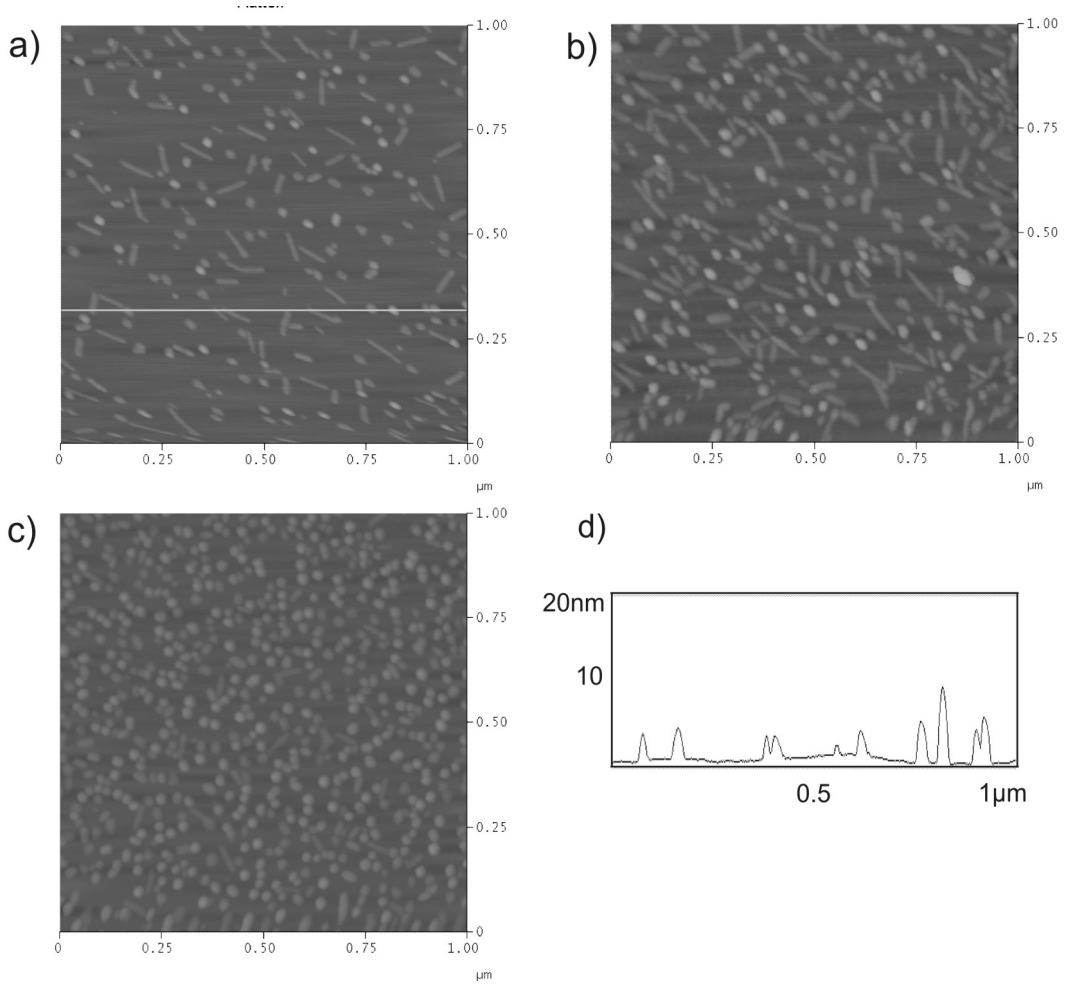

Figure 3.2: AFM images from two substrates grown with F=0.01 Å/s for coverages of (a) 1 ML, (b) 2 ML, and for image (c) F=0.09 Å/s 2 ML. Island densities are 2.3×10^{10} cm^{-2}, 3.3×10^{10} cm^{-2}, and 5.4×10^{10} cm^{-2} respectively. (d) shows the trace of the scanline shaded in image (a).

Island densities from the three scans are (a) 2.3×10^{10} cm^{-2}, (b) 3.3×10^{10} cm^{-2}, (c) 5.4×10^{10} cm^{-2}. Comparing (a) and (b), grown at the same conditions but for different coverage, the higher island density of (b) suggests nucleation is not saturated at 1 ML. Figure 3.2 (c), with F=0.09 Å/s has a higher island density than (b) when F=0.01 Å/s. The increase in island density with flux indicates nucleation is occurring via adatom-adatom collisions rather than at defect sites.

Figure 3.2 (c) has a higher proportion of the rounded islands than Figure 3.2 (a) or (b), although a few oblong shaped islands are visible. The change from elongated to circular morphologies with higher flux suggests the flatter oblong structures have a more thermodynamically favourable shape. The higher density of islands in Figure 3.2 (c) reduces the amount of material reaching each island. Possibly the oblong structures require both the slow growth environment at low flux, and the greater amount of material per island caused by the smaller island density.

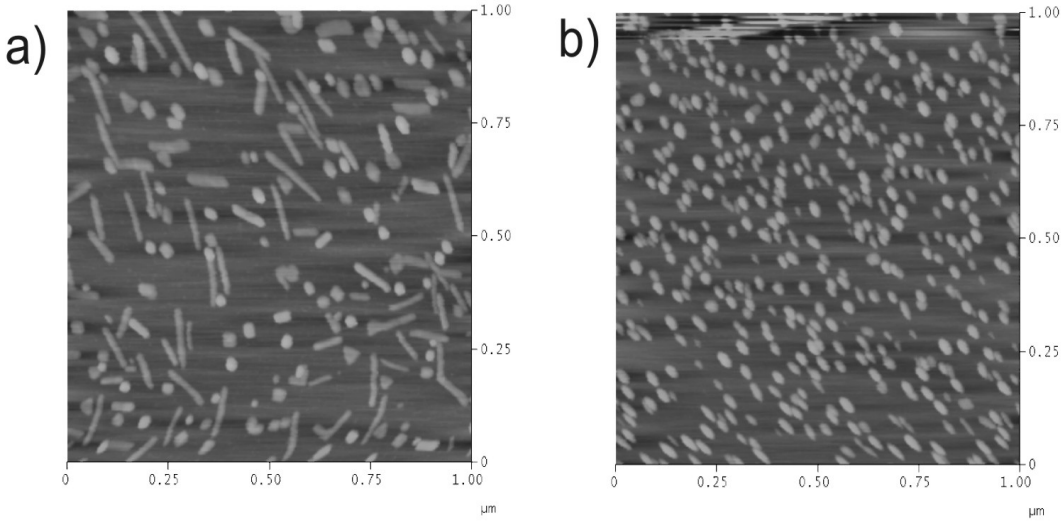

Figure 3.3: Two samples grown with F=0.0016 Å/s and 2 ML, with island densities of (a) 2.0×10^{10} cm^{-2} and (b) 3.8×10^{10} cm^{-2}.

There is no obvious reason for the favoured 4 nm and 9 nm island heights, or why there is a factor of ∼2 difference between the two island heights. Preferred thicknesses have been observed, for example, for Pb islands growing on Cu(111) surfaces, shown to be a quantum size effect due to confinement of electrons within the islands [101, 102]. Assuming the bulk Fermi energy for bismuth electrons of $E_F = 0.027$ eV, and an effective electron mass of $m^* = 0.29 \times m_e$ [9] (the largest effective mass and therefore the smallest wavelength), we estimate the Fermi wavelength using $\lambda \sim \frac{hc}{\sqrt{2 \times m^* c^2 KE}}$. This yields $\lambda = 14.0$ nm, and a minimum layer thickness might be expected to be $\frac{\lambda}{2} \approx 7$ nm. The calculated values do not clearly match the experimental results, however the effective electron masses and Fermi energy of Bi are known to vary depending on crystallographic directions [10].

Additional samples were grown with F=0.0016 Å/s, and 2 ML. Results are displayed in Figure 3.3. Figure 3.3 (a) shows the familiar combination of oblong and sphere shaped islands, with a measured density of 2.0×10^{10} cm^{-2}. Figure 3.3 (b) contains roughly 380 circular shaped islands within a square micrometre, an island density of 3.8×10^{10} cm^{-2}. Figure 3.3 (b) is a scan taken from a second substrate on the sample holder, the position of the second substrate locating it closer to the deposition rate monitor i.e. further from the oven.

The island density of Figure 3.3 (a) is smaller than the F=0.01 Å/s sample of Figure 3.2 (b) by a factor of five, reinforcing the belief that nucleation occurs via adatom-adatom collisions. Note that the oblong structures are larger and more frequent than in Figure 3.2 (b). Due to the holder/oven design the samples in the rear position do not fully enter the oven. Substrates in this position are poorly

annealed, especially since a lower annealing temperature is used for mica, leading to a greater residual contamination and high island density. For instance the island density of Figure 3.3 (b) is comparable with Figure 3.2 (b), though the flux differs by a factor of five. Hence most samples grown at the rear position produced examples of defect nucleation.

3.2.3 Discussion

Islands were found to exhibit two characteristic morphologies: a circular island with height 9 nm, and a randomly oriented oblong shape of height 4 nm. The oblong shapes appear more commonly at low flux, while at high flux the overall island density increases, largely consisting of the circular islands. The low flux environment allows the oblong islands to gather more material.

Island densities measured from surfaces without obvious defect nucleation increase as the particle flux is increased. The saturated island density increases from $N_{sat} = 2 \times 10^{10}$ islands cm^{-2} at F=0.0016 Å/s to $N_{sat} = 5.4 \times 10^{10}$ islands cm^{-2} at F=0.09 Å/s. The island densities are slightly lower than the T=308 K results of Terajima [76], though Terajima does not state the exact flux used. It is unclear whether the island densities from each of the AFM pictures is representative of bismuth diffusion on clean mica.

An XRD study [16] of 0.5 nm thick bismuth films deposited on alkali halides pointed to the presence of amorphous bismuth islands. Coverage dependent phase transitions from amorphous to crystalline islands have been observed for antimony (another group-V element) on HOPG. A determination of the island crystallography for the circular and oblong morphologies might reveal whether such a transition occurs for Bi.

Due to the difficulty of preparing clean samples for diffusion studies, and the issues around sample imaging and gaining meaningful statistics of island nucleation a decision was made to forgo any further experiments. Given a more productive experimental procedure, the bimodal island heights, and differing island shapes warrant further investigation.

3.3 Bismuth on MoS_2

Since MoS_2 conducts, Bi samples on MoS_2 were imaged using both the AFM and an SEM. In addition to the island morphology and island density analysis, Bi film crystallography was briefly investigated using the EBSD technique to check for a

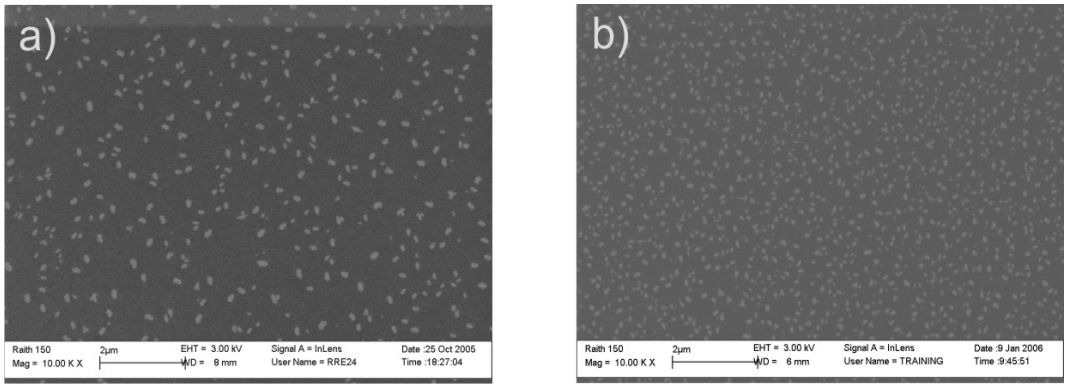

Figure 3.4: SEM images of room temperature island growth for (a) F=0.005 Å/s and (b) 0.14 Å/s, with coverage at 0.2 ML.

coverage dependent orientation transition.

3.3.1 Morphology

In this Section, the morphologies of bismuth films grown on MoS_2 substrates are analysed, in the flux range F=0.004 Å/s to 0.14 Å/s, with coverage between 0.2 ML and 35 ML.

Figure 3.4 displays two 0.2 ML films deposited with F=0.005 Å/s and 0.14 Å/s, showing numerous compact islands. In Figure 3.4 (a) islands typically have a lateral extent of 100 nm, in (b) the island size is reduced with higher flux.

Figure 3.5 displays SEM images for coverage of (a) 1 ML and (b) 2 ML, the samples prepared at F=0.02 Å/s. Figure 3.5 (c) is an AFM scan from the 1 ML sample. At 1 ML island morphologies have a characteristic hexagonal shape, more noticeable than for the small islands grown at 0.2 ML (Figure 3.4 (a)). For a number of islands in Figure 3.5 (a), the points of the hexagons extend towards bare terrace regions, capturing more material than the island edges. For 2 ML (Figure 3.5 (b)) the hexagonal morphology is maintained, though there is a greater competition for material between neighbouring islands.

The hexagonal morphologies observed in Figure 3.5 are generally distorted, either by the elongation or rounded corners. The hexagonal morphology is believed to be an early stage of the six-pointed, star-shaped islands observed for thin Bi films on HOPG substrates [13, 85] (see Figure 3.1). The distortions are more obvious for larger island sizes in Figure 3.5 (b), since smoothing effects at the island perimeter are less effective. Therefore the distortions are due to a Mullins-Sekerka type instability at the island edges [37].

A number of the islands in Figure 3.5 contain a striped feature on top of the island

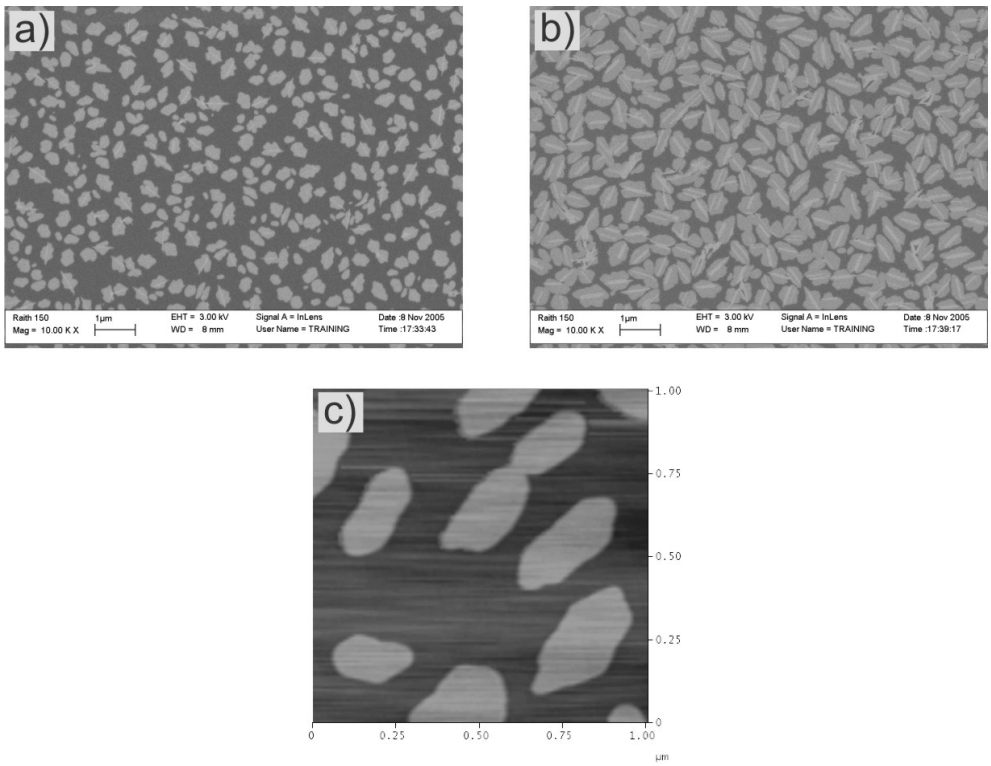

Figure 3.5: SEM images taken from samples grown at F=0.02 Å/s, and coverages of (a) 1 ML, and (b) 2 ML. In (c) an AFM scan from the sample shown in (a) reveals the hexagonal island morphology.

base, the striping more frequent in (b) when coverage is 2 ML. Generally islands contain a single stripe, which grows along a single direction. Striped features have been observed for the Bi/HOPG system [13, 85], where the material contributing to stripe growth was determined to be atoms impinging on island tops directly from the vapour, rather than an interlayer transport process. Observing that stripes are larger and more numerous at higher coverage (compare Figure 3.5 (a) and (b)), we expect the stripes for the Bi/MoS_2 system grow by the same process.

Figure 3.6 displays two images of a 7 ML sample grown at F=0.005 Å/s, (a) an SEM image taken at magnification of 10 kx and (b) an AFM image with scan size 1 μm^2. The high coverage allows broad islands to develop. At 7 ML the lateral growth of the islands leads to coalescence at island boundaries, though the boundaries are barely discernible. Small dark holes are visible in the SEM and AFM images, the dark spots likely the substrate viewed through gaps in the film.

The variation in contrast in the SEM image is indicative of the stripe growth, the stripes visible in the higher resolution AFM scan. From the AFM image, the stripes previously observed in SEM images of Figure 3.5 are clearly more numerous. The striping features (and other similarities to the Bi/HOPG results) suggest the

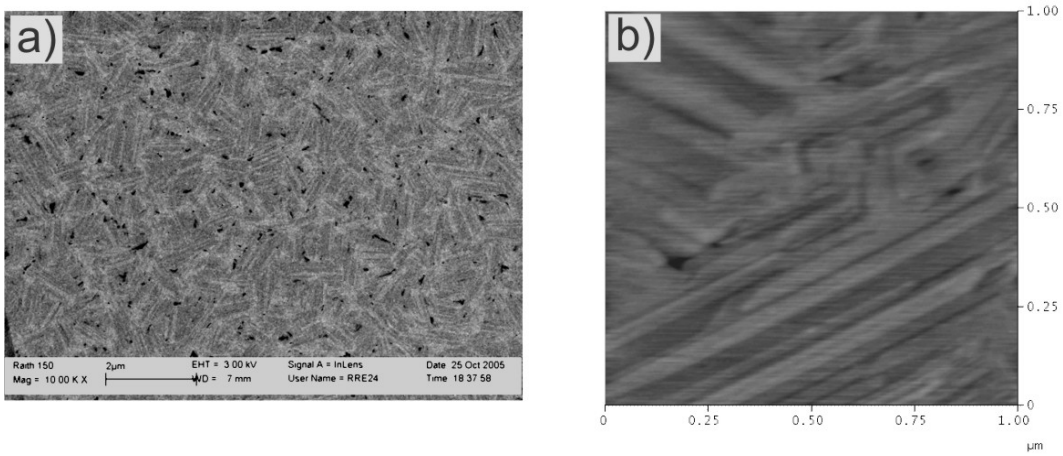

Figure 3.6: Two images taken from a 7 ML sample grown at F=0.005 Å/s. (a) an SEM image at 10 kx (b) a 1 μm^{-2} AFM scan.

islands are crystalline, and presumably the imperfect matching of grains at the island boundaries prevents full coalescence.

3.3.2 Island Heights

Island heights were collected from AFM scans within the flux range F=0.005 Å/s to 0.14 Å/s, and coverages up to 2 ML. Figure 3.7 (a) displays an AFM scan from an island, for a sample prepared at F=0.005 Å/s and 1 ML, and highlights a single scan line across an island. Figure 3.7 (b) contains the trace from the highlighted scan line, showing island tops to be uniformly flat except for the striped features. Figure 3.7 (c) presents combined base height measurements for the entire flux range, and coverages $\leq$2 ML.

The AFM scan in Figure 3.7 (a) reveals the island morphology in higher resolution than the SEM images, showing smooth island perimeters broken only by striped features. Island base heights in the scan are 1 nm, with the peak of the stripe at roughly 2 nm.

The histogram (Figure 3.7 (c)) reveals a distribution centred at 1.5 nm, island base heights peaking at either 1 nm or 2 nm. Reference [14] gives a bismuth monolayer to be 3.3 Å thick, the height distribution therefore ranges between 3 and 7 monolayers. Compared to Bi islands on Mica substrates, the spread in the data does not suggest a preferred island height. Consistently, the measured island heights are lower than islands grown on Mica. Height measurements of low coverage Bi/HOPG films have found a distribution which peaks around 1 nm [13] pg 94, with a subset of heights centred at 2 nm for islands grown at F=0.0074 Å/s. The Bi island heights measured from Bi/MoS_2 samples are therefore comparable to values

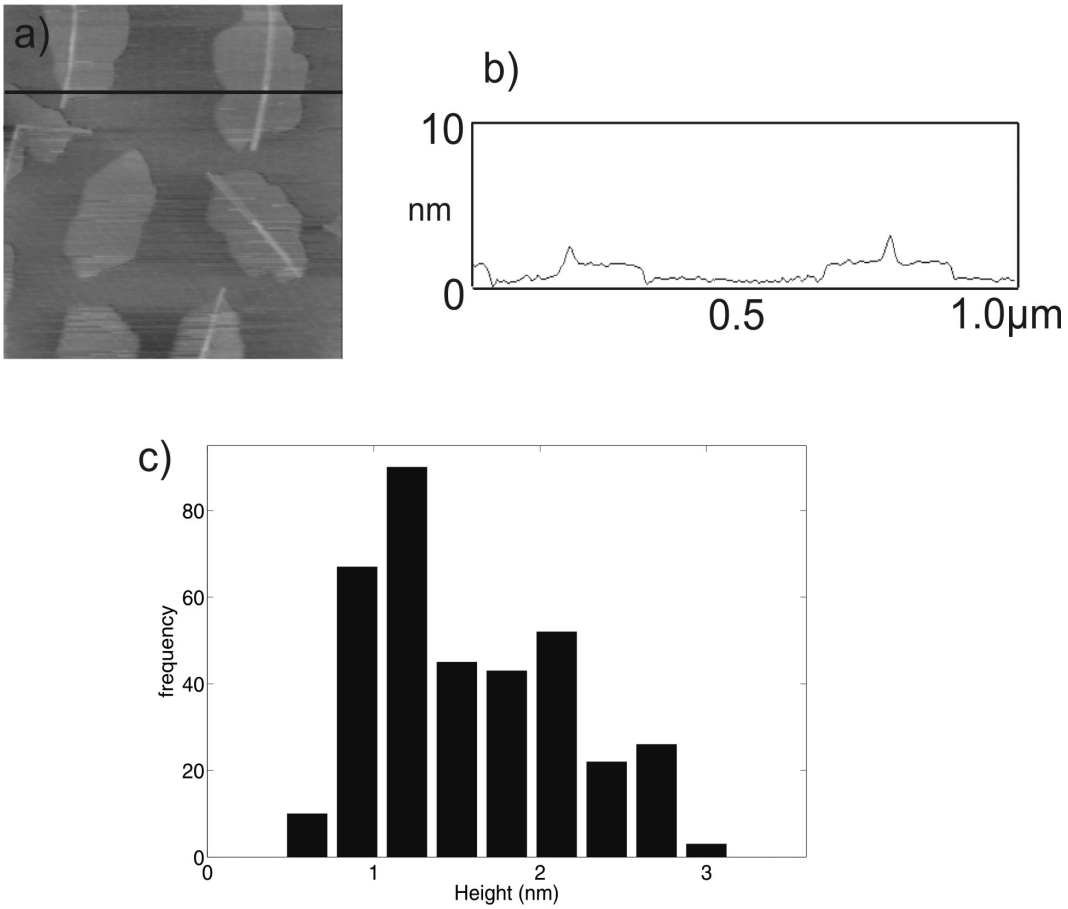

Figure 3.7: (a) AFM scan of an F=0.005 Å/s, 1 ML sample, with an associated trace (b) showing feature heights in nm. (c) displays the combined heights of from all the measured islands in a single histogram.

measured from Bi/HOPG samples.

Figure 3.7 (c) has no dependence on coverage, flux, or island density, the measured island heights can show large variations for different samples grown at similar conditions. For example, scans from a sample grown at F=0.02 Å/s and 0.2 ML found a mean height of 1 nm, while scans from a second deposition performed for the same growth conditions found a mean height of 1.9 nm. Both samples have island densities of roughly 5×10^8 cm^{-2}, measured from SEM images. AFM scans do not provide visualisation of large surface regions, and scans are taken from random sites on a substrate, without distinguishing between areas of low or high island density. It is not known whether island heights in defect nucleated regions are comparable to heights measured from clean terrace regions.

3.3.3 Film Crystallography

A number of films with coverage ranging from 12 to 35 ML were grown for EBSD experiments, to determine the orientation of the Bi film relative to the substrate. Collected electron backscatter patterns (EBSP) were compared to Bi and MoS_2 crystals.

Figure 3.8 displays two pole figures from a 15 ML film grown at F=0.014 Å/s, with the SEM accelerating voltage set at 8 kV. The two pole figures are created assuming the Bi$\{0001\}$, and Bi$\{01\bar{1}2\}$ planes are parallel to the MoS_2 surface (the latter orientation was observed for 12 ML films on graphite). The bright spot located in the centre of the $\{0001\}$ pole figure shows the favouring of the Bi$\{0001\}$ plane parallel to the MoS_2 surface. The pole figure of Figure 3.8 is from a $20 \times 20\mu m^2$ surface region, data taken automatically in 500 nm steps, producing a set of 1600 points. Of the 1600 data points, 1455 were indexed as belonging to the bismuth crystal and the remainder were indexed as MoS_2, or were not matched to either crystal.

The AFM scan shows a layered triangle film morphology at 20 ML. For 12 ML Bi films grown on HOPG substrates (see Figure 6.29 of Ref. [13], or Ref. [80]), the same triangular morphology was observed to coexist with a striped morphology similar to the 7 ML film in Figure 3.6 (b).

Previous work, using an EBSD equipped FE-SEM [13] pg 126, indexed striped Bi islands from a 12 ML film grown on graphite with a Bi$\{01\bar{1}2\}$ orientation. 15 ML films on graphite [13] were found to have 75% of the grains with the $\{0001\}$ trigonal orientation, and roughly 25% with the $\{01\bar{1}2\}$ orientation. On HOPG, the layered triangle morphology was characteristic of the trigonal Bi$\{0001\}$ film orientation.

The low coverage $\{01\bar{1}2\}$ orientation was never observed on MoS_2 substrates (for film thicknesses >15 ML), suggesting any orientation transition of the film occurs below 15 ML. 12 ML films grown on MoS_2 did not produce sufficiently clear patterns for indexing. 12 ML samples were imaged using 4 kV accelerating voltages to reduce backscatter interference between the substrate and film patterns, but the lower resolution could not resolve patterns adequately. The striped island morphology in the AFM scan of Figure 3.6 (b), taken from a 7 ML sample, indicates a transition may occur between 7 ML and 15 ML. AFM scans are however an inaccurate method for determining a coverage dependent orientation transition, since scans are taken from random substrate positions, and the transition is not uniform across the entire film (e.g. two orientations exist for 15 ML Bi/HOPG samples).

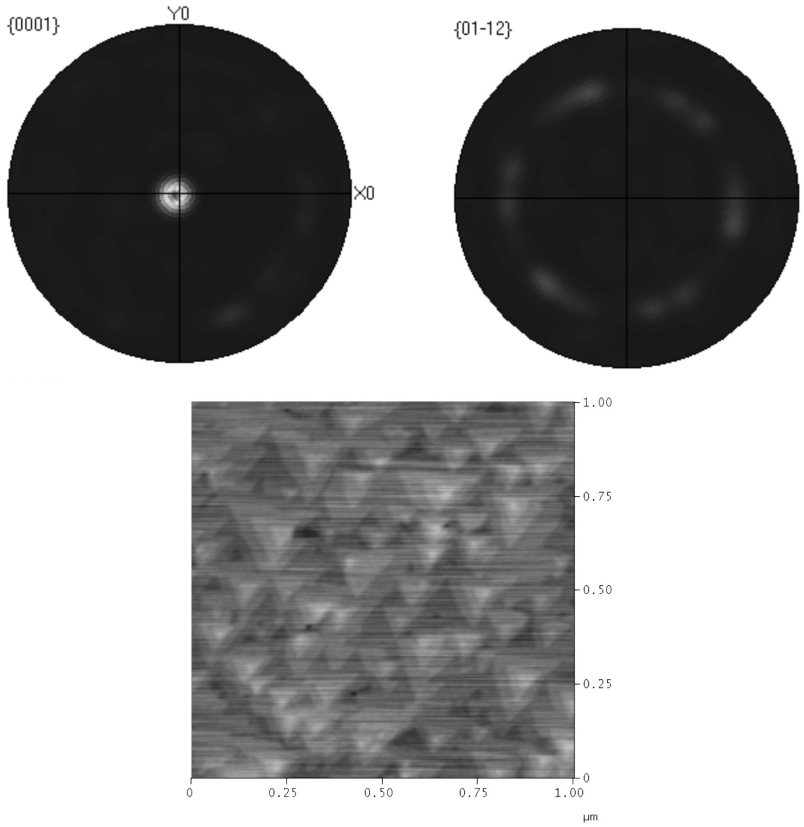

Figure 3.8: Pole figures from a 15 ML bismuth film deposited at 0.014 Å/s, taken from a 20 × 20μm^2 surface region. The two poles are the trigonal Bi{0001}, and Bi{01$\bar{1}$2} orientations observed by Scott [13] pg 126. The concentration of points at the centre of the {0001} pole figure confirms it is the only orientation observed for this Bi film. The AFM scan is taken from a different, 20ML film, showing a layered triangle morphology.

3.3.4 Island Density

In this Section the flux dependence of the island nucleation is measured, to test whether nucleation is homogeneous, and to determine the critical Bi island size on MoS_2. Island densities were measured from SEM scans, using the method described in Chapter 2. Images with large terrace regions were selected for analysis, thereby avoiding island growth near steps. Nucleation and consequently island sizes are not uniform across the entire substrate, some regions are clearly affected by defects. Hence images were selected from regions exhibiting the lowest island density.

Nucleation of an atomic vapour can occur via two mechanisms: heterogeneously when particles are trapped by defects or contaminants, and homogeneously when diffusing particles aggregate with one another. For 2D homogeneous nucleation, nucleation theory predicts the saturated island density has a functional dependence on flux of the form $N_{sat} \propto F^{\chi}$ [97, 34]. Figure 3.9 (a) contains a schematic of the two nucleation regimes, illustrating the flux dependence of heterogeneous and

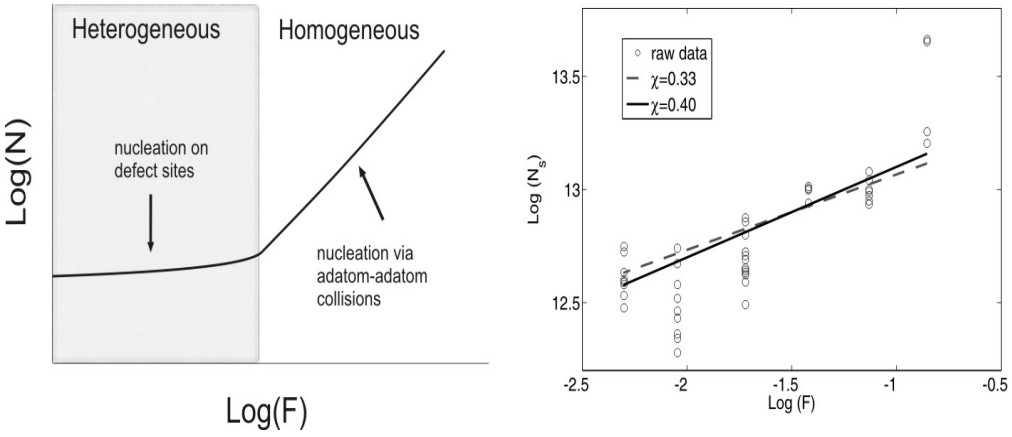

Figure 3.9: (a) Schematic showing the flux dependence of the saturated island density. (b) Raw saturated island densities plotted as a function of flux using a log-log scale, for room temperature samples grown between θ = 0.2 ML and 1 ML. Two lines are included assuming a $N_{sat} \propto F^{\chi}$ dependence, $\chi = 0.33$ (dotted line), and $\chi = 0.40$ (full line).

homogeneous nucleation. Figure 3.9 (b) plots Bi island densities on MoS_2, measured within the flux range F=0.005 Å/s to 0.14 Å/s, on a logarithmic scale, including data from samples with coverages of 0.2 ML or 1.0 ML[2] . Data points in Figure 3.9 are widely dispersed for each flux, in some cases varying up to three hundred percent. Below log(F) = −2, the island densities appear to plateau at 3×10^{12} m^{-2} (12.5 on the y-axis). Above log(F) = −2 on the x-axis the island densities increase with flux.

Assuming desorption is minimal and the island densities are described by the relation $N_{sat} \propto F^{\chi}$, fits are shown for $\chi = 0.33$ and $\chi = 0.40$ (see Section 3.4.3). $\chi = 0.33$ is predicted to be valid when the critical island size is a single particle, and only monomers can diffuse. $\chi = 0.40$ is predicted to be valid when the critical island size is a single particle, but both monomers and dimers can diffuse [97]. From Figure 3.9 $\chi = 0.40$ is a better fit to the data than $\chi = 0.33$, however the large spread in the data does not allow confirmation of χ.

The island densities of Figure 3.9 range from 0.4 to 3.0×10^{13} m^{-2} depending on flux. Compared with island densities observed on the cleanest mica substrates, the island density at F=0.01 Å/s is roughly two orders of magnitude lower on MoS_2 substrates. Considering the small change in island density below log(F) = −2, an upper bound for the defect density on annealed substrates is estimated at 4.0×10^{12} m^{-2}, slightly lower than 2×10^{13} m^{-2} determined by Stegemann [77].

[2]Island densities were comparable for either coverage, suggesting saturation occurs θ <0.2 ML. This agrees with island densities measured on HOPG which found saturation θ <0.2 ML [13] pg 100

3.3.5 Discussion

Bismuth islands on MoS_2 develop via a 2D growth mode, with base heights of 1 nm to 2 nm. Island morphologies are commonly hexagonal, with the points of the hexagons extending towards relatively bare terrace regions. Island tops develop stripes for θ >1 ML, the stripes more frequent and broader at high coverage. We conclude there is a large Ehrlich-Schwoebel barrier preventing material transport between the substrate and island tops.

Many of the island and film characteristics seen for the Bi/MoS_2 combination were previously observed for Bi islands on HOPG surfaces [13, 85]. The hexagonal islands of Figure 3.5 have the same symmetry as the six pointed stars observed on HOPG. Island heights on HOPG are centred about 1 nm, whereas on MoS_2 they range between 1 nm and 2.5 nm. Striped features are common to both systems. The similarites suggest low coverage MoS_2 films have the same Bi$\{01\bar{1}2\}$ crystal orientation as the low coverage Bi films on HOPG.

Films with $\theta \geq$15 ML exhibit only the trigonal Bi{0001} orientation. Assuming the striped 7 ML islands have the Bi$\{01\bar{1}2\}$ crystal orientation parallel to the surface, the transition to the trigonal orientation must occur between 7 ML and 15 ML. Bismuth films on Si(111)-7×7 surfaces have an orientation transition at 4 ML [14], the Bi/Si combination expected to have strong interactions relative to the Van der Waals bonds on MoS_2 and HOPG. Bi island densities on MoS_2 are higher than on HOPG, suggesting a stronger film/substrate interaction, and a reason why an orientation transition on MoS_2 occurs at a lower coverage than on HOPG.

Island densities plotted in Figure 3.9 suggest for F$\leq$0.02 Å/s and room temperature conditions, nucleation is defect dominated.

3.4 A Temperature Dependent Study of the Bi/ HOPG System

In this Section a temperature dependent study of bismuth islands nucleating on terraced regions of the HOPG substrate is described. The work complements the flux dependent investigations of Scott [13], where kinetic limitations during growth resulted in a morphology transition from hexagonal to star-shaped islands as the particle flux was increased. Studying crystal growth as a function of temperature can provide information on the energy barriers limiting the growth, as the system shifts between kinetic and equilibrium regimes. This section presents a transition from 2D to 1D island morphologies as substrate temperatures are increased from

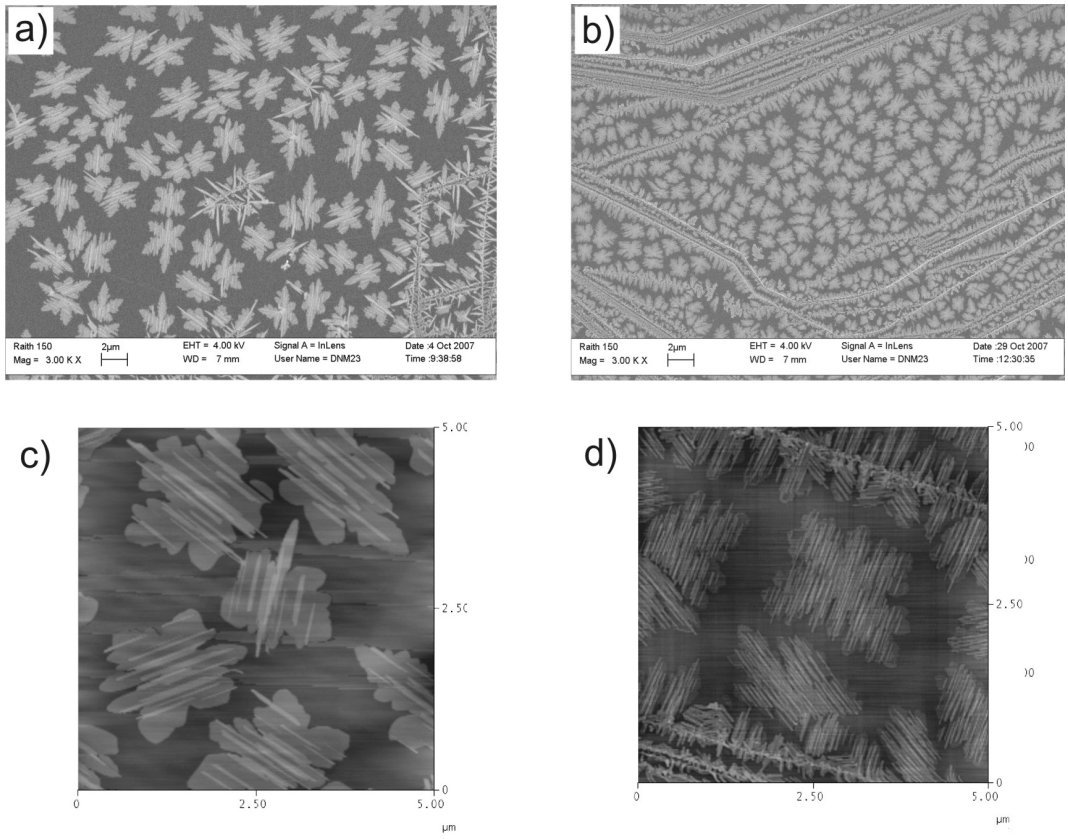

Figure 3.10: (a) SEM and (c) AFM image of a sample grown at F=0.011 Å/s. (b) SEM and (d) AFM images of sample grown at F=0.54 Å/s. θ =2 ML and T=303 K.

room temperature. Island densities are monitored as a function of temperature. Using an Arrhenius analysis the activation energies for nucleation are calculated, then discussed in terms of adatom and cluster diffusion.

3.4.1 Island Morphology

Figure 3.10 contains SEM images from samples grown at T=303 K and 2 ML, for flux of (a) F=0.01 Å/s and (b) F=0.54 Å/s. The high resolution images of Figures 3.10 (c) and (d) are AFM scans taken from the samples (a) and (b) respectively.

Figure 3.10 (a) shows typical film morphologies for samples grown at low atomic flux. On terrace regions islands develop a six pointed star morphology, while aggregates growing from steps on the graphite surface prefer a 1D mode (rods - discussed in Chapter 4). Branches of the six-pointed stars elongate toward bare terrace regions. Figure 3.10 (b) displays high flux island growth, the island densities comparatively higher, mean island sizes smaller, and step-edge growths are stunted.

The AFM images of Figures 3.10 (c) and (d) show the island dendrites in more detail, and reveal striped features on island tops. In (c), the island stripes are broad,

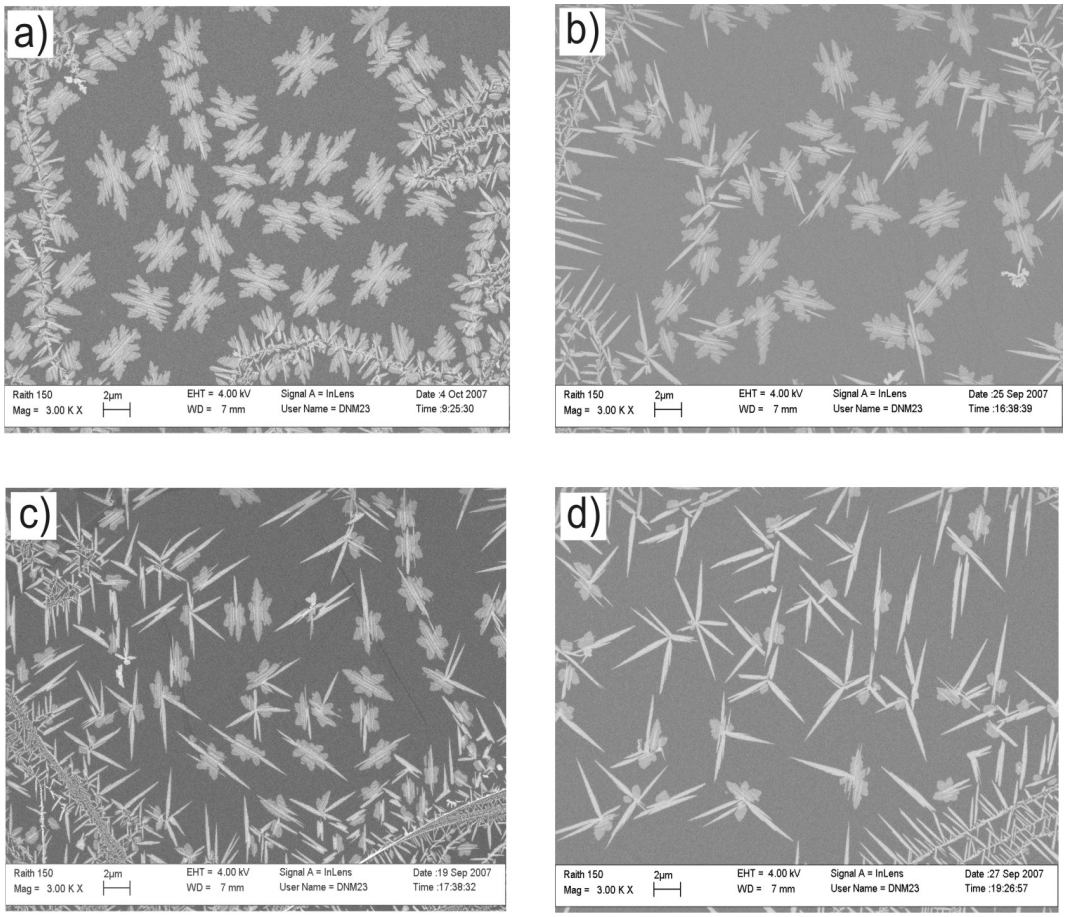

Figure 3.11: Temperature dependence of the island morphology, (a) T=303 K, (b) 313 K, (c) 323 K, (d) and 333 K. θ = 2 ML, and F=0.01 Å/s. Note the increased occurrence of spiked features, and the apparent reduction in island density.

and roughly ten per island. A number of stripes extend past the island base, and occasionally there are stripes growing on stripes. Stripes on the high flux islands of (d) are thinner and more densely packed.

Figure 3.11 displays images from samples grown with F=0.01 Å/s and 2 ML, for the temperature range T=303 K to 333 K. As the temperature is increased from T=303 K in 10 K steps, the terrace nucleated islands evolve from 2D morphologies into 1D shapes (termed spikes).

At T=303 K (Figure 3.11 (a)) barely any 1D features are observed, and in general the island morphologies grown at this temperature are no different to room temperature depositions [13]. The Mullins-Sekerka type instability discussed in Section 3.3 for Bi islands on MoS_2 is apparent in the dendritic, star shaped morphologies. At T=313 K (b) a number of islands develop spike features, the spikes generally parallel to island stripes, and along the direction of island elongation. When spikes develop, they appear to replace one of the six branches of the star shape, i.e. a 2D branch is

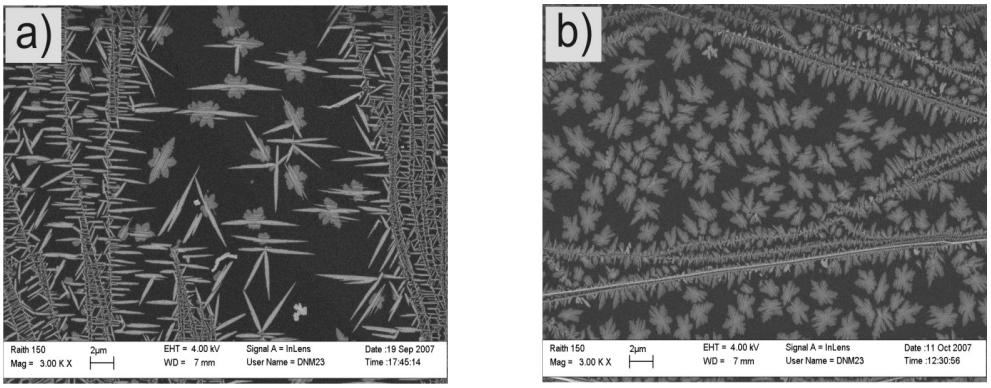

Figure 3.12: Island morphologies for θ =2 ML films, (a) T=308 K and F=0.013 Å/s, (b) T=333 K and F=0.15 Å/s.

replaced by a 1D spike. At T=323 K (c) most islands have spikes, and a number have spikes growing in more than one direction. At T=333 K (d) spiked features are clearly the favoured growth mode. Generally, the 1D structures formed at T=333 K contain remnants of 2D islands at the centre of the growth, indicating the nucleus still prefers a 2D mode. Looking through the sequence of images (a) to (d), the 2D remnants clearly decrease in size with higher temperature.

The common alignment of the spike and island stripes, seen for the central island in Figure 3.10 (c), suggests a connection between the two features. Considering the spikes as larger versions of island stripes ties in with previous work [13] pg 95, where island stripes often extend into 1D features from the island edges. These extended stripe features are visible in Figure 3.10 (c). Likely the elevated temperature enhances the stripe growth, allowing it to collect material which would otherwise have formed a star-branch.

With T=333 K in Figure 3.11 (d), a number of spikes appear to be isolated from other aggregates, i.e. they do not share a common nucleus. These lone spikes have a 1D morphology which completely lacks the six pointed symmetry of the star-shaped islands, but are similar to rods growing from graphite step-edges (seen in the bottom right corner of Figure 3.11 (d)). Room temperature rod growth is believed to occur due to the small local flux at step edges brought on by competitive capture [13, 60]. Island shapes seen in Figure 3.11 (d) suggest a higher substrate temperature has the same effect on crystal morphology as low flux.

Figure 3.12 contains SEM images from θ = 2 ML films grown at (a) T=333 K and F=0.013 Å/s, (b) T=333 K and F=0.15 Å/s. The images show a progression from spiked morphologies at low flux and T=333K, to the familiar star-shaped islands with F=0.15 Å/s. Figure 3.12 illustrates the competing effects of flux and temperature on the island morphologies. Clearly the 1D spikes require a slow growth

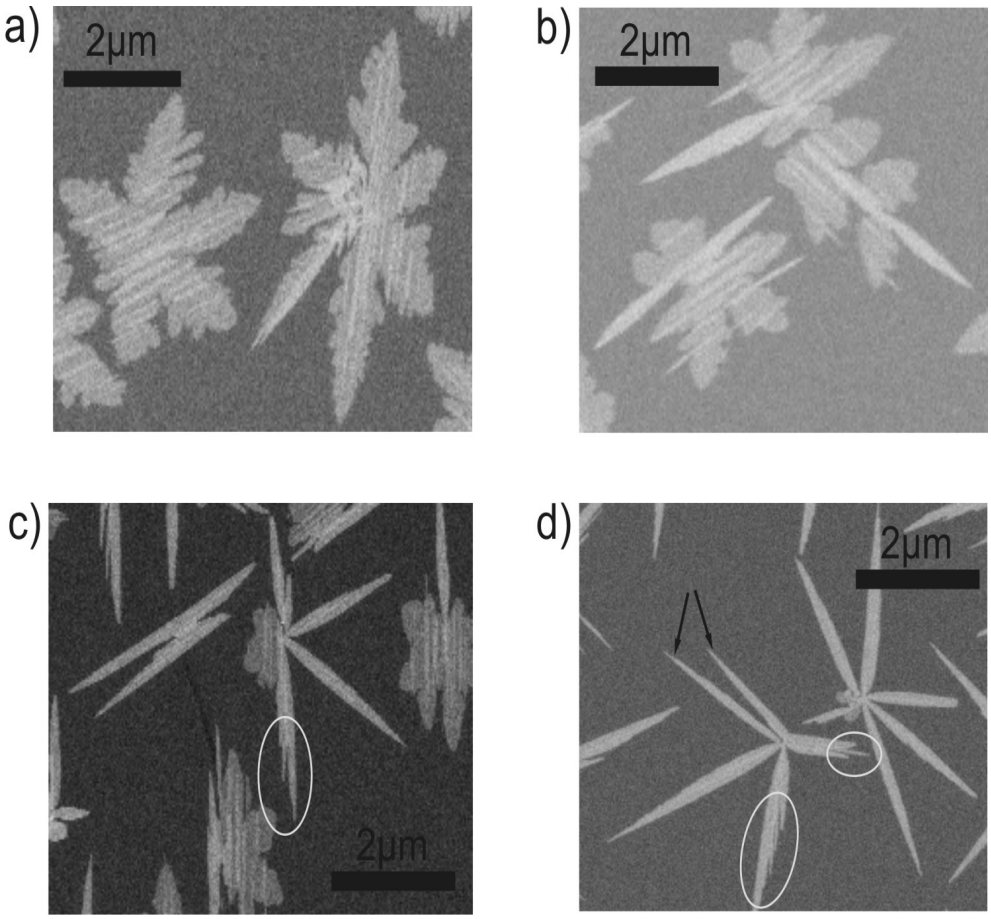

Figure 3.13: Magnified images of the F=0.01 Å/s, $\theta = 2$ ML samples shown in Figure 3.12. The sample temperatures were (a) T=303 K, (b) T=313 K, (c) T=323 K, and (d) T=333 K. The ellipses in (c) and (d) enclose rod tips with obvious instabilities. The arrows in (d) show two spikes growing near one of the star branch directions.

environment.

Figure 3.13 displays spikes in more detail at each of the deposition temperatures. Spikes typically have a tapered morphology, with the midpoint of each spike generally the broadest section. Spikes exhibit smooth, straight lengths, presumably allowing efficient adatom transport along edges. Diffusion on graphite is expected to be isotropic, therefore Bi dimers condensing onto island edges will arrive from random positions. A likely reason why spikes prefer such high aspect ratios is anisotropic surface energies for the long and short edges [13] pg 145.

Spike tips enclosed with ellipses in Figures 3.13 (c) and (d) have a jagged profile, with finely shaped extensions. Jagged features can usually be associated with spikes of wider profile, suggesting adatom rearrangements on the tip are slow relative to the arrival rate of material. The jagged tips are not apparent at low temperature, possibly due to less of the 2D island base material transferring to the spikes, the spikes therefore smaller in size. Beyond some width atoms on the tip cannot rearrange

sufficiently between each arrival event, and instabilities develop.

Note again in Figures 3.13 (a) and (b) the common alignment of spikes with island branches or stripes. In Figure 3.13 (c) the central island has four spikes separated by 60° rotations. At T=333 K the spike alignment is more erratic: the two arrows in Figure 3.13 (d) point at two spikes growing from a single nucleus, along a similar direction. The spikes of this island are clearly not symmetric under 60° rotations.

Crystallographic studies [13] pg 131 of Bi islands grown on HOPG at room temperature have shown island stripes (and step-edge nucleated rods) run parallel to the Bi$\langle 11\bar{2}0\rangle$ direction, and the Bi film has a preferred in plane orientation $\langle 11\bar{2}0\rangle$Bi||HOPG$\langle 10\bar{1}0\rangle$. HOPG surfaces are symmetric under rotations of 60°, hence each branch of the six-pointed star islands points along the HOPG $\langle 10\bar{1}0\rangle$ direction. The matching alignment of spikes and star branches at low temperature suggests the spikes also point along the HOPG$\langle 10\bar{1}0\rangle$ direction. Presumably the fast growth for T=333 K and F=0.01 Å/s (Figure 3.13 (d)) causes the spikes to lose their favoured alignment.

Spike Heights

From SEM images the spikes display a higher contrast with the substrate than the 2D islands, indicative of a thicker cross-section. Evidently the raised substrate temperature allows atoms to migrate onto island tops more frequently.

Figure 3.14 shows an AFM scan of a spiked island, with a scanline over a spike and a step nucleated rod. The trace reveals both the spike and rod to be 2.5 nm in height.

Roughly thirty spikes were measured from additional AFM scans, finding a mean height of 2.4±0.4 nm. Previous results from the flux dependent study found 2D island base-heights have a mean value of 1±0.3 nm, and rods between 2 nm and 2.4 nm [13] pg 144. Measured spike heights therefore have similar heights to rods.

Figure 3.1 in Section 3.1.3 contains two SEM images from previous work [13], showing the two characteristic island morphologies co-existing for samples grown at F=0.0074 Å/s (room temperature and θ =1.5 ML). One is a compact hexagonal island with a height of 2.5 nm, the second morphology is the familiar six pointed star shape, but with elongated branches. Spikes have both the elongated morphology of the star, and the same base height as the hexagons.

3.4.2 Summary of Morphologies

Bi islands on HOPG undergo a transition from 2D to 1D island growth with increasing substrate temperature. At T=303 K 2D islands spread laterally by incorporating

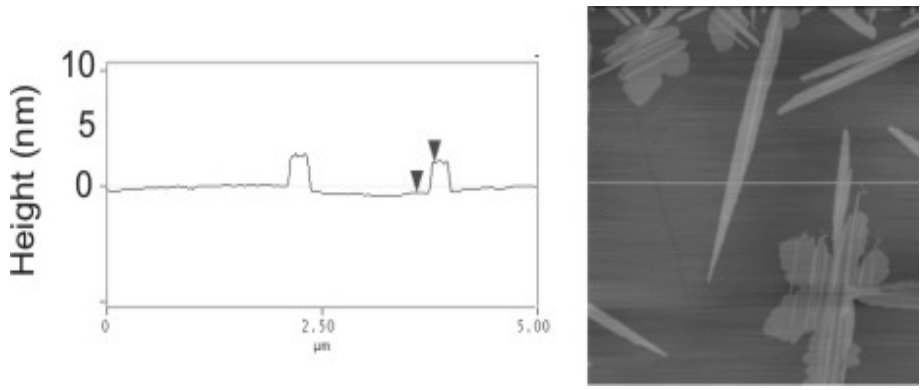

Figure 3.14: AFM scan of the Bi/HOPG surface for a sample grown at F=0.013 Å/s and T=323 K, θ = 2ML. The trace is taken from a 5μm wide scan across an island spike and a step nucleated rod, revealing the heights of both features equal 2.5 nm.

material from the terrace at the island edges. At T=303 K, the star-shaped morphology is believed to result from a Mullins-Sekerka instability, which modifies the initially hexagonal shaped islands. With increased substrate temperatures, island morphologies begin to grow anisotropically, which favours 1D structures aligned with stripes on the island surfaces. With F=0.01 Å/s and T=333 K, a 1D morphology is the preferred structure.

A similar temperature dependent morphology transition has been observed for antimony (Sb) aggregates grown on graphite [89], though low temperature growth is predominantly in an amorphous phase. When the amorphous phase crystallises a planar structure of height 3 nm forms, commonly with 1D extensions.

Spikes appear to have all the characteristics of the rods: growth direction into the diffusion field, heights roughly 2 nm, both ends tapering to points, high aspect ratios, and apparently the same crystallographic alignment at low temperature and low flux. The suggestion is that rods and spikes are identical, the elevated substrate temperature allowing terrace nucleated islands to develop a 1D morphology.

3.4.3 Bi Island Densities

Since the sample holder and spacer were replaced for the temperature study, it was necessary to check island densities in the new configuration against room temperature depositions from [13] pg 103. New elements can introduce contaminants to the UHV system, potentially adding defects to substrate surfaces. Comparisons of island morphologies for depositions at T=303 K with room temperature depositions [13] pg 90 did not suggest any significant difference, but a more robust test of the nucleation is to study the flux dependence of N_{sat}.

Relations between the saturated island density, deposition rate, diffusion barrier,

and critical island size i above which islands are stable against dissociation, are derived from mean-field rate-equations by Pimpinelli and Villain [34]. For the general case where all particles greater than one atom are immobile, [34] predicts

$$N_{sat} \sim (F/a^2\nu)^{\chi} \exp(\frac{\chi E_1 + \frac{E_i}{i}}{k_B T}), \tag{3.1}$$

where F is the deposition flux in ML/s, a the lattice constant, ν is the vibrational frequency, E_1 is the single particle diffusion barrier, E_i is the binding energy of the critical cluster ($E_{i=1} = 0$), and $\chi = \frac{i}{i+2}$ for isotropic 2D diffusion. Equation 3.1 is appropriate when islands greater than one atom are immobile, and the exponent χ takes the values $chi_{(i=1)} = 1/3,\ \chi_{(i=2)} = 1/2,\ \chi_{(i=3)} = 3/5, ...$ depending on the critical island size. Room temperature nucleation studies for bismuth dimers on HOPG found $\ln(N_{sat}) \propto \chi \ln(F)$ with $\chi = 0.36 \pm 0.03$ [13] pg 89, the linear relationship evidence that nucleation occurs via adatom-adatom collisions. Within uncertainties the calculated exponent was equal to $\chi_{(i=1)} = \frac{1}{3}$, indicating the critical island size is a Bi dimer, i.e. dimer pairs do not dissociate at room temperature.

Figure 3.15 displays island densities measured for the new setup, plotted as a function of flux using a log-log scale. Samples were grown within the flux range F=0.002 Å/s to 0.54 Å/s. Island densities were collected from SEM images taken at 3 kx magnification, for sample coverages between 1 ML and 2 ML, and growth temperature T=303 K. Previous work has shown island densities to saturate above 0.2 ML, therefore variations in coverage above 0.2 ML are not expected to affect the data. Figure 3.15 (a) shows the raw island densities for the three different sample positions. Figure 3.15 (b) plots the mean island densities, the uncertainty bars representing the standard deviation of the data. If island nucleation predominantly occurs on defects we would expect no dependence of the island density on flux. The positive slope of Figure 3.15 indicates that within the flux range F=0.002 Å/s to 0.54 Å/s, island nucleation occurs via adatom collisions. Assuming a power law dependence of $N_{sat} \propto F^{\chi}$, the exponent $\chi = 0.40$ (full line) fits the data best, while the exponent $\chi = 0.36$ (dotted line) determined by Scott [13] pg 89 lies just within the error bars.

Worth noting are the prefactors used to produce the fits of Figure 3.15 (b), we find $A_{\chi=0.36} = 4.7 \times 10^{11}$ m^{-2} and $A_{\chi=0.40} = 5.6 \times 10^{11}$ m^{-2}, compared with $A = 5.7 \times 10^{11}$ m^{-2} as measured previously [13] pg 89. The consistency of the flux dependence (slope and ν) with previous work suggests the addition of button heaters to the sample holder has not adversely affected island growth.

The raw island density data of Figure 3.15 (a) is classified by the position of the

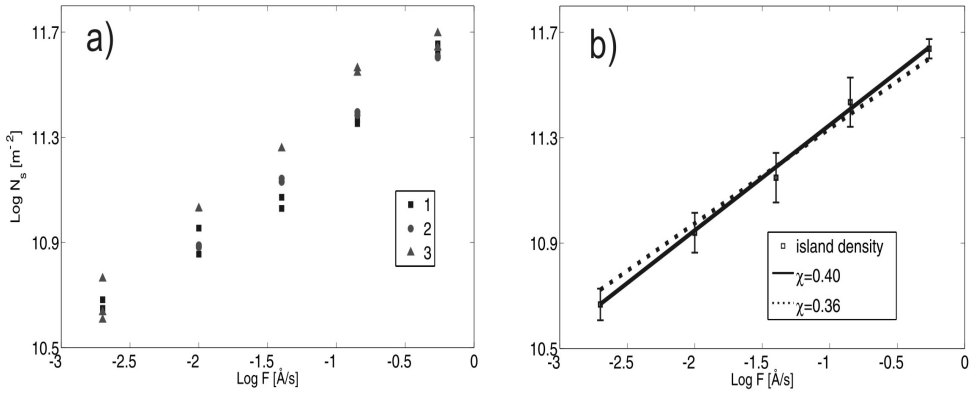

Figure 3.15: (a) Raw saturated island density data for samples grown within the range F=0.002 Å/s to 0.54 Å/s, T=303 K, and θ = 1 ML to 2 ML. Symbols distinguish individual pieces of graphite. (b) Mean island density, fitted assuming powerlaw dependence with exponents contained in the legend.

substrate on the sample holder. There is a clear distinction between the densities associated with position 3 and those of the other two positions. By cycling the substrate positions along the holder for different depositions, it is clear that the higher densities were associated with a particular piece of graphite taken from a different bulk crystal, rather than the position on the sample holder. With nucleation shown to be homogeneous for all three substrates (illustrated by the slope of Figure 3.15 (b)), the conclusion is that particles diffuse more slowly on the third substrate (since N_{sat} is inversely proportional to the diffusion coefficient).

The exponent $\chi = 0.40$ found in Figure 3.15 is not predicted for any i$\geq$ 1 when clusters (i.e. dimers, trimers...) are immobile. Villain *et al.* [97, 34] have however predicted an additional scaling regime is applicable when dimers diffuse appreciably before dissociation, with trimers and larger clusters immobile. Island densities in the mobile dimer regime scale as

$$N_{sat} \sim (F/a^2\nu)^{\frac{2}{5}} \exp(\frac{E_1 + E_2}{5k_BT}), \tag{3.2}$$

where E_2 is the diffusion barrier for dimer diffusion. Monte Carlo simulations [103, 92] have confirmed the modified scaling predicted by Equation 3.2. When dimers diffuse at significant rates the island densities are reduced compared to when dimers are immobile. Bardotti *et al.* [92] perform simulations allowing trimers and larger particles to diffuse, and find N_{sat} scales as $F^{0.42}$, suggesting χ saturates near 0.40 when clusters larger than a dimer are mobile.

The flux dependence $\chi = 0.40$ found in Figure 3.15 suggests particles larger than

the basic particle size (a Bi_2 particle) are diffusing. Cluster diffusion experiments [104, 90, 91, 92, 93] have found clusters containing up to 2300 atoms move appreciably on graphite surfaces at room temperature. Hence we believe the exponent $\chi = 0.40$ results from the diffusion of small bismuth aggregates on the HOPG surface.

3.4.4 Island Density Temperature Dependence

Nucleation theory (Equations 3.1 and 3.2 [97, 34]) predicts smaller saturated island densities at higher temperature; the reduction in island density exponentially proportional to $\sim \frac{E}{3k_B T}$, for i=1 and diffusion barrier E. Hence measuring the saturated island density as a function of temperature may provide an estimate for the diffusion barrier, E, of bismuth particles on graphite.

In Section 3.4.1 the preferred 1D terrace island morphology at F=0.01 Å/s and T=323 K, was replaced by the 2D star shaped morphology when F=0.14 Å/s. Island geometries are understood to have a weak influence on nucleation density, as isotropic and anistropically shaped islands present different obstacles to diffusing atoms on a substrate [105, 106]. Therefore to avoid the 2D to 1D morphology transition, the temperature dependent study of the island density is performed with F=0.14 Å/s. Island morphologies should be comparable at each temperature.

Figure 3.16 plots island densities measured from SEM images, for F= 0.14 ± 0.01 Å/s and substrate temperatures ranging between 303 K and 353 K. Consistent with Figure 3.15, the data points are distinguished according to the specific substrate piece. Each graph in Figure 3.16 is plotted with the natural logarithm of N_{sat} on the y-axis, and either T or $\frac{1000}{T}$ on the x-axis.

Figures 3.16 (a) and (b) contain the raw and mean island densities expressed as a function of temperature, while Figure 3.16 (c) plots N_{sat} as a function of $\frac{1}{T}$, anticipating an Arrhenius dependence. Even with F=0.14 Å/s, islands grown at T=353 K on substrates 1 and 3 contain spiked features similar to the examples shown in Figure 3.11. Hence Figure 3.16 (d) contains only the mean island densities measured from substrate 2, plotted against $\frac{1}{T}$. The error bars represent the standard error.

At each temperature in Figure 3.16 (a) the data has a large spread, but there is a clear downwards trend with temperature. Comparing mean densities for T=303 K and T=353 K (Figure 3.16 (b)), the raw island densities differ by a factor of 2. Once again island densities measured from substrate 3 (squares) are slightly higher than the other pieces.

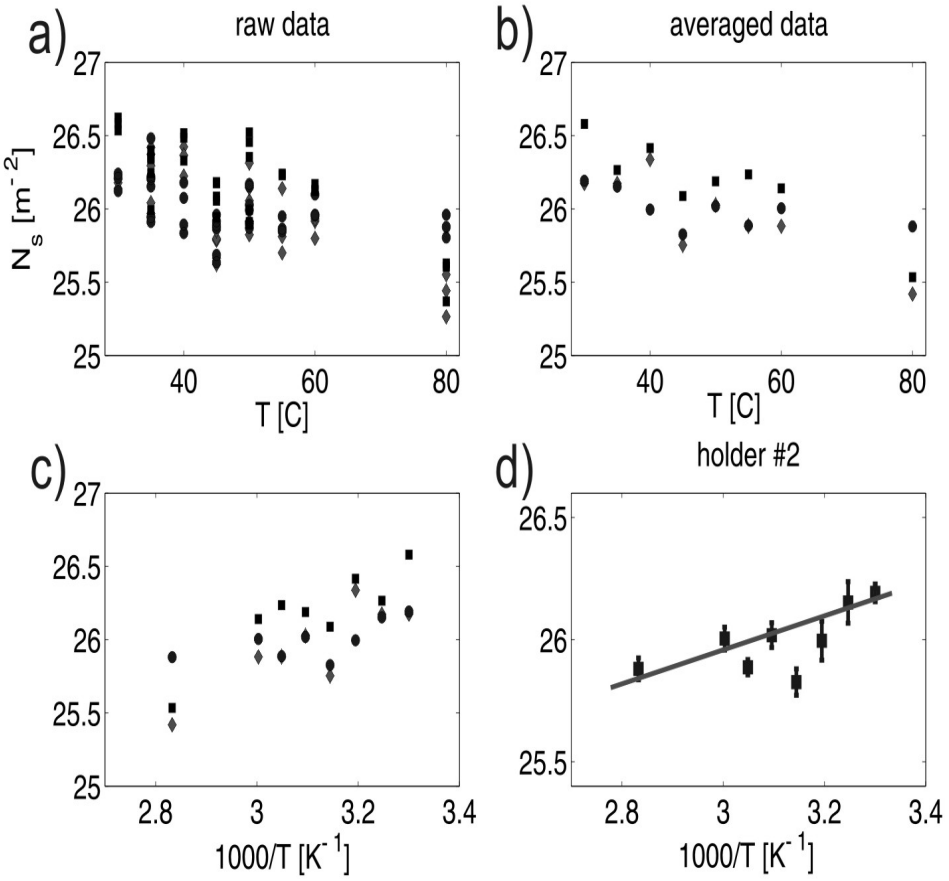

Figure 3.16: The temperature dependence of N_{sat} for F=0.14 Å/s, θ = 1 ML to 2 ML, within the range T=303 K to 353 K. Island densities are plotted on the y-axis using a natural log scale. Densities from each piece of substrate are plotted using different symbols: diamonds (1), circles (2), and squares (3). (a) Raw island densities plotted against T, (b) mean densities against T, (c) mean densities against $\frac{1}{T}$, (d) mean data from sample No.2 against $\frac{1}{T}$.

The data in Figure 3.16 (d) is fitted with an activation energy $E_A = 0.06$ eV. Jensen *et al.* [107] have calculated diffusion barriers for gold atoms on graphite to be $E_d \approx 0.05$ eV. We now compare the measured island densities, experimental parameters, and E_A, with predictions from nucleation theory.

Fitting Nucleation Parameters

By substituting experimental parameters into Equations 3.1 and 3.2 to predict island densities, the applicability of the Equations to the Bi/HOPG system can be tested. For T=333 K, we have

$$N_{sat} \sim (\frac{0.04}{1 \times 10^{13}})^{\chi} \exp(\frac{0.06}{8.62 \times 10^{-5} \times 333}), \tag{3.3}$$

where χ is either 1/3 or 2/5, $E_A = 0.06$ eV is the activation energy measured

from Figure 3.16 (d), F= $\frac{0.142}{3.3}$ = 0.04 ML/s, and $\nu = 1 \times 10^{13}$ s^{-1} the Debye frequency [83]. When $\chi = 1/3$ the equation predicts $N_{sat} = 1.3 \times 10^{-4}$ islands/site, and with $\chi = 2/5$ $N_{sat} = 1.8 \times 10^{-5}$ islands/site. Assuming an atomic density of 9.3×10^{14} atoms/cm^2 [14] for a monolayer of Bi atoms, at T=333 K the experimentally determined density is $(\frac{2.0 \times 10^7 islands/cm^2}{9.3 \times 10^{14} sites/cm^2}) = 2.1 \times 10^{-8}$ islands per site. The experimental island density is orders of magnitude smaller than predictions of Equation 3.3, irrespective of whether χ equals 1/3 or 2/5. Hence neither of these simple nucleation pictures adequately describes N_{sat} for the Bi/HOPG system.

Beginning with $N_{sat} = 2.1 \times 10^{-8}$ islands per site at T=333 K, we estimate energy barriers or prefactors which could predict the low N_{sat}. Assuming $\nu = 1 \times 10^{13}$ s^{-1} and $\chi = \frac{1}{3}$, Equation 3.1 predicts $\ln(2.1 \times 10^{-8}) = \chi \ln(\frac{0.04}{1 \times 10^{13}}) + \frac{E_1}{3 \times k_B \times 333}$ which simplifies to $-17.6 = -11 + \frac{E_1}{3 \times k_B \times 333}$, which cannot be satisfied unless $E_1 < 0$, i.e. an unphysical solution. A similar result is achieved with $\chi = \frac{2}{5}$. A second approach is to let ν vary, while using $E_A = 0.06$ eV. For $\chi = \frac{1}{3}$ we find $\nu = 6.6 \times 10^{23}$ s^{-1}, far higher than typical atomic vibration frequencies [22]. With $\chi = \frac{2}{5}$ a vibration frequency $\nu = 4.2 \times 10^{19}$ s^{-1} is required. Such high vibration frequencies have no physical justification that we are aware of.

Clearly the experimental island densities cannot be explained by Equation 3.3, since the prefactor term is too high. For instance assuming no energy barrier to diffusion (the exponential term therefore equaling one), the prefactor $(\frac{F}{\nu})^{\chi}$ is still greater than the experimental island densities. We conclude that the simple growth regimes of Equation 3.1 (mobile monomer), or Equation 3.2 (mobile monomers and dimers) do not apply to nucleation in the Bi/HOPG system.

The exponent $\chi = 0.40$ measured from the flux dependent study of Section 3.4.3 suggests small Bi clusters are mobile. Simulations by Lewis *et al.* [99], discussed in Section 3.1.3, find N_{sat} scales as N_{max}^{-1}, where N_{max} is the largest mobile aggregate in terms of constituent atoms, and clusters diffuse at rates $D_N = \frac{D_0}{N^{2/3}}$. Island densities will likely scale differently depending how the cluster diffusion coefficients are defined, though a first approximation is to apply the result of Lewis to the Bi/HOPG system. Assuming a 0.05 eV diffusion barrier for both Bi_2 and $(Bi_2)_2$ particles (the diffusion barrier found for Au adatoms on graphite), $\nu = 1 \times 10^{13}$ s^{-1}, and $\chi = \frac{2}{5}$ for mobile clusters, Equation 3.2 predicts $N_{sat} \sim 4 \times 10^{-6}$ islands per site. Assuming clusters containing two hundred atoms diffuse appreciably on graphite, the predicted island density reduces to $\sim 4 \times 10^{-8}$, close to the 2.1×10^{-8} islands per site determined from experiments. Becker [79] found experimental evidence for the diffusion of self-assembled Cu_{400} clusters on MoS_2, a size which might explain Bi island densities on graphite.

Another possible explanation for the apparent low island densities is the desorption of Bi particles from the surface. From SEM images the surface area covered by islands can be measured. For θ =2 ML films grown at F=0.14 Å/s, and T=308 K or T=353 K, the surface coverage is 40%. Assuming a base island height of 1.2 nm [13] pg 97 (4 monolayers), the actual coverage is calculated to be 1.6 ML, indicating roughly 0.4 ML has desorbed. Desorption is more likely at early growth stages, at low film coverage [22].

Particles reside on a surface for a length of time

$$\tau = (\nu^{-1}) \exp(\frac{\mathrm{E_a}}{\mathrm{k_B T}}), \tag{3.4}$$

where E_a is the atomic energy of adsorption. Within this time, a particle can diffuse a distance [108]

$$\lambda = \frac{\mathrm{a}}{2} \exp(\frac{\mathrm{E_a - E_d}}{2\mathrm{k_B T}}), \tag{3.5}$$

where $\mathrm{E_d}$ is the surface diffusion barrier (assuming vibration frequencies for desorption and diffusion are equal), and a is the hop distance. Equation 3.5 predicts a large diffusion distance when $\Delta \mathrm{E} = \mathrm{E_a} - \mathrm{E_d}$ is large. None of our data gives direct evidence for the desorption barrier $\mathrm{E_a}$, though a rough estimate for λ is the distance at which neighbouring aggregates show competitive capture. From SEM images this distance is likely a few hundred nanometres at T=303 K (see Figure 3.17), similar to results for Au on HOPG [83, 84]. With λ = 200 nm, and using a= 0.14 nm and $\mathrm{E_d}$ = 0.05 eV from Jensen *et al.* [107], we calculate $\mathrm{E_a}$ = 0.46 eV.

The separation between island centres ($\geq 2\mu$m, see Figure 3.11 (a)) is much larger than the diffusion distance $\lambda \sim$ 200 nm. Anton *et al.* [83, 84] found a similar result for the Au/HOPG system, and concluded island nucleation occurred on defects, the active desorption preventing nucleation via adatom-adatom collisions. Figure 3.15 in Section 3.4.3 proves island nucleation is homogeneous at T=303 K (i.e. not on defects). We are unsure how to reconcile the large inter-island spacing with the small diffusion length λ. A number of equations for $\mathrm{N_{sat}}$ similar to Equations 3.1 and 3.2 are predicted when adatom desorption is active [109, 34], yet none of them predict $\chi = 0.40$, and are not clearly applicable to the Bi/HOPG system.

3.4.5 Discussion

Bismuth islands grown with F=0.01 Å/s above room temperature develop 1D spikes, which are the preferred morphology at T=333 K. The spikes display the same alignment as the island stripes and step nucleated rods, and therefore likely have the same

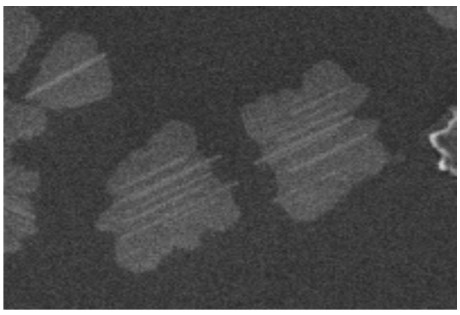

Figure 3.17: SEM image taken of two star-shaped islands displaying competitive capture. The image width is 2μm.

crystal orientation. Higher substrate temperatures produce more rearrangements at the island edges, allowing the equilibrium crystal shape to develop. A similarly favoured morphology is observed at room temperature depositions, for aggregates nucleating in low flux environments (at step edges).

A study of the flux dependence of the island density found a scaling exponent of $\chi = 0.4$, suggesting the critical island size is a bismuth dimer, and that small dimer-clusters can diffuse. The island density also displayed a weak Arrhenius dependence, with an activation energy of $E_A = 0.06$ eV.

Basic nucleation theories for monomer and dimer diffusion fail to explain island densities of 10^{-8} islands per site. Our flux dependent results, and other work [90, 91, 92, 93, 94, 95], suggest cluster diffusion is activated on HOPG substrates. Whether the low island density is due purely to the diffusion of self-assembled clusters, or to short adatom lifetimes because of a small adsorption energy is unclear. Quite possibly the island density is a combination of the two effects.

3.5 Summary of Bismuth Island Growth

This chapter has examined the growth of low coverage Bi films on Mica, MoS_2, and HOPG substrates. Investigations on Mica and MoS_2 were performed at room temperature for variations in flux and coverage, while for HOPG substrates the growth temperature ranged between T=303 K and 353 K.

Islands on all three substrates show a Volmer-Weber growth mode. Island base heights are either 4 nm or 9 nm on Mica, depending on island morphology, or between 1 nm and 2 nm on MoS_2. Bi island heights on MoS_2 are comparable to heights measured from HOPG substrates [13] pg 97. Spike heights on the HOPG substrates are 2.4$\pm$0.4 nm. The island stripes observed for MoS_2 substrates indicates a significant Ehrlich-Schwoebel barrier at room temperature, preventing material

transport between the substrate and island top.

Islands grown on the weakly interacting substrates (HOPG and MoS_2) display some important similarities; island perimeters are hexagonal or have six points of symmetry, and stripes develop on top of island bases. It is unclear whether the hexagonal symmetry of the substrates is responsible for the star-shape morphology, or whether the morphology is characteristic of the Bi$\{01\bar{1}2\}$ plane. Mica surfaces are understood to have a pseudo-hexagonal symmetry [110], but a hexagonal island morphology was not apparent from the AFM images.

A transition from 2D planar to 1D morphologies was observed on HOPG substrates, for F=0.01 Å/s and T=303 K to 333 K. The higher substrate temperature allows more atomic rearrangements at the island edges, avoiding the kinetically limited 2D shape. The favoured 1D morphology results from anisotropic bonding to the Bi$\{01\bar{1}2\}$ plane edges [13].

From the scaling of island densities with flux, on HOPG substrates a bismuth dimer is believed to be the critical island size, but with appreciable diffusion of small clusters. From the temperature dependence of the island density, an activation energy 0.06 eV was measured, though it is unclear how the activation energy relates to dimer diffusion.

Chapter 4

Analysis of Bismuth Rod Growth

This chapter details experimental and theoretical investigations of the anisotropically shaped aggregates observed to grow from terrace step edges when bismuth dimers are deposited onto HOPG substrates. The growth of these anisotropic structures (termed rods) was studied for various atomic fluxes, in the temperature range of T=303 K to 353 K, and for ∼monolayer coverages. Section 4.1 discusses the results of previous investigations into Bi/HOPG step nucleated features, where a comprehensive study of flux and coverage dependences was performed [13, 60]. New investigations of the temperature dependence of rod morphologies are then presented. Section 4.2 provides an overview of the experimental and theoretical literature on the growth of anisotropic structures. The development of a kinetic Monte Carlo (KMC) model to study step-nucleated features is presented in Section 4.3, and Section 4.4 presents results from the different models for generating anisotropic growth. In Section 4.5 KMC simulations of the temperature dependence of rod aspect ratios (defined as length/width) are presented. Section 4.6 includes a short investigation of rod coalescence using simulations. Section 4.7 summarises the experimental and simulational results.

4.1 Experimental Results

This section focuses on the growth characteristics of step nucleated features on the graphite surface. Previous results from a flux dependent growth study are discussed, the results illustrated using images from new samples. Results from a new temperature dependent study are then presented. Initially the basic rod morphologies are compared for each set of growth conditions, then a statistical analysis of the aggregate dimensions is presented as a function of temperature. Finally the Arrhenius dependence of the rod Aspect Ratios (ARs) is discussed.

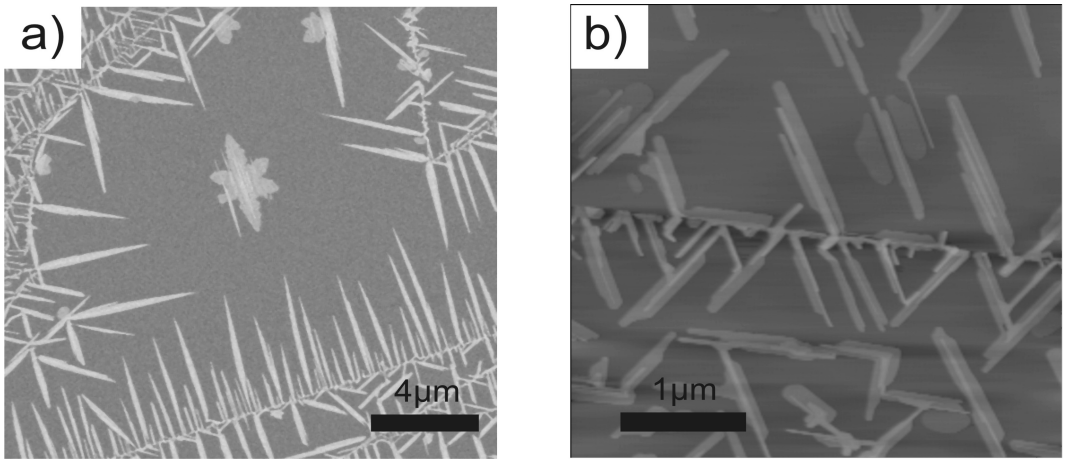

Figure 4.1: Typical SEM (a) and AFM (b) images of rod growth, taken from new samples to illustrate the large number of rods relative to islands, and the smooth, straight edges of the rods. The SEM image is roughly 12 by 12μm, the AFM scan is 4 by 4μm.

4.1.1 Previous Work

Typical (a) SEM and (b) AFM scans of rod features are shown in Figure 4.1, from new samples with identical results to [13]. Figure 4.1 (a) shows rods have smooth straight edges compared to the 2D islands, and are typically hundreds of nanometres in length. The smooth edges imply efficient transport and rearrangement of material at the rod perimeter, otherwise a more fractal like appearance would be expected [39, 41].

Previous work performed by Scott [13, 60] investigated rod heights and ARs as a function of the deposition rate (F=0.005 Å/s and 0.2 Å/s) and film coverage. At room temperature and low flux, bismuth aggregates nucleating at step edges prefer high aspect ratio shapes, with widths $\sim$ 100 nm, and lengths frequently beyond a micrometer. AFM scans revealed the rods to be $\sim$ 2 nm high, corresponding to $\sim$ 6 atomic layers (assuming a Bi monolayer is 3.3 Å high [14]). The preference of high AR at low flux suggests elongated structures require a slow growth environment to develop.

Rod ARs show an inverse dependence with flux [13] pg 143. For low fluxes (F= 0.005 Å/s) the mean rod AR approaches 7, while at higher flux (F= 0.2 Å/s) aggregate growth was more stunted, with typical AR $\leq$ 2. Rod ARs did not exhibit a coverage dependence within the range 0.2 ML to 2 ML. Rod widths and lengths increase for higher coverages (maintaining a fixed AR), implying that extra material is incorporated into rods without affecting the growth kinetics.

Figure 4.1 (a) demonstrates the high density of step nucleated features relative to terrace nucleated islands. Although no study of the rod density was presented

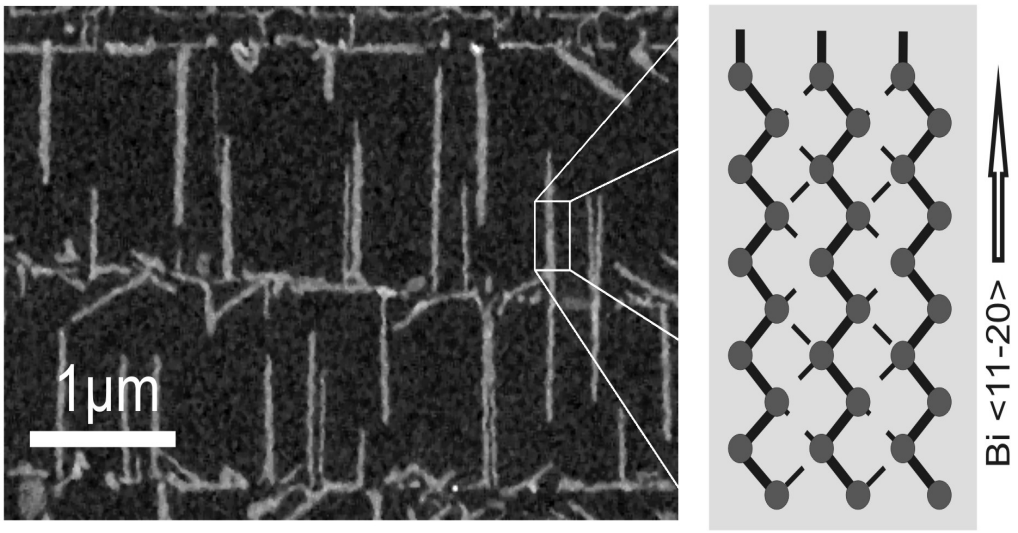

Figure 4.2: SEM image of bismuth rods growing perpendicularly from the graphite steps, F=0.03 Å/s, T=320 K and θ =0.5 ML. A schematic reproduced from [13] shows the crystal orientation relative to the rod growth direction, showing unsatisfied intralayer bonds on the small facet.

in [60], the high density of step nucleated aggregates implied nucleation occurred at defect sites along the step edges. Reduced diffusion coefficients along the steps could provide an argument for the increased density of aggregates, but the lack of a clear flux dependence for the aggregate density (refer to Figure 2 in Ref.[60]) suggested nucleation predominantly occurred at defect sites.

Crystallographic studies (Chapter 6.5.3 Ref.[13], [60]) have shown rods orient with the Bi$\{01\bar{1}2\}$ plane parallel to the graphite surface, with a preferred in-plane orientation of Bi$\langle 11\bar{2}0\rangle$ parallel to the HOPG$\langle 10\bar{1}0\rangle$ direction. The Bi$\langle 11\bar{2}0\rangle$ direction is also found to be parallel to the direction of rod elongation. Figure 4.2 displays an SEM image of rods and a schematic of the Bi$\{01\bar{1}2\}$ plane, with the Bi$\langle 11\bar{2}0\rangle$ direction indicated by the arrow. The Bi$\langle 11\bar{2}0\rangle$|| $\langle 10\bar{1}0\rangle$HOPG alignment most commonly has rods growing perpendicular to the graphite step-edge, directly into the diffusion field. A common misorientation of the rods was at 30° with respect to the preferred orientation, an alignment of Bi$\langle 11\bar{2}0\rangle$|| $\langle 11\bar{2}0\rangle$HOPG [13, 60].

The schematic of Figure 4.2 illustrates the zig-zag like arrangement of atoms in the Bi$\{01\bar{1}2\}$ plane. Each atom is bonded to six other atoms, four of which lie in the Bi$\{01\bar{1}2\}$ plane. Of the four in-plane bonds, two bonds have length 3.1 Å (intralayer bonds drawn with full lines in Figure 4.2) and two have length 3.5 Å (interlayer bonds, dotted lines). Energies for the intralayer and interlayer bonds cannot be found in the literature, though bulk bismuth has a cohesive energy E = 2.0 eV per Bi atom [111]. Atoms in a rhombohedral bismuth crystal form six bonds [46],

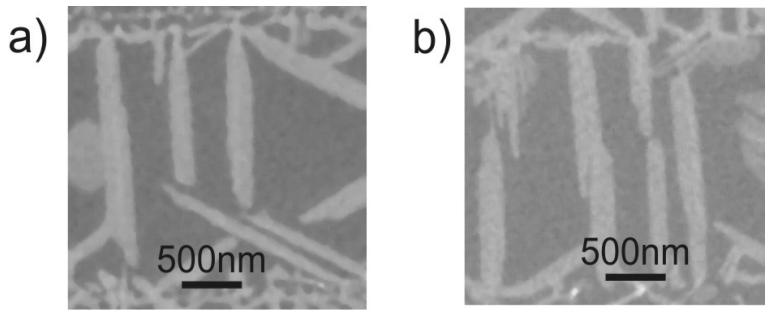

Figure 4.3: SEM images taken from new samples grown at F=0.01 Å/s and (a) T=333 K and (b) T=313 K. Located near the centre of each image, (a) shows an example of two rods avoiding each other during growth, while (b) shows the collision of two growing tips.

three each of length 3.1 Å and 3.5 Å.

The orientation of the rods leaves the rod tips terminated by broken 3.1 Å and 3.5 Å bonds, while the sides have broken 3.5 Å bonds. The broken intralayer bonds at the rod tips are expected to bind dimers more efficiently than the broken interlayer bonds on the rod sides, providing an understanding for the anisotropic growth. An estimated binding energy for atoms on the short edges is one third of the total cohesive energy i.e. $E = \frac{2.0}{3} \approx 0.7$ eV.

A frequent observation in the previous work [13] was the intersection and coalescence of nearby rods, demonstrated in Figure 4.3. Rods nucleating on opposite sides of a terrace and therefore growing into the same region from different directions show two different responses when approaching each other. In Figure 4.3 (a), rod tips show competitive capture i.e. the tips avoid one another due to a lack of material between them. Competitive capture is apparent when tips in close proximity have cavities etched into the rod morphology. The inference is that material arrives at the tips purely from the diffusion field. Figure 4.3 (b) shows an alternative example where tips expand into one another to form a continuous structure, this mode implies transport of material to the tip from the length. These apparently different growth modes are difficult to reconcile.

4.1.2 Temperature Dependence of Step Aggregates

Attaching heaters to the sample holder as described in Chapter 2 allows a study of step nucleated features as a function of substrate temperature. Increases in temperature and flux are expected to generate opposite responses in the observed rod morphologies. Higher temperatures allow more atomic rearrangements in each given time period, allowing the system to achieve a more thermodynamically favourable state. Increasing the particle flux reduces the time between aggregation events,

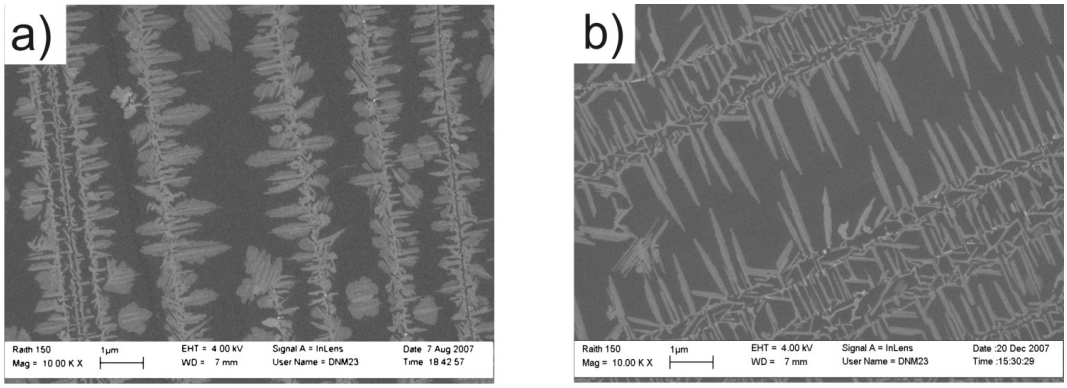

Figure 4.4: SEM images of rods grown at (a) T=308 K, and (b) T=353 K. For both samples F=0.14 Å/s and θ =2 ML.

shortening the time in which rearrangements can occur. Hence increasing the temperature should give comparable results to reducing the material flux.

Temperature dependence of rod morphologies

Figure 4.4 displays the typical effect of increasing the substrate temperature on the morphology of step-nucleated features. A particle flux of F=0.14 Å/s was selected as previous room temperature investigations had shown these conditions to produce small, kinetically limited aggregates (Figure 6.4.3 [13]). These kinetically limited shapes are reproduced in a sample grown at T=308 K (Figure 4.4 (a)), the aggregates displaying a more isotropic morphology. Figure 4.4 (b) is taken from a sample grown at 353 K, showing the growth of pseudo-1D rods with sharp tips. Rod morphologies in the latter image are similar to shapes previously observed for low flux (F=0.005 Å/s) room temperature samples (Figure 6.4.3 [13]).

In Figure 4.4 (a), at T=308 K and F=0.14 Å/s, the small interval between aggregation events does not allow sufficient time for atoms to rearrange on the crystal boundary before additional atoms arrive. Hence the aggregates develop a 2D morphology. However, the 2D aggregates are interspersed with smaller 1D features, indicating there are competing growth modes at the step edge. Step edges have a high density of nuclei and consequently each nucleus is in competing for material with neighbouring aggregates, possibly reducing the local flux and allowing 1D rods to grow.

At T=353 K (Figure 4.4 (b)), 2D growth is almost entirely suppressed, and rods grow hundreds of nanometres wide, and up to two micrometres in length. The increased temperature allows more atomic rearrangements at crystal interfaces, leading to more thermodynamically favourable shapes. In some instances multiple branches extend from a single nucleus (these examples having broad bases as a

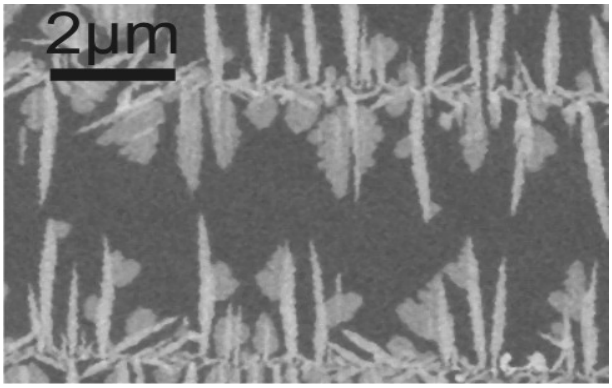

Figure 4.5: An image from a 2 ML sample grown at F=0.013 Å/s, T=323 K, where a number of rods have developed 2D morphologies from their sides.

common element), indicating some non-equilibrium processes are still active. We assume the multiple branching indicates a Mullins-Sekerka type instability [37], where the growth of small perturbations is enhanced in a high flux environment, the perturbations developing faster than rearrangement processes acting to smooth the facet edge. Hence even at T=353 K the high flux causes non-equilibrium growth.

Further illustration of the competing 1D and 2D growth modes is found in the SEM image of Figure 4.5, which is from a 2 ML sample grown at relatively low flux (F=0.013 Å/s), and T=323 K. 1D features are most commonly observed in the image, but a number of rods show 2D extensions. The 1D-2D aggregates are more common on the lower step-edge of Figure 4.5, and the 2D growth is frequently found on the side of the rods that is exposed to large regions of bare terrace. The suggestion is that these 2D extensions develop due to a high local flux near the rod edge, the high local flux a result of the local arrangement of rods (small number of rods means less capture, and higher local flux).

Many of the larger rods seen in Figure 4.1 (a) and Figure 4.4 (b) exhibit tapering at each end (while most apparent for the ends growing into the diffusion field, tapering can also be observed near the step edge). Crystals grow quickly when material arriving at a step edge can be incorporated into existing kink sites. As the majority of new material arrives via the terrace, the rods presumably have a natural tendency to grow into the terrace. Rods shown in Figure 4.1 (a) are typically broadest in the middle, evidence that nucleation of additional layers occurs on the long edges during growth. Figure 4.6 provides a schematic of the expected tapering process. Nucleating new atomic layers increases the density of kinks along a facet, the kinks providing favourable absorption sites for material diffusing along the edge. Two important conclusions can be drawn from the rod morphology; rods have small widths relative to their lengths, indicating nucleation occurs more quickly on the rod

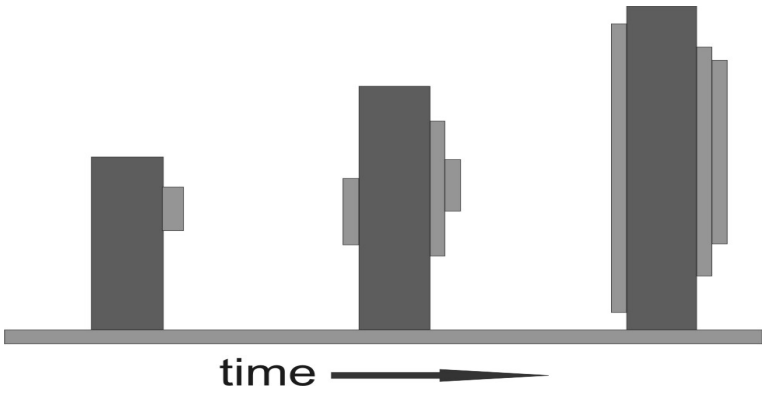

Figure 4.6: Illustration of rod tapering during growth. If atomic layers on the long edges do not complete before additional layers nucleate, each subsequent layer will have a shorter extent.

tips than on the sides. Secondly, the smooth straight edges of the rod sides indicates kinks are quickly saturated with material, suggesting atoms diffuse quickly on long edges.

Figures 4.7 (a) and (b) are taken from two samples produced with F=0.14 Å/s and T=308 K and T=353 K respectively. Step-edges in Figure 4.7 (a) are saturated with material i.e. a continuous line of bismuth traces out each HOPG step, comparing with the high temperature example of Figure 4.7 (b), where bare regions of the HOPG step separate neighbouring rods. Diffusion along graphite step edges should be more highly activated at higher substrate temperatures, in agreement with observation of bare step regions. Figure 4.7 (b) also reveals a number of small rods on the step edge shielded from the terrace by large rods. The variation in rod size implies rods which grow into the terrace at early stages preferentially capture diffusing material, preventing the development of later nucleated rods, in a competitive capture type scenario.

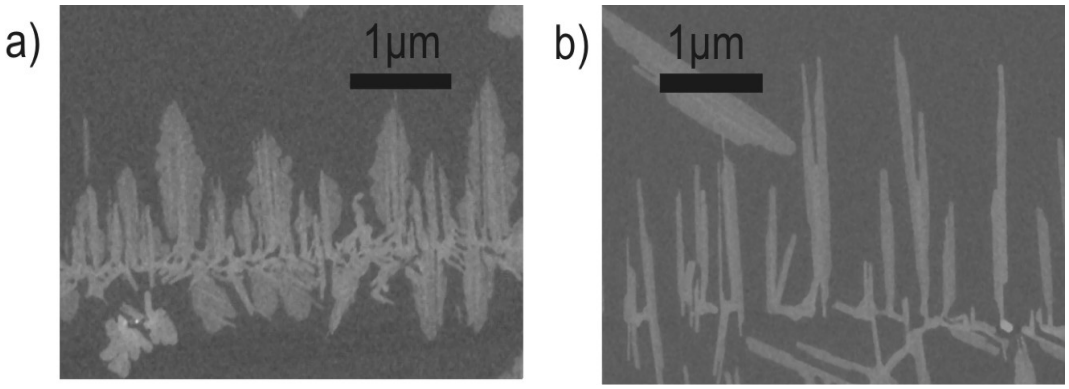

Figure 4.7: High resolution SEM images looking at material along the step edge for F=0.14 Å/s and (a) T=308 K, and (b) T=353 K. Both samples have $\theta = 2$ ML.

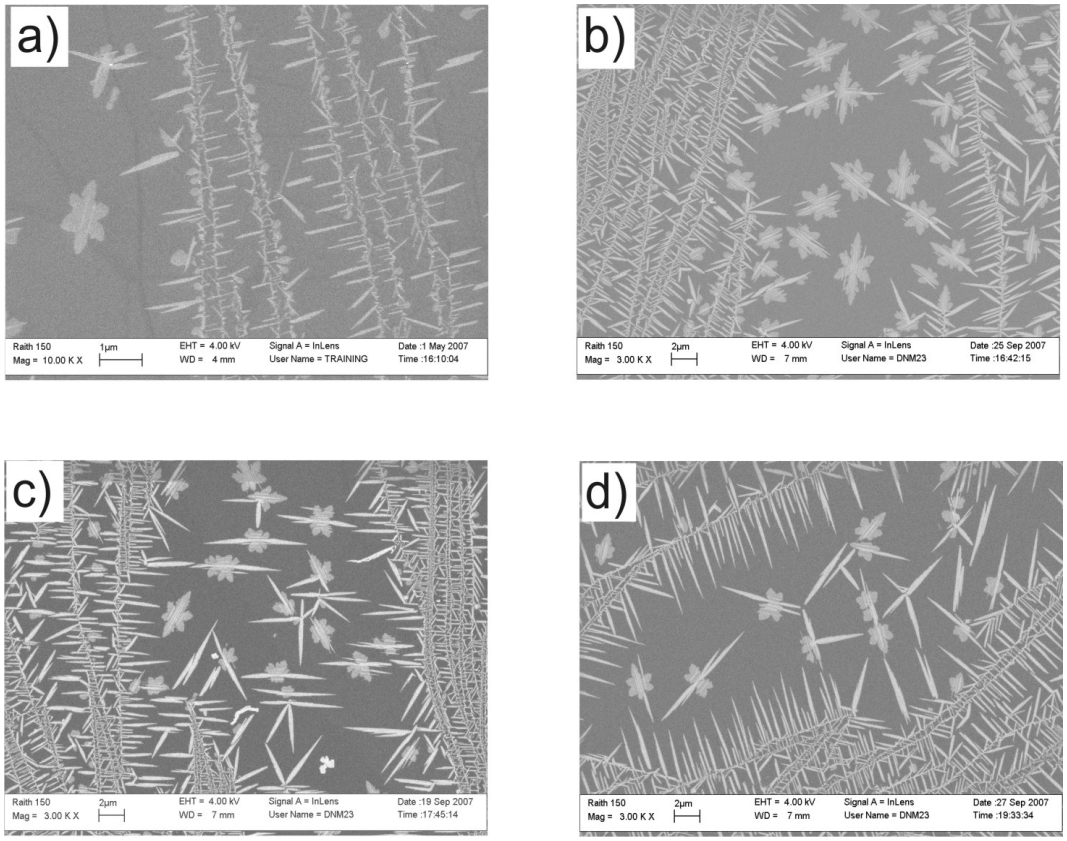

Figure 4.8: Changes in rod morphology as temperature is increased from a) T=303 K, b) T=313 K, c) T=323 K, to d) T=333 K. Each sample was grown at Flux=0.01 Å/s, and 2 ML, except for a) where the coverage is 1 ML (note the reduced scalebar).

Temperature dependence of rod dimensions

To gather quantitative information on rod size and shape as a function of temperature, samples were grown at four different temperatures; T=303 K, 313 K, 323 K, and 343 K, with F=0.01 Å/s. Figure 4.8 displays a representative SEM image from each of these samples, the images taken from regions where rods grow relatively uninhibited by islands or nearby steps. Competitive capture type effects can stunt the rod growth, potentially distorting any statistics extracted from the images.

A competitive capture type problem affecting the T=303 K samples is the more frequent occurrence of 2D features. Since both 1D and 2D aggregates grow at low substrate temperatures, depositing only 1 ML of material for the low temperature (T=303 K) sample reduces the size of 2D aggregates, reducing their influence on 1D rods. Scott [13] finds rod ARs do not exhibit a coverage dependence within the range 0.2 ML to 2 ML, for F=0.005 Å/s and F=0.2 Å/s. Hence we expect the ARs from 1 ML samples to be consistent with results from 2 ML samples, though the width and length dimensions will be reduced.

Measurements of rod dimensions were taken from each sample set, using images

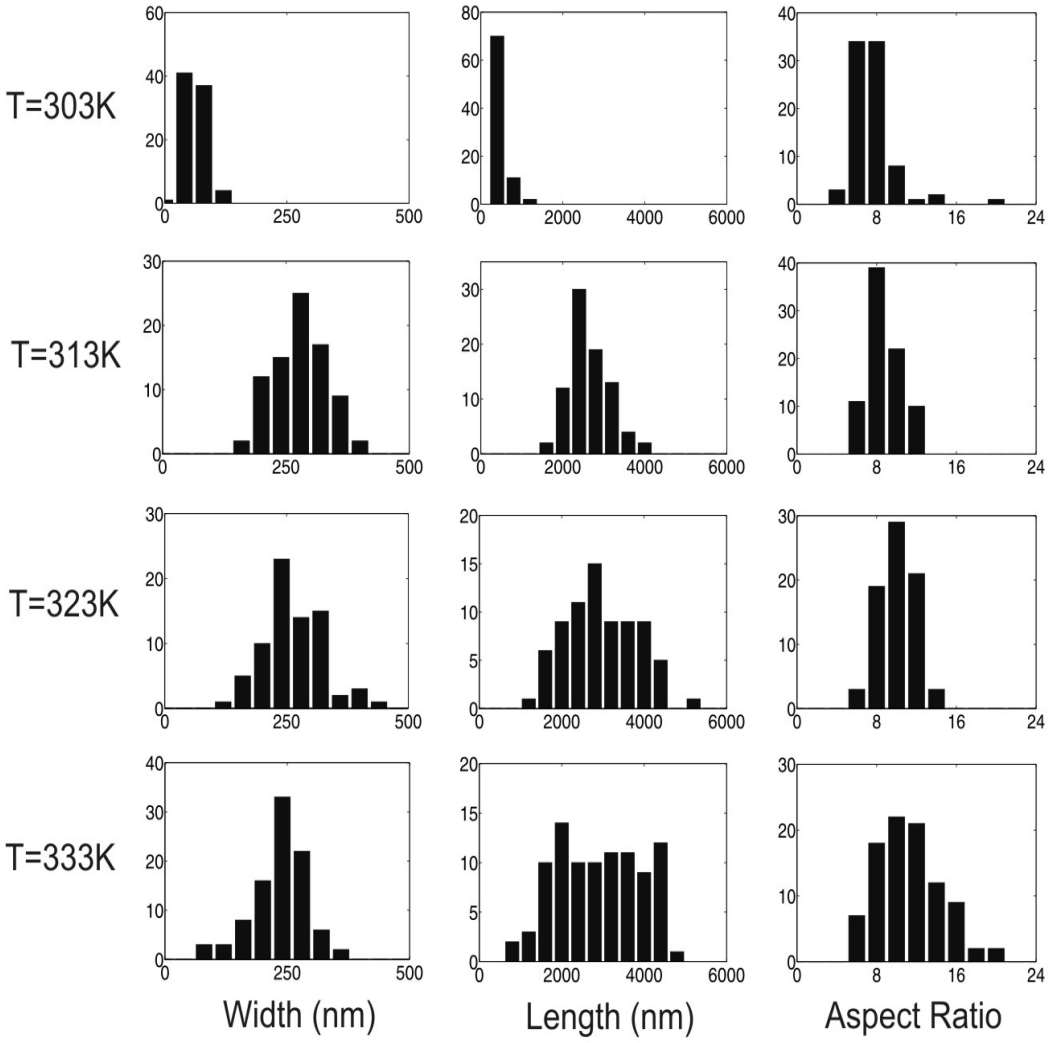

Figure 4.9: Histograms of step aggregate width, length, and aspect ratio, for T=303 K, 313 K, 323 K, and 333 K. The samples were grown at F=0.01 Å/s. The temperature is indicated for each row.

similar to those in Figure 4.8 which contained large terrace regions and few islands. Rods with tip branching or 2D growths were not considered. Typically eighty rods from each sample set were measured. Rod dimensions vary considerably along each step edge, due to different local conditions, however the large number of rods is intended to account for the variations.

Figure 4.9 contains histograms of rod widths and lengths collected using the above analysis, while Figure 4.9 (c) shows histograms of ARs calculated for each rod. Substrate temperature is indicated alongside each set of histograms. Focusing on the histograms from 2 ML samples (T=313 K, 323 K, and 333 K) reveals rod widths between 200 nm and 300 nm, and lengths ranging between 2 μm and 4 μm. The distribution of widths and lengths is quite broad at each temperature, and

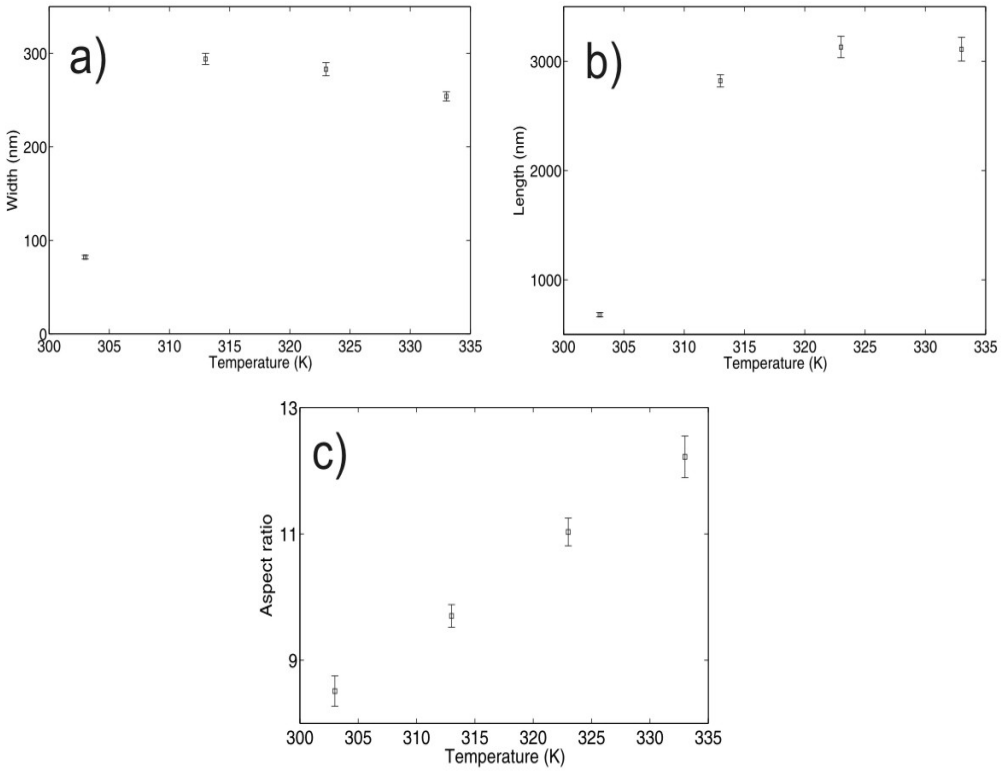

Figure 4.10: Plots of the mean (a) widths, (b) lengths, and (c) aspect ratios, as a function of temperature, for samples grown at F=0.01 Å/s. Note the reduced mean width and length of the low temperature data, due to the smaller deposited coverage. Error bars are included using the standard error, $\sigma_{\bar{x}}$.

has a roughly Gaussian profile (more apparent for T=313 K, 323 K, and 333 K). ARs also appear to have a roughly Gaussian form, suggesting the variations in rod dimensions are correlated and have little effect on AR, in agreement with the AR coverage dependence observed by Scott [13].

Mean values from the histograms of Figure 4.9 are displayed in Figure 4.10. Error bars included with each data point represent the standard error of the mean ($\sigma_{\bar{x}} = \frac{\sigma_x}{\sqrt{N}}$, where N is the sample population). Excluding the T=303 K data point (taken from a 1ML sample), the data shows small variations in the mean width and length as temperature is increased. Aspect ratios (Figure 4.10 (c)) show a more obvious increase with temperature. An interesting observation is the consistency of the 1 ML ARs with the 2 ML data points, consistent with results of Scott *et al.* [13] pg 143 that found coverage does not significantly affect the aspect ratio. At T=303 K the mean AR is 8.5 ± 0.2, increasing to 11.9 ± 0.2 at T=333 K.

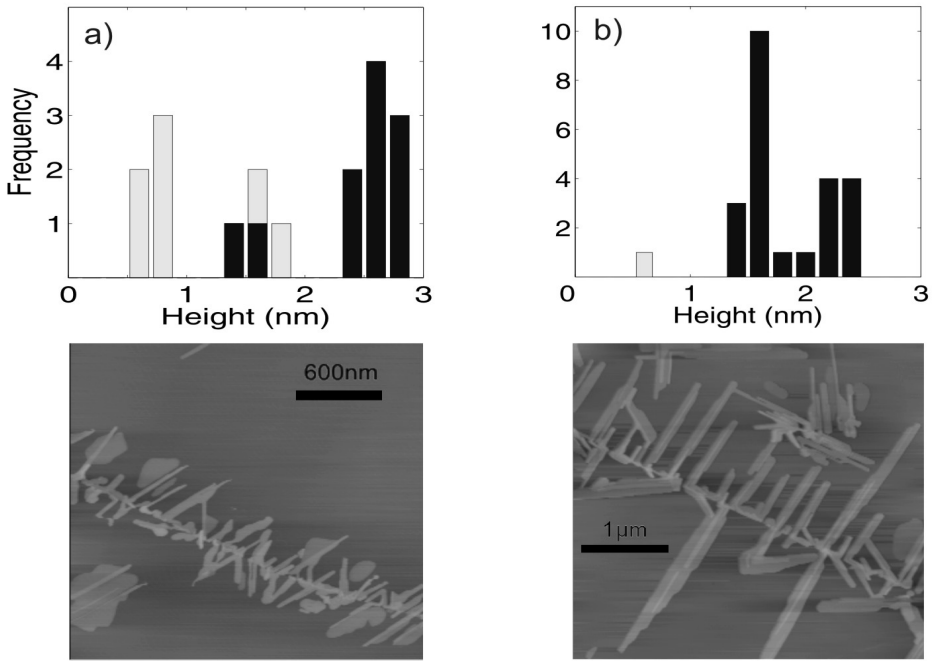

Figure 4.11: Histograms of measured rod heights from a small sample set, each histogram has an associated AFM image. In the histograms, grey bars represent 2D morphologies and dark bars represent the elongated rods. The growth conditions were (a) T=308K, F=0.14 Å/s, coverage=1ML, and (b) T=353K, F=0.14 Å/s, coverage=2ML. Note the differing morphologies in each AFM scan.

4.1.3 Rod Heights

Previous work [13] has shown the heights of step-edge aggregates to be ∼1 nm or ∼2 nm, depending whether the aggregates are 1D (rods) or 2D. The 1D rods were predominantly 2nm in height. As discussed in Section 4.1.1, the 2D morphologies occur more frequently at high flux, therefore the height study was performed within a low flux regime (in Chapter 6.5 of Scott [13]). Rod heights did not exhibit any coverage dependence.

Figures 4.11 (a) and (b) contain AFM images and histograms of rod heights taken from two different samples, at different substrate temperatures. Material flux for each sample was kept at 0.14 ± 0.01 Å/s, and the deposited coverages were (a) 1 ML, and (b) 2 ML. The dark bars in the histograms represent heights of rods, and the grey bars are from aggregates with the characteristic 2D morphology. At low temperature the variety in feature heights is apparent, ranging from 0.7 nm to 3 nm, reflecting the 1D and 2D morphologies. At T=353 K nearly all the step nucleated features are 1D, the heights centred about 2 nm. Stripes (thin bright lines on rod tops) are seen on rods grown at T=353 K, have heights ∼0.9 nm, these heights are not included in the histograms.

An interesting result from Figure 4.11 (b) is that the favoured 2 nm rod height

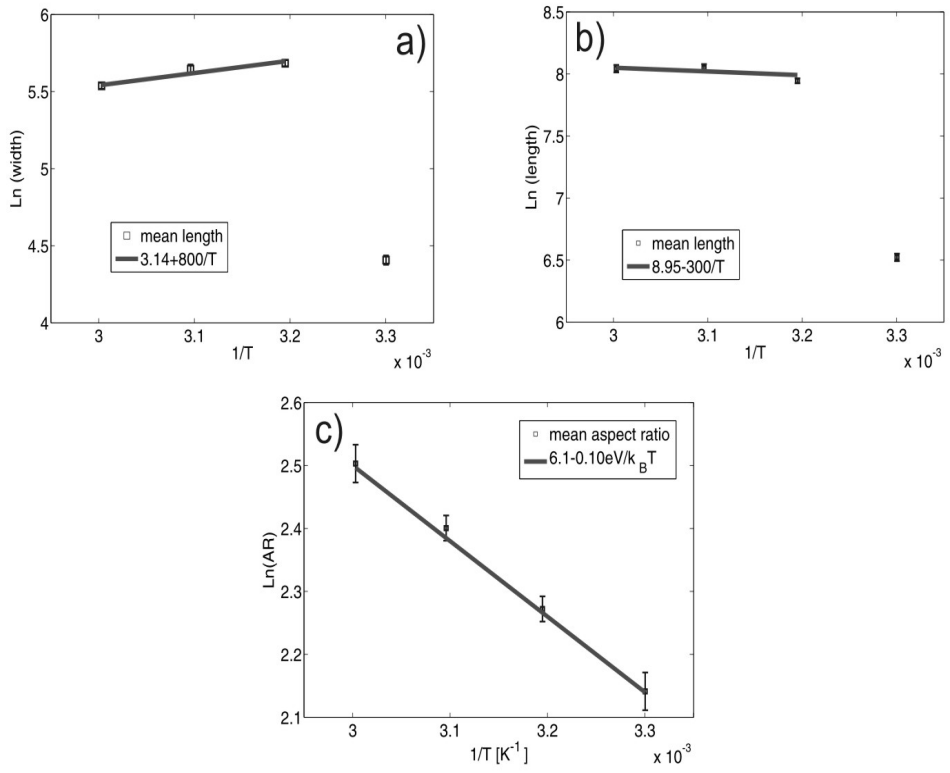

Figure 4.12: Mean widths (a), lengths (b), and ARs (c) plotted as functions of inverse temperature, for the samples grown at F=0.01 Å/s. The legend contains the parameters used to create the linear fit.

has not changed from the room temperature/low flux growth. It is unclear whether an Ehrlich-Schwoebel barrier prevents particles climbing onto rod tops for T$\leq$ 353 K, or whether low coverage Bi islands have a preferred thickness due to energy considerations [14].

4.1.4 Temperature Dependence of Rod ARs

An Arrhenius analysis assumes a limiting energy barrier for thermally activated events of the form $AR = \nu \exp(\frac{-E_A}{kT})$, where ν is a dimensionless prefactor and E_A an energy barrier. Figure 4.12 displays the data from Figure 4.10 plotted against inverse temperature. The natural log of the mean widths (a), lengths (b), and ARs (c) are shown, with the fit parameters displayed in the legend. In each plot the last datapoint corresponds to the 1 ML sample, and is only included in the fitting procedure for the aspect ratio data. The fits indicate activation energies (and prefactors) of (a) 0.07 eV (23), (b) 0.03 eV (7700), and (c) 0.10 eV (446).

The origins of the prefactor and activation energy for the ARs is unclear. For

example, the activation energies are clearly smaller than the attachment energy of ∼0.7 eV for an atom on the end of a Bi$\{11\bar{2}0\}$ plane, estimated in Section 4.1.1. Investigations of anisotropic crystal growth for metal on metal systems [62], using experimental and theoretical methods, indicate a more appropriate relation of $E_A = \chi E_b$, where E_b is the energy binding an atom to a facet, and the fractional component χ is a scaling parameter. $E_A = 0.10$ eV measured from Figure 4.12 may therefore provide a measure of the binding energy to rod sides, so in the following Sections we investigate how the binding and activation energies are related. Anisotropic crystal growth is reviewed in the following Section, then a number of possible rod growth scenarios are simulated in Section 4.4 and 4.5, to find a candidate model for the experimental results plotted in Figure 4.12.

4.2 Anisotropic growth in epitaxial systems

This section provides an overview of thermodynamic and kinetic effects which produce anisotropically shaped crystals. A classic epitaxial system which exhibits anisotropic growth is the metal on metal fcc(110) surface. Experimental and simulated results (from the literature) from such systems are discussed. Although the metal on metal system is not directly related to Bi growth on the graphite surface (the graphite surface is expected to have less influence on the growth), the Bi rod morphologies have similar temperature and flux dependences to islands on the (110) surface.

Equilibrium crystal shapes result from the minimisation of surface free energy [34]. Crystal facets of different orientation can have different surface energies, therefore crystals often require irregular shapes at equilibrium to minimise the surface energy. Away from equilibrium (in the kinetic regime), timescales associated with aggregation are shorter than restructuring timescales, leading to structures which have not minimised the surface energy. Modifications of the growth parameters can allow transitions from non-equilibrium to equilibrium structures [41, 44]. Analysis of these transitions can give quantitative information on the activation barriers for kinetically limited processes.

Crystal facets of different surface energy nucleate new layers at different rates [112], leading to structures with non-uniform shapes. Nanowires and nanobelts [113, 114] grown from the vapour or liquid are common examples of anisotropically shaped structures. Crystal growth can be understood via particle diffusion and nucleation. Atoms arriving at an interface (crystal edge) diffuse randomly until finding a kink site, or by forming a nucleus with other diffusing atoms. In the first case there

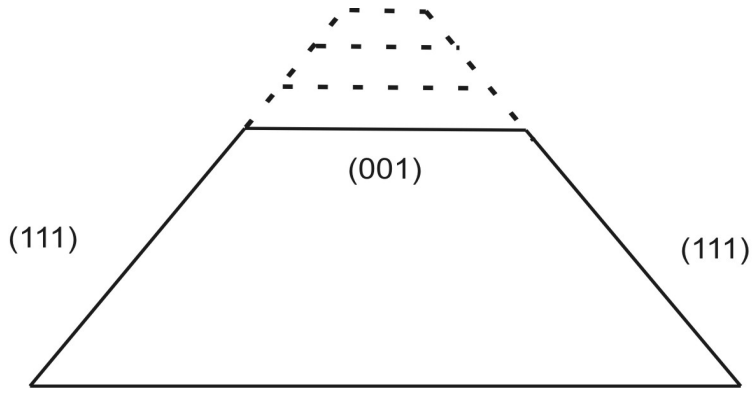

Figure 4.13: Illustration of the change in surface area attributed to (001) planes during crystal growth. For FCC crystals, (001) facets nucleate new layers faster than (111) facets. The schematic shows the addition of (001) layers (dotted lines) onto an (001) and (111) faceted crystal, causing a reduction in (001) surface area, and the expansion of (111) planes.

is accumulation of material by an existing layer, and in the second case there is nucleation of a new atomic layer. Facets with high surface energy have high densities of broken chemical bonds, providing sites of stronger binding, as the atoms satisfy many broken bonds. If atoms can move between facets, they will spend more time on facets of stronger binding, either nucleating a new layer or adding to an existing one. A simple principle from crystal growth [21](illustrated in Figure 4.13) is that the facets that nucleate new layers most frequently keep reducing in surface area, eventually removing themselves from the system. Facets with the lowest surface energy dominate the final shape, helping to minimise the total surface energy of the final structure.

4.2.1 Island growth on corrugated surfaces

Classic examples of anisotropic growth for epitaxial systems are found on substrates with corrugated (channeled) surfaces e.g. fcc(110) or reconstructed surfaces [115]. De-Giorgi *et al.* [116] present an experimental investigation of the Ag/Ag(110) homoepitaxial system, then examine their results using Monte Carlo simulations. Experimentally, elongated islands are observed to grow between T=140 K and 210 K, at given flux (F= 0.0012 ML/s) and coverage (0.16 ML). A transition from roughly isotropic aggregates at low temperature to highly anisotropic (1D) shapes at T=210 K is observed, with the islands elongating *along* the Ag(110) channels. A kinetic Monte Carlo model developed by the authors to replicate experimental results determines the important atomic events are: in-channel diffusion, cross-channel diffusion, and the breaking of in-and cross-channel bonds to island edges. Comparing simulations with experiments, estimates of cross-channel bond energies 0.04 eV and

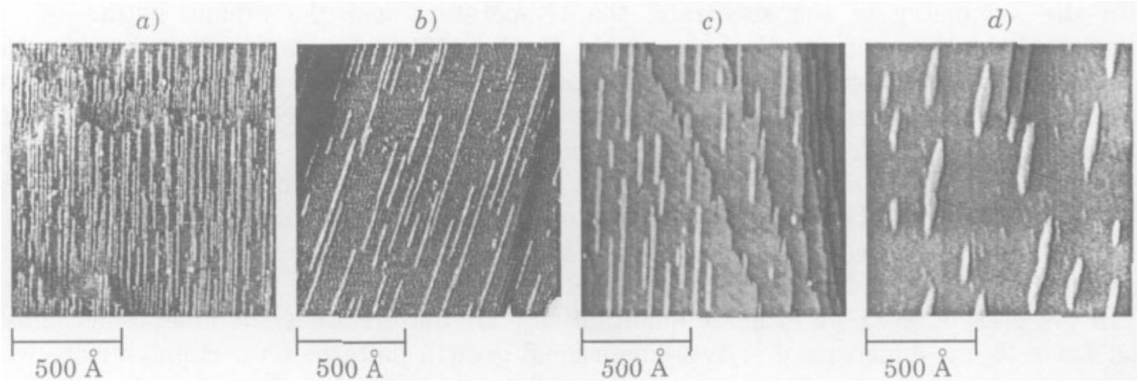

Figure 4.14: Image reproduced from Ref [119], showing the growth of Cu islands on Pd(110) at temperatures (a) 265K, (b) 300K , (c) 320K, (d) 350K.

in-channel diffusion barriers 0.28 eV are determined, with an estimate for the in-channel attachment energy of 0.4 eV. The authors conclude island elongation is due to the anisotropic bonding at the island edges.

Mo *et al.* [117, 118] studied the diffusion of Si adatoms on the Si(001) surface. A cleaved Si(001) surface reconstructs due to the strong nature of the broken Si bonds, forming a corrugated surface similar to the fcc(110) metal surface. Diffusion of Si atoms on the Si(001) surface is found to be highly anisotropic, diffusion along channels ∼1000 times faster than across channels. In contrast to fcc-(110) metal systems however, for sub-monolayer coverages Si islands develop *across* the channels [117] . The authors believe the cross-channel island growth is due to surface reconstructions and directional bonding of Si atoms. Mo *et al.* [118] reproduce the Si/Si(001) growth using a model which includes anisotropic surface diffusion, and anisotropic bonding to the aggregate facets. Atom transport between island edges occurs via an evaporation-condensation type process.

Gunther *et al.* [35] studied the diffusion of Au adatoms on the 'hex' reconstructed Au(001) surface, finding elongated islands for sub-monolayer coverages. Their rectangular shaped islands have increasing aspect ratios as particle flux is lowered, or as the substrate temperature is raised. Plotting ln (AR) as a function of inverse temperature reveals an Arrhenius dependence with activation energy 0.1 eV, in the temperature range 315 K to 435 K. The results suggest the elongated growth is thermodynamically driven, where equilibrium structures are elongated due to anisotropic bonding energies at the island edges, and islands with low ARs are examples of kinetically limited growth. The authors do not discuss the significance of the 0.1 eV activation energy.

Figure 4.14 shows submonolayer island morphologies for Cu/Pd(110) as temperature is increased from T=265 K to 350 K (reproduced from Ref. [119]). Work by

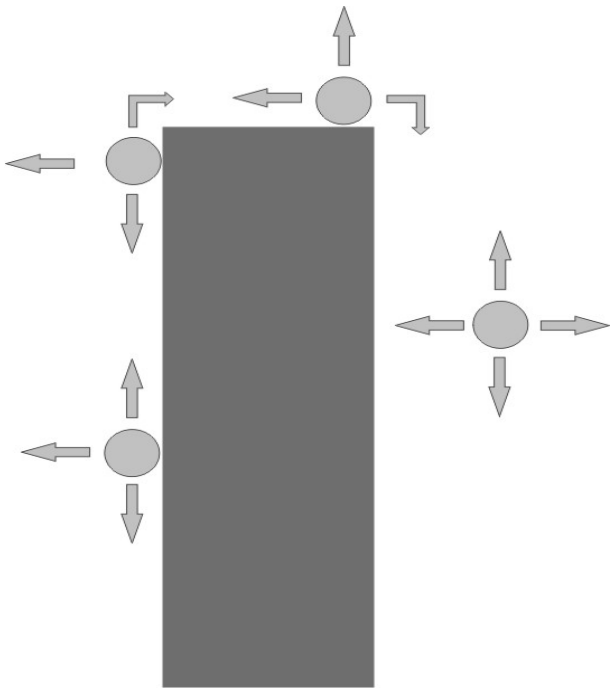

Figure 4.15: Atomic diffusion events predicted to be relevant on (110) surfaces [54]. Diffusion falls into two categories: diffusion between sites of similar coordination (terrace and edge movements), and diffusion between sites of different coordination (corner crossing and detachment).

Bucher *et al.* [119] and Roder [44] for the Cu/Pd(110) system finds monoatomic chains developing along surface corrugations for T<300 K, with reduced ARs at higher temperatures. Island elongation is parallel to the direction of fast atom diffusion, and from an Arrhenius analysis of the island densities, the authors predict the elongated islands are due to the anisotropic terrace diffusion barriers, i.e. cross-channel versus in-channel. In particular, the transition from one-dimensional chains to two-dimensional islands above T=300 K is due to cross channel diffusion 'switching on', reducing the island ARs, and the island density.

4.2.2 Modeling of island growth for fcc(110) metal systems

For fcc(110) metal systems, island elongation along channels (the direction of fast diffusion) was first believed to be a consequence of the anisotropy in terrace diffusion. Li *et al.* [61] investigated island growth on a fcc(110) surface using KMC simulations, finding that anisotropic terrace diffusion barriers cannot recover the temperature dependent island elongation discovered experimentally. Instead, atom rearrangements at the island boundary are necessary. Li *et al.* propose two mechanisms via which material moves between island edges: atoms are irreversibly attached to an island but can move between edges via corner rounding events (termed perimeter diffusion),

or via detachment of atoms from one edge followed by attachment at the adjacent edge, where the detachment/attachment process is mediated by terrace diffusion. Each of the diffusion paths is shown in the schematic of Figure 4.15. Arrows depict possible diffusion directions for atoms on the (110) surface, without distinguishing between directions of higher or lower energy barrier.

Li *et al.* successfully applied the perimeter diffusion model to the Cu/Pd(110) system [119, 44]. Incorporating stronger bonding at short edges relative to long edges via the use of anisotropic corner crossing barriers, the simulations of Li *et al.* reproduced temperature dependences of the island densities and ARs. The presence of anisotropic corner crossing barriers was postulated as early as 1966 by Schwoebel *et al.* [120], and more recently for the fcc(111) surface by Brune *et al.* [42].

Mottet *et al.* [54] investigated the Ag/Ag(110) and Cu/Cu(110) surfaces using calculated diffusion barriers and KMC simulations. Their model incorporates both the perimeter diffusion and attachment/detachment mechanisms discussed by Li [61]. With increasing temperature, an evolution from 1D in-channel chains to compact 2D islands is observed, due to the activation of in-channel detachment, followed by reattachment of atoms on the long edges. The simulation results suggest the attachment/detachment mechanism is more important for island elongation than the perimeter diffusion model used by Li for the Cu/Pd(110) system. The simulation results of Mottet are confirmed in subsequent experiments by De-Giorgi [116], with a slight discrepancy in the island density.

Heyn [62] investigated the scaling properties of island aspect ratios using an attachment/detachment model. The simulations produce a transition from near-isotropic island shapes at low temperatures, to 1D chain like structures at medium temperature, to 2D islands at high temperature. Heyn derives a scaling law for the island AR,

$$\langle \mathrm{AR} \rangle \cong \left(\frac{\mathrm{cF} + \mathrm{R}_1}{\mathrm{cF} + \mathrm{R}_2} \right)^{\chi}, \tag{4.1}$$

with F the atomic flux, c a free parameter, and $\chi = \frac{1}{3}$. R_1 and R_2 are respectively the detachment rates of atoms from long and short edges of an island i.e.

$$\mathrm{R_i} = \mathrm{R}_0 \exp(\frac{-\mathrm{E_i}}{\mathrm{k_B T}}), (i = 1, 2) \tag{4.2}$$

where R_0 is an attempt frequency. Equation 4.1 is in good agreement with the simulations of Heyn [62], and the experimental results for the Cu/Pd(110) system (see Bucher *et al.* [119]).

Note that in the temperature range where detachment from short edges is rela-

tively inactive (i.e. $R_1 >> R_2$), Equation 4.1 reduces to

$$\langle AR \rangle \approx (\frac{R_1}{cF})^{\chi}, \tag{4.3}$$

and the Arrhenius dependence of the mean AR has an activation energy $E_A = \chi E_1$.

Summarising the work discussed above, there is a consensus that elongated growth results from anisotropic bonding strengths at island edges. Simulation results show anisotropic terrace diffusion alone cannot generate the temperature dependent shape transitions observed on fcc(110) surfaces [116, 119, 44]. Two mechanisms for material transport between facets have been discussed, with simulations [54] suggesting that if both the perimeter diffusion and attachment/ detachment mechanisms are activated, the latter is more important. Importantly, when detachment from one facet is largely inactive, the activation energy for the AR Arrhenius dependence scales as $E_A = \frac{1}{3}E_1$, where E_1 is the energy barrier binding atoms to the edge where detachment is active.

4.3 Development of a Model for Rod Growth

In Section 4.2 the growth of anisotropically shaped islands was discussed. Equation 4.1 describes the dependence of island ARs on temperature and flux. Since a theoretical explanation for the exponent $\chi = \frac{1}{3}$ of Equation 4.1 is not provided, the applicability of Equation 4.1 to anisotropic growth from step-edges is unclear. Hence we develop a series of models to simulate step nucleated growth, then compare the model behavior to experimental results of Section 4.1. The aim is to derive a model which has the correct flux and temperature scaling relation for rod ARs.

This Section uses the rod growth algorithm presented in Chapter 2 to simulate rod growth. We present the approximations to the real Bi/HOPG system necessary for our simulations, due to memory and computation time considerations. In Sections 4.4, 4.5, and 4.6 we present simulation results, and a summary and conclusions in Section 4.7.

4.3.1 FCC Lattice

In this Section the use of an fcc(001) lattice to model the rod growth of Section 4.1 is discussed.

From SEM images and crystallographic studies, rods have been shown to develop with the Bi$\{01\bar{1}2\}$ crystal plane parallel to the graphite surface [13]. Figure 4.2 in Section 4.1 contains a schematic of the Bi$\{01\bar{1}2\}$ plane. The schematic has two-fold symmetry, since the long and short edges have different bonding characteris-

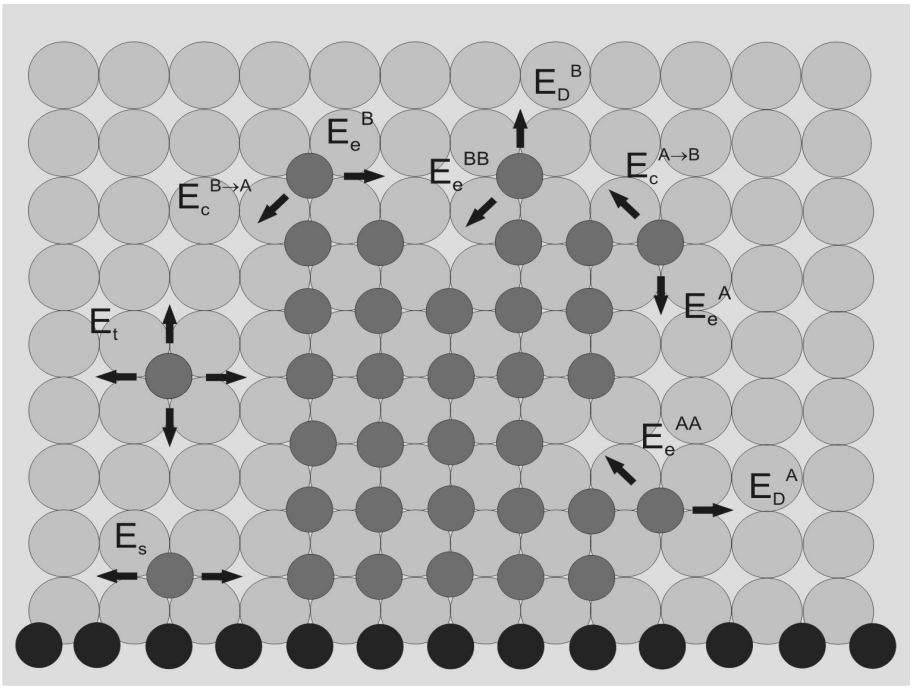

Figure 4.16: Reproducing the schematic of key diffusion events within the simulations. Further explanation is provided in Chapter 2.6.

tics. The two-fold symmetry is translated onto the square fcc(001) lattice, shown in Figure 4.16, by defining rods with distinct A and B facets. Diffusion on and attachment to the A and B facets can be defined differently. Therefore the expected anisotropic bonding strengths of the Bi$\{01\bar{1}2\}$ plane edges can be incorporated into the simulations, without using a rhombohedral lattice.

Although terrace diffusion on the square (001) surface has a different symmetry to diffusion on the honeycomb surface of HOPG, the high AR rod morphology observed in experiments (Section 4.1) is believed to result from anisotropic bonding to rod facets. The literature simulation and experimental results presented in Section 4.2 for the fcc(110) surface show anisotropic bonding at island edges is necessary for anisotropic growth, and the specifics of terrace diffusion are relatively unimportant. Hence approximating the diffusion of Bi atoms on HOPG with diffusion on a square lattice is not expected to compromise the results[2] .

Steps-edges are defined by creating an extra layer of atoms at the bottom edge of the 2D system (black atoms in Figure 4.16). Simulated rods then only grow perpendicular to the steps, a consequence of the square lattice and the definition of

[2]Clearly there is an important interaction between the bismuth crystal and substrate lattice, evidenced by the favoured $\langle 11\bar{2}0\rangle$Bi||HOPG$\langle 10\bar{1}0\rangle$ crystallographic alignment [13]. The interaction is expected to determine the alignment of the Bi$\{01\bar{1}2\}$ plane, but not the diffusion of particles about the rod perimeter.

A and B facets. SEM images have shown rods are usually oriented perpendicular to the step edge, or at 60° from the normal. Neighbouring rods typically have the same alignment (see Figure 4.1), hence the fixed alignment of rods growing on a square lattice is a convenient approximation to the real system.

4.3.2 Further Details

Rods expand by nucleating new atomic layers. Nucleation of a new atomic layer occurs when atoms diffuse into sites with two in-plane neighbours. Atoms with two in-plane neighbours are immobile, and as shown in Figure 4.16, there are no diffusion events for atoms with two in-plane neighbours. A single exception is for atoms located at the intersection of an A facet and a step-edge (at the base of the rod), since the step-edge represents a line of carbon atoms (rather than the Bi particles on the terrace).

Experimental results suggest rods nucleate at defects along step-edges. To standardise the nucleation process so that rod morphology is studied as a function of growth conditions, without competition for material between neighbouring rods, the simulations begin with small 2 by 2 aggregates initially fixed along the step edge. Aggregates grown from seeds with different initial sizes and shapes were indistinguishable after a small amount of material had been deposited. The 2 by 2 island is chosen as it is the smallest immobile seed, each atom has two in-plane neighbours and is therefore locked in place.

In every simulation, both the terrace and step-edge diffusion barriers (E_t and E_s in Figure 4.16) are set lower than edge diffusion barriers and deposition rate. The belief is that diffusion on the graphite terrace occurs faster than any other process, as suggested by the low island density and reasonably low rod density, therefore justifying low terrace diffusion and step-edge diffusion barriers. In each simulation $E_t = E_s = 0.05$ eV. Hence atoms landing on the surface from a deposition event diffuse quickly to a growing aggregate, either directly from the terrace or via the step edge, preventing nucleation of additional aggregates at the step edge or on the terrace. The simulated rod density is therefore determined by the number of seeds.

One further approximation is to set the energy barriers $E_e^{AA} = E_e^A$ and $E_e^{BB} = E_e^B$, and therefore vacancy filling events occur on a similar timescale to edge diffusion. In reality the energy barriers for vacancy filling and edge diffusion are likely different, but rods exhibit smooth straight edges, indicating that vacancy filling is not a rate limiting process.

4.4 Flux Dependence for Single Rod Simulations

In this section, the flux dependence of a system containing a single nucleus is investigated. Therefore a single rod is grown in each simulation. Three candidates for anisotropic growth are investigated; anisotropic edge diffusion, anisotropic corner crossing, and anisotropic detachment barriers. Results from the three models are compared with the experimentally observed rods discussed in Section 4.1.

4.4.1 System Shape

SEM images in Section 4.1 show a high density of aggregates nucleating at graphite step-edges. Rods appear evenly spaced, with rod lengths generally greater than the distance separating adjacent rods e.g. Figure 4.1 (a). The proximity of adjacent rods creates a competition for material along the rod lengths, suggesting additional material is most likely to arrive at the tip from the terraces. Clearly the rod capture regions are anisotropic in shape, with ARs>1.

Single rod simulations are performed on a 300 by 600 lattice, with periodic boundary conditions on the long edges, reflecting conditions on the top edge (atoms diffusing across the top boundary are shifted ten spaces back into the lattice), and a step-edge on the bottom edge. The top and bottom lattice edges are not treated as a continuous boundary since experiments do not show adatom transport across graphite steps (see Figure 4.1 (b)). The reflecting boundary is not ideal when high AR rods approach the top of the system, hence the rod ARs are only considered when rod tips are more than 100 atoms away from the boundary.

4.4.2 Anisotropic Edge Diffusion Barriers

We begin by investigating the effects of an anisotropically shaped diffusion field and anisotropic edge diffusion barriers, i.e. $E_e^A < E_e^B$. Edge diffusion energy barriers were trialled in the range $E_e^A = 0.25$ eV to 0.5 eV, and $E_e^B = 0.45$ eV to 0.7 eV. Simulations were performed for conditions similar to the experimental conditions, i.e. with T=300 K and flux varied between F=0.001 Å/s and 0.18 Å/s. Detachment and corner crossing events are effectively prohibited by setting $E_c^{A\rightarrow B} = E_c^{B\rightarrow A} = E_D^A = E_D^B =$ 1 eV.

Figure 4.17 demonstrates the large bases and multiple extensions exhibited by rods grown with $E_e^A = 0.3$ eV and $E_e^B = 0.5$ eV, for (a) F=0.001 Å/s and (b) F=0.18 Å/s. The different rod colours indicate coverages of 0.15 ML and 0.2 ML. With high flux, the multiple tip growth observed at F=0.001 Å/s is exacerbated, resulting in

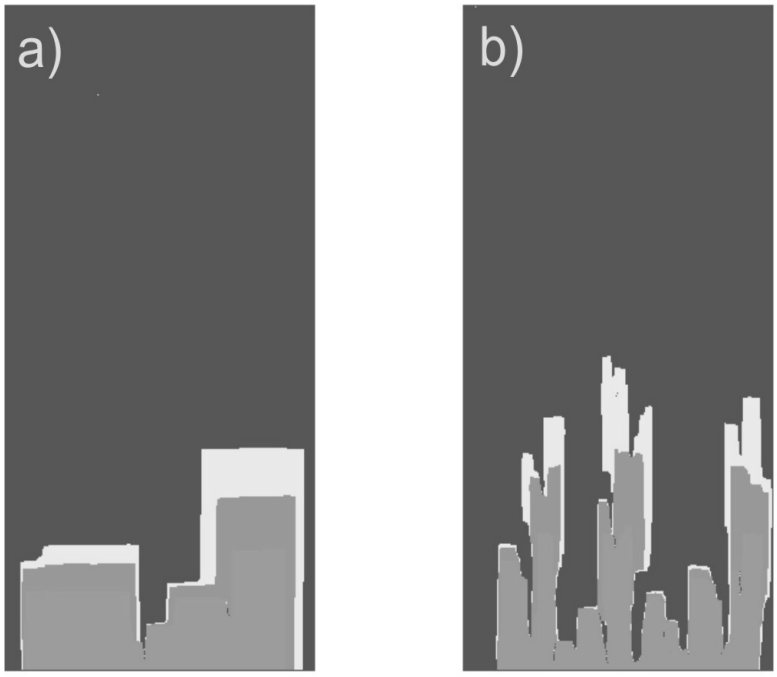

Figure 4.17: Typical rod growth for the anisotropic edge diffusion model, these simulations with $E_e^A = 0.3$ eV and $E_e^B = 0.5$ eV. (a) F=0.001 Å/s, and (b) F=0.18 Å/s. The rod shading corresponds to $\theta = 0.15$ ML and 0.2 ML.

an array of high AR branches. Higher fluxes lead to a greater number of nucleation events along the tip, and rapid branch growth. For the range of edge diffusion barriers trialled, neither the large ARs seen in Figure 4.1, or the isotropic structures observed at high flux (Figure 4.7 (a)) can be reproduced by simulation.

The large bases of the rods in Figure 4.17 demonstrate the importance of material transport between the facets in the experimental system. Starting from a nucleus only 2 atoms across, by 0.2 ML nearly the entire step-edge is covered in material. Atoms diffusing on the A facet have no path off the facet, and so the lateral growth only slows as long edges approach one another across the continuous boundary i.e. the lateral growth only slows due to competitive capture.

Anisotropic Edge Diffusion with Isotropic Corner Crossing

Next we consider the model proposed by Scott [13, 60], i.e. anisotropic edge diffusion barriers, while allowing atom transport between the facets via an isotropic corner crossing barrier i.e. $E_c = E_c^{A\rightarrow B} = E_c^{B\rightarrow A}$. The concept of different potentials at step edges (effectively corners in our model) was first discussed by Schwoebel *et al.* [120], in their model of step growth in epitaxial systems. The justification for the modified potential is due to the change in coordination an atom experiences as it diffuses across a step edge. Simulations were performed at T=300 K with diffusion barriers ranging from $E_e^A = 0.3$ eV to 0.40 eV, $E_e^B = 0.4$ eV to 0.55 eV, and $E_c = 0.25$

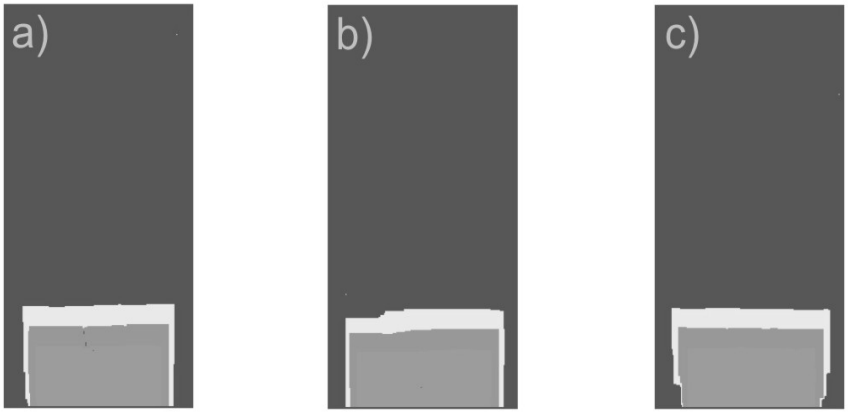

Figure 4.18: Rod growth for the anisotropic edge diffusion and isotropic corner crossing, with F=0.005 Å/s. Three scenarios are depicted, using energy barriers (a) $E_e^A = 0.35 < E_e^B = 0.45 < E_c = 0.55$, (b) $E_e^A = 0.30 < E_c = 0.40 < E_e^B = 0.50$, and (c) $E_c = 0.35 < E_e^A = 0.40 < E_e^B = 0.45$. The rod shading corresponds to $\theta = 0.15$ ML and 0.2 ML.

eV to 0.55 eV. Flux was varied between F=0.001 Å/s and 0.18 Å/s.

Figure 4.18 displays three different simulation results with isotropic corner crossing; (a) $E_e^A < E_e^B < E_c$, (b) $E_e^A < E_c < E_e^B$, and (c) $E_c < E_e^A < E_e^B$. The rods are grown with a relatively low flux, F=0.005 Å/s. In each case isotropic morphologies are produced, with smooth edges (i.e. few kink sites), without the tip branching observed in Figure 4.17. Edge atoms have enough time between successive adatom arrivals to find sites of high coordination.

The isotropic shapes of Figure 4.18 are not kinetically limited (they are grown at low flux). Since isotropic shapes are preferred for each combination of corner crossing and edge diffusion barriers, it suggests the thermodynamically favourable shape in all cases is nearly square.

Figure 4.22 (a) shows (full circles) the flux dependence of rod ARs for a simulation with $E_e^A = 0.3$ eV, $E_e^B = 0.4$ eV, and $E_c = 0.4$ eV. From F=0.0015 Å/s to 0.18 Å/s, the rod AR remains roughly constant at 0.7. Further discussion of Figure 4.22 is provided in Section 4.4.3.

Further simulations, with simulation parameters within the stated ranges, were unable to produce the elongated structures of Figure 4.1. We conclude that anisotropic edge diffusion [13] cannot reproduce the experimental results.

An understanding of the preference for low AR rods in the anisotropic edge diffusion/activated corner crossing model can be realised by imagining the potential an atom 'sees' when approaching a corner. With diffusion barriers chosen such that $E_e^A < E_e^B < E_c$ (Figure 4.19 (a)), atoms on the A facet attempting to jump to the B facet face a reflecting barrier, as do atoms on the B facet attempting to jump

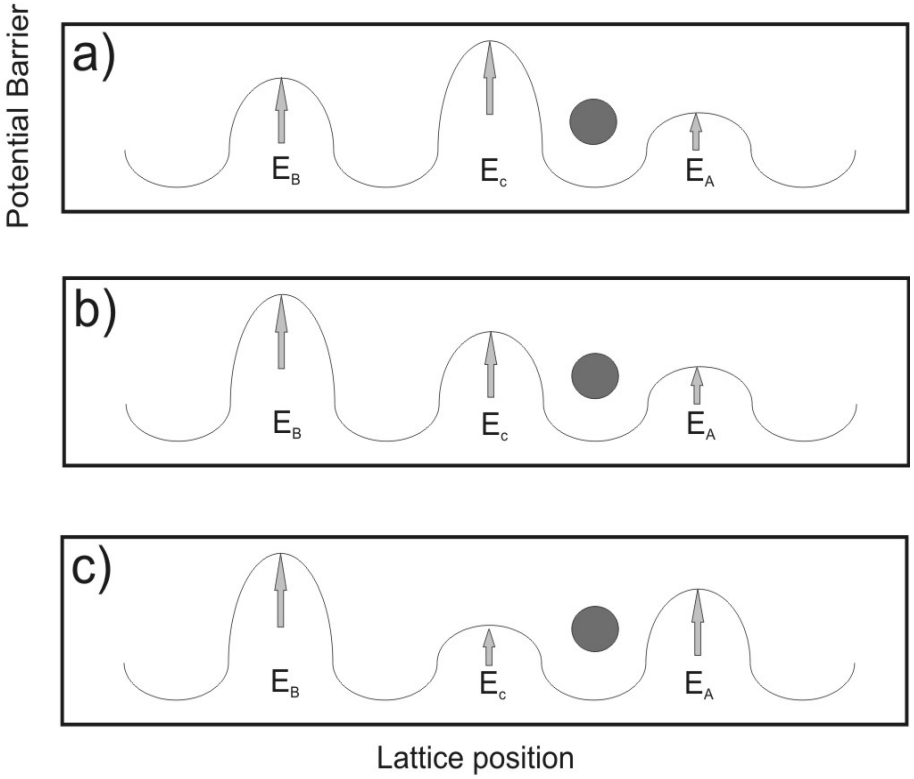

Figure 4.19: An illustration of the potential barrier atoms on the A facet 'see' when attempting to cross onto B facets, for each of the three energy barrier combinations used in Figure 4.18. (a) $E_e^A < E_e^B < E_c$, (b) $E_e^A < E_c < E_e^B$, and (c) $E_c < E_e^A < E_e^B$.

onto the A facet. Hence atoms prefer to remain on the facet they first occupy, although there will be net movement of atoms from the B facet to the A facet. At early growth stages most material arriving at the rod arrives via the step edge, the reflecting barrier therefore promotes nucleation on the A facet, broadening the rod base. Reducing E_c such that $E_e^A < E_c < E_e^B$ (Figure 4.19 (b)) means that atoms on the B facet approaching a corner are directed onto the A facet more efficiently. With $E_c < E_e^A < E_e^B$ (Figure 4.19 (c)) atoms at the corner bounce between the two corner sites, with a slight preference for atoms to diffuse onto the A facet. Hence no matter the relative magnitudes of edge and corner crossing barriers, defining $E_e^A < E_e^B$ increases the adatom density on the A facet, leading to wide rod bases and therefore low ARs.

An interesting observation from the above analysis is that the funneling situation of $E_e^A < E_c < E_e^B$ can be reversed by swapping the values of E_e^A and E_e^B. Simulations for this situation do show a slight increase in rod AR (see Figure 4.20) when the flux is reduced by two orders of magnitude. However, since the limiting process is diffusion on the A facet atoms spend most of their time on the A facet, and the

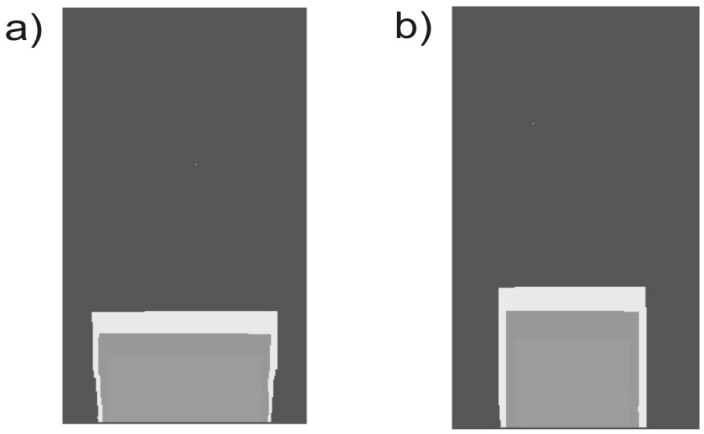

Figure 4.20: Two simulations with energy barriers satisfying $E_e^B < E_c < E_e^A$. In image (a) F=0.18 Å/s and (b) F=0.001 Å/s. The rod shading corresponds to $\theta = 0.15$ ML and 0.2 ML.

favoured morphology has a low AR.

4.4.3 Anisotropic Corner Crossing

In this section anisotropic corner crossing barriers are incorporated into the model, the anisotropy reflecting the bonding strengths of the respective facets. The need for anisotropy in the corner crossing barriers stems from the stronger bonding at the rod tips (see Section 4.1), and the expectation that atoms diffuse off the tips at a slower rate than from rod sides.

Direct detachment events are prohibited by setting $E_D^A = E_D^B = 1.0$ eV. With T=300 K and F within the experimental range of 0.001 Å/s to 0.18 Å/s, simulations were performed for 0.3 eV$< E_c^{A\rightarrow B} <$0.4 eV and 0.40 eV$< E_c^{B\rightarrow A} <$0.5 eV, with the anisotropy $E_c^{A\rightarrow B} < E_c^{B\rightarrow A}$ ($E_c^{A\rightarrow B} = E_c^{B\rightarrow A}$ was considered in the previous Section). To reduce the probability of tip splitting on the short facet, edge diffusion barriers were set at E_e^A =0.3 eV, and E_e^B =0.4 eV, maintaining the edge diffusion anisotropy of Section 4.4.2. Smaller edge diffusion barriers significantly increase simulation run-time.

Figure 4.21 shows rods grown with $E_c^{A\rightarrow B}$ =0.35 eV and $E_c^{B\rightarrow A}$ =0.45 eV, for four different values of flux. Large ARs are observed at low flux, and the rods become progressively shorter as flux is increased. In Figure 4.21 (d) the rod tip forms two branches, the tip-splitting a consequence of the high flux, and the inability of edge atoms to diffuse across the tip between each arrival event. In simulations of larger systems the branches would be expected to widen and split again, resulting in tree-like structures.

Figure 4.22 (a) compares the flux dependence of the model with the flux depen-

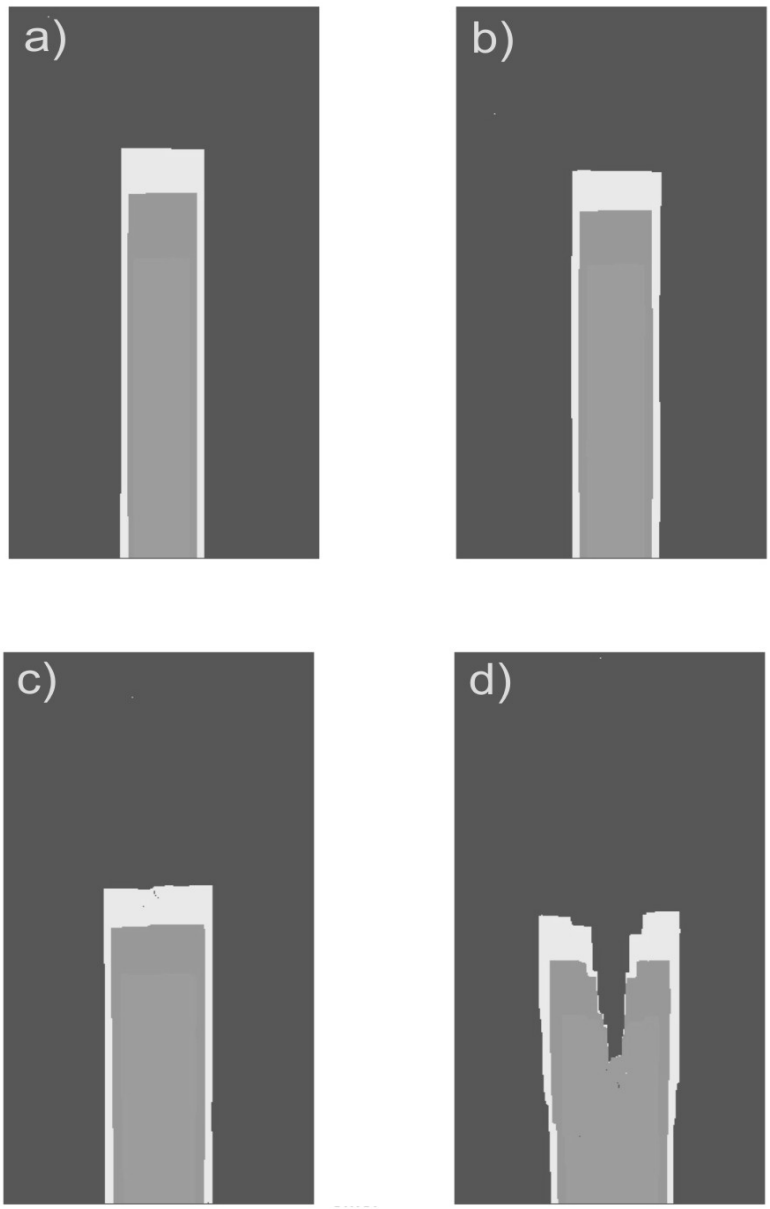

Figure 4.21: Simulation results are presented using anisotropic corner crossing barriers $E_c^{A\to B} = 0.35$ eV and $E_c^{B\to A} = 0.45$ eV. Deposited coverage is 0.2 ML, and for each simulation the flux is (a) 0.001, (b) 0.005, (c) 0.031, and (d) 0.18 Å/s. The rod shading corresponds to $\theta = 0.15$ ML and 0.2 ML.

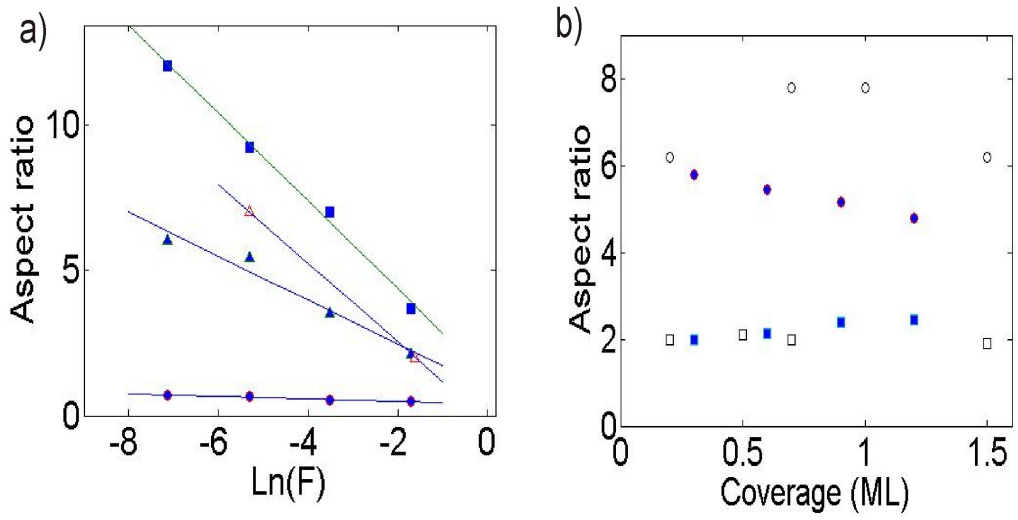

Figure 4.22: (a) Aspect ratios (AR) as a function of material flux for the isotropic corner crossing model with $E_c = 0.4$ eV (filled circles), anisotropic corner crossing model with $E_c^{A\rightarrow B} = 0.35$ and $E_c^{B\rightarrow A} = 0.45$ eV (filled triangles), and experimental results from Figure 6.46 of Ref. [13] (open triangles). Simulated coverage is 0.1 ML, experimental coverage is 0.6 ML. The filled squares are from the anisotropic corner crossing model with $E_c^{A\rightarrow B} = 0.35$ and $E_c^{B\rightarrow A} = 0.5$ eV. (b) AR as a function of surface coverage for the anisotropic corner crossing model F=0.005 Å/s (filled circles) and F=0.18 Å/s (filled squares), with experimental results F=0.005 Å/s (open circles) and F=0.18 Å/s (open squares).

dent experimental results of Scott *et al.* [13] (open triangles), as the flux is increased over two orders of magnitude, and at a constant coverage of 0.1 ML. Rod aspect ratios are plotted on a linear scale while the natural log of the flux is shown on the x-axis. The simulations are for; $E_c^{B\rightarrow A} = 0.45$ eV (filled triangles) and $E_c^{B\rightarrow A} = 0.50$ eV (filled squares), both with $E_c^{A\rightarrow B} = 0.35$ eV. Clearly the higher the anisotropy between the corner crossing barriers the higher the AR, and the steeper the slope.

Figure 4.22 (b) compares the coverage dependence of simulations with $E_c^{B\rightarrow A} = 0.45$ eV (filled symbols) to experimental results (open symbols), for F=0.005 Å/s and 0.18 Å/s. In the real system rod heights are ∼2 nm, corresponding to six atomic layers, therefore we compare experimental data with simulated coverages that are six times lower than is observed experimentally. Simulations at low flux show a slight decrease of mean AR with increasing coverage, but this is a finite system effect due to the elongated rods approaching the top edge of the system at higher coverage. The high flux simulations show a slight increase in AR for higher coverage, due to more severe tip splitting at higher coverage (calculated ARs are considered as upper limits when tip splitting is present). Experimental ARs are roughly independent of coverage.

Figures 4.22 (a) and (b) show the anisotropic corner crossing model can generate high AR rods. The rods remain relatively compact at high coverage and high flux,

but high AR morphologies are preferred at low flux, in agreement with experiments (Figure 6.46 [13]). As shown in Figure 4.22 (a), the greater the anisotropy between the two corner crossing barriers, the greater the rod AR.

Small edge diffusion barriers were required to minimise kinetic effects such as tip splitting. This is consistent with experiment, where the clean rod edges are interpreted as resulting from fast edge diffusion. At the highest flux considered (F=0.18 Å/s) the tip splitting in the simulations is consistent with the kinetically limited morphologies from experiment, where rod branching and 2D morphologies are observed (see Figure 4.4 (a)).

Changing the flux manipulates the interval (τ_{arr}) between each aggregation events. With high flux τ_{arr} is small, and atoms arrive at the rod edges before atoms can diffuse off either A or B facets, leading to isotropic rod morphologies. For low flux τ_{arr} is large, allowing atoms sufficient time to find sites of high coordination (i.e. kink sites), and generally more compact structures (see Figure 4.17).

Further simulations (presented later in Section 4.5) show that anisotropic edge diffusion barriers are not essential for generating rods, i.e. setting $E_e^A = E_e^B = 0.3$ eV, anisotropically shaped rods can be produced as long as the corner crossing barriers satisfy $E_c^{A\rightarrow B} < E_c^{B\rightarrow A}$.

4.4.4 Anisotropic Detachment

This section investigates the production of elongated structures using anisotropic rates of atom detachment from the A and B facets. Again, the need for anisotropic detachment barriers stems from the expectation of stronger bonding at the rod tips (Section 4.1).

For these attachment/detachment simulations, corner crossing events are prohibited by setting $E_c^{A\rightarrow B} = E_c^{B\rightarrow A} = 1$ eV, while the anisotropic edge diffusion barriers ($E_A = 0.3$ eV, and $E_B = 0.4$ eV) used in Sections 4.4.2 and 4.4.3 are maintained. With T=300 K and flux between F=0.001 Å/s and 0.18 Å/s, simulations were run with detachment energy barriers ranging from 0.35 eV to 0.8 eV, and an anisotropy $E_D^A \leq E_D^B$ (Figure 4.16). Simulations for the detachment model typically require more iterations than the corner crossing model due to the indirect way in which atoms are transported between facets.

Simulated rods are shown in Figure 4.23, for E_D^A =0.45 eV and E_D^B =0.6 eV, and four different values of flux. With F=0.001 Å/s the rods have AR ∼5, and as the flux is increased the rods become shorter. Note that tip splitting appears in Figure 4.23 (c), at a lower flux than the corner crossing simulations in Figure 4.22, even though

the edge diffusion barriers are the same.

Figure 4.24 displays the (a) flux (coverage is 0.1 ML) and (b) coverage dependence of rod ARs simulated using the detachment model, plotted alongside experimental results. The filled triangles of Figure 4.24 (a) are from simulations with $E_D^A = 0.45$ eV and $E_D^B = 0.6$ eV, i.e. an anisotropy of 0.15 eV. The slope of the simulated data is comparable to the experiment [13] (open triangles).

In Figure 4.24 (b), simulated rods grown at F=0.001 Å/s (filled triangles) and F=0.005 Å/s (filled circles) show a slight reduction in AR with coverage, while simulated ARs at F=0.18 Å/s (filled squares) increase slightly, due to tip splitting (see Figure 4.23 (d)). The lack of an AR coverage dependence for simulations with F=0.001 Å/s or F=0.005 Å/s is consistent with experiment.

Clearly the detachment model can generate high AR rods. At low flux, high ARs are preferred, while kinetically limited shapes are more common at high flux. Since the detachment model requires large simulation times, the detachment barriers are relatively high (to allow fewer detachment events) compared to the barriers used in the anisotropic corner crossing simulations (compare $E_D^A = 0.45$ eV and $E_D^B = 0.6$ eV of Figure 4.24 with $E_c^{A\rightarrow B} = 0.35$ eV and $E_c^{B\rightarrow A} = 0.45$ eV of Figure 4.22). Direct comparisons between the two models is not possible (since they use different energy barriers), however an interesting point is the matching slopes of simulation and experimental data, in both Figures 4.22 (a) and 4.24 (a), when the anisotropy $E_c^{B\rightarrow A} - E_c^{A\rightarrow B}$ and $E_D^B - E_D^A$ both equal 0.15 eV.

For the attachment/detachment model, anisotropic structures only form if atoms detaching from a facet of weak bonding diffuse to a facet of stronger bonding i.e. the detachment-attachment process is mediated by terrace diffusion. For late growth stages, when simulated rods have long A facets and short B facets, atoms detaching from an A facet will most likely reattach to the A facet. Hence to generate large AR aggregates, the energy barrier for detachment must be small enough that many detachment-attachment steps occur between each arrival event. Figures 4.24 (a) and (b) illustrate the point, since lowering the flux increases the length of time between arrival events, and there is a correlated increase in rod AR.

4.4.5 Summary

The flux dependence of rod morphologies grown via three different models has been discussed. The results found that anisotropic edge diffusion cannot reproduce experimentally observed structures, with or without isotropic corner crossing. Both the anisotropic corner crossing and the anisotropic attachment/ detachment models

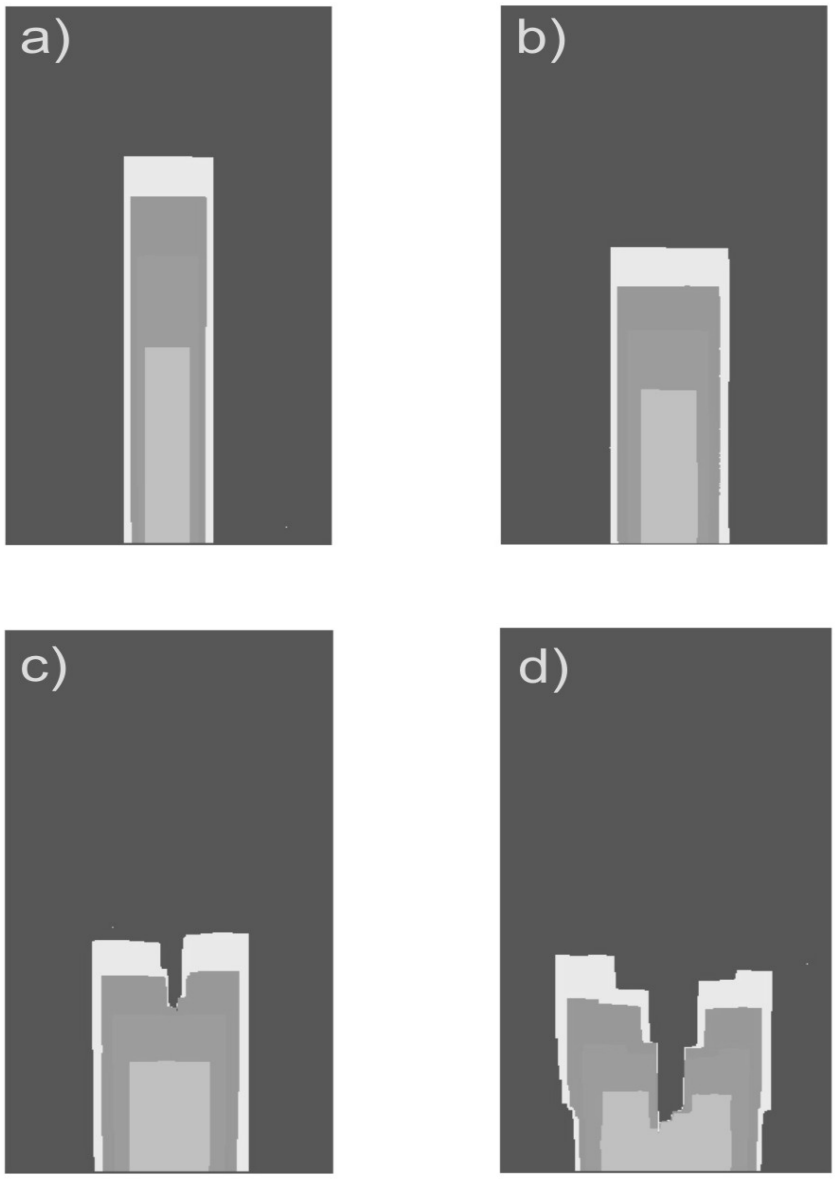

Figure 4.23: Four simulation results using anisotropic detachment barriers $E_d^A = 0.45$ eV and $E_d^B = 0.60$ eV. Deposited coverage is 0.2 ML, and for each simulation the flux is (a) 0.001, (b) 0.005, (c) 0.030, and (d) 0.18 Å/s. The rod shading corresponds to $\theta = 0.05$ ML, 0.15 ML, and 0.2 ML.

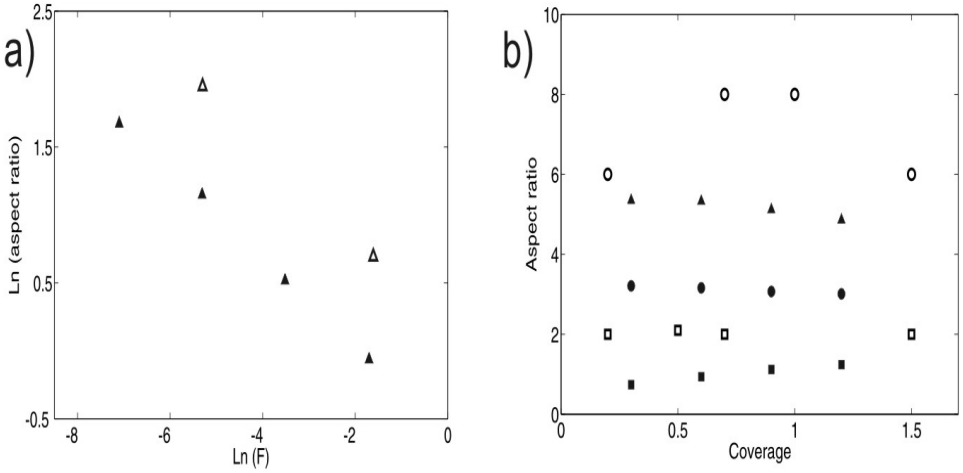

Figure 4.24: (a) Aspect ratios (AR) as a function of flux for the anisotropic detachment model with $E_d^A = 0.45$ eV and $E_d^B = 0.60$ eV (filled triangles) and experimental results from Figure 6.46 of Ref. [13] (open triangles). Simulated coverage is 0.1 ML, experimental coverage is 0.6 ML. (b) AR as a function of surface coverage for the anisotropic detachment model using F=0.001 Å/s (filled triangles), F=0.005 Å/s (filled circles), and F=0.18 Å/s (filled squares), with experimental results F=0.005 Å/s (open circles), and F=0.18 Å/s (open squares).

reproduced experimental morphologies and ARs, and could yield the experimental flux dependence of the AR with the appropriate choice of diffusion energy barriers.

The simulation results of this Section were not compared with the model in Section 4.2 (Equation 4.1), since the relative contributions of both the flux and temperature need to be considered. In the next Section the temperature dependence of simulated rod ARs is investigated, and the results compared with the model in Section 4.2.

4.5 Temperature Dependence of Multiple Rods

In this section the temperature dependence of rod ARs is investigated, for both the anisotropic corner crossing and attachment/detachment models, in order to compare with the temperature dependence observed in experiments. Modifications to the rod simulations are discussed, then results from the two models presented. The coalescence of rods for both models is also investigated.

According to Heyn [62], if mean ARs increase with increasing temperature, it suggests detachment from short edges is relatively inactive. ARs in the experiments of Section 4.1 increase with temperature, suggesting atoms on rod tips are irreversibly attached. To simplify the simulations for both models, in this set of simulations diffusion off the B facet via corner crossing or detachment events is prohibited by setting $E_c^{B\rightarrow A} = E_D^B = 2$ eV (this effectively sets R_2 of Equation 4.1 to zero).

The aim of this Section is to test whether rod ARs obey the relation of Equation 4.3, found by Heyn [62] for anisotropic islands using the attachment/detachment model. Assuming Equation 4.3 (see Section 4.2), the temperature and flux dependent contributions to the rod ARs can be separated i.e.

$$\ln \langle AR \rangle \cong \ln(\frac{R_0}{F})^{\chi} - \chi \frac{E}{k_B T}. \tag{4.4}$$

Here E is the energy barrier preventing an atom leaving a facet, R_0 is some attempt frequency (we have combined the parameter c from Equation 4.3 with R_0), F is the flux, and the exponent χ is to be determined. An Arrhenius analysis of the rods is performed by plotting ln(AR) against $\frac{1}{T}$. If Equation 4.4 is accurate, the analysis should produce an activation energy $E_A = \chi E$, and a fitted prefactor $\nu = \chi \ln(\frac{R_0}{F})$.

4.5.1 Modifications to the Single Rod Simulations

Statistics for the AR data were improved by using a system with two step edges, and by increasing the number of rod seeds to 6 on each step. The system size is 400 by 400 sites. For 0.1 ML and a rod density of 0.015 nuclei per step site, each rod contains ≈1300 atoms. The seed density is higher than for single rod simulations (where the density was 0.003 nuclei per site), and individual capture regions have AR∼6, therefore material arrives more slowly at each rod. Hence the ARs here are not directly comparable to results presented in Section 4.4, though the algorithms remain the same.

As was found in Section 4.4.3, anisotropy in the edge diffusion barriers is not required for anisotropic growth, therefore we set $E_e^A = E_e^B = E_e = 0.30$ eV. From

Section 4.1 we expect atoms are more strongly attached to rod tips than at the sides. There is experimental and theoretical evidence from fcc(001) surfaces that atomic diffusion coefficients are not necessarily proportional to the energy which binds an atom to a particular site [105, 121, 122, 71]. For instance, atoms at island edges on a fcc(001) plane have smaller diffusion barriers than atoms diffusing on a fcc(001) terrace, though the barrier for an atom to detach from an island edge onto the terrace *is* larger than the edge diffusion barrier. Clearly diffusion from strongly bonded sites to other strongly bonded sites is not necessarily slower than diffusion between sites of weak bonding. However atoms diffusing from strongly bonded sites to weakly bonded sites are likely to face a large barrier. We also set $E_t = E_s = 0.01$ eV, slightly reduced from the previous Section, to reduce potential contributions to E_A.

One advantage of having multiple steps is that rods can grow into the terrace from opposite directions, as in the experiment (see Figure 4.4). This allows an investigation of rod coalescence for the corner-crossing and detachment models (see Section 4.6), using a geometry with extra step edges.

4.5.2 Anisotropic Corner Crossing

First we study multiple rod growth with anisotropic corner crossing barriers. Setting $E_D^A = 2$ eV to eliminate detachment altogether, the remaining simulation variables are temperature, flux, and $E_c^{A\rightarrow B}$.

Simulation results are shown in Figure 4.25 with $E_c^{A\rightarrow B} = 0.45$ eV, for (a) T=280 K, and (b) T=400 K. Square morphologies are favoured in Figure 4.25 (a), while the higher temperature for (b) promotes rods with higher ARs.

At T=280 K the arrival time of atoms to each rod is likely comparable to the time spent on the A facet (the sides of the rods), and consequently rods have ARs close to one. Rod ARs increase in Figure 4.25 (b) relative to (a) because of the higher frequency of A→B corner crossing events at T=400 K, and the shorter periods each atom spends on A facets. The increase in rod AR with temperature is consistent with experiment.

Figure 4.26 shows the temperature dependence of the rod ARs, with $E_c^{A\rightarrow B} = 0.45$ eV, for F=1.0 ML/s (squares) and F=0.01 ML/s (triangles). For each set of conditions (F, and T), 10 different simulations are produced, to account for competitive capture affects in the rod growth. The mean rod AR is measured from each simulation. Each data point in Figure 4.26 represents the mean of the 10 different simulation results. The error bars about each point in Figure 4.26 represent the

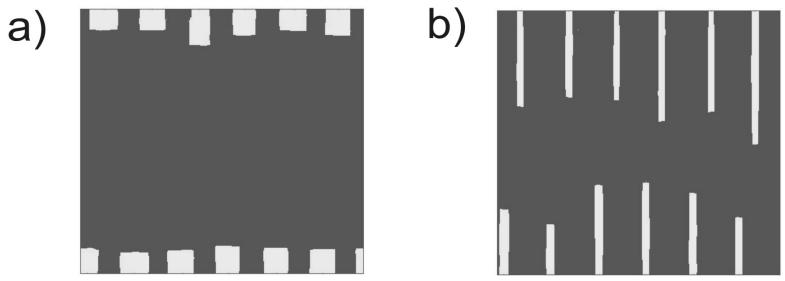

Figure 4.25: Rod growth for the anisotropic corner crossing model with $E_c^{A\rightarrow B} = 0.45$ eV, F=1.0 ML/s, $\theta = 0.1$ ML and (a) T=280 K (b) T=400 K.

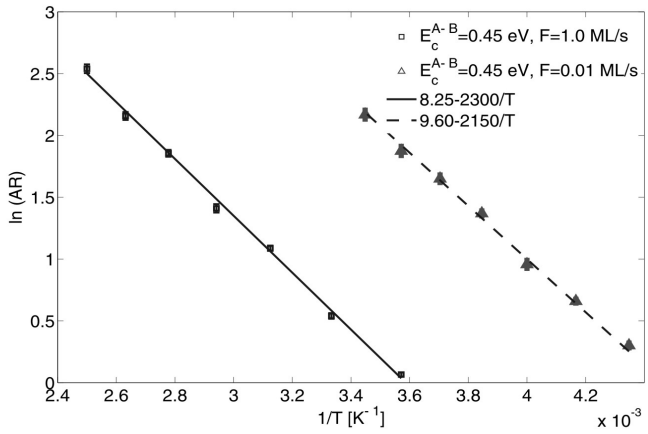

Figure 4.26: Temperature dependence of rod dimensions with $E_c^{A\rightarrow B} = 0.45$ eV, with $\theta = 0.1$ ML, for F=1.0 ML/s (squares) and F=0.01 ML/s (triangles). An Arrhenius analysis is used to fit the data. The error bars for each data point are a similar size to the symbols.

standard error of the 10 simulation results. Note that the low flux simulations are performed at lower temperatures, so the rod ARs span a similar range to the high F, high T simulations.

The data sets are fitted assuming an Arrhenius dependence. The activation energies in Figure 4.26 are 0.20±0.01 eV for F=1.0 ML/s, and 0.19±0.01 eV for F=0.01 ML/s. The errors were calculated using line of best and worst fit. From Equation 4.4, the activation energy is related to the corner crossing barrier via $E_A = \chi E_c$. For the activation energies measured in Figure 4.26 we calculate $\chi \sim \frac{0.20}{0.45} = 0.44 \pm 0.02$. Heyn [62] found $\chi = 1/3$ for islands grown via the attachment/detachment model.

Within experimental uncertainties, the F=0.01 ML/s and F=1.0 ML/s data are fitted with equal activation energies. Unfortunately the different activation energies for each parameter set plotted in Figure 4.26 means χ cannot be solved for using simultaneous equations. However, assuming $R_0 = 10^8$ s^{-1} (determined later in Section 4.5.3), and using the relationship $\chi = \frac{\nu}{\ln(R_0/F)}$ (see Equation 4.4), the fit prefactors from Figure 4.26 can be used to estimate χ. With $\nu = 9.60 \pm 0.05$ when

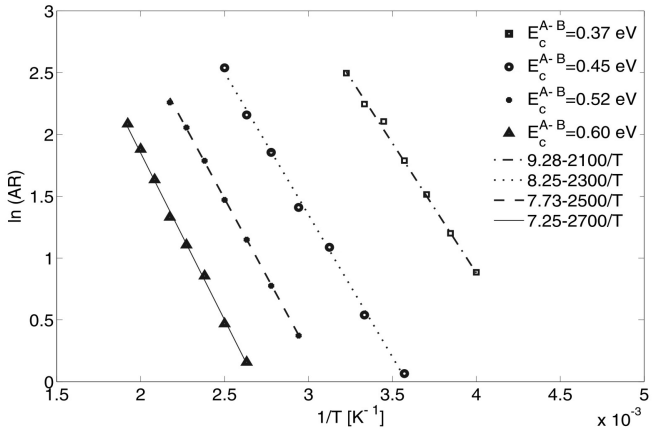

Figure 4.27: Temperature dependence of the mean rod AR as the corner crossing barrier is varied. The standard parameters are F=1.0 ML/s, and a coverage of 0.1 ML. $E_c^{A\rightarrow B} = 0.37$ eV (squares), $E_c^{A\rightarrow B} = 0.45$ eV (circles), $E_c^{A\rightarrow B} = 0.52$ eV (dots), $E_c^{A\rightarrow B} = 0.60$ eV (triangles). The error bars are the same size as the symbols.

F=0.01 ML/s, $\chi = 0.45$. With $\nu = 8.25 \pm 0.05$ when F=1.0 ML/s, $\chi = 0.44$. These values are consistent with $\chi = 0.44 \pm 0.02$ calculated by comparing the activation energy and corner crossing barrier.

To further investigate the temperature dependence of the corner crossing model, simulations were performed with corner crossing barriers of $E_c^{A\rightarrow B} = 0.37$ eV, $E_c^{A\rightarrow B} = 0.52$ eV, and $E_c^{A\rightarrow B} = 0.60$ eV. Figure 4.27 presents the temperature dependence of rod ARs for simulations with $E_c^{A\rightarrow B} = 0.37$ eV (squares), 0.45 eV (circles), 0.52 eV (dots), and 0.60 eV (triangles).

Activation energies are fitted to each new data set, and we find $E_A = 0.18 \pm 0.01$ eV when $E_c^{A\rightarrow B} = 0.37$ eV, $E_A = 0.22 \pm 0.01$ eV when $E_c^{A\rightarrow B} = 0.52$ eV, and $E_A = 0.23 \pm 0.01$ eV when $E_c^{A\rightarrow B} = 0.60$ eV. Determining χ for each combination we have $\chi_{E_c^{A\rightarrow B}=0.37} = 0.49 \pm 0.02$, $\chi_{E_c^{A\rightarrow B}=0.45} = 0.44 \pm 0.02$, $\chi_{E_c^{A\rightarrow B}=0.52} = 0.41 \pm 0.02$, $\chi_{E_c^{A\rightarrow B}=0.60} = 0.39 \pm 0.02$. The parameter χ consistently decreases as the corner crossing barrier increases, and is clearly not constant across each set of simulation parameters as suggested by Heyn [62].

In summary, rod growth for the anisotropic corner crossing model has a similar temperature dependence to the experiments. For each parameter set in Figures 4.26 and 4.27, the ARs increase via a constant activation energy. However the relationship between the corner crossing barrier $E_c^{A\rightarrow B}$ and the activation energy E_A (as predicted by Equation 4.4) is not constant, as the scaling parameter χ is found to increase from 0.39±0.02 to 0.49±0.02, as $E_c^{A\rightarrow B}$ is decreased from 0.60 eV to 0.37 eV. Recalling Heyn [62] found $\chi = \frac{1}{3}$ using an attachment/detachment model, the next Section investigates the temperature dependence of rod ARs using the same growth

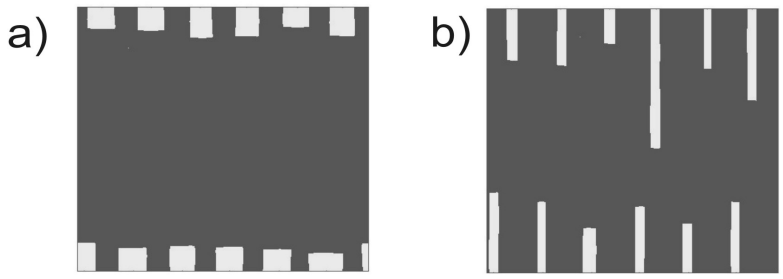

Figure 4.28: Rod growth for the anisotropic detachment model with $E_D^A = 0.45$ eV, F=1.0 ML/s, and $\theta = 0.1$ ML for (a) T=280 K, and (b) T=400 K.

mechanism.

4.5.3 Anisotropic Detachment

In this section the temperature dependence of rod ARs are investigated using the detachment model. Barriers are set at $E_c = E_D^B = 2$ eV, forbidding detachment from the B facet, and forbidding corner crossing events. Diffusion off the A facet occurs via the detachment barrier, E_D^A.

Figure 4.28 shows representative simulation results with F=1.0 ML/s and $\theta = 0.1$ ML, for (a) T=280 K, (b) and T=400 K, both with $E_D^A = 0.45$ eV. In Figure 4.28 (a) the rods have low ARs, while in (b) the ARs are larger because the elevated temperature of T=400 K allows atoms on the A facet to overcome the detachment barrier more frequently. The net result is a greater amount of material diffusing onto the B facet, from which atoms cannot leave.

Figure 4.29 shows the temperature dependence of the rod ARs, with $E_d^A = 0.45$ eV, for F=1.0 ML/s (squares) and F=0.01 ML/s (triangles). The activation energies in Figure 4.29 are 0.19±0.01 eV when F=1.0 ML/s or F=0.01 ML/s. Using Equation 4.4, the activation energies are compared with the detachment barrier to calculate $\chi \sim \frac{0.19}{0.45} = 0.43 \pm 0.02$.

In Figure 4.29, the fitted prefactor when F=0.01 ML/s is ν=9.90±0.05, compared with ν=7.95±0.05 when F=1.0 ML/s. Since the activation energies for the F=0.01 ML/s and F=1.0 ML/s data sets are equal, it directly follows from Equation 4.4 that $\nu_{F=0.01} - \nu_{F=1.0} = \chi \ln(\frac{1.0}{0.01})$, which allows an estimate of $\chi = \frac{1.95}{4.6} = 0.42 \pm 0.02$. Selecting ν=9.90±0.05 when F=0.01 ML/s, and $\chi = 0.42 \pm 0.02$, by substituting the values into $\nu = \chi \ln(\frac{R_0}{F})$ we find $R_0 \approx 10^8$ s^{-1}.

To further investigate the temperature dependence of the detachment model, simulations were performed with detachment barriers of $E_d^A = 0.37$ eV, $E_d^A = 0.52$ eV, and $E_d^A = 0.60$ eV. Figure 4.30 presents the temperature dependence of the ARs

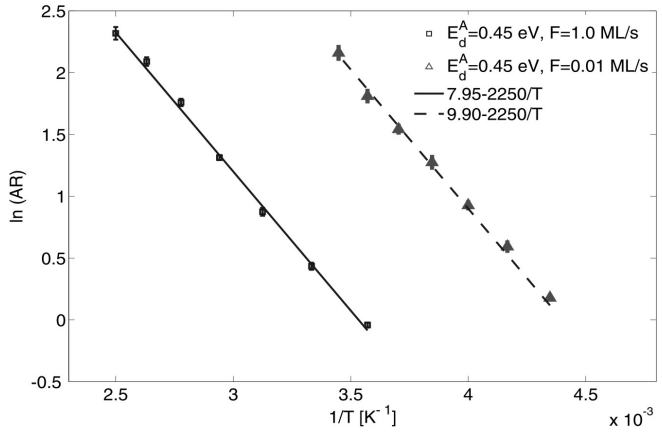

Figure 4.29: Temperature dependence of rod ARs with $E_d^A = 0.45$ eV, with $\theta = 0.1$ ML, for F=1.0 ML/s (squares) and F=0.01 ML/s (triangles). The error bars are the same size as the symbols.

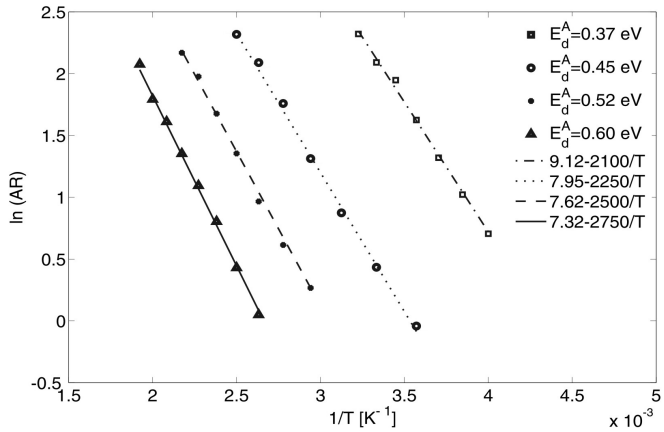

Figure 4.30: Temperature dependence of the mean rod AR as the detachment barrier is varied. The standard parameters are F=1.0 ML/s, and $\theta = 0.1$ ML. $E_d^A = 0.37$ eV (squares), $E_d^A = 0.45$ eV (circles), $E_d^A = 0.52$ eV (dots), $E_d^A = 0.60$ eV (triangles). The error bars are the same size as the symbols.

for simulations with $E_d^A = 0.37$ eV (squares), 0.45 eV (circles), 0.52 eV (dots), and 0.60 eV (triangles).

Activation energies for the additional data sets are $E_A = 0.18 \pm 0.01$ eV when $E_d^A = 0.37$ eV, $E_A = 0.22 \pm 0.01$ eV when $E_d^A = 0.52$ eV, and $E_A = 0.24 \pm 0.01$ eV when $E_d^A = 0.60$ eV. Determining χ for each combination we have $\chi_{E_d^A=0.37} = 0.49 \pm 0.02$, $\chi_{E_d^A=0.45} = 0.43 \pm 0.02$, $\chi_{E_d^A=0.52} = 0.41 \pm 0.02$, and $\chi_{E_d^A=0.60} = 0.40 \pm 0.02$. The parameter χ consistently decreases as the detachment barrier increases, and is clearly not constant across each set of simulation parameters as suggested by Heyn [62].

The attachment/detachment model has a similar temperature dependence to the experiments, i.e. higher AR structures are favoured as temperature is increased.

Again the flux and temperature dependences of rod ARs are described by Equation 4.4. Interestingly, E_A does not have a consistent relationship to E_d^A, as found by Heyn [62] for anisotropic islands growing via the same mechanism. We find the scaling parameter χ decreases as the magnitude of E_d^A increases, ranging from 0.49 ± 0.02 to 0.40 ± 0.02.

4.5.4 Summary

Rods grown by both the anisotropic corner crossing and attachment/detachment models exhibit the same temperature dependence of the AR as experiments. An interesting result is that the simulation results from each model (shown in Figures 4.25 and 4.28) are essentially the same. There is also agreement in the activation energies measured for either model, when the energy barriers limiting diffusion off the A facets are equivalent. Simulation results from either model are virtually indistinguishable for equivalent parameter sets.

Results plotted in Figures 4.26 and 4.29 found the activation energies for both models are independent of the flux, consistent with Equation 4.4. Using Equation 4.4, we find the prefactors and temperature dependent terms are both modified by the same scaling parameter χ. For both the anisotropic corner crossing and attachment/detachment models, the scaling parameter χ of Equation 4.4 is found to decrease as the effective detachment barrier increases. Our results indicate the activation energy is related to the effective detachment barrier via a factor χ, which ranges from $\sim 1/2$ when barriers to edge diffusion and effective detachment are similar, to $\sim 1/3$ when elongation is strongly limited by the effective detachment barrier.

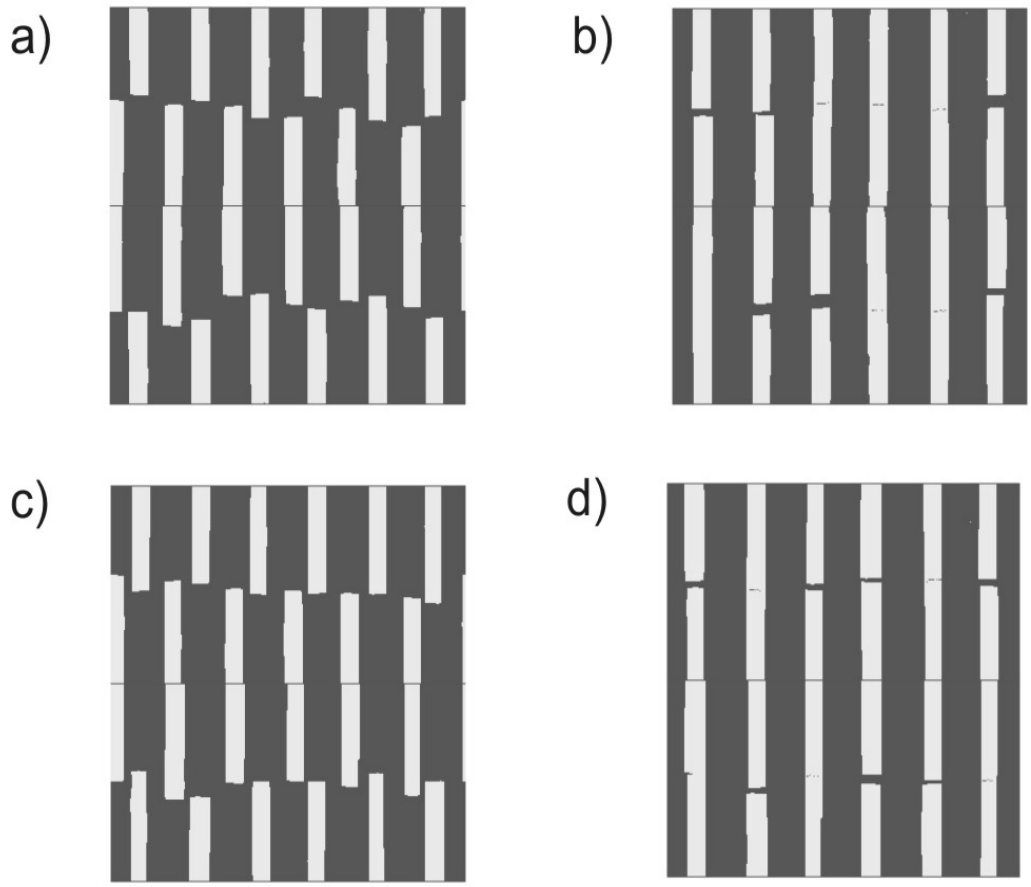

Figure 4.31: Depiction of rod coalescence at 0.3 ML for the (a) and (b) anisotropic corner crossing, and (c) and (d) anisotropic detachment models. The left-hand column contains simulations results when rods are seeded at intervals out of step with seeds on the opposing step. Rods in the right-hand column are seeded directly across from seeds on the opposite step.

4.6 Rod coalescence

By increasing coverage to 0.3 ML, and two extra step edges, for the simulations presented in Sections 4.5.2 and 4.5.3, rod coalescence can be investigated for the corner crossing and detachment models. The edge diffusion energy barrier is set at 0.30 eV to encourage high aspect ratio structures. Figures 4.31 (a) and (b) display results for the corner crossing model ($E_c = 0.45$ eV). Figures 4.31 (c) and (d) are results for the detachment model ($E_D = 0.45$ eV). In Figures 4.31 (a) and (c) the rod nuclei on opposing steps are offset from one another, illustrating the typical rod lengths when there is no possibility of coalescence. Nuclei in Figures 4.31 (b) and (d) are situated directly opposite one another to encourage rod coalescence.

Figure 4.31 (a) illustrates that six pairs (a pair being rods on opposite steps) of rods have growth fronts which extend *past* the tip of their pair, i.e. if the rods were shifted to lie directly in line 6 rod pairs would coalesce. In Figure 4.31 (b),

where rods are seeded opposite their pair, 6 pairs have coalesced, in agreement with the statistics determined from image (a). So for the corner crossing model, the growth rate of the rod tip does not change when in close proximity to another tip, i.e. competitive capture is not significant at the tip.

Figure 4.31 (c), produced using the detachment model, shows every rod growing past the tip of their pair, i.e. if the twelve rods nucleating on the middle step were shifted to the right, then every pair would overlap. In image (d), where rods are seeded opposite their pair, over half of the rods are still separated by a gap at 0.3 ML. The slightly fatter rods of image (d), and the presence of gaps, suggests the tips of rods grown via the detachment model grow more slowly at small tip separations.

Rods grown via a corner crossing mechanism do not exhibit competitive capture at the tip, since material attaching to the A facet is transported via a direct path onto the B facet. The detachment/attachment model however clearly exhibits competitive capture, since atoms have difficulty terrace diffusing into the small region separating the rod tips.

Comparing the simulation results with experiment (shown in Figure 4.3), the detachment model (Figures 4.31 (c) and (d)) appears to be a better candidate for the experimental system. Rods grown via the corner crossing model do not appear to slow when nearing other aggregates. Rods grown via experiment show obvious competitive capture when nearing other objects (Figure 4.3), though coalescence does occur. In Figure 4.31 (d) half the rod pairs have coalesced, therefore coalescence is merely slowed within the detachment model, not prohibited.

A useful extension to the work would be to generate similar rod coalescence statistics from experiments. By comparing ARs from rods growing in clean regions with ARs measured from rods which compete for material, the reduction in mean ARs due to competitive capture may be calculated.

4.7 Summary of Rod Growth

Experimental Results

Bismuth rods develop high AR structures at high temperature and low flux. Previous room temperature growth found rod ARs increasing from 2 to 7 when flux is reduced from F=0.2 Å/s to 0.005 Å/s [13, 60]. Temperature dependent experiments presented in Section 4.1.2 with F=0.01 Å/s, show mean ARs increase from AR=8.5 at T=303 K to 12 at T=333 K. The rod ARs displayed an Arrhenius dependence, fitted with an activation energy of -0.10 eV and $\nu = 6.1$. With F=0.14 Å/s, a transition from 2D planar growth at T=308 K to 1D rods at T=353 K is

found (Figure 4.4). The morphology transition with raised temperature confirms the 2D crystals are a kinetically limited state.

The anisotropic rod morphology is believed to result from an anisotropy in the bonding on different rod facets. Crystallographic studies support this, the alignment of rods with the Bi$\langle 11\bar{2}0\rangle$ direction creating broken interlayer bonds along the rod sides (relatively weak), and broken intra-layer bonds at the tips (relatively strong). The expected higher surface energy of the short facet favours anisotropically shaped structures at equilibrium.

The effects of rod density, terrace size, and competitive capture on rod AR are difficult to quantify experimentally. Measurements of rods from closely spaced step edges were found to have smaller ARs than rods measured from large terraces. To reduce the variation between sample sets, an effort was made to find terraces of comparable size within each image, but some variation cannot be avoided, especially for the low coverage samples shown in Figure 4.8 (a).

Simulation Results

Section 4.4 found anisotropic edge diffusion barriers were not sufficient to create single, high AR rods. Instead, without material transport between facets, rods consistently had wide bases and multiple branches. Even with isotropic material transport (via an isotropic corner crossing barrier), high AR rods could not be grown using anisotropic edge diffusion barriers. The experimental results were instead reproduced by simulations using either anisotropic corner crossing, or anisotropic detachment barriers (with the appropriate parameter set).

In Section 4.5 an Arrhenius investigation of the anisotropic corner crossing and detachment models was performed with diffusion off the B facet forbidden. Mean rod ARs were found to have a temperature dependence matching an activation energy of $E_A = \chi E_c^{A\rightarrow B}$, or $E_A = \chi E_D^A$, for either model. Mean ARs were also found to scale $\propto (\frac{1}{F})^{\chi}$. For either model, the parameter χ was found to range between $\sim 1/2$ and $\sim 1/3$, as the effective detachment barrier off the rod sides was increased. Therefore Equation 4.4 does describe the temperature and flux dependence of rod ARs for both models, though the parameter χ needs to be determined for unique combinations of energy barriers.

Comparison with Experiment

With a range of values determined for χ, we can apply Equation 4.4 to the rod temperature dependence found experimentally (Section 4.1), to estimate a detachment barrier from the sides of Bi rods. An activation energy $E_A = 0.10$ eV was measured from Figure 4.12 (c), the detachment barrier then ranging between

$E = 0.2, 0.30$ eV. Considering that atom detachment from Bi rod sides requires the breaking of relatively weak *inter*-layer Bi bonds (recall energy of formation of 2 eV for bulk Bi), the $0.2 - 0.3$ eV range agrees with the expected weak bonding.

The growth of rods via the corner crossing mechanism did not slow in the presence of an oppositely seeded rod. Rods grown using the attachment/detachment model did react due to the difficulty in transporting atoms onto the tip. Bi rods grown experimentally provide clear examples of competitive capture, which suggests they develop via the attachment/detachment mechanism.

Chapter 5

KMC Modelling of Cluster Coalescence

In addition to modelling 2D film growth, a portion of work was undertaken to help understand the coalescence of atomic clusters. This particular topic has relevance within the cluster research group, where processes which modify clusters post-deposition have consequences for device conductance and long term stability. The versatility of the KMC coding method allows for simulations of 3D systems as easily as it does for 2D situations, as long as lattice-based Brownian motion is expected to be the dominant diffusion process. In reality this means the application is limited to crystalline systems kept below their melting temperature. This chapter describes an investigation of FCC clusters coalescing via surface diffusion.

5.1 Overview of Literature

Coalescence has been a thoroughly studied field through history due to its importance in numerous situations, from the natural (droplet formation in clouds) to the more applied (sintering of particles for new materials). Coalescence via diffusion occurs by three mass transport modes [123]; surface diffusion, hydrodynamic flow, or volume diffusion. Each has its own area of relevance. Below the bulk melting temperature, and for particles less than 1μm in size, the dominant mass transport mechanism is expected to be surface diffusion [124]. The influences of cluster size and temperature are not yet entirely understood and so, using an atomistic method, we investigate the coalescence of nanoscale objects (termed clusters) via surface diffusion.

The coalescence of two spherical particles via surface diffusion was investigated during the 1960's by Mullins and Nichols [124, 125, 126]. This work predicted

velocities of surface normals, and provided estimations of coalescence times,

$$\tau_{\mathrm{eq}} \approx \mathrm{L}^4, \tag{5.1}$$

(where L is the linear dimension), as well as time dependences for the neck radius $\mathrm{r} \propto \mathrm{t}^{\frac{1}{6}}$. The calculations assumed isotropic surface tension and isotropic surface diffusion. These assumptions are most applicable to liquid droplets, which have continuously curved surfaces and isotropic surface tension.

Numerically and theoretically, the coalescence problem is difficult to solve [127]. Prior to the work of Mullins, solutions by Kuczynski [123] predicted the neck radius developing as $\mathrm{r} \propto \mathrm{t}^{\frac{1}{7}}$. The paper of Eggers [127] reproduces this result, at least for small neck radii, before trending to the $\mathrm{t}^{\frac{1}{6}}$ result of Nichols, while also discovering the formation of voids during the coalescence. The model of Eggers assumes isotropic surface diffusion, consistent with the models of Kuczynski and Nichols.

Coalescence of Nanoparticles

Nanoparticle coalescence has been studied using molecular dynamics (MD) simulations by Lewis *et al.* [128]. In their work, Au clusters of roughly 1000 atoms were modeled coalescing at temperatures of 800 K for three coalescence cases: liquid-liquid, liquid-solid, and solid-solid. They found relaxation times for the liquid-solid and solid-solid scenarios were substantially increased from times predicted using the macroscopic sintering theories of Nichols [126]. Although the neck radius initially evolves much faster than the predicted $\mathrm{t}^{1/6}$ because of elastic and plastic deformations not included in earlier numerical studies [123, 126, 127], it slows down at long times due to the presence of facets. Using MD simulations, Lummen and Kraska [129] determine a three-step coalescence process for colliding metal clusters. The first stage occurs very quickly and is related to the initial neck formation at the point of contact of the particles. This quickly transforms the clusters into a dumbell shape, which evolves more slowly during the next stage into an ovoid. The final transformation from an ovoid into a sphere is the longest, as the driving force, the difference in surface energy of the two configurations, is very small. For solid clusters, the dumbell→ovoid→sphere phases occur via diffusion of atoms on the cluster surface.

Coalescence kinetics of free and supported metal clusters have been studied by Tian [130] *et al.* using kinetic Monte Carlo techniques and diffusion barriers calculated using a Lennard-Jones type potential. In this work, cluster sizes ranged up to 39-atoms, and the dependence of the final cluster morphology on temperature was analysed. Above a determined coalescence temperature $\mathrm{T_c}$, cluster aggregates were

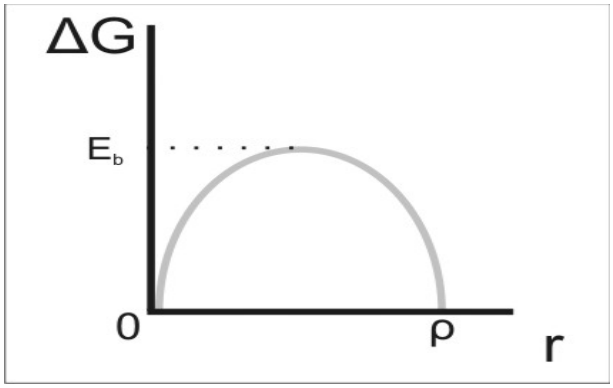

Figure 5.1: Free energy function for a crystal at equilibrium, showing the energy barrier for transferring a nucleus of radius ρ from one facet to another.

found to relax to the most stable structure, however below T_c clusters relaxed to a metastable structure. T_c was found to increase for metal elements with greater binding strengths.

Relaxation of Nanoparticles

Investigations of nanoparticle relaxation has become a topic of current interest [68, 131], due to the increased interest in nanometre sized particles. Nanoparticles can form compact structures with surfaces terminated by large facets, invalidating the assumptions of continuous curvature used in the theories of Nichols and Mullins. For faceted objects to achieve more thermodynamically favourable shapes (i.e. more spherical in appearance), the nucleation of new facets or 'germs' on existing facets is required. Using kinetic Monte Carlo (KMC) simulations, Combe *et al.* [68] investigated the equilibration of three dimensional crystallites as a function of size and temperature. Below the roughening temperature, they show relaxation is governed by the timescale of nucleation of new germs on a facet. Mullins [131] arrives at similar conclusions regarding the nucleation barrier on faceted nanoparticles, when the driving force for relaxation is the reduction of surface energy. Their work estimates the maximum facet size on which nucleation is appreciable to be $\approx$ 1 nm.

Repeating the formula (Equation 1.5) for the change in free energy when nucleating a germ of atomic height is [68, 131, 34],

$$\Delta G = [2\pi r\gamma - \pi r^2 \Delta\mu]a \tag{5.2}$$

where r is the germ radius, γ the line tension, a is the atomic layer height, and μ the chemical potential difference for an atom going from the surface to the germ. A depiction of the free energy curve is shown in Figure 5.1 as a function of germ

radius, the maximum of the curve is termed the nucleation barrier E_b. Note that $\Delta G_{r=0} = 0 = \Delta G_{r=\rho}$, implying there is no net change in free energy when shifting a germ of radius ρ in either direction.

Combe and Mullins both conclude that the nucleation barrier E_b, via the chemical potential term, is inversely proportional to the particle's curvature (or proportional to particle size). Illustrating this size dependence using a slightly different geometry, consider shifting a square atomic layer of length L on the (001) plane, onto an adjacent (001) plane. At an intermediate stage, the diffusing material forms a square of side $\frac{L}{\sqrt{2}}$ on each (001) plane. The difference in surface energy between this state and the final state where all the material is located in one facet is $\gamma(2(4 \times \frac{L}{\sqrt{2}}) - 4L)a = 1.66\gamma La$. Therefore the free energy barrier is $E_b = 1.66\gamma La$, proportional to the length of the facet. Larger particles require larger facets to shift around the surface in order for relaxation, meaning larger changes in perimeter, and therefore higher nucleation barriers.

Other work

While the results of Combe, Mullins, and Lewis discuss the importance of nucleation, recent work published by Rankin and Sheldon [132, 133] for the sintering of cubic MgO particles shows a novel pathway to relaxation which avoids the nucleation of new germs. During growth MgO particles develop large (001) facets which are resistant to nucleation. Figure 5.2 provides a schematic of two particles during early sintering stages, illustrating the curvature reversal at the neck beyond a critical radius. When the curvature is reversed, steps are created on the bare (001) of each particle providing attachment sites for material from the cuboid edges and vertices, allowing the particles to relax into more spherical shapes. Lewis *et al.* [128] observed a similar result, where the coalescence of two solid clusters from one MD simulation produced an extremely small equilibration time. The understanding for this rapid relaxation was based on a favourable initial orientation of the clusters. Therefore the effects of orientation are considered to play an important role in coalescence.

This work

In this chapter, three variables influencing coalescence via surface diffusion are considered - temperature, cluster size, and cluster orientation. The first two of these variables have intuitive repercussions for equilibration times. Since diffusion occurs via thermal activation, higher temperatures lead to greater atomic diffusion coefficients, leading to a faster rearrangement of atoms and smaller coalescence times. At constant temperature, increased particle sizes will lead to longer coalescence times as more particles must now diffuse over larger regions. These regions will be of lower

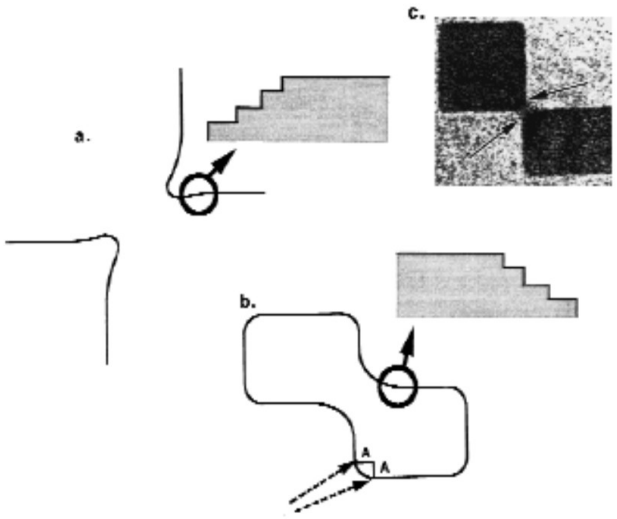

Figure 5.2: Image taken from Ref [132] showing a curvature reversal at the neck during coalescence of two MgO particles. The reversal creates stepped features on the flat (001) faces, the steps providing favourable attachment sites for material from the edges, the steps therefore grow across the surface.

curvature, providing a smaller net driving force for the atoms.

The third variable considered is the initial orientation of the clusters, in particular the crystal planes at which the clusters intersect. Results of Leite *et al.* [134] for colloidal systems of SnO_2 nanoparticles show evidence for grain rotation. MD simulations by Zhu and Averback [135] show a similar phenomenon for 4.8 nm Cu clusters, which rotated to form a low energy boundary. With these latter results in mind, to a first approximation cluster coalescence can be considered to occur at perfect grain boundaries. In reality large clusters are expected to maintain grain boundaries, at which atomic diffusion will be complicated by lattice strain, yet it is still instructive to model the ideal conditions of no grain boundary.

To date, no studies of the coalescence kinetics for large (i.e. $\geq$ 5 nm) clusters has been performed using the KMC technique. In this chapter we detail the results from such an investigation using FCC clusters intersecting at (001), (110), and (111) planes. A major focus of this chapter is the growth of the neck region connecting the two clusters. Comparisons are drawn with the results of Mullins and Eggers, where isotropic diffusion was a chief assumption. Diffusion on crystalline surfaces is inherently anisotropic, so we use a KMC algorithm which simulates systems with anisotropic diffusion. Therefore the results presented here are expected to provide a more accurate picture of the coalescence of crystalline particles (i.e. clusters) than earlier predictions [123, 126]. We also devote a portion of work to the equilibration times for two coalescing clusters, relating the results to classical models of diffusion and nucleation.

Most bulk transition metals have FCC crystallography, but extremely small particles with large surface to volume ratios have high internal strains. Strain commonly causes the formation of icosahedral and decahedral structures. Baletto *et al.* [136] used MD simulations to predict maximum sizes for these strained particles to be $\approx$ 30000 atoms, depending on material composition. Above this size, the equilibrium particle shape is calculated to be a crystalline truncated octahedron. Other researchers have calculated similar results for different materials [137]. These theoretical results are supported by experimental work [138, 139], where the equilibrium shape of lead crystals on graphite or Ru(001) is a 3D mound terminated by a (111) facet at the top, surrounded by three (111) and three (100) facets, showing the preference of (001) and (111) terminated surfaces for FCC crystals. Unsupported copper clusters produced by Reinhard *et al.* [140] show a transition from icosohedral to FCC at 3.8 nm, corresponding to 2500 atoms. Cluster sizes in our simulations were chosen to be 7 to 15 nm, all larger than 30000 atoms, hence the FCC lattice used here is likely to be an accurate representation of real systems.

5.2 KMC Model

The code follows the routine outlined in Chapter 2, and has been previously used by [68, 69, 141]. Atomic motions are dependent on the number of initial neighbours i an atom has, the configuration after the jump having no influence on the diffusion. Therefore diffusion rates are proportional to $\exp(-iE_0/k_bT)$, the sole parameter in this model being E_0, the bond energy between two atoms. The activation barrier an atom must overcome in order to move is then $E_A = iE_0$. The probability p_i per unit time that an atom with i neighbours will move is $p_i = \nu \exp(-E_A/k_BT)$, where $\nu = \frac{k_BT}{h} \sim 10^{13}$ s^{-1} at T=500 K. A consequence of this model is that atoms with many neighbours have smaller selection probabilities than atoms with only one or two neighbours, hence they diffuse more slowly. This follows the principle that atoms in regions of high curvature (i.e. high chemical potential) have fewer bonds, and diffuse to regions of low curvature where they are more favourably located (lower chemical potential). The bond barrier energy is chosen to be $E_0 = 0.1$ eV for these simulations, an average value garnered from calculations of diffusion barriers for the Al(111) surface [142], and used extensively in previous works [68, 69, 141].

Through varying the temperature T, the selection probabilities can be influenced. For example, as p_i is proportional to $T\exp(-\frac{1}{T})$, raising the temperature reduces the difference in selection probability of an atom with three neighbours to an atom with four neighbours. Additionally, sweeping the temperature from low to high

values will activate particular events, i.e. atoms with seven neighbours have negligibly small selection probabilities at T=400 K, therefore contributing little to the coalescence, but are relatively free to move at T=500 K. Simulating coalescence at different temperatures allows investigations of kinetic effects which affect the relaxation timescale.

The use of the described model for a coalescence scenario is justified by previous work [68, 69, 141], but its simplicity means care must be taken with results. Kinetic Monte Carlo simulations suffer from a lack of detail, therefore the first task for the model is to show that it correctly demonstrates the expected physics. One such test is the reproduction of theoretical predictions. For simulations at T=500 K, clusters maintain rough surfaces during coalescence, closely approximating conditions of continuous curvature. As will be shown in Section 1.3.3, simulations at 500 K show a size dependence in accordance with the macroscopic theories [126] (i.e. Equation 5.1 is satisfied). Hence the model does produce the correct diffusion behaviour (and physics) at T=500 K. For temperatures above T=500 K, the increased occurrence of desorption events meant clusters lost material during the simulation. Hence an upper bound of T=500 K was chosen for the simulations.

KMC simulations are the most efficient method for modelling coalescence where surface diffusion is the dominant mass transport mechanism. Volume diffusion occurs via the diffusion of vacancies within a crystal, and although technically possible using the described code, such a process could only occur with significant probability at temperatures higher than those considered here. Hydrodynamic flow requires a non-lattice based approach, such as that found in MD simulations [128] which show the initial stages of coalescence (for small clusters) may involve plastic deformation. The model presented here simulates a system of free clusters in a constant temperature environment, such as the scenario where clusters are in contact with a non-interacting, thermally conductive substrate such as graphite.

5.3 Simulations and Results

The simulations were performed for two clusters in free space initially connected via a small neck region. As discussed above, the coding method we use selects atomic movements solely based on the number of neighbours of an atom, hence the selection process favours atoms with the least neighbours. Figure 5.3 shows typical islands on each of the three major FCC planes. The expectation for this code is that (110) planes, on which isolated surface atoms have the highest number of neighbours and therefore the slowest diffusion, will nucleate facets the fastest. Since slow growing

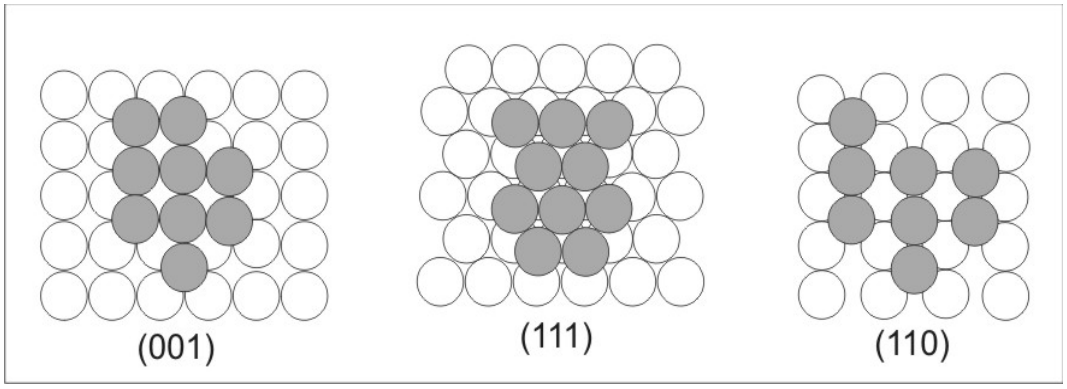

Figure 5.3: Typical islands on each of the low index FCC planes. Surface atoms are shaded grey, substrate atoms are white. Note that the (001) surface atoms have 4 substrate neighbours, (111) atoms have 3, and (110) atoms have 5 (the fifth atom sitting directly beneath the surface atoms).

facets dominate the final shape, the expected relaxed state of coalescing clusters using this code will be an object dominated by (001) and (111) planes. Figure 5.4 shows the relaxed state for clusters using this code is a truncated octahedron, an object with six (001) and eight (111) facets.

5.3.1 Calculations during the simulations

As the intersection plane between the two clusters is known prior to the simulation, by monitoring the number of atoms within this plane (the occupancy) as time progresses, the neck radius r can be calculated. However since the neck is never perfectly circular, and the density changes depending on packing i.e. (001) versus (111) planes, the radius cannot be accurately calculated using the occupancy alone. The method which gave the most reliable results involved recording the positions of all the atoms in this plane which have fewer than twelve neighbours. Those with twelve neighbours must be internal atoms, while those with less than twelve must lie on the circumference of the neck. Taking the mean distance of these exterior atoms from the centre of the plane gives an estimate of the neck radius. Using this method, fully relaxed cluster pairs were found to have a radius $\approx 2^{1/3}$ times the original cluster radius, supporting the use of this averaging method[1].

A standard [123, 126, 128, 127] method for gauging the development of the neck radius is to assume a power law dependence of the form $r \propto t^a$. Determining the slope of log(r(t)) vs log(t) from a plot of the data gives the power law exponent a. The slopes from the KMC simulation results can be compared with the predictions

[1]Another method was to calculate the occupancy, and assuming a circular profile, multiply the occupancy by a factor depending on the packing density of the plane where the intersection occurred. As the neck develops facets around the circumference the circular approximation was never accurate, and calculated radii disagreed with the expected $\approx 2^{1/3} \times$ radius

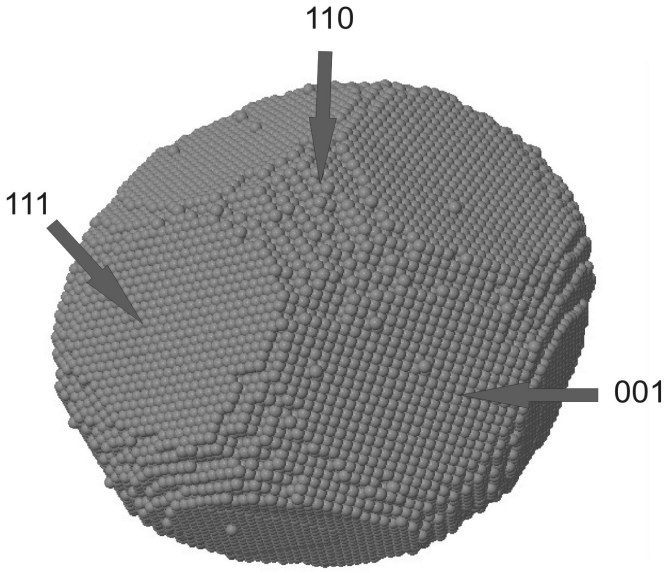

Figure 5.4: Morphology of a fully relaxed cluster pair coalescing at T=400 K. Note the large (001) and (111) planes, separated by small (110) regions.

of isotropic diffusion ($a \approx \frac{1}{6}$), or MD simulations ($a > \frac{1}{6}$).

To quantify the progression of coalescence, the object's aspect ratios (ARs) are monitored. Comparing the length of the cluster pair with the radius at the neck region gives a first approximation to the AR. Since the direction of the long axis is known (i.e. the direction normal to the intersection plane), the length was chosen to be the distance separating the origin from the atom furthest along this axis. Although this method[2] gives inaccurate results for early stages of the growth when the neck region is small compared to the cluster diameter, at later stages when the neck is larger the method becomes more reliable.

In conjunction with the radius and AR calculations, a summation of the total number of bonds connecting atoms within the object was made $\Sigma_b(t) = \sum \text{bonds}$. $\Sigma_b(t)$ provides an estimate of the internal energy, whereas summing unsatisfied bonds provides an estimate of the surface energy. $\Sigma_b(t)$ increases with time as more bonds are formed within the coalescing particle, and the surface area decreases. This method has been used previously in Refs [68, 141], where monitoring $\Sigma_b(t)$ was used to provide information on important stages of the relaxation process. Since the particles are crystalline, relaxation occurs via the creation and annihilation of exterior facets. Plotting $\Sigma_b(t)$ vs time can give the timescales and energy barriers

[2]Calculating the radius of gyration may give a better picture of the coalescence as it considers atomic positions from the centre of mass. However the AR calculations of this work, alongside snapshots of the clusters, provide sufficient information on the later coalescence stages to allow accurate values of relaxation times to be found.

for these creation and annihilation processes.

5.3.2 Coalescence of Spherical Clusters

The first batch of simulations were run using spherically symmetric clusters, with an initial neck approximately 3 atoms in diameter, each cluster ranging in size from 28000 (R=12) to 68000 (R=16) atoms. The cluster radii R have units equal to the fcc lattice constant. After coalescence, the resulting object consists of twice the initial number of atoms as desorption events are forbidden. For the work described in this section, just two intersecting planes are considered, the (001) and the (111) cases (reasons why only these two are initially chosen will be discussed in Section 5.3.5). In each case the coalescence was monitored for a sufficiently large number of iterations so as to allow the equilibration/relaxation to be complete.

(001) Intersection

Figure 5.5 shows six stages during the coalescence of two clusters, along with neck radius and $\Sigma_b(t)$ data plotted as functions of time. The $\Sigma_b(t)$ data has a linear scale (left-hand axis) while the neck radius is plotted using a log scale (right-hand axis). Time is plotted on the x-axis using a log scale. Using the 3D molecule viewing program Jmol [143], snapshots of the coalescence can be taken at points of interest. These snapshots provide a visual counterpart to the radius and $\Sigma_b(t)$ data, and help ascertain the important processes. The first snapshot (Figure 5.5 (a)) is taken after the early noisy period, which is a reordering of the initial spherical shapes into a more faceted object. Both Figures 5.5 (a) and (b) show the neck region to be highly curved, the neck therefore providing a sink for atoms, and the radial development being limited by dissociation of existing layers of atoms into the region. continuing until large (111) facets have developed adjacent to the neck region (see Figure 5.5 (c)).

Figure 5.5 (c) is taken when there are few sites of high coordination at the neck, making attachment more difficult than when the region was highly curved. Figure 5.5 (d) shows a rough neck region, due to the presence of (110) surfaces. During the interval Figure 5.5 (c)→(d) the faceted dumbell shape evolves into an object with a rough central region while retaining the faceted ends, and log(r(t)) has a shallow slope reflecting the greater difficulty of attaching atoms around the neck. Additionally, $\Sigma_b(t)$ maintains a flat profile indicating the period of Figure 5.5 (c)→(d) does not reduce the number of unsatisfied bonds. Since the fraction of surface area attributed to (110) planes is increasing, these planes having higher coordination number than the dissociating (111) or (001) layers, the benefit of adding

material to the neck is countered by the larger (110) surface area.

Atoms diffuse slowly on (110) planes, allowing them to nucleate new atomic layers with relative ease. During the period Figure 5.5 (d)→(e), the exposed (110) surfaces at the neck capture material at the expense of the outermost (001) and (111) facets (see Figure 5.6), hence the limiting process during this stage is the dissociation of facets. Both log(r(t)) and $\Sigma_b(t)$ increase with greater slopes during this period. Eventually the dumbbell shape is replaced by a faceted cylinder (Figure 5.5 (e)), with the circumference made up from alternating (001) and (110) planes.

Final growth stages involve a length reduction via the elimination of (001) and (111) facets at the cluster ends (cf Figure 5.6), and the corresponding nucleation of new atomic layers on the central region. Nucleation on (001) facets takes longer than on (110) facets because atoms have lower coordination on (001) facets. Note that the slope of log(r(t)) between Figure 5.5 (d)→(e) is much steeper than between (e)→(f).

Figure 5.7 shows six plots of the neck radius and $\Sigma_b(t)$ development for various R and T in the (001) intersection case. Each row represents an increase in particle size of 40000 atoms, the columns correspond to T=400 K and T=500 K. Similar data sets produced at 450 K are omitted as they merely show an intermediate behaviour to the T=400 K and 500 K examples shown. Assuming a power law relationship of $r \propto t^a$, log(r(t)) is fitted for early (dashed line) and intermediate (full line) stages of coalescence with exponents of $a = \frac{1}{3}$ and $a = \frac{1}{5}$ respectively. Coalescence continues (and data is collected) until the particles have aspect ratios ≈ 1, i.e. the particles all have the same profiles.

Focusing on the size dependence of log(r(t)) in Figure 5.7, little variation is apparent between each of the plots. The main point of difference is the time at which the neck radius plateaus i.e. when the relaxation finishes. This is a fairly trivial observation, as larger clusters require more atoms to travel further in order to reach the most favourable sites, and coalescence takes longer. A less obvious size dependence is apparent for clusters coalescing at T=400 K. Considering the section of the log(r(t)) curve at late stages (cf Figure 5.5 (e)→(f)) where the slope is shallowest, as the cluster size is increased the lengths of these shallow portions increases relative to other sections of the slope (most obvious comparing R=12 to R=16). We infer the late stage length contraction and nucleation phase is size dependent. From the recent work of Combe and Mullins [68, 131], this reduced exponent is believed to result from the increased nucleation timescales at lower temperature.

Early stages of the neck growth and $\Sigma_b(t)$ development show similar behaviour

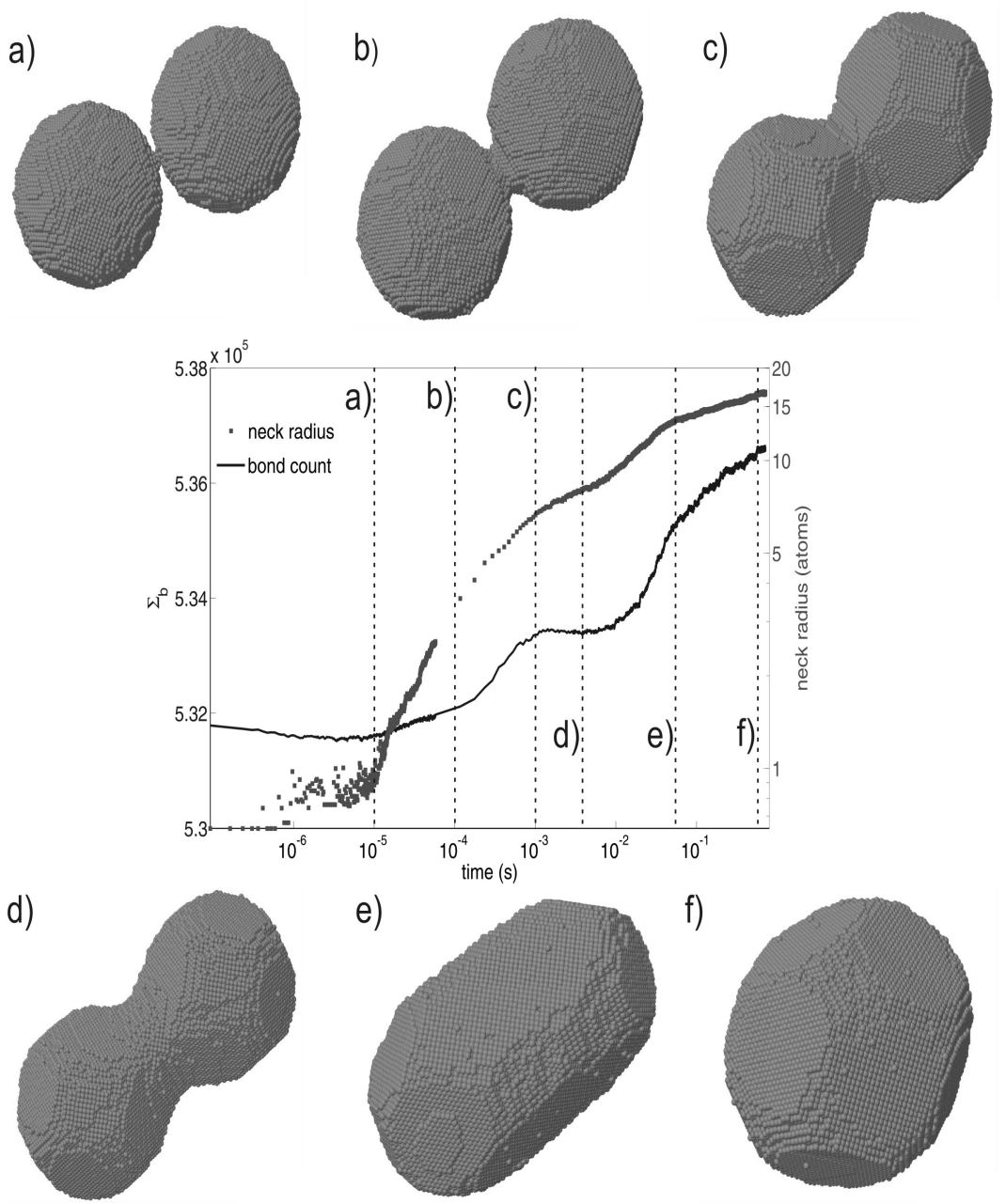

Figure 5.5: Six images taken during the coalescence of two R=14 clusters intersecting at the (001) plane, T=400 K. The development of the neck radius and $\Sigma_b(t)$ during coalescence are plotted. Snapshots are taken at a) t=1×10^{-5}, b) 1×10^{-4}, c) 1×10^{-3}, d) 4×10^{-3}, e) 5×10^{-2}, and f) 8×10^{-1} seconds.

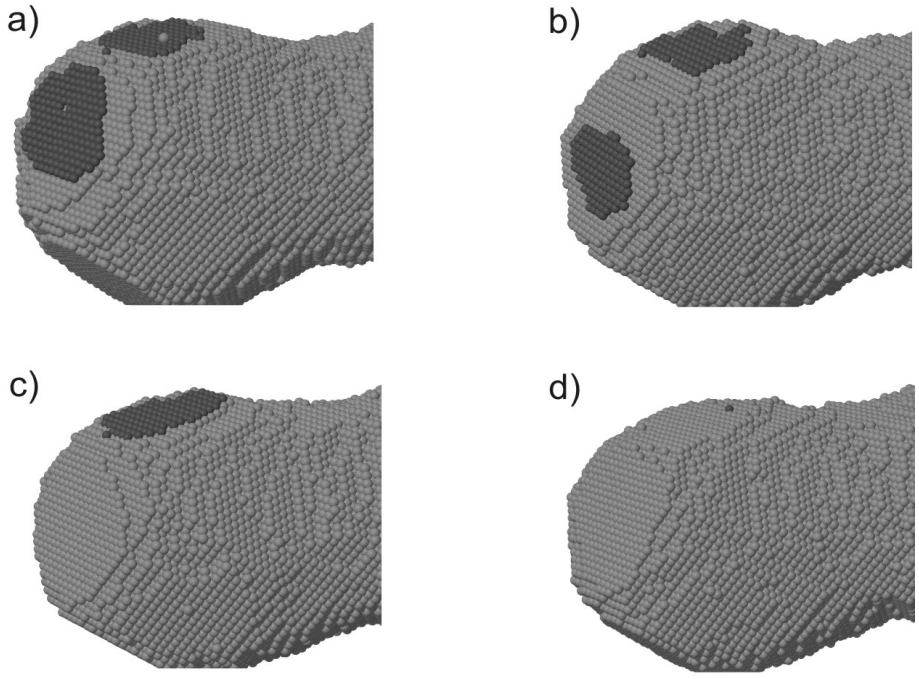

Figure 5.6: Snapshots taken during the coalescence of the R=14 clusters, at T=400 K (between d) and e) of Figure 5.5). A particular set of (001) and (111) planes have been selected to highlight the facet dissociation between t= 1.2×10^{-2} and 1.5×10^{-2} seconds.

whether clusters are at T=400 K or 500 K, indicating no significant temperature dependence. This is because the clusters initially contain large numbers of relatively weakly bound atoms and small facets, which diffuse/dissociate quickly independent of the temperature. Additionally (as shown in Figure 5.5 (a) and (b)), the neck region is highly curved providing a strong attraction for diffusing atoms. By r ≈ 5, there is a reduction in curvature at the neck as faceting becomes more prominent, providing an explanation why the fitted exponent drops from a $= \frac{1}{3}$ to a $= \frac{1}{5}$.

Comparing the intermediate stages of log(r(t)) for T=400 K and 500 K, the T=400 K data does not closely follow the a $= \frac{1}{5}$ line. Recalling snapshots (c)→(e) of Figure 5.5 at T=400 K, the intermediate stages involved the expansion and nucleation of (110) layers along the neck. When a small surface fraction is attributed to (110) planes, log(r(t)) undercuts the a $= \frac{1}{5}$ line, while for larger fractions (Figure 5.5 (d)) the slope appears closer to a $= \frac{1}{3}$. During the intermediate stages, at T=500 K the $\frac{1}{5}$ line is closely followed for all cluster sizes.

For the faceted cylinder→truncated octahedron phase, when the (001) and (110) planes along the length must nucleate additional layers for further relaxation, the effect of temperature is most apparent. As observed for clusters coalescing at T=400 K in Figure 5.5, the exponent fitting log(r(t)) reduces i.e. the exponent drops from 1/5 to $\approx 1/16$. Contrasting the low T results, when clusters coalescing at T=500

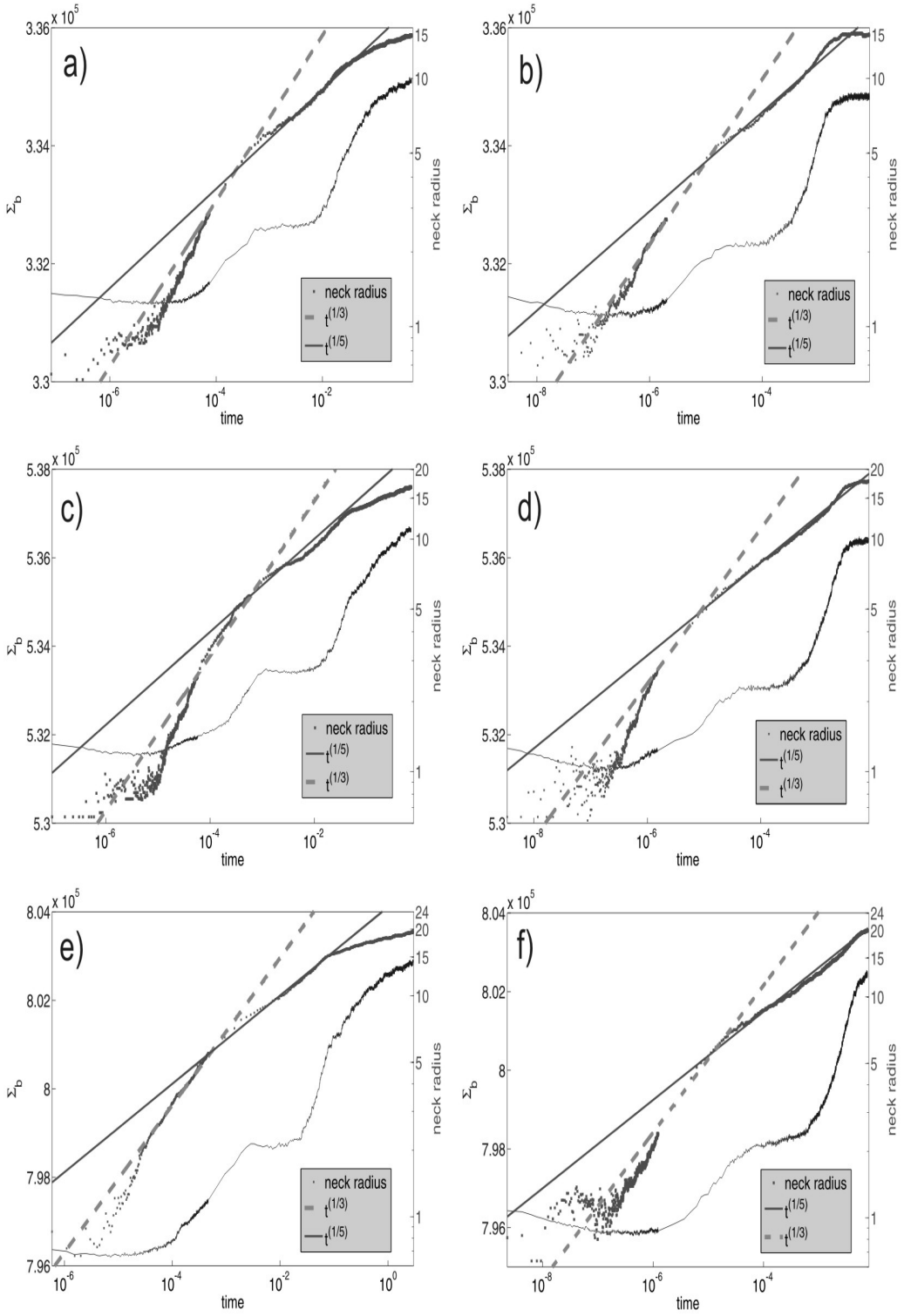

Figure 5.7: Plots of neck radius and $\Sigma_b(t)$ for spherical clusters coalescing at the (001) plane. a) R=12, T=400 K, b) R=12, T=500 K, c) R=14, T=400 K, d) R=14, T=500 K, e) R=16, T=400 K, f) R=16, T=500 K. The radial growth is plotted using a log scale, and the solid line provides a best fit to the data assuming a power law dependence. The legend contains the exponent used to fit the radial data. $\Sigma_b(t)$ is plotted using a standard scale.

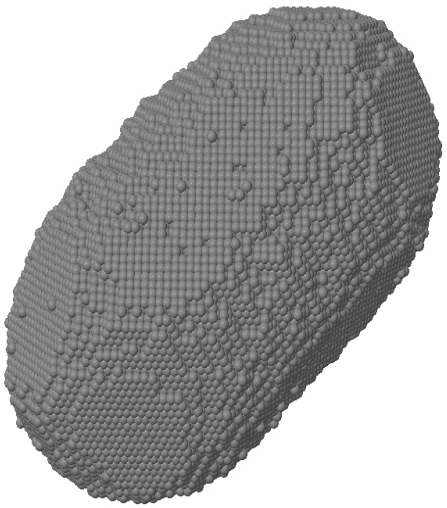

Figure 5.8: A snapshot for the cluster coalescence plotted in Figure 5.7 (d) when T=500 K, taken at the same coalescence stage as Figure 5.5 (e) i.e. when neck radius=13. A number of atoms and dimers are visible on the (001) plane, contrasting the T=400 K cluster, indicating the nucleation barrier is relatively small at T=500 K.

K have formed a faceted cylinder the slope of log(r(t)) increases more steeply than the a = $\frac{1}{5}$ line (see Figure 5.7 (b), r>10).

The reduction in slope of log(r(t)) occurs when the clusters have formed a cylindrical shape with large facets along its length (Figure 5.5 (e)). Further relaxation of this object into a sphere requires the nucleation of germs on these bare regions. Assuming there is a free energy barrier E_b to nucleation, then there is a characteristic time between nucleation events of $\tau_{nucl} \propto \exp(\frac{E_b}{kT})$ [34]. Hence the nucleation timescales are proportional to $\exp(\frac{1}{T})$. Reducing the temperature to 400 K reduces the rate of nucleation events, and the growth of critically sized germs on (001) planes becomes a significant obstacle to relaxation. Figure 5.8 displays an R=14 cluster coalescing at T=500 K, the snapshot taken when r(t) = 13, i.e. at the same stage in coalescence as Figure 5.5 (e). A number of atoms/small nuclei are clearly visible on the (001) plane. The image, along with the trends of log(r(t)), suggests T=500 K is near the roughening temperature for nucleation on the (001) plane.

Considering the temperature dependence of $\Sigma_b(t)$, the main difference between coalescence at T=400 K and T=500 K occurs after the central plateau region. The sharp increase at T=500 K is replaced by a more gradual increase when T=400 K. A close look at this latter slope reveals stepped features in the curve, these steps becoming broader and more numerous for larger clusters. Note that the stepped behaviour becomes significant at the same time as the slope of log(r(t)) drops, i.e. when the bare (001) facets are present.

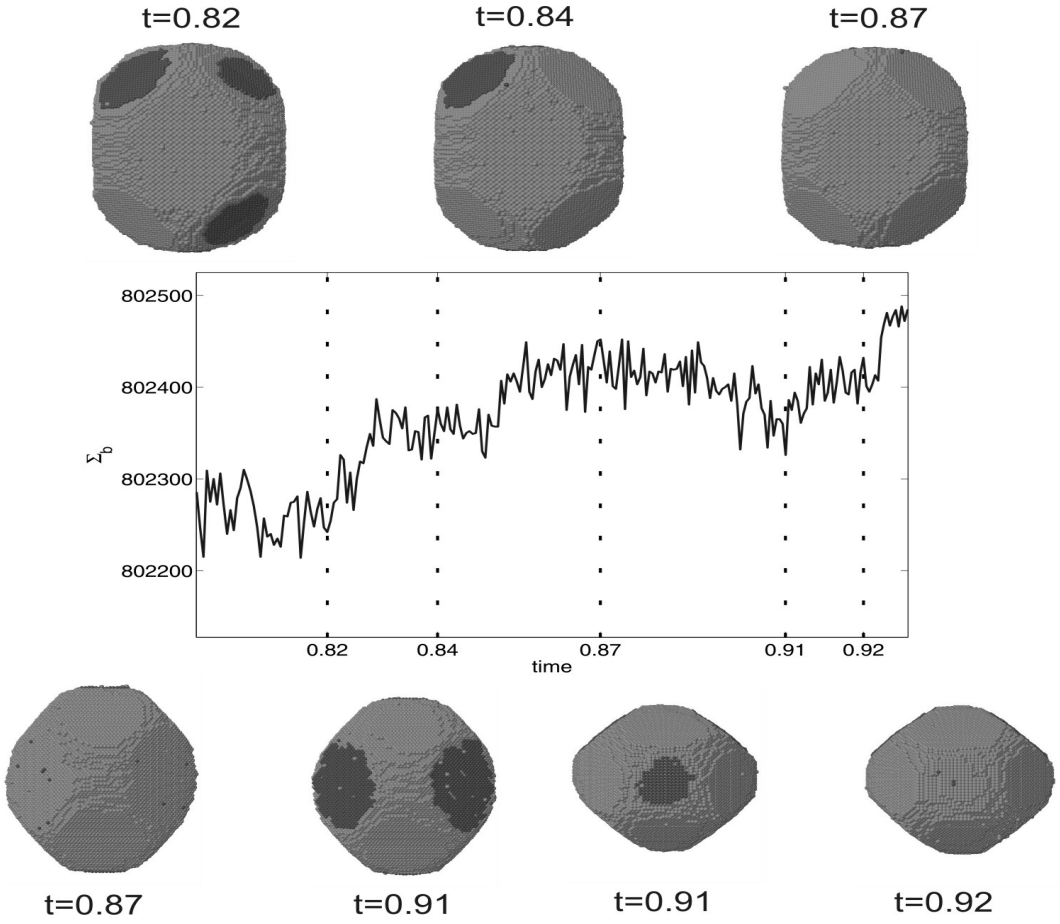

Figure 5.9: An expanded view of $\Sigma_b(t)$ showing the staircase behaviour. The full data set can be found in Figure 5.7 (e). The upper images view the cluster along a (001) plane normal, showing the dissociation of (111) oriented atomic layers, between t=0.82 and t=0.87 s. The lower left images view the cluster from along a (110) plane normal, and shows the nucleation of atomic layers on (001) planes between t=0.87 and t=0.91 s. The images at bottom right view down the length of the object, showing the dissociation of an atomic layer on the (001) plane at the cluster end, between t=0.91 and t=0.92 s.

Figure 5.9 shows an expanded portion of Figure 5.7 (e), during the latter stages of coalescence when steps are most obvious. Magnifying the trace reveals a noisy behaviour, due to the cluster switching back and forth between states of differing surface energy. Included in the Figure are images showing the dissociation and nucleation of atomic layers, each process is associated with a response in the trace.

In the top set of images three layers of (111) oriented atoms dissociate, without any new layers nucleating. Dissociated material is incorporated around the edges of nearby planes, reducing the total perimeter associated with (111) planes, while roughly maintaining the amount of exposed (111) surface area. Figure 5.10 provides a schematic for the dissociation of a shaded (111) layer, and subsequent incorporation of the shaded atoms at nearby edges. Perimeter atoms provide sites of high coordination, hence a reduction in perimeter, caused when a layer of (111) atoms

dissociates, leads to an increase in $\Sigma_b(t)$.

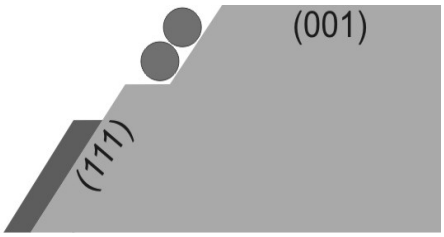

Figure 5.10: Schematic of the dissociation of a (111) layer, and incorporation of material at the edges of layers beneath.

In the bottom left set of images nucleation on (001) planes is correlated with a reduction in $\Sigma_b(t)$. Forming new layers of (001) atoms requires material to dissociate from edges of nearby (111) planes, and as (001) planes have a higher coordination than (111) planes, there is a net decrease of $\Sigma_b(t)$, and a downwards step is observed in the trace. The last example (bottom right) depicts the dissociation of a small layer of (001) atoms from the tip of the object, affecting $\Sigma_b(t)$ in the opposite manner to nucleation on (001) planes.

Summarising the information contained in Figure 5.9, there is an overall increase in $\Sigma_b(t)$ as coalescence progresses. Stepped features seen at low magnifications of the trace have been associated with the nucleation and dissociation of atomic layers. From t= 0.82 $\rightarrow$ 0.92 s, the particle gradually shifts material from the end planes onto the central planes. Comparing aspect ratios taken at t=0.82 and t=0.92 we find $AR_{t=0.82} = 1.25$ and $AR_{t=0.92} = 1.18$. Clearly $\Sigma_b(t)$ is related to the compactness of the cluster.

Referring back to the papers of Combe and La Magna [68, 141], their suggestion is that the onset of steps in $\Sigma_b(t)$ corresponds to periods when reduction in surface energy is reliant on the nucleation of new facets, the steps in $\Sigma_b(t)$ being the signature of such nucleation events. Steps are most prominent at lower temperatures because the nucleation barrier is harder to overcome. The situation is exacerbated for larger clusters, as greater numbers of facets (of greater size) are required to nucleate in order for the clusters to relax fully, leading to relaxation timescales in the order of seconds (see Figure 5.7). An extension to this work would be to further investigate the frequency and length of these stepped features, to try and draw clearer conclusions as to their origins and temperature dependence, as well as the magnitudes of the facet nucleation barriers.

(111) Intersection

A similar batch of simulations was performed for spherical clusters intersecting

at a (111) plane. The long axis of the cluster pair was defined normal to the (111) plane, and the point where the two clusters intersect lies at the origin of the lattice. Minor adjustments to radial and AR calculations are required to account for the new geometry, but cluster sizes are the same as for (001) intersections, and the initial neck radius remains < 1.

Figure 5.11 depicts five stages during the coalescence for a cluster pair using this new intersection, along with the neck radius and $\Sigma_b(t)$ data. The clusters have initial radii R=14, and the simulation was performed at T=400 K. Figure 5.11 (a) shows the clusters soon after the simulation is begun. At this early stage small facets have appeared on the surface, and the neck region remains highly curved. Figure 5.11 (b) is taken a short period later, when the neck region is still curved, but with larger facets appearing on the object surface. Using Jmol to rotate the image, each cluster is observed to have six exposed planes growing into the neck, three each of (001) and (111). Across the neck region, the (001) surface planes of one cluster intersect with the (111) surface planes of the opposite cluster. Figures 5.11 (a) and (b) correspond to a period during which the slope of log(r(t)) is relatively steep (the slopes are discussed in detail later).

By Figure 5.11 (c), the (001) and (111) facets extend from the midpoint of each cluster into the apex of the neck, so that the neck loses its highly curved nature. Between Figures 5.11 (c) and (d) log(r(t)) clearly exhibits a shallower slope, and there is a brief plateau in $\Sigma_b(t)$ around t= 10^{-2} s. During this period atomic layers nucleating at the apex of the neck develop across the midpoint of the object, until a series of continuous atomic steps can be drawn around the neck circumference (one such example has been highlighted with darker atoms in (d)). Between Figure 5.11 (d) and (e), the step edges of these (111) planes capture diffusing atoms and consequently spread across the object, increasing the neck radius while reducing the cluster length. This latter 'step growth' period is characterised by steep slopes for both log(r(t)) and $\Sigma_b(t)$.

To understand the plateau in $\Sigma_b(t)$ at 10^{-2} s, specific layers of atoms at the cluster ends were highlighted and monitored via a series of snapshots (shown in Figure 5.12). Images are taken between t=0.003 and t=0.013 s for the plot shown in Figure 5.11 (between images (c) and (d)). In the sequence of images layers of (001) and (111) atoms at the cluster extremities reduce in size or dissociate completely. As already observed in Figure 5.13 (d), layers of (111) atoms at the neck capture the released material, leading to the stepped configuration of Figure 5.11 (d). We infer that the increased perimeter of the growing steps retards the energy reduction associated with the removal of atomic layers, depicted in Figure 5.12. Once step features develop

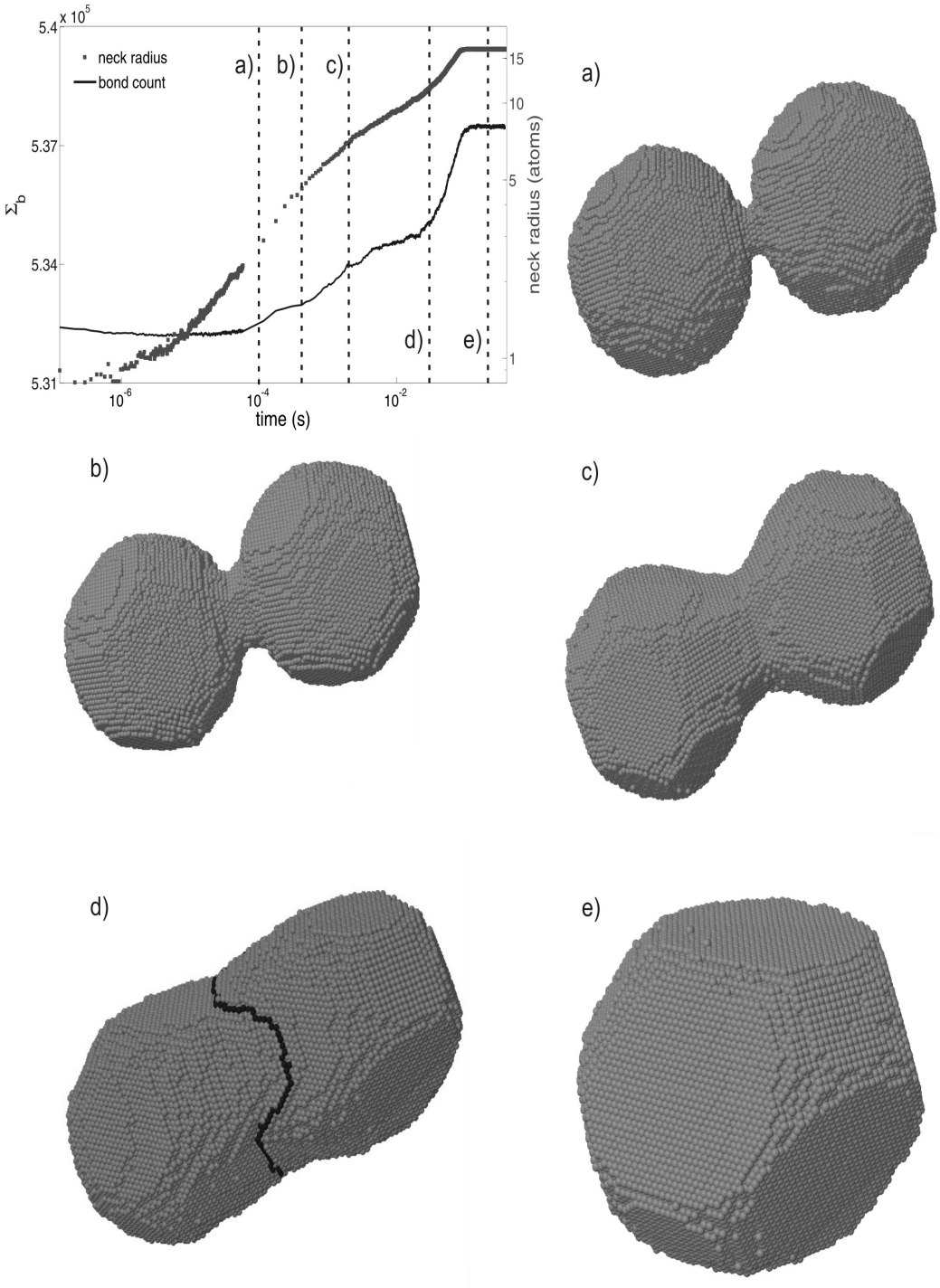

Figure 5.11: Five images taken during the coalescence of two R=14 clusters intersecting at a (111) plane, T=400 K. Also shown is the development of the neck radius and Σ_b(t). Images were taken at a) t=1×10^{-4}, b) 4×10^{-4}, c) 2×10^{-3}, d) 3×10^{-2}, and e) 2×10^{-1} seconds.

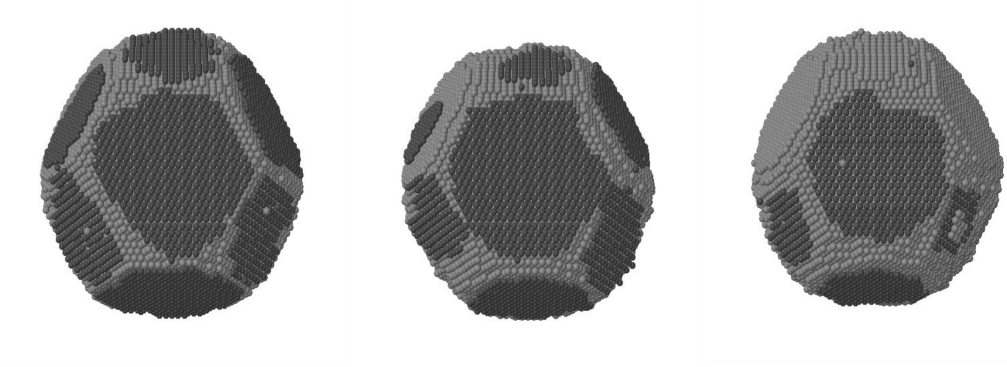

Figure 5.12: An end-on view of the cluster pair, showing atomic layers of (001) and (111) orientation dissociating between t=0.003 and t=0.013 seconds (between images (c) and (d) of Figure 5.11).

around the circumference of the neck (highlighted atoms of Figure 5.11 (d)) the total perimeter begins to decrease (compare (d) with the clean facets of Figure 5.11 (e)) and $\Sigma_b(t)$ increases more steeply.

Figure 5.13 shows six plots of neck radius and $\Sigma_b(t)$ development for clusters of differing size and temperature coalescing with (111) intersections. The most striking feature of these plots is the steeper slope of log(r(t)) for later coalescence stages compared to Figure 5.7. Assuming a $r \propto t^a$ dependence, the later stages are best fitted with an exponent of $a = 1/3$ compared with $a = 1/5$ seen for the (001) intersection.

There are three distinct regions in the r(t) plots of Figure 5.13. Until $r \approx 5$, log(r(t)) develops in a similar manner to clusters coalescing at (001) intersections. In these early stages, the neck region is highly curved due to the use of spherically symmetric clusters, so the lack of a dependence on intersection plane is unsurprising. For intermediate stages the slope of log(r(t)) drops, and can be fitted with an exponent $a \approx 1/6$ (see Figure 5.13 a)). After this middle period the slope increases to 1/3, and tracks the fitted line until r plateaus and the relaxation is complete. The three main features of the radial development just discussed appear in all plots irrespective of particle size and temperature. Similar to the (001) intersection case, the most obvious size dependence is the increased relaxation times of larger clusters.

Unlike the (001) intersection case, the data in Figure 5.13 show very little temperature dependence. There is no change in the slope of log(r(t)) for the initial stages, and a $r \propto t^{1/3}$ behaviour is observed for all six plots. During the intermediate stages there is a slight difference in the radius at which the data first falls onto the a=1/3 fit line. Considering the two R=14 plots, at T=400 K the fit line and radius data clearly coincide at r=10, while for T=500 K the lines coincide only for r>10. For both the

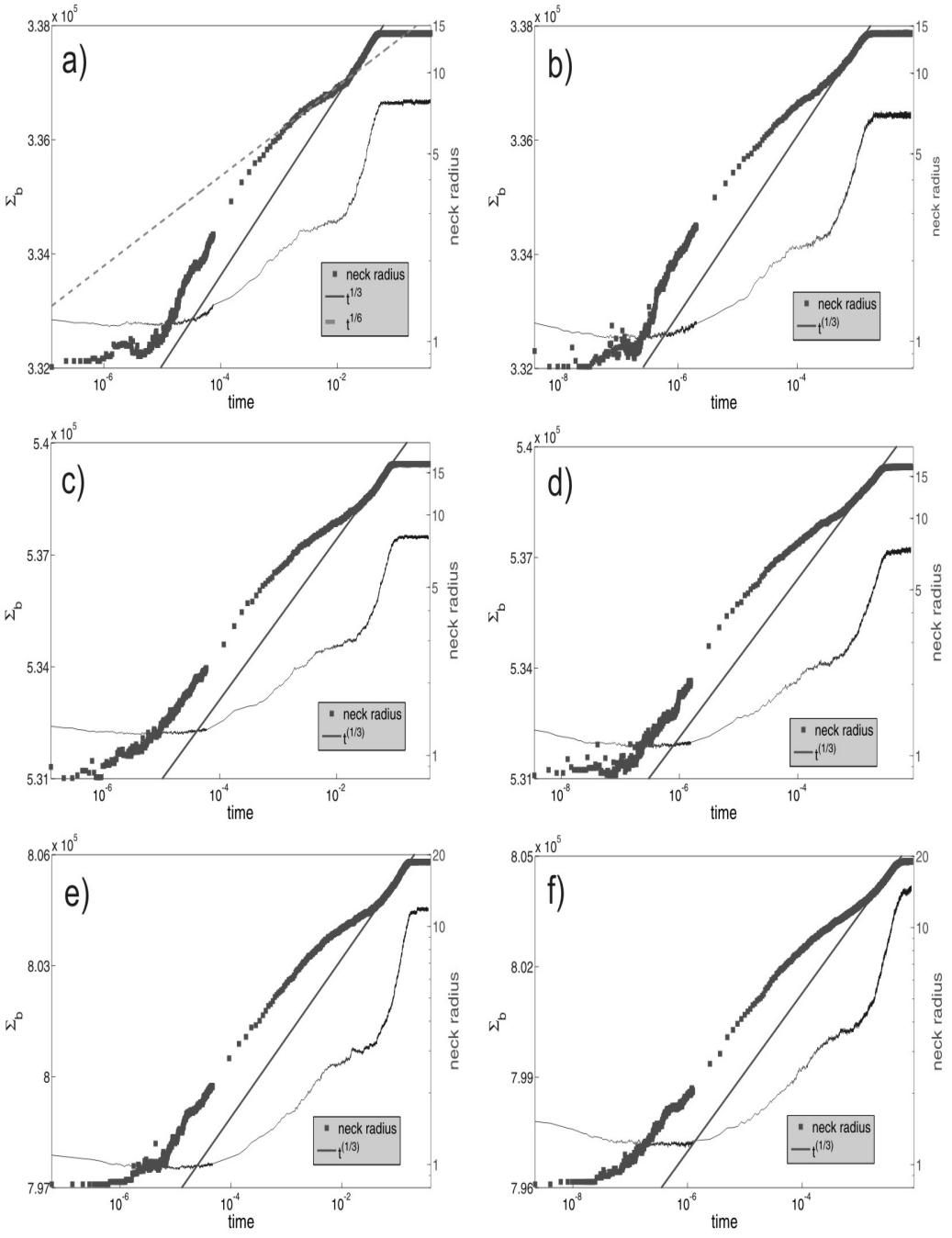

Figure 5.13: Plots of neck radius and $\Sigma_b(t)$ for spherical clusters coalescing at the (111) plane. a) R=12, T=400 K, b) R=12, T=500 K, c) R=14, T=400 K, d) R=14, T=500 K, e) R=16, T=400 K, f) R=16, T=500 K. The radial growth is plotted using a log scale, and the solid line provides a best fit to the data assuming a power law dependence. The legend contains the exponent used to fit the radial data. $\Sigma_b(t)$ is plotted using a standard scale.

T=400 K and 500 K cases, the point at which the neck radius stops increasing is very sharp. This is a significant point of difference to the (001) intersection case, where low temperatures caused a reduction in the slope of log(r(t)) during the latter coalescence stages, evidently due to the difficulty of nucleating new atomic layers.

Until r$\approx$ 2, $\Sigma_b(t)$ hardly changes, as seen for early coalescence stages of the (001) scenario. After r=2, $\Sigma_b(t)$ increases steadily until the period when the exponent used to fit log(r(t)) drops to 1/6, at which point the $\Sigma_b(t)$ value plateaus. This plateau is maintained until log(r(t)) shifts back to the $a = 1/3$ behaviour, when $\Sigma_b(t)$ increases sharply to its maximum value. Unlike the (001) intersection case, $\Sigma_b(t)$ does not exhibit any clear size dependence. The features just described appear in each of the plots shown in Figure 5.13.

Comparing $\Sigma_b(t)$ plots of Figure 5.13 as temperature is increased from T=400 K to T=500 K for fixed cluster size, a reduction in the $\Sigma_b(t)$ plateau width can be seen, implying the intermediate coalescence stages are influenced by changes in temperature. Recall the plateau occurs while (111) layers are growing along the length of the cluster. By monitoring the number of occupied atomic layers at the cluster ends (e.g. the layers highlighted in Figure 5.12), it can be shown that when $\Sigma_b(t)$ plateaus, clusters at T=500 K have dissociated more of these exterior facets than clusters at T=400 K. Since more layers have dissociated from the extremities at T=500 K, the neck has a larger radius (compare log(r(t)) at the beginning of the plateau for fixed cluster size). A consequence of adding greater amounts of material to the neck is the earlier development of steps around the neck circumference. These continuous step features have been identified as the precursor to the final growth period where $r \propto t^{\frac{1}{3}}$. At T=500 K the width of the $\Sigma_b(t)$ plateau is smaller than when T=400 K, because more material has been released into the neck region by the time the plateau occurs.

The staircase behaviour seen for $\Sigma_b(t)$ for clusters intersecting at (001) planes does not appear in the plots of Figure5.13, even at low temperatures and large cluster sizes. This reinforces the observation that nucleation of germs is avoided during the latter growth stages, as the result of Combe *et al.* [68] predicts greater nucleation barriers with larger particle sizes, which would be apparent as steps in $\Sigma_b(t)$. Hence the step-flow growth observed during the late stages, occurring because of the initial orientation of the clusters, allows relaxation to proceed without nucleation events.

5.3.3 Equilibration times for spherical clusters

As stated at the beginning of the chapter, macroscopic theories predict equilibration times proportional to the fourth power of an object's linear dimension (see Equation 5.1). This theory helps explain why large objects can maintain irregular shapes for long periods, whilst microscopic particles relax to more thermodynamically favourable shapes in microseconds. In this Section we analyse the equilibration times for spherical clusters as a function of size and temperature.

At every millionth iteration during the simulation a calculation of the objects aspect ratio was performed. Typically the simulations required several billion iterations, therefore data points taken this frequently provided dense data sets. Especially at later stages in the simulation, when the coalescence proceeds slowly relative to the Monte Carlo timestep, the data points are sufficiently close that any structural changes take much longer than the intervals between data points. When the AR reached a benchmark value of 1.2 the simulated time τ_{eq} was recorded, this AR value having been used previously as a benchmark value for equilibration [68]. For our simulations the clusters appear fully relaxed at this value, and the value itself changes little for further iterations. The same benchmark value is used for both (001) and (111) coalescence scenarios.

Aspect ratio calculations were performed for five different initial cluster sizes coalescing at three different temperatures, for both the (001) and (111) intersections. Results of τ_{eq} are plotted in Figure 5.14. Equilibration times are plotted on the y axis using a log scale. Particle size (N) is plotted on the x-axis using a log scale, in this case N is the *total* number of atoms in each simulation. The filled symbols represent τ_{eq} for (001) intersections, while results from (111) intersections are represented by open symbols. The legend contains the temperature at which each coalescence occurred, along with the slope of the line fitting the symbols, created assuming a power law dependence N^a. The slope therefore equals the power law exponent a.

Comparing the data point positions as temperature is decreased for fixed cluster size, for both intersection cases an increase in τ_{eq} is observed. The increase is related to the temperature dependence of atomic diffusion on the cluster surface, where $D_s \propto T \exp(\frac{E}{k_B T})$ with E some diffusion barrier. As temperature is lowered, diffusion speeds rapidly drop, resulting in lengthier relaxation times.

The clearest trend observed in the diagram is the increasing equilibration times with particle size. Recalling $\tau_{eq} \propto L^4$ from macroscopic theory, and making the approximation that the linear dimension $L \approx N^{1/3}$, a slope of $4/3 \approx 1.33$ matches the expected scaling behaviour (Equation 5.1). At T=500 K both intersection cases are fitted with a=1.33, giving confidence that the model simulates the expected

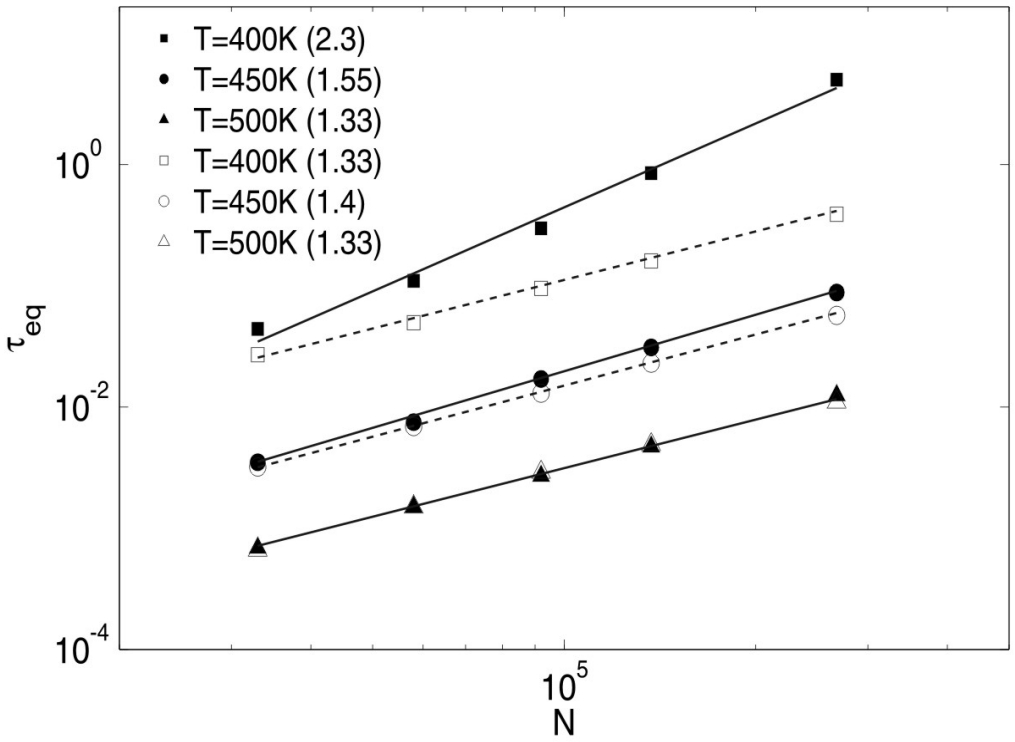

Figure 5.14: Equilibration times for the coalescence of spherical clusters intersecting at (001) and (111) planes. The filled symbols represent times for (001) intersections, while (111) intersections have open symbols. The legend contains the temperatures and slopes of the lines used to fit the data.

physics of the system at this temperature. Lowering the temperature from T=500 K, the filled symbols of (001) intersections are fitted with progressively larger exponents, increasing to a=2.3 by T=400 K. The (111) intersections however show little temperature dependence, increasing to 1.4 at T=450 K, but reducing to a=1.33 at T=400 K. Exponents greater than 1.33 indicate processes with timescales longer than those predicted by the theory are interfering with the relaxation.

Size dependent correlations can be made between the radial data of Figure 5.7 and Figure 5.13, and the equilibration times shown in Figure 5.14. Coalescence at T=400 K for (001) intersection cases showed lengthier periods of reduced slope (when $\log(r(t)) \propto \frac{1}{16}$) for larger cluster sizes, as well as equilibration times which move progressively further from expected values (assuming a=1.33). Clearly the difficulty of nucleating germs at T=400 K on (001) planes affects the equilibration time. When T=500 K the nucleation barrier is overcome quickly enough that plotting $\log(\tau_{eq})$ against log(N) gives the predicted exponent a=1.33. Such an exponent is further evidence to T=500 K being near the roughening temperature on (001) planes. In contrast, the (111) intersection case does not exhibit the same size dependence, and there is virtually no change in the exponent fitting the equilibration times

for different sized clusters intersecting at (111) planes. Due to the absence of facet nucleation for (111) intersection cases, the predicted exponent is maintained at lower temperatures.

Combe [68] investigated the equilibration of elongated particles $\leq$ 13000 atoms in size, finding a decrease in temperature can cause facet nucleation to interfere with relaxation. Their results reproduce the predictions of Equation 5.1 at 800 K, while their simulations at T=400 K exhibit size dependences of $\tau_{eq} \propto N^{5.4}$. Crystal facets with different surface energies have nucleation barriers of differing size [34]. For the neighbour counting code presented here, (111) surfaces have the lowest coordination and therefore the highest nucleation barrier. Clusters intersecting at (001) and (111) planes do not develop large (111) facets during coalescence, meaning the facet with the largest nucleation barrier does not have an opportunity to limit coalescence. We believe the higher relaxation temperatures of Combe [68] were neccessary for germs to nucleate on (111) planes. As stated in Section 5.2, for T $\geq$ 500 K the frequency of desorption events increases preventing simulations at 800 K. It is possible the code used by Combe [68] prohibited desorption events.

5.3.4 Arrhenius dependence of equilibration times

Using an Arrhenius analysis technique, the temperature dependence of τ_{eq} for the two coalescence scenarios is analysed to determine activation energies for the relaxation. Atomic movements are thermally activated, and the unit diffusion rate of each atom can be expressed as (see Chapter 1)

$$D \sim \frac{a^2\nu}{4} = D_0 \exp(\frac{-E}{k_B T}), \tag{5.3}$$

where $D_0 = \frac{a^2 k_B T}{4h}$ is the diffusion coefficient ($\frac{k_B T}{h}$ is the simulation prefactor, see Chapter 2), E is the relevant diffusion barrier, and a the lattice constant. An Arrhenius analysis is expected to determine the limiting process in the relaxation, i.e. the barrier E. To determine temperature dependent trends accurately, extra simulations at T=375, 425, and 475 K were performed for two cluster sizes R=12, and 16 (and both intersection cases). It is important to extend the temperature range below T=400 K, as this puts coalescence further into a regime where nucleation is the limiting factor.

Figure 5.15 displays the natural logarithm of τ_{eq} plotted as a function of inverse temperature. Results from (111) intersections are plotted using open symbols, from (001) intersections using filled symbols. Circles correspond to R=12 clusters, squares

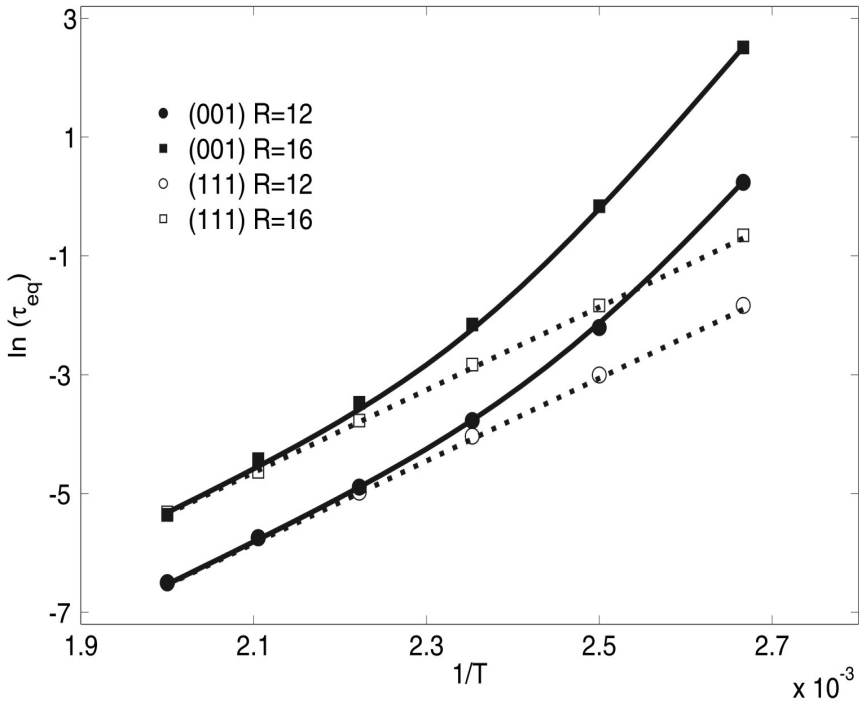

Figure 5.15: Arrhenius dependence of the equilibration times. Data from coalescence at (001) intersections is plotted using squares, (111) intersections using circles. Fitted lines are produced using the equations shown in Table 1.1.

for R=16. Data from (111) intersections show a linear trend, while data from (001) intersections curve steeply upwards as temperature is lowered. Data points have been fitted using classical diffusion and nucleation equations (discussed in detail below), the equations and parameters producing each fit are shown in Table 5.1. Fits for (111) intersections are shown with dotted lines, for (001) intersections using full lines.

111 Intersections

The equilibration time is assumed to take the form $\tau_{\text{eq}} = \tau_{\text{Diff}} + \tau_{\text{Nucl}}$, where τ_{Diff}

Fit line	Intersection Plane	Radius	Parameters
·····	111	circle R=12	$\ln[1.3 \times 10^{-9} \exp(\frac{0.6eV}{k_B T})]$
·····	111	square R=16	$\ln[4.3 \times 10^{-9} \exp(\frac{0.6eV}{k_B T})]$
———	001	circle R=12	$\ln[1.3 \times 10^{-9} \exp(\frac{0.6eV}{k_B T}) + \frac{2.5\times10^{-18}}{T^{0.5}} \exp(\frac{1.41}{k_B T})]$
———	001	square R=16	$\ln[4.3 \times 10^{-9} \exp(\frac{0.6eV}{k_B T}) + \frac{3.0\times10^{-18}}{T^{0.5}} \exp(\frac{1.48}{k_B T})]$

Table 5.1: Parameters and equations used to fit each data set of Figure 5.15

(Equation 5.1) represents the equilibration time assuming diffusion is the limiting factor, and τ_{Nucl} represents the sum of the times required to nucleate new atomic layers. Coalescence at (111) intersections is analysed first, since no nucleation is observed. Hence τ_{eq} can be obtained from the diffusion limited equilibration time of Nichols [126],

$$\tau_{\mathrm{Diff}} = \frac{\mathrm{k_B T L^4}}{\mathrm{C D_s \gamma a^4}}, \tag{5.4}$$

where the subscript of $\mathrm{D_s}$ denotes atoms diffusing on the cluster surface, γ the surface energy, L the linear dimension, and C a numerical constant (25 according to Ref. [126]). The size dependence ($\mathrm{L^4}$) of τ_{Diff} is contained in the prefactor for the dotted fitlines, and a comparison of the prefactors ($\frac{1.3}{4.3} = 0.30$) for the two cluster sizes ($(\frac{\mathrm{R=12}}{\mathrm{R=16}})^4 = 0.32$) gives the expected ratio.

Using Equation 5.3, estimates for $\mathrm{D_0}$ and $\mathrm{E_s}$ can be extracted from Figure 5.15, the fitting parameters shown in Table 5.1. Both dotted lines have slope $\mathrm{E_s} = 0.6$ eV, the activation energy for diffusion. To find $\mathrm{D_0}$, the RHS of Equation 5.4 is equated with the simulated $\tau_{\mathrm{eq}} = 0.0015$ s, when R=12 and T=500 K. Taking $\gamma = 1$ $\mathrm{Jm^{-2}}$ [128, 131], $\mathrm{k_B} = 1.23 \times 10^{-23}$ J $\mathrm{K^{-1}}$, and L=38.7 lattice sites ($\mathrm{L} \approx \mathrm{N}^{\frac{1}{3}}$, gives $\mathrm{D_0} = 4.6 \times 10^{-7}$ $\mathrm{m^2\ s^{-1}}$. Hence $\mathrm{D_s} = 4.1 \times 10^{-13}$ $\mathrm{m^2\ s^{-1}}$ at T=500 K, reducing to $\mathrm{D_s} = 1.3 \times 10^{-14}$ $\mathrm{m^2\ s^{-1}}$ at T=400 K. These diffusion coefficients compare with values $\mathrm{D_s} \approx 1 \times 10^{-15}$ $\mathrm{m^2\ s^{-1}}$ at T=400 K, and $\mathrm{D_s} \approx 1 \times 10^{-14}$ $\mathrm{m^2\ s^{-1}}$ at T=500 K, obtained by Nichols [126] for the sintering of copper spheres.

In our code, diffusion barriers on the low index planes are (111)= 0.3 eV, (001)= 0.4 eV, and (110)= 0.5 eV, all smaller than 0.6 eV, implying the calculated activation energy is not due to diffusion on these planes. Instead the measured activation energy is likely a rate limiting process for diffusion on the low index planes, i.e. a process neccessary for coalescence which takes longer than basic surface diffusion. Figure 5.3 (Section 5.3) gives a close-up view of common island shapes and neighbour configurations on the low index planes which cover the cluster surface (see Figure 5.4). Relaxation requires the dissociation of such islands, dissociation being limited by the removal of atoms located at island vertices, these atoms commonly having six nearest neighbours. Hence the calculated activation energy is the energy barrier for dissociation, 6×0.1 eV = 0.6 eV.

(001) Intersections

Parameterising the equilibration times for (001) intersections in Figure 5.15 requires the inclusion of nucleation terms in the expression for τ_{eq}. Since diffusion is limited by the activation energy of facet dissociation, a process which is orientation independent, the parameters found for τ_{Diff} from the (111) scenario are transferable

to τ_{eq} for the (001) scenario. Evidence supporting this assumption is the matching equilibration times of both intersection scenarios at 500 K. We now need to find a suitable expression for the nucleation term.

A classical expression for the nucleation rate of critical nuclei on infinite facets is given by Hirth [144] and Mullins [131] to be

$$I = A \exp(\frac{-E_b}{k_B T}), \tag{5.5}$$

where A is proportional to $\frac{D_s}{T^{\frac{1}{2}}}$, and has units of $m^{-2}\ s^{-1}$, and E_b is the maximum of the free energy barrier which the system must overcome in order to nucleate a new facet. E_b corresponds to the nucleation barrier on the (001) facets which dominate the cluster length. Extracting the temperature dependent parts of D_s (see Equation 5.3) the expression for I can be rewritten as,

$$I = B T^{\frac{1}{2}} \exp(\frac{-E_b - E_s}{k_B T}). \tag{5.6}$$

τ_{Nucl} is the number of nucleation events, multiplied by the time required for each nucleation event (equivalent to the inverse of the nucleation rate, I). This leads to,

$$\tau_{Nucl} = D T^{-\frac{1}{2}} \exp(\frac{E_b + E_s}{k_B T}), \tag{5.7}$$

which includes two free parameters, namely D which contains the size dependence of τ_{Nucl} and has units of [s $K^{\frac{1}{2}}$], and the energy barrier $E_b + E_s$.

Table 5.1 contains the values of D and $E_b + E_s$ found by fitting the data for R=12 and R=16. As a rule, changing D shifts the fit up or down, while manipulating E_b affects the curvature of the fit. Subtracting the 0.6 eV activation energy from the fitted values (1.41 and 1.48 eV) gives the nucleation barriers $E_{b,R=12} = 0.81$ eV and $E_{b,R=16} = 0.88$ eV on the (001) planes. The greater value of E_b for larger clusters is in agreement with the expectation that smaller curvatures have smaller differences in chemical potential, leading to larger nucleation barriers [68] (cf Equation 5.2). Combe [68] suggests the nucleation barrier is inversely proportional to curvature (equivalently proportional to radius) thus predicting a ratio $\frac{E_{b,R=12}}{E_{b,R=16}} = 0.75$. We find a ratio of $\frac{0.81}{0.88} = 0.92$, disagreeing with the prediction [68], most likely due to faceting and the discontinuous curvature. Note that as relaxation progresses for clusters with (001) intersections, facets at the ends of the clusters (which need to be transferred onto the neck region for relaxation) get larger, which increases the maximum of the free energy barrier (see discussion in Section 5.1).

Prefactor values of $D_{R=12} = 2.5 \times 10^{-18}$ m^{-2} and $D_{R=16} = 3.0 \times 10^{-18}$ m^{-2} give the best fits to the data, but we lack an understanding why $D_{R=12} < D_{R=16}$. Larger clusters require more nucleation events to relax, purely because they fill a greater volume, suggesting a linear size dependence, $\tau_{Nucl} \propto R$. Larger clusters also have greater surface area, increasing the nucleation probability, and suggesting $\tau_{Nucl} \propto \frac{1}{R^2}$. An appropriate expression for the nucleation time then is $\tau_{Nucl} \propto (\frac{R}{a})(\frac{1}{R^2})\frac{1}{I}$, where the first term corresponds to the space filling argument including the lattice constant a to keep the term dimensionless, and the second term allows for the greater surface area of larger clusters. The last term is just the inverse nucleation rate. Cancelling the factors of R, the above expression predicts τ_{Nucl} is inversely proportional to cluster size, contrary to the results of Table 5.1 (where $D_{R=16} > D_{R=12}$).

Another problem is the expected magnitude of the prefactor D. Mullins [37] has provided an upper bound for the prefactor in Equation 5.5 of $A = 1 \times 10^{31}$ m^{-2} s^{-1}, which after extracting temperature dependent terms and converting units into nm reduces to 2×10^{12} [nm^{-2} s^{-1} K$^{-\frac{1}{2}}$]. Including an approximate value for the cluster radii of 6 nm, the above expression suggests a *lower* limit of the prefactor in Equation 5.6 to be $D \approx 3 \times 10^{-13}$ [s K$^{\frac{1}{2}}$]. Comparing this to the values in Table 1.1, the prefactors found by fitting the data points are five orders of magnitude *smaller* than the lower limit. This suggests the nucleation rate in the simulations is at least five orders of magnitude higher than predicted by Equation 5.6. An explanation for this discrepancy is yet to be found.

Lastly we discuss the variations in τ_{eq} for simulations using different random number seeds. For low temperatures and large cluster radii, extra simulations have shown τ_{eq} to vary by $\approx$ 15%, relatively insignificant when using log scales as in Figure 5.15. As a comparison, equilibration times at T=375K and T=400 K vary by $\approx$ 400% depending on intersection plane and cluster size, swamping variations due to number seeds. Comparable fits to the ones shown in Figure 5.15 can be produced when changing D by 20% and E_b by 0.01 eV, suggesting the energy barriers are accurate within a few percent. The accuracy of D may be improved by performing simulations at lower T, as better estimates of both E_b and D would be required to match the data points. Simulations at lower temperatures require prohibitively large runtimes, and for this reason were not included in this work.

5.3.5 Coalescence of Faceted Clusters

Snapshots (Figures 5.5, 5.11) at relatively early stages in the coalescence of spherical clusters show facets quickly developing on the cluster surface, but the question

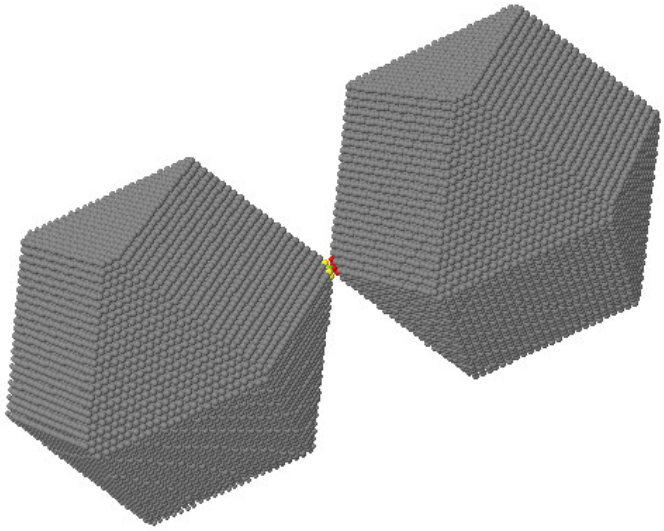

Figure 5.16: Initial configuration of two truncated octahedrons which was used to study the coalescence of faceted clusters. Note the apex of the neck contains a single atom.

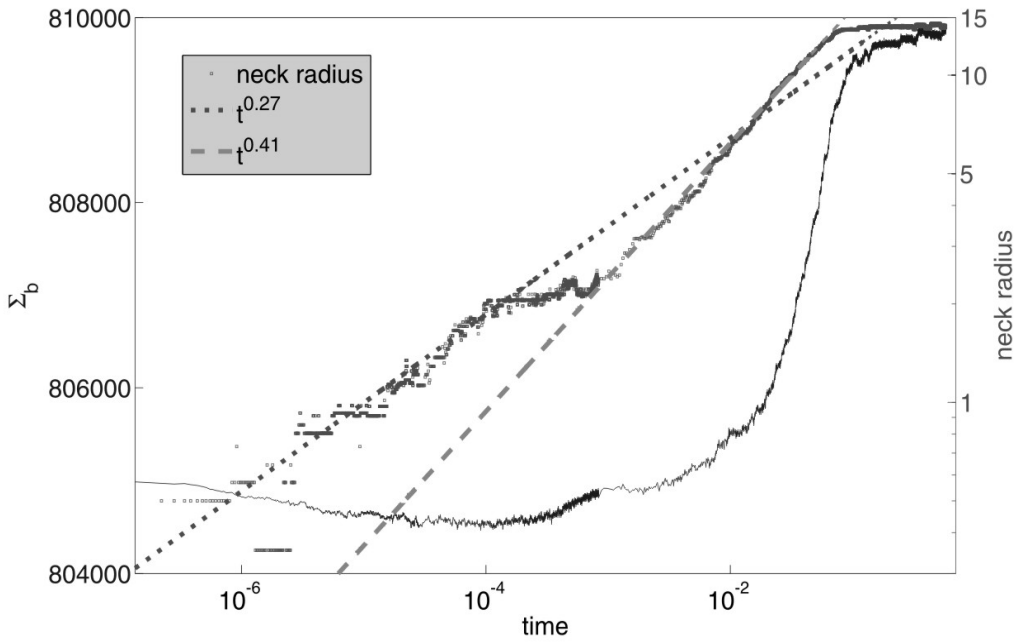

Figure 5.17: Radius and $\Sigma_b(t)$ plotted in the usual format. Coalescence is for T=400 K, for two R=16 clusters. Note the exponents used to fit the log(r) data at early and late stages have different values to those seen for spherical clusters.

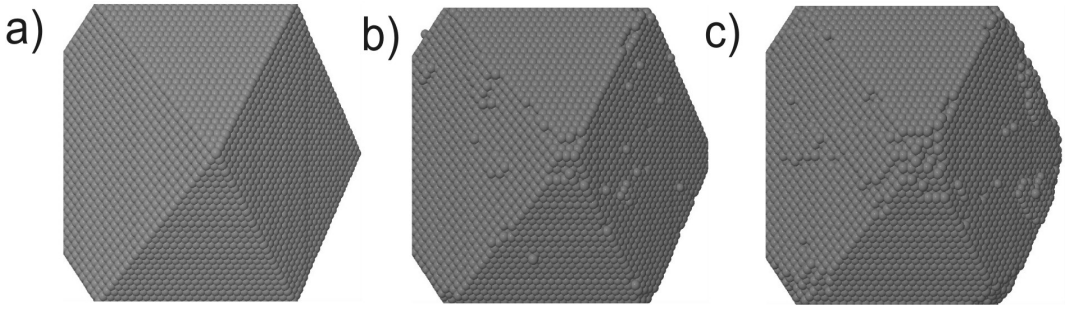

Figure 5.18: With the cluster pair side-on, a single cluster is viewed, with the neck region out of frame and to the left of each image. Images are taken at t=0, $4 \times 10^{-5}, 6 \times 10^{-5}$ s during the coalescence of the clusters of Figure 5.17. The images show the dissociation of atoms from cluster vertices during early stages.

still remains to what degree has the imposed initial shape affected the coalescence. To test this, the code was adjusted to simulate the coalescence of two truncated octahedrons, shown in Figure 5.16. These faceted clusters have large (001) and (111) planes on the surface, so for small initial neck radii the clusters must intersect at the cluster vertices ((110) intersection plane). To draw direct comparisons between the faceted and spherical scenarios, spherical clusters coalescing with (110) intersections were also simulated.

An example of the typical development of log(r(t)) and $\Sigma_b(t)$ is shown in Figure 5.17, for two faceted, R=16 clusters at T=400 K. Fitted exponents are included to illustrate the slopes of log(r(t)). The early stage exponent is $a \sim \frac{1}{4}$ (compared with $a = \frac{1}{3}$ for spherical clusters), and for $t \leq 1 \times 10^{-4}$ s, $\Sigma_b(t)$ actually decreases. The initial growth stage lasts until $r \approx 2$, at which point the radial development pauses for a short period. $\Sigma_b(t)$ increases slightly during the pause, suggesting material is rearranging into a more energetically favourable configuration. Beginning at $t \approx 1 \times 10^{-5}$ s the neck growth resumes and can be fitted with a comparatively large exponent $a = \frac{1}{2.5}$ ($a = \frac{1}{5}$ for spherical clusters). Beyond $t \approx 1 \times 10^{-5}$ s $\Sigma_b(t)$ increases slowly until $t \approx 1 \times 10^{-2}$ s, at which point the increase accelerates.

Each of the three major stages of log(r(t)) are examined more carefully using a series of snapshots. For the case of spherical clusters, high curvature at the neck and a large number of loosely bound atoms contributed to an initially steep slope for log(r(t)). With faceted clusters, material must dissociate from sites of high coordination in order for atoms to contribute to the neck region's growth. Figure 5.18 views a vertex from one of the two clusters of Figure 5.17, showing that atoms located at vertices and edges are removed during early coalescence stages. This sequence of dissociation followed by diffusion takes longer than pure diffusion, providing a simple explanation for the slower increase of r(t) for faceted clusters.

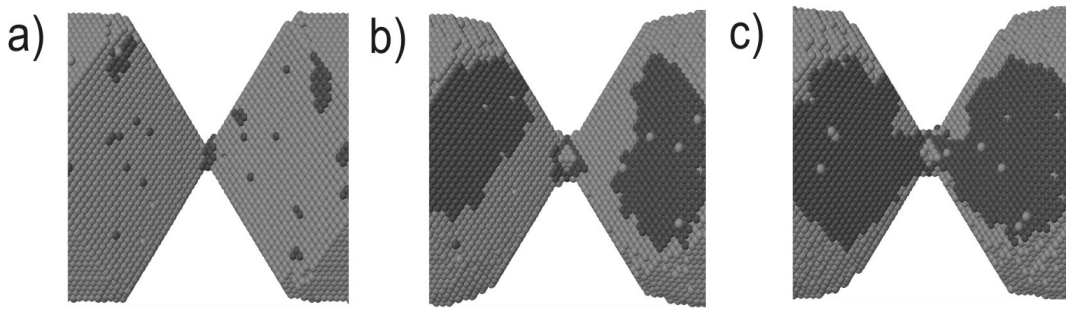

Figure 5.19: Images of the neck region taken at t=$1.5 \times 10^{-4}, 5 \times 10^{-4}, 1 \times 10^{-3}$ s during the coalescence of the clusters of Figure 5.17. Atoms sitting on the initial (001) surface layer are shaded a darker colour.

Figure 5.19 contains three images of the neck region during the 'pause' (t=$10^{-4} \rightarrow 10^{-3}$ of Figure 5.17), the final image taken when log(r(t)) begins to increase. Figure's 5.19 (a) and (b) show the number of atoms (dark coloured atoms) on (001) planes adjacent to the neck increasing, with many dimers and small islands visible. To reach the neck atoms must diffuse across the (001) planes, but due to the large number of diffusing atoms these (001) planes are quickly saturated with germs (see Figure 5.19 (a)), preventing material from reaching the neck. Hence the pause in log(r(t)) is likely due to competition with nucleation on (001) planes adjacent to the neck, i.e. the small number of high coordination sites at the neck limits its ability to capture material. Once the (001) islands attach to the neck in Figure 5.19 (c), log(r(t)) in Figure 5.17 begins to increase. When the (001) islands attach to the neck the number of five fold coordinated sites around the neck substantially increases, and neck growth becomes favoured over nucleation on adjacent (001) planes.

After t = 1×10^{-3} s in Figure 5.17 the neck develops a profile consisting of four (111) and two (001) planes. Figure 5.20 consists of three snapshots taken while $r(t) \propto t^{0.41}$. The cluster pair has been rotated to give a clearer view of the (001) and (111) planes on the neck circumference. In contrast to the images shown in Figure 5.19, there is no evidence of island nucleation on (001) planes *adjacent* to the neck. Atoms diffusing onto the neck are preferentially situated at sites where (001) and (111) planes intersect. Layers of (111) atoms develop across the neck region from both clusters in a similar manner to the period between Figures 5.11 (c) and (d) for spherical clusters with (111) intersections. The (111) layers continue growing across the neck region until the object's length is dominated by (111) planes, at which point relaxation halts (discussed in detail later).

Figure 5.21 shows radial and $\Sigma_b(t)$ coalescence data for several (110) intersection cases, using faceted *and* spherical clusters. Due to the absence of loosely bound atoms for the faceted case, all of the simulations were performed at T=500 K to help

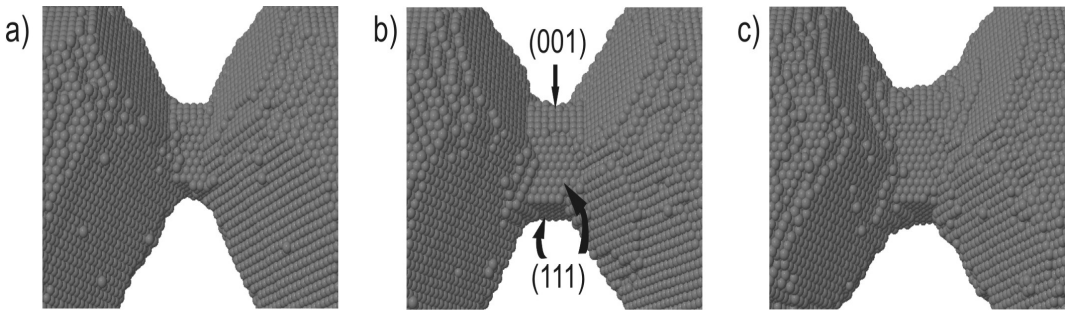

Figure 5.20: A zoomed in series of snapshots taken with the cluster pair side-on, though the clusters have been rotated slightly to view both the (001) and (111) planes at the neck, highlighted in (b). Images are taken at t=$2 \times 10^{-3}, 4 \times 10^{-3}, 8 \times 10^{-3}$ s of Figure 5.17, illustrating the rapidly growing neck.

speed the coalescence. Figure 5.21 contains data for spherical and faceted clusters in the left and right hand columns respectively. Considering the data for spherical clusters, log(r(t)) exhibits the major trends seen for (001) intersection cases (refer T=500 K examples of Figure 5.7) i.e. early stage slopes are fitted with exponents of a = 1/3, reducing for middle stages to a = 1/5, and continuing on this slope until reaching a plateau. Consistent with Figure 5.17, the early stages for faceted clusters can be fitted using an exponent of a $\approx$ 1/4 (not shown to reduce clutter in the diagrams), and middle stages by a $\approx$ 0.37. The transition from a $\approx$ 1/4 to a $\approx$ 0.37 coincides with a brief plateau in log(r(t)), though it is less apparent than when T=400 K (Figure 5.17). Surprisingly, given the differing exponents fitting the spherical and faceted cases, the time when log(r(t)) plateaus is comparable for spherical and faceted clusters of equal size.

From the log(r(t)) data, faceted clusters follow the a = 0.37 exponent after r = 2, while spherical clusters tend to the a = 1/5 exponent after r = 5. To ascertain reasons for the different exponents, Figure 5.22 contains snapshots of spherical and faceted clusters coalescing between r = 8 and r = 10.8, for the simulations plotted in Figures 5.21 (c) and (e). The most obvious difference in Figure 5.22 is the greater amount of curvature around the neck for spherical clusters. Using Jmol to compare the lengths of each cluster pair, the faceted clusters are roughly 5% longer when r = 8. Comparing the absolute time each scenario takes to move from r = 8 $\rightarrow$ r = 10.8 (see Figure 5.21), the spherical clusters require 3.5×10^{-4} s, while the faceted clusters require 6.7×10^{-4} s. Hence the higher curvature exhibited by spherical clusters promotes faster growth of the neck region, because more atoms are loosely bound atoms and able to diffuse. Importantly, the analysis illustrates the large exponent a = $\frac{1}{2.5}$ observed for faceted particles is not due to rapid coalescence.

At the neck radii shown in Figure 5.22, both spherical and faceted clusters coalesce

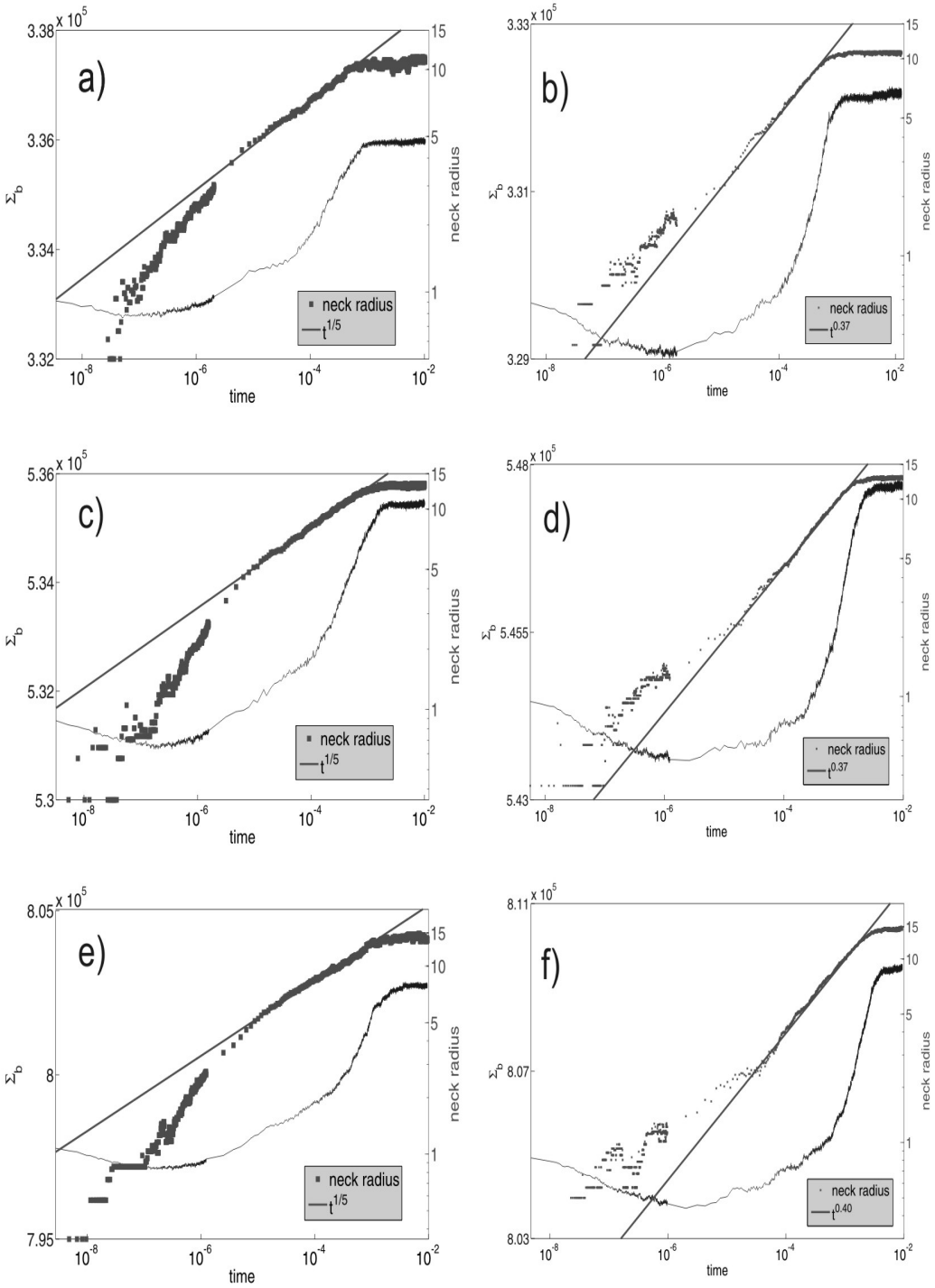

Figure 5.21: Plots of neck radius data and $\Sigma_b(t)$ for clusters coalescing at the (110) plane. Results from spherical clusters are shown in the lefthand column a) R=12, c) R=14, e) R=16. The results from faceted clusters are in the righthand column b) R=12, d) R=14, f) R=16. Simulations were performed at 500 K. The legend contains the exponent used to fit the radial data.

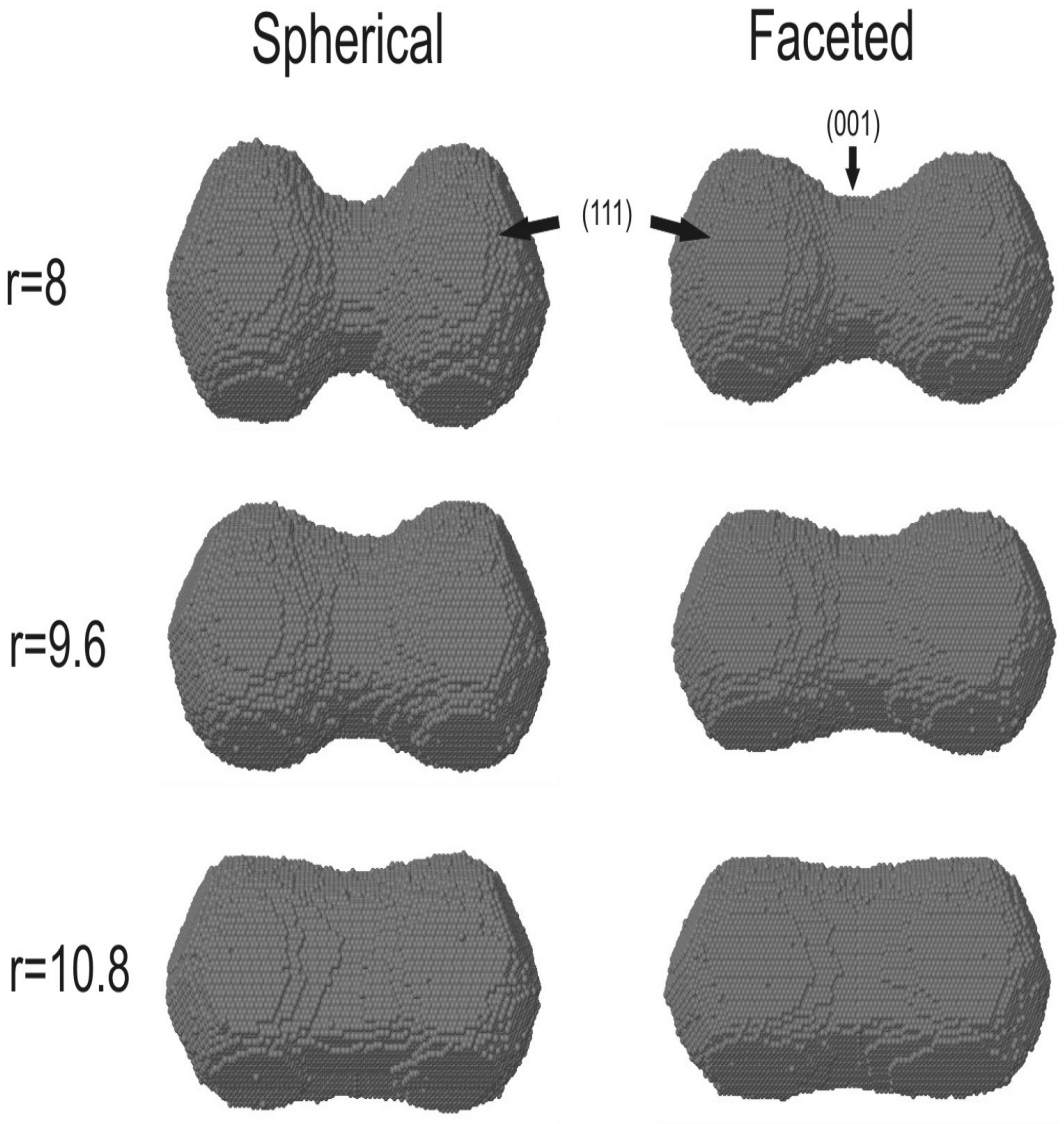

Figure 5.22: Snapshots taken during the coalescence of spherical and faceted cluster pairs, at r=8, 9.6, and 10.8. (111) and (001) planes are labeled, the images illustrating the development of (111) layers across the neck region during coalescence.

via the extension of (111) layers across the neck region, yet the slopes of log(r(t)) for each case are fitted with different exponents. The initially slow coalescence of the faceted particles (due to requirement for dissociation) effectively delays the point at which coalescence starts. Hence the t_0 for faceted particles is most likely different to the spherical clusters, leading to the different exponents $a = \frac{1}{5}$ (spherical) and $a \sim \frac{1}{2.5}$ (faceted).

A feature common to all the $\Sigma_b(t)$ plots (particularly the faceted clusters), which was not obvious for (001) (Figure 5.7) and (111) (Figure 5.13) intersections, is the initial decrease of $\Sigma_b(t)$. From an energetics point of view this simulates the unrealistic situation of the cluster pairs moving into a less thermodynamically favourable state i.e. more bonds are broken in the initial stages than new ones are created. Some justification for allowing this to occur is that the clusters are forced to take non-equilibrium shapes from the outset. Clusters are forced to intersect at desired planes (i.e. (001), (111), or (110)), yet the contact region is non-smooth. The situation is clearly worse for faceted clusters, as they have a number of sharp edges and vertices. The decrease of $\Sigma_b(t)$ only occurs for very small neck radii, as the rearrangement of surface atoms quickly smooths the curvature at the neck and around the surface, and typically once a value of $r = 1$ is reached the clusters act to reduce the surface area, leading to an increase in $\Sigma_b(t)$.

Irrespective of the choice of variables (R and T, spherical or faceted clusters), when clusters intersect at (110) planes the neck radius plateaus at a value less than $2^{1/3}R$. Aspect ratios approach 0.5, at which the object surface is characterised by large (111) facets along its length. Figure 5.23 shows the faceted shape common to all the simulations of Figure 5.21. Recalling the initial configuration of the clusters (Figure 5.16), across the neck region planes of like index match up i.e. (111) opposite (111), (001) opposite (001). Diffusion on (001) planes is slower than on (111) planes, consequently the (001) planes capture more material (see Figure 5.19). (001) planes grow new layers more quickly, but the edges terminate at (111) planes and so the size of adjacent (111) planes grows. Consequently there is a reduction in width of (001) planes, and increased widths of (111) planes. As coalescence proceeds, the clusters length develops four broad (111) planes and two narrow (001) planes.

Achieving a more relaxed state than that shown in Figure 5.23 requires new facets to nucleate on the (111) planes. (111) planes are relatively stable, as edge atoms typically have six or seven neighbours, hence the configuration of Figure 5.23 provides few weakly bound atoms to nucleate new planes (note the lack of free atoms on the facets). Sites on (111) planes have lower coordination than sites on either (001) or (110) planes, and consequently nucleation of new atomic layers is

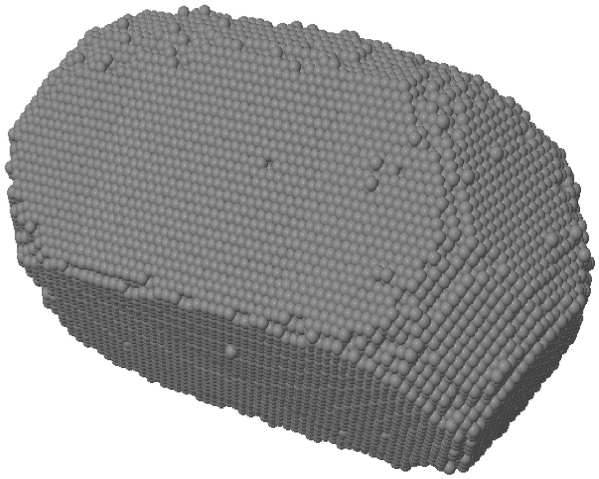

Figure 5.23: Final morphology for clusters intersecting at (110) planes. Note the large (111) planes along the object length, and at the ends. The top (and bottom) planes are (001).

more difficult. A germ consisting of three atoms on a (111) plane has comparable stability to a germ of two atoms on a (001) plane (using a neighbour counting exercise). The probability of three atoms collecting together is small compared with the probability of two atoms collecting on one of the (001) planes, especially when the number of diffusing atoms is low. These two problems, low densities of diffusing atoms and high nucleation barriers, act together to leave the cluster in a kinetically limited state. It is expected that increasing the temperature above 500 K would promote the nucleation of new atomic layers on (111) planes, and relaxation of the cluster.

Effect of varied initial neck size

Sections 5.3.2 and 5.3.5 investigated coalescence for clusters initially connected by a small ($\approx$ 2 atoms in diameter) neck. A fair assumption for films produced by cluster deposition techniques is for deposited clusters to impact on the film with high velocity, causing deformation at the neck region. Depending on the degree of deformation, clusters will begin coalescing with different neck radii. We briefly investigate coalescence of R=14 spherical clusters for initial neck sizes of r <1, 3, 5, and 7 lattice spacings, intersecting at the (001) plane. All the simulations were performed at T=500 K.

Figure 5.24 contains the plots of log(r(t)) and $\Sigma_b(t)$ for several initial neck radii, along with snapshots for $r_0 = 3$ and $r_0 = 7$. Figure 5.24 (a) is the same as Figure 5.7 (c), and has a fitted exponent of $a = \frac{1}{5}$ for middle and late coalescence stages.

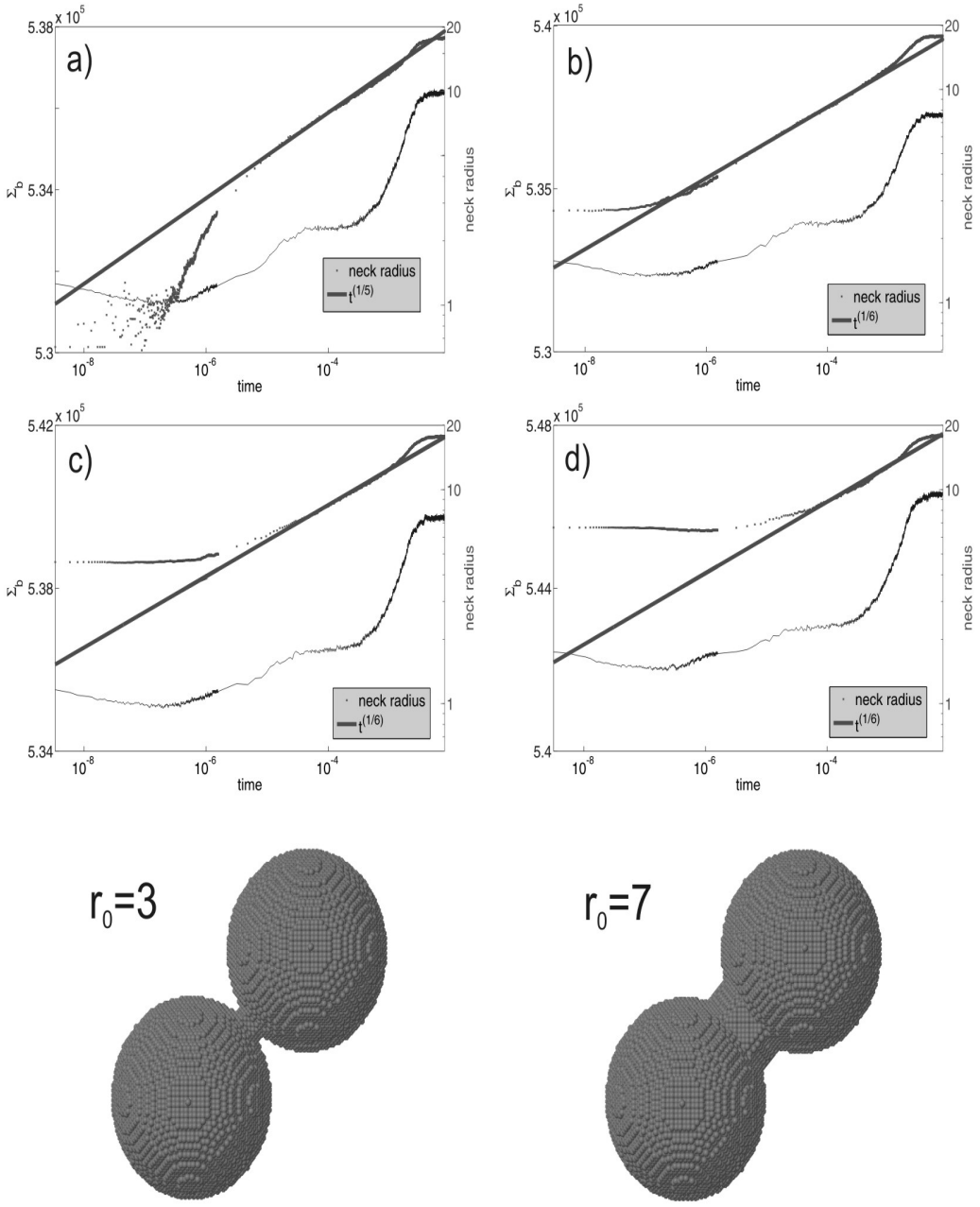

Figure 5.24: Data plots are shown for difference initial neck radii (a) $r_0 < 1$, (b) $r_0 = 3$, (c) $r_0 = 5$, and (d) $r_0 = 7$. The clusters are R=14, intersecting at (001) planes, and T=500 K. Two snapshots are shown at t = 0 to illustrate how the neck is defined.

Figures 5.24 (b), (c), and (d) can be fitted with $a = \frac{1}{6}$ for at least some period during coalescence, generally the fits are poorer for larger r_0. At early stages, the clusters with small necks show large changes in r, while clusters with large necks maintain a steady value. It appears the system requires a period of time (during which some rearrangement is occurring) before the neck begins to expand, the length of this period increases with r_0. The introduction of larger neck sizes has little effect on the time the cluster pairs take to coalesce, typically these times are 2.6×10^{-3}s.

5.4 Cluster Coalescence Summary

In this chapter the coalescence of atomic clusters via anisotropic surface diffusion has been investigated. A simple model was developed which allowed atoms to diffuse on the cluster surface, at rates dependent on the number of atomic neighbours. The model reproduces theoretical predictions of particle size dependences at T=500 K for clusters intersecting at (001) and (111) planes, below this temperature surface faceting causes kinetic effects to increase coalescence times beyond the expected times of Equation 5.1.

The motivation for studying kinetically limited coalescence came from studies [68, 131] on the importance of nucleation in the relaxation of nanoscale objects. Kinetic effects during cluster coalescence had not been studied in detail, and this work investigates the kinetics using an atomistic model, differing from the continuum and MD methods used in previous investigations of neck growth and coalescence times.

Section 5.3.2 shows early coalescence stages for spherical clusters are not inhibited by kinetics within the range T= 400 $\rightarrow$ 500 K. The initial configuration of the clusters creates high curvature at the neck, and a large number of weakly bound atoms distributed across the cluster surface, resulting in a large atomic flux to the neck region. Material diffusing into the neck is locked in place by additional material, and neck growth occurs quickly. As a general observation, the sphere$\rightarrow$dumbell$\rightarrow$ovoid$\rightarrow$sphere results of previous MD studies [128, 129] are corroborated.

For temperatures below 500 K and at late stages of coalescence, spherical clusters intersecting at (001) planes (Figure 5.7 (a), (c), (e)) exhibit kinetic effects i.e. increased relaxation times, and stepped features in $\Sigma_b(t)$ associated with the nucleation or dissociation of atomic layers. Figure 5.5 (d) shows the presence of large (001) facets during this period, where sites are only four-fold coordinated. Nucleation events on bare facets have longer timescales than relaxation due to pure diffusion, consequently increasing the relaxation time beyond the prediction

of Equation 5.1. An Arrhenius analysis of τ_{eq} for these clusters found nucleation barriers of 0.81 eV and 0.88 eV respectively for R=12 and R=16 clusters. Greater nucleation barriers for larger particles is in agreement with [68, 131], however our fitted prefactor disagrees with [131].

Contrasting the temperature dependent equilibration times for clusters with (001) intersections, clusters intersecting at (111) planes (Figure 5.13) closely follow the predictions of Equation 5.1. Snapshots in Figure 5.11 show stepped features around the object's circumference at late stages of coalescence, the steps preventing the need for new atomic layers to nucleate in order for further relaxation. The initial orientation causes bare (001) planes to intersect (111) planes at the neck, allowing the step features to develop. An Arrhenius analysis of equilibration times for clusters intersecting at (111) planes produced an activation energy of $E_A = 0.6$ eV, the energy barrier limiting detachment of atoms from a facet edge. An interesting note, $E_A = 0.6$ eV compares with a measured $E_A = 0.7$ eV for atom detachment from islands on Ag(111) surfaces [145]. If dissociation of islands is the rate limiting step for coalescence of Ag clusters, then our simplistic KMC model may provide an accurate approximation to the coalescence.

Clusters intersecting at (110) planes coalesce differently to both the above examples. Due to the initial configuration, the development of large (111) planes along the cluster length is favoured, leading to an object dominated by four broad (111) planes and two smaller (001) planes (Figure 5.4). For temperatures between 400 K and 500 K, the relaxation of these objects is not possible, due to the prohibitively high nucleation barrier on (111) planes. According to results of Combe [68], full relaxation of clusters with large (111) planes should be possible at 800 K, and an Arrhenius analysis at these higher temperatures may provide a nucleation barrier on the (111) planes.

Comparing the results from the differing orientation scenarios, it is apparent that the initial cluster configuration determines the path to relaxation. For coalescence at (110) intersections, the higher nucleation rates of (001) and (110) planes results in the relatively slow growing (111) planes covering a large percentage of surface area, locking the system into a unrelaxed state due to the high nucleation barrier on (111) planes. Clusters at (111) intersections coalesce via a step growth mechanism which avoids significant nucleation, hence coalescence with these intersections occurs over a much larger temperature range. Clusters intersecting at (001) planes develop large (001) planes along the cluster length during coalescence, the nucleation barrier sufficiently small as to allow coalescence at T=400 K.

Radial development of the neck region was monitored for all the coalescence

scenarios. Table 5.2 provides a summary of the power law exponents observed in the simulations of spherical clusters. Irrespective of the cluster size or plane of intersection, in the initial stages of coalescence it was found that $r \propto t^{1/3}$. Snapshots of the clusters during early periods (Figures 5.5 and 5.11) show the neck region to be highly curved, providing high coordination sites for material diffusing from the cluster ends. The $a = \frac{1}{3}$ exponent is maintained until $r/R \approx 0.3$, when the apex of the neck is intersected by broad planes. A reduction in surface energy continues driving material into the central region, expanding the neck, but the smaller curvature makes neck growth more difficult.

Simulations at T=500 K show log(r(t)) fits an $a = \frac{1}{5}$ exponent after $r/R \approx 0.3$, while for simulations at T=400 K (Figures 5.7 and 5.11, (a), (c), (e)), the fitted exponent drops from $a = \frac{1}{3}$ to a value smaller than $a = \frac{1}{5}$. The period is depicted in Figures 5.5 and 5.11 (c)→(d), when the neck is characterised by a small number of capture sites, therefore the limiting process to relaxation is capture at the neck. Clearly the smaller exponent when T=400 K implies a greater difficulty in growing the neck during this phase at low temperature. Hence the period characterised by broad planes intersecting at the neck region is kinetically limited at T=400 K, a limitation which should be more apparent at lower temperature.

Once the neck region develops sufficient capture sites (Figures 5.5 and 5.11 (d)), the exponents fitting log(r(t)) at T=400 K increase to $a \sim= \frac{1}{3}$. For clusters with (111) intersections, the development of steps around the neck at $r/R \approx 0.7$ allows easy capture of atoms from the extremities, and the $a = \frac{1}{3}$ exponent is maintained until coalescence finishes for both T=400 K and T=500 K. Clusters with (001) intersections maintain the respective exponents ($a = \frac{1}{3}$ T=400 K, $a = \frac{1}{5}$ T=500 K) until $r/R \approx 0.9$ (see Figures 5.7 (a) and (b)), when the ovoid shape is achieved and large (001) planes are present. Here the exponent fitting log(r(t)) drops to $\sim 1/16$ at T=400 K, while for T=500 K log(r(t)) increases faster than the $a = \frac{1}{5}$ line.

Nichols [126] gives exponents that fall within a tight band, ranging from 1/5.9 when $\frac{r}{R} \sim 0.05$, to 1/6.9 at $\frac{r}{R} \sim 0.60$. Recalling the exponent $a = \frac{1}{7}$ predicted by Kuczynski and Eggers for continuous surfaces and isotropic diffusion, clearly different to the exponents we observe from the KMC model (Tab 5.2), where anisotropic diffusion is inherent. Recent work by Hendy [146] recalculates the radial profile for two spheres coalescing via the same mechanics as those of Eggers and Nichols. In this new work, the neck radius develops as $r \propto t^{0.3}$ for $r/R \geq 0.05$, reducing to $r \propto t^{0.2}$ when $r/R \geq 0.30$. Hendy's result is remarkably similar to the case of two spherical KMC clusters intersecting at an (001) plane.

Truncated octahedra intersecting at (110) vertices show (Figure 5.17) a small

Exponent	Limiting Process
$\frac{1}{3}$	early stages for all intersections and temperatures, high curvature and loosely bound atoms promotes fast neck growth
$\sim \frac{1}{6}$	Figure 5.5 and 5.11 (c)→(d) T=400 K, faceting at slows coalescence due to the small number of capture sites at the neck
$\frac{1}{3}$	Figure 5.5 (d)→(e) T=400 K, more capture sites at the neck enhance coalescence, now limited by dissociation of the end layers
$\frac{1}{5}$	Figure 5.5 (c)→(e) T=500 K, the higher temperature increases dissociation producing a more consistent log(r(t)) development, repeated for (110) intersections shown in Figure 5.21
$\frac{1}{16}$	Figure 5.5 (e)→(f) T=400 K, a high nucleation barrier on (001) facets slows relaxation
$\frac{1}{3}$	Figure 5.5 (e)→(f) T=500 K, near the roughening temperature on (001) facets therefore coalescence is limited by dissociation
$\frac{1}{3}$	Figure 5.11 (d)→(e), dissociation of end layers limits the speed at which stepped features extend across cluster
~ 0	plateau of log(r(t)) in Figure 5.21 at $\frac{r}{R} < 1$ due to (111) facets preventing coalescence at T $\leq$ 500K

Table 5.2: The table lists the power law exponents fitting log(r(t)) at different coalescence stages for spherical clusters of each temperature and intersection scenario. A description of the rate limiting process at each stage is provided.

exponent ($a = \frac{1}{4}$) for early neck growth early stages, which increases to $a = \frac{1}{2.5}$ after a brief pause in the development of log(r(t)). The small early stage exponent was related to the dissociation of atoms from vertices and edges of the clusters, which delayed the onset of coalescence. The pause in log(r(t)) was identified as a period when the neck region competed for material with adjacent (001) planes. Although after the pause log(r(t)) exhibited the highest observed exponent for any coalescence scenario, the steep slope was related to the delayed onset of coalescence. During the dumbell→ovoid stages, truncated octahedra were in fact shown to have smaller radial velocities than their spherical counterparts.

Chapter 6

Conclusions and Outlook

Bi films grown on Mica, MoS_2, and HOPG substrates provide a direct illustration of how different island morphologies can be observed for otherwise equivalent growth conditions. Bi films on Mica displayed the highest island densities, typically with small circular island morphologies. For low flux, slow growth environments, a number of islands develop into oblong shapes, which are probably thermodynamically favoured. On MoS_2 substrates, with lower island densities, broader hexagonal islands are preferred. The points of the hexagons are slightly distorted at higher coverage, a manifestation of the Mullins-Sekerka instability. On HOPG substrates, which yield the lowest island density, islands are still larger leading to enhanced instabilities and dendritic island morphologies.

The hexagonal island morphology commonly found on MoS_2 substrates was also observed on HOPG substrates at extremely low flux [13]. Features such as island striping at low coverage, and trigonal morphologies at high coverage suggest Bi films on MoS_2 and HOPG substrates have the same crystallography, i.e. the Bi$\{01\bar{1}2\}$ plane orients parallel to the substrate surface.

Bi islands nucleating on HOPG terraces favour a 1D morphology at low flux and high temperature. A comparison of the 1D islands and morphologies of rods growing at step-edges of the HOPG found the two structures to be closely related. The high substrate temperature therefore has a similar effect on crystal morphology as the locally reduced flux at step edges. The 1D shape results from anisotropic bonding to edges of the Bi$\{01\bar{1}2\}$ crystal plane, with unsatisfied intralyer bonds at rod tips, and unsatisfied interlayer bonds at the rod sides.

Bi island densities on HOPG were measured as functions of flux and temperature. The flux dependence of the island density proved island nucleation was homogeneous, and strongly suggested cluster diffusion is activated. Island densities were plotted using an Arrhenius analysis, the island density determined to have an activation

energy of 0.06 eV. The extremely low island densities could not be explained using classical nucleation theory, though we believe the combination of adatom desorption, and the diffusion of self-assembled clusters, is a likely reason for the measured density.

ARs of step-nucleated Bi rods on HOPG substrates were studied with variations in the substrate temperature, and found to have an Arrhenius dependence with activation energy $E_A = 0.10$ eV. KMC simulations of structures growing from step-edges via two different mechanisms (anisotropic corner crossing or attachment/detachment), were found to have activation energies $E_A = \chi E_c^{A \to B}$ or χE_D^A, where $E_c^{A \to B}$ and E_D^A are the effective detachment barriers from rod sides. The parameter χ was found to range between $\sim 1/2$ and $\sim 1/3$, depending on the magnitude of the effective detachment barrier. Applying the scaling relation devised from the simulations to the experimental results, we calculate an attachment energy for Bi dimers at rod sides between ~ 0.2 and 0.3 eV.

An investigation of rod coalescence for the corner crossing and detachment models found that pairs of rods growing via the attachment/detachment mechanism slow as they approach one another, whereas for the corner crossing model there was no apparent slowing. Rods grown in experiment display a similar competitive capture effect, suggesting that the Bi rods grow via the attachment/detachment mechanism.

The coalescence of crystalline clusters via surface diffusion was investigated using a KMC algorithm. An analysis of the neck radius r as a function of simulation time found characteristic power laws for early stage, middle stage, and late stages of coalescence. For initially spherical clusters, the neck region has high curvature, and we find $r(t) \propto t^{1/3}$ for early coalescence stages. During the middle coalescence stages, when facet nucleation is required about the neck, we find $r(t) \propto t^{1/5}$ or $r(t) \propto t^{1/6}$. At late coalescence stages, when relaxation is limited by the dissociation and nucleation of large facets, radial development is sensitive to temperature, and cluster size.

In the simulations the intersection plane of two clusters determines which planes dominate the surface during the middle stage. Since planes of different orientation have different nucleation barriers, the middle and late stages of coalescence were affected by the initial configuration. Clusters intersecting at (111) planes coalesced via a step flow mechanism. Clusters intersecting at (110) planes however develop large (111) surface planes, on which nucleation is difficult, thereby leaving the cluster in a kinetically limited state.

An investigation of the coalescence of truncated octahedra found power laws for the neck radius have different exponents to the spherical cluster simulations. During early coalescence stages faceted clusters dissociate atoms from edges and vertices.

The dissociation occurs slowly because of the small number of high coordination sites at the neck. This effectively delays the coalescence, and is the reason for the observed difference in powerlaws.

Outlook

New experiments are currently underway to compare the morphology of low temperature bismuth films grown on HOPG to films grown at T > 100°C, and films annealed at T > 100°C post-deposition [147]. Interestingly, desorption appears to be a major factor for films grown at temperatures above 100°C. Preliminary results from high temperature depositions found structures with extremely high ARs (up to seventy) are favoured. Results comparing annealed films with unannealed, low temperature films indicates significant crystal rearrangements on annealing. Annealed films show isolated groups of 1D structures, which are believed to be the remnants of island stripes. The lack of a 2D island base suggests the base material has been incorporated into the stripes.

A new Scanning Tunneling Microscope equipped with a Knudsen Cell has been purchased by the group, which will allow the growth and characterisation of Bi films under vacuum. The STM will allow a more detailed characterisation of Bi film morphology on mica substrates. Atomic resolution should allow determination of the surface crystallography of the circular and oblong shaped morphologies. It will also allow electrical characterisation of Bi films, islands and rods.

An unanswered question from the Bi/HOPG island nucleation study is the role which cluster diffusion and adatom desorption play. The STM is equipped with a cryostat which allows depositions at substrate temperatures as low as 50 K. Measurements of the adatom diffusion length at low temperatures may determine the adsorption energy of Bi atoms to the graphite surface. Low temperature STM may observe the diffusion (and identify the sizes) of self-assembled clusters, and find the temperature at which cluster diffusion is activated. Such information may provide a novel method for growing size specific clusters on HOPG via self-assembly.

Bibliography

[1] C. B. Murray, C. R. Kagan, and M. G. Bawendi, Science **270**, 1335 (1995).

[2] http://www.intel.com/pressroom/archive/releases/20070918corp_a.htm.

[3] R. Edelstein et al., Biosensors & Bioelectronics **14**, 805 (2000).

[4] M. Ferrari, Nature Reviews **5**, 464 (2005).

[5] W. C. W. Chan and S. Nie, Science **281**, 2016 (1998).

[6] J. D. Hartgerink, E. Beniash, and S. I. Stupp, Science **294**, 1684 (2001).

[7] S. I. Stupp and P. V. Braun, Science **277**, 1242 (1997).

[8] K. G. Libbrecht, Reports on Progress in Physics **68**, 855 (2005).

[9] Z. Zhang, X. Sun, M. S. Dresselhaus, J. Y. Ying, and J. Heremans, Physical Review B **61**, 4850 (2000).

[10] Z. Zhang, X. Sun, M. S. Dresselhaus, J. Y. Ying, and J. P. Heremans, Applied Physics Letters **73**, 1589 (1998).

[11] J. Heremans et al., Physical Review B **61**, 2921 (2000).

[12] Y.-M. Lin, X. Sun, and M. S. Dresselhaus, Physical Review B **62**, 4610 (2000).

[13] S. Scott, *Self-Assembly of Sb and Bi Nanostructures on Graphite*, PhD thesis, University of Canterbury, 2005.

[14] T. Nagao et al., Physical Review Letters **93**, 105501 (2004).

[15] A. Patel, Journal of Materials Science (letters) **12**, 635 (1977).

[16] H. Ikemoto, T. Miyanaga, and T. Kiuchi, Journal of Non-Crystalline Solids **353**, 3394 (2007).

[17] J. Schmelzer, S. A. Brown, A. Wurl, M. Hyslop, and R. J. Blaikie, Physical Review Letters **88**, 226802 (2002).

[18] R. Reichel et al., Applied Physics Letters **89**, 213105 (2006).

[19] J. van Lith et al., Applied Physics Letters **91**, 181910 (2007).

[20] A. Lassesson, M. Schulze, J. van Lith, and S. A. Brown, Nanotechnology **19**, 015502 (2008).

[21] H. Brune, Surface Science Reports **31**, 121 (1993).

[22] J. A. Venables, G. D. T. Spiller, and M. Hanbucken, Reports on Progress in Physics **1984**, 399 (47).

[23] P. Jensen, Reviews of Modern Physics **71**, 1695 (1999).

[24] T. Ala-Nissila, Advances in Physics **51**, 949 (2002).

[25] S. Y. Liem and K.-Y. Chan, Surface Science **328**, 119 (1995).

[26] G. Ehrlich and F. Watanabe, Langmuir **7**, 2555 (1991).

[27] T.-Y. Fu, Y.-J. Hwang, and T. T. Tsong, Surface Science **566**, 462 (2004).

[28] G. Ayrault and G. Ehrlich, The Journal of Chemical Physics **60**, 281 (1974).

[29] G. Ehrlich and F. G. Hudda, The Journal of Chemical Physics **44**, 1039 (1966).

[30] M. Bott, M. Hohage, M. Morgenstern, T. Michely, and G. Comsa, Physical Review Letters **76**, 1304 (1996).

[31] J. A. Stoscio, D. T. Pierce, and R. A. Dragoset, Physical Review Letters **1993**, 3615 (70).

[32] G. L. Kellogg, Physical Review Letters **73**, 1833 (1994).

[33] O. S. Trushin, P. Salo, M. Alatalo, and T. Ala-Nissila, Surface Science **482**, 365 (2001).

[34] A. Pimpinelli and J. Villain, *Physics of Crystal Growth*, Cambridge University Press, 1998.

[35] S. Gunther, E. Kopatzki, M. Bartelt, J. Evans, and R. Behm, Physical Review Letters **73**, 553 (1994).

[36] M. Eden, in *Proceedings of the Fourth Berkeley Symposium on Mathematical Statistics and Probability*, edited by B. J. Neyman (University of California Press, volume 4, page 223, 1961.

[37] W. Mullins and R. Sekerka, Journal of Applied Physics **34**, 323 (1963).

[38] A. Pimpinelli and R. Ferrando, Physical Review B **60**, 17016 (1999).

[39] T. A. Witten and L. M. Sander, Physical Review Letters **47**, 1400 (1981).

[40] http://algorithmicbotany.org/vmm-deluxe/section-04.html.

[41] T. A. Witten and L. M. Sander, Physical Review B **27**, 5686 (1983).

[42] H. Brune et al., Surface Science **349**, L115 (1996).

[43] H. Brune, C. Romainczyk, H. Roder, and K. Kern, Nature **369**, 469 (1994).

[44] H. Roder, E. Hahn, H. Brune, J.-P. Bucher, and K. Kern, Nature **366**, 141 (1993).

[45] T. Michely, M. Hohage, M. Bott, and G. Comsa, Physical Review Letters **70**, 3943 (1993).

[46] F. Jona, Surface Science **8**, 57 (1967).

[47] H. Plank, R. Resel, A. Andreev, N. Sariciftci, and H. Sitter, Journal of Crystal Growth **237-239**, 2076 (2002).

[48] http://www.cathode.com/.

[49] http://www.omega.com/.

[50] H. Noh et al., Journal of Vacuum Science and Technology B **12**, 2097 (1994).

[51] G. S. Bales and D. C. Chrzan, Physical Review B **50**, 6057 (1994).

[52] S. Glasstone, K. J. Laidler, and H. Eyring, *The Theory of Rate Processes*, 1941.

[53] A. G. Naumovets and Z. Zhang, Surface Science **500**, 414 (2002).

[54] C. Mottet, R. Ferrando, F. Hontinfinde, and A. Levi, Surface Science **417**, 220 (1998).

[55] M. S. Daw and M. I. Baskes, Physical Review B **29**, 6443 (1984).

[56] R. Dreizler and E. Gross, *Density Functional Theory*, Plenum Press, 1995.

[57] H. Jonsson, G. Mills, and K. Jacobsen, *Classical and Quantum Dynamics in Condensed Phase Simulations*, chapter 16, page 385, World Scientific, 1998.

[58] T. P. Schulze, Physical Review E **65**, 036704 (2005).

[59] S. K. Park and K. W. Miller, Proceedings of the ACM (1988).

[60] S. A. Scott, M. V. Kral, and S. A. Brown, Physical Review B **72**, 205423 (2005).

[61] Y. Li et al., Physical Review B **56**, 12539 (1997).

[62] C. Heyn, Physical Review B **63**, 033403 (2001).

[63] A. F. Voter, *Radiation Effects in Solids: Introduction to the Kinetic Monte Carlo Method*, Springer, NATO Publishing Unit, Dordrecht, The Netherlands, 2005.

[64] P. Mulheran and J. Blackman, Surface Science **376**, 403 (1997).

[65] J. A. Blackman and P. A. Mulheran, Physical Review B **54**, 11681 (1996).

[66] C. D. Pownall and P. A. Mulheran, Physical Review B **60**, 9037 (1999).

[67] S. Hendy and T. Schulze, Private communication.

[68] N. Combe, P. Jensen, and A. Pimpinelli, Physical Review Letters **85**, 110 (2000).

[69] P. Jensen and N. Combe, Computational Materials Science **24**, 78 (2002).

[70] P. Jensen et al., The European Physical Journal B **11**, 497 (1999).

[71] C. R. Stoldt et al., Physical Review Letters **81**, 2950 (1998).

[72] A. L. Weisenhorn, P. N. Henriksen, H. T. Chu, R. D. Ramsier, and D. H. Reneker, Journal of vacuum Science Technology B **9**, 1333 (1991).

[73] Y. Komnik, Soviet Physics - Crystallography **16**, 352 (1971).

[74] A. A. Zav'yalova, Soviet Physics - Crystallography **14**, 305 (1969).

[75] E. I. Rogacheva, S. N. Grigorov, O. N. Nashchekina, S. Lyubchenko, and M. S. Dresselhaus, Applied Physics Letters **82**, 2628 (2003).

[76] H. Terajima, Japan Journal of Applied Physics **Supplementary 2, Part 1**, 571 (1974).

[77] B. Stegemann, B. Kaiser, and K. Rademann, New Journal of Physics **4**, 89 (2002).

[78] M. Volmer and A. Weber, Z. Phys. Chem **119**, 277 (1926).

[79] U. Becker, K. M. Rosso, R. Weaver, M. Warren, and M. F. Hochella, Geochimica et Cosmochimica Acta **67**, 923 (2003).

[80] S. Scott, M. Kral, and S. Brown, Surface Science **2005**, 175 (587).

[81] T. P. Darby and C. M. Wayman, Journal of Crystal Growth **28**, 41 (1975).

[82] T. P. Darby and C. M. Wayman, Journal of Crystal Growth **29**, 98 (1975).

[83] R. Anton and I. Schneidereit, Physical Review B **58**, 13874 (1998).

[84] R. Anton and P. Kreutzer, Physical Review B **61**, 16077 (2000).

[85] S. A. Scott, M. V. Kral, and S. A. Brown, Physical Review B **73**, 205424 (2006).

[86] S. Scott and S. Brown, The European Physical Journal D **39**, 433 (2006).

[87] B. Stegemann, C. Ritter, B. Kaiser, and K. Rademann, Journal of Physical Chemistry B **108**, 14292 (2004).

[88] B. Kaiser, B. Stegemann, H. Kaukel, and K. Rademannl, Surface Science **496**, L18 (2002).

[89] X. Wang, S. S. Kushvaha, Z. Yan, and W. Xiao, Applied Physics Letters **88**, 233105 (2006).

[90] S. J. Carroll, K. Seeger, and R. E. Palmer, Applied Physics Letters **72 (3)**, 305 (1998).

[91] L. Bardotti, P. Jensen, A. Hoareau, M. Treilleux, and B. Cabaud, Physical Review Letters **74**, 4694 (1995).

[92] L. Bardotti et al., Surface Science 367 (1996) 276-292 **367**, 276 (1996).

[93] F. Carlier et al., Nano Letters **6**, 1875 (2006).

[94] A. Lando, N. Keba?li, P. Cahuzac, A. Masson, and C. Brechignac, Physical Review Letters **97**, 133402 (2006).

[95] M. Schulze et al., The European Physical Journal D **24**, 291 (2003).

[96] J. M. Wen, S. L. Chang, J. W. Burnett, J. W. Evans, and P. A. Thiel, Physical Review Letters **73**, 2591 (1994).

[97] J. Villain, A. Pimpinelli, L. Tang, and D. Wolf, Journal of Physics 1 France **2**, 2107 (1992).

[98] W. D. Luedtke and U. Landman, Physical Review Letters **82**, 3835 (1999).

[99] L. J. Lewis, P. Jensen, N. Combe, and J.-L. Barrat, Physical Review B **61**, 16084 (2001).

[100] Y. Maruyama and J. Murakami, Physical Review B **67**, 085406 (2003).

[101] R. Otero, A. L. V. de Parga, and R. Miranda, Physical Review B **66**, 115401 (2002).

[102] R. Otero, A. L. V. de Parga, and R. Miranda, Surface Science **447**, 143 (2000).

[103] S. Liu, L. Bonig, and H. Metiu, Physical Review B **52**, 2907 (1995).

[104] P. Jensen and X. Blase, Physical Review B **70**, 165402 (2004).

[105] J. Zhong, T. Zhang, Z. Zhang, and M. Lagally, Physical Review B **63**, 113403 (2001).

[106] M. C. Bartelt and J. W. Evans, Physical Review B **46**, 12675 (1992).

[107] P. Jensen, X. Blase, and P. Ordejon, Surface Science **564**, 173178 (2004).

[108] W. K. Burton, N. Cabrera, and F. C. Frank, Philosophical Transactions of the Royal Society of London **A243**, 299 (1951).

[109] J. L. Robins, Applied Surface Science **33**, 379 (1988).

[110] X. Liu et al., Science **307**, 1763 (2005).

[111] http://www.webelements.com/.

[112] G. Cao, *Nanostructures and Nanomaterials: Synthesis, Properties and Applications*, Imperial College Press, 2004.

[113] S. Kodambaka, J. Tersoff, M. C. Reuter, and F. M. Ross, Physical Review Letters **96**, 096105 (2006).

[114] Y. Ding, P. X. Gao, and Z. L. Wang, Journal of the American Chemical Society **126**, 2066 (2004).

[115] J. W. Evans, P. A. Thiel, and M. C. Bartelt, Surface Science Reports **61**, 1 (2006).

[116] C. De-Giorgi et al., Surface Science **487**, 49 (2001).

[117] Y. Mo, J. Kleiner, M. Webb, and M. Lagally, Surface Science **268**, 275 (1992).

[118] Y. W. Mo, J. Kleiner, M. B. Webb, and M. Lagally, Physical Review Letters **66 (15)**, 1998 (1991).

[119] J. P. Bucher, E. Hahn, P. Fernandez, C. Massobrio, and K. Kern, Europhysics Letters **27**, 478 (1994).

[120] R. L. Schwoebel and E. J. Shipsey, Journal of Applied Physics **37**, 3682 (1966).

[121] A. F. Voter, Physical Review B **34**, 6819 (1986).

[122] H. Mehl, O. Biham, I. Furman, and M. Karimi, Physical Review B **60**, 2106 (1999).

[123] G. Kuczynski, Journal of Applied Physics **20**, 1160 (1949).

[124] W. Mullins, Journal of Applied Physics **28**, 333 (1957).

[125] W. W. Mullins, Journal of Applied Physics **30 (1)**, 77 (1959).

[126] F. Nichols and W. Mullins, Journal of Applied Physics **36**, 1826 (1965).

[127] J. Eggers, Physical Review Letters **80 (12)**, 2634 (1998).

[128] L. J. Lewis, P. Jensen, and J.-L. Barrat, Physical Review B **56**, 2248 (1997).

[129] N. Lummen and T. Kraska, Physical Review B **71**, 205403 (2005).

[130] D.-X. Tian and X.-Y. Guo, Computational Materials Science **34**, 14 (2005).

[131] W. Mullins and G. Rohrer, Journal of the American Ceramic Society **83**, 214 (2000).

[132] J. Rankin and B. W. Sheldon, Journal of the American Ceramic Society **82 (7)**, 1868 (1999).

[133] B. W. Sheldon and J. Rankin, Journal of the American Ceramic Society **82 (7)**, 1873 (1999).

[134] E. R. Leite et al., Applied Physics Letters **83 (8)**, 1566 (2003).

[135] H. Zhu and R. Averback, Philosophical Magazine Letters **73 (1)**, 27 (1996).

[136] F. Baletto, R. Ferrando, A. Fortunelli, F. Montalenti, and C. Mottet, Journal of Chemical Physics **116 (9)**, 3856 (2002).

[137] H. Bonzel, D. Yu, and M. Scheffler, Applied Physics A **87**, 391 (2007).

[138] J. Metois and J. Heyraud, Journal of Crystal Growth **57**, 487 (1982).

[139] K. Thurmer, J. E. Reutt-Robey, and E. D. Williams, Surface Science **537**, 123 (2003).

[140] D. Reinhard, B. Hal, P. Berthoud, S. Valkealahti, and R. Monot, Physical Review Letters **79 (8)**, 1459 (1997).

[141] A. La-Magna, Surface Science **601**, 308 (2007).

[142] A. Bogicevic, J. Strmquist, and B. I. Lundqvist, Physical Review Letters **81**, 637 (1998).

[143] http://jmol.sourceforge.net/.

[144] J. P. Hirth, Acta Metallurgica **7**, 755 (1959).

[145] K. Morgenstern, G. Rosenfeld, E. Lgsgaard, F. Besenbacher, and G. Comsa, PHYSICAL REVIEW LETTERS **80**, 556 (1998).

[146] S. Hendy, Coalescence via continuum method.

[147] D. Robertson and S. Brown.